Report No. 62

Characterization of Microwave MESFET Circuits under Laser Illumination: Applications to Phased Array Radar, Microwave Communications and Digital Clock Control

Sheryl M. Genco

October 1994

Guided Wave Optics Laboratory
Department of Electrical and Computer Engineering
University of Colorado at Boulder
Boulder, Colorado 80309-0425

This work was supported by the Army Research Office under Grant #DAAL-03-92-G-0289 and by the Office of Naval Research under Grant #DOD-ONRN00014-92-J-1190.

unclassified
SECURITY CLASSIFICATION OF THIS PAGE

REPORT DOCUMENTATION PAGE

Form Approved
OMB No. 0704-0188

1a. REPORT SECURITY CLASSIFICATION: unclassified	1b. RESTRICTIVE MARKINGS: none
2a. SECURITY CLASSIFICATION AUTHORITY: DISCASS	3. DISTRIBUTION/AVAILABILITY OF REPORT: unrestricted
2b. DECLASSIFICATION/DOWNGRADING SCHEDULE: N/A	
4. PERFORMING ORGANIZATION REPORT NUMBER(S): ECE/GWOL/ 62	5. MONITORING ORGANIZATION REPORT NUMBER(S): DOD-ONRN00014-92-J-1190
6a. NAME OF PERFORMING ORGANIZATION: University of Colorado 6b. OFFICE SYMBOL (If applicable):	7a. NAME OF MONITORING ORGANIZATION: Office of Naval Research Attn: Dr. Arthur Jordan, Code 1114 SE
6c. ADDRESS (City, State, and ZIP Code): Electrical & Computer Engineering Dept. Boulder, CO 80309-0425	7b. ADDRESS (City, State, and ZIP Code): 800 N. Quincy Avenue Arlington, VA 22217-5000
8a. NAME OF FUNDING/SPONSORING ORGANIZATION: Office of Naval Research 8b. OFFICE SYMBOL (If applicable):	9. PROCUREMENT INSTRUMENT IDENTIFICATION NUMBER:
8c. ADDRESS (City, State, and ZIP Code): 800 N. Quincy Avenue Arlington, VA 22217-5000	10. SOURCE OF FUNDING NUMBERS PROGRAM ELEMENT NO. / PROJECT NO. / TASK NO. / WORK UNIT ACCESSION NO.

11. TITLE (Include Security Classification)
(u) Characterization of Microwave MESFET Circuits under Laser Illumination: Applications to Phased Array Radar, Microwave Communications, and Digital Clock Control

12. PERSONAL AUTHOR(S): Sheryl M. Genco

13a. TYPE OF REPORT	13b. TIME COVERED	14. DATE OF REPORT (Year, Month, Day)	15. PAGE COUNT
technical (PhD thesis)	FROM _____ TO _____	October 1994	393

16. SUPPLEMENTARY NOTATION

17. COSATI CODES			18. SUBJECT TERMS (Continue on reverse if necessary and identify by block number)
FIELD	GROUP	SUB-GROUP	

19. ABSTRACT (Continue on reverse if necessary and identify by block number)

Optical injection of MESFETs directly affects the operating characteristics of the devices. The MESFET properties, induced by optical injection, can stabilize oscillator operating frequency, control amplifier gain, and open the door for feasible integrated microwave-optical devices. The optical injection of DC MESFETs, oscillators, and amplifiers is explored. Systems applications, including phased array radar, wave division multiplexing (WDM) and computer clock control, are provided.

The main contributions of this research are analyzing the modulation properties of the locked laser subsystem, using the locked laser system to inject MESFET devices and characterizing the photo-effects in MESFET circuits, reducing the phase noise in a microwave oscillator via optical injection and developing a theoretical description of the injection properties of oscillators that can be used to describe an injection locked laser and a microwave oscillator with a change of constants.

20. DISTRIBUTION/AVAILABILITY OF ABSTRACT	21. ABSTRACT SECURITY CLASSIFICATION	
☑ UNCLASSIFIED/UNLIMITED ☐ SAME AS RPT. ☐ DTIC USERS	unclassified	
22a. NAME OF RESPONSIBLE INDIVIDUAL: Alan R. Mickelson	22b TELEPHONE (Include Area Code): 303/492-7539	22c. OFFICE SYMBOL

DD Form 1473, JUN 86 Previous editions are obsolete.

SECURITY CLASSIFICATION OF THIS PAGE

Characterization of Microwave MESFET Circuits under Laser Illumination: Applications to Phased Array Radar, Microwave Communications and Digital Clock Control.

by

Sheryl M. Genco

B.S., Northeastern University, 1984

M.S., Syracuse University, 1987

A thesis submitted to the

Faculty of the Graduate School of the

University of Colorado in partial fulfillment

of the requirement for the degree of

Doctor of Philosophy

Department of Electrical Engineering

1994

Genco, Sheryl M. (Ph.D., Electrical Engineering)

Characterization of Microwave MESFET Circuits under Laser Illumination:
Applications to Phased Array Radar, Microwave Communications and Digital Clock Control.

Thesis directed by Professor Alan R. Mickelson

Optical injection of MESFETs directly affects the operating characteristics of the devices. The MESFET properties, induced by optical injection, can stabilize oscillator operating frequency, control amplifier gain and open the door for feasible integrated microwave-optical devices. The optical injection of DC MESFETs, oscillators, and amplifiers, is explored. Systems applications, including phased array radar, wave division multiplexing (WDM) and computer clock control, are provided.

The main contributions of this research are analyzing the modulation properties of the locked laser subsystem, using the locked laser system to inject MESFET devices and characterizing the photo-effects in MESFET circuits, reducing the phase noise in a microwave oscillator via optical injection and developing a theoretical description of the injection properties of oscillators that can be used to describe an injection locked laser and a microwave oscillator with a change of constants.

Acknowledgment

I would like to gratefully acknowledge IBM for the honor of being awarded a Resident Study Fellowship for my first three years at the University of Colorado. In particular, Dr. D. Grice and Mr. Bruno Bonetti worked diligently to get my appointment. I am forever thankful.

The final year was made possible by Professor Alan Mickelson's contracts with the Army Research Office. Finally, I would like to thankfully acknowledge Professor Mickelson's guidance during my Ph.D. research.

CONTENTS

LIST OF TABLES

CHAPTER 3

CHAPTER 4

CHAPTER 5

CHAPTER 7

CHAPTER 8

CHAPTER 9

LIST OF FIGURES

CHAPTER 1

CHAPTER 2

CHAPTER 3

CHAPTER 4

CHAPTER 5

CHAPTER 6

CHAPTER 7

CHAPTER 8

CHAPTER 9

CHAPTER 1

INTRODUCTION

1.1 Statement of Purpose

The main contributions of this Thesis are analyzing the modulation properties of the locked laser subsystem (Chapter 2), using the locked laser system to inject MESFET devices and characterizing the photo-effects in MESFET *circuits* (Chapters 3,6,7 and 8), reducing the phase noise in a microwave oscillator via optical injection (Chapter 7) and developing a theoretical description of the injection properties of oscillators that can be used to describe an injection locked laser and a microwave oscillator with a change of constants (Chapter 4).

The motivation for studying locking phenomenon is the increased signal purity when an oscillator is locked. For both the laser and the microwave oscillator, the device exhibits reduced phase noise, increased harmonic content and line narrowing due to damped phase changes. Also, the photo-effects in the illuminated MESFET produce optical gain of approximately 100 which can be used as an integrated receiver. The illuminated MESFET is modeled in this Thesis by using a voltage superimposed on the gate bias. The result is 3-5% deviation between the experiment and the theory.

Optical injection of MESFETs directly affects the operating characteristics of the devices. The MESFET properties, induced by optical injection, can stabilize oscillator operating frequency, control amplifier gain and open the door for feasible integrated microwave-optical devices. The optical injection of DC MESFETs, oscillators, and amplifiers, is explored in this thesis. The design and application of a sample-and-hold circuit (i.e., latch which could be interfaced with a digital circuit) is discussed. Systems applications, including phased array radar, wave division multiplexing (WDM) and computer clock control, are provided.

Most previous work in MESFET injection has centered around the use of simple LED systems as the source of optical power with low coupling efficiency into the device's active region. Our work takes advantage of lasers locked to a reference laser for mode stability and a focused optical beam at the MESFET surface. The lasers are direct current modulated at RF frequencies and heterodyned prior to injecting the microwave devices.

The laser spectrum is studied for locked and unlocked cases as different types of signal modulation are used. An optically injected microwave amplifier is investigated as a novel detector which replaces the standard photodetector and preamplifier stages. It is shown that the microwave amplifier has excellent responsivity and recovers information from an optical signal without additional amplification. Oscillators are frequency tuned and frequency locked to the modulated optical signal.

1.2 Thesis organization

The thesis is organized as follows: Chapter 1 is an overview of the goals of the project, brief justification of optical-effects modeling and MESFET optical injection, and a discussion of the benefits, limitations and solutions to optically injected MESFETs.

In Chapter 2, the background of locked laser theory, the results of RF modulation experiments, the reduced linewidth of injection locked lasers with RF, square, sine, and triangle wave modulation, the AM and FM characteristics, and the experimentally derived relaxation oscillation frequency are given. In Chapter 3, the physics of the dark and illuminated MESFET are discussed and the optical-effects model is investigated. In Chapter 4, the analytic discussion of oscillation theory and locking phenomenon is presented. Because both laser locking (Chapter 2) and MESFET oscillator locking (Chapter 7) are studied in detail in this Thesis, it was important to make the theoretical analogy between both types of oscillations. The design of the microwave circuits with MESFET active elements and the executed experiments are fully described in Chapter 5. In Chapter 6, 7 and 8, the experimental results and comparison with the theory is discussed for optically injected MESFETs terminated in 50Ω line, and of MESFETs in oscillator and amplifier circuits, respectively. A description of optically injected MESFET applications that serve as the motivation for this project is discussed in Chapter 9. Some conclusions are drawn in Chapter 10.

1.3 Overview

The goal is to describe the physical operation of GaAs MESFET under illumination versus dark conditions and to utilize reduced noise from a modulated locked laser system as the injection source. Figure 1 System Overview shows a block diagram of the three main areas: locked laser system, the focusing optics, and the MESFET circuits. The device physics will be developed to describe standard MESFET operation (no injection) and injected conditions. A formulation for DC, microwave modulated laser injection (or electrical injection) is investigated. Both saturated and non-saturated regimes of the photocurrent are analyzed. Primary assumptions include low level generation and no trapping or diffusion effects.

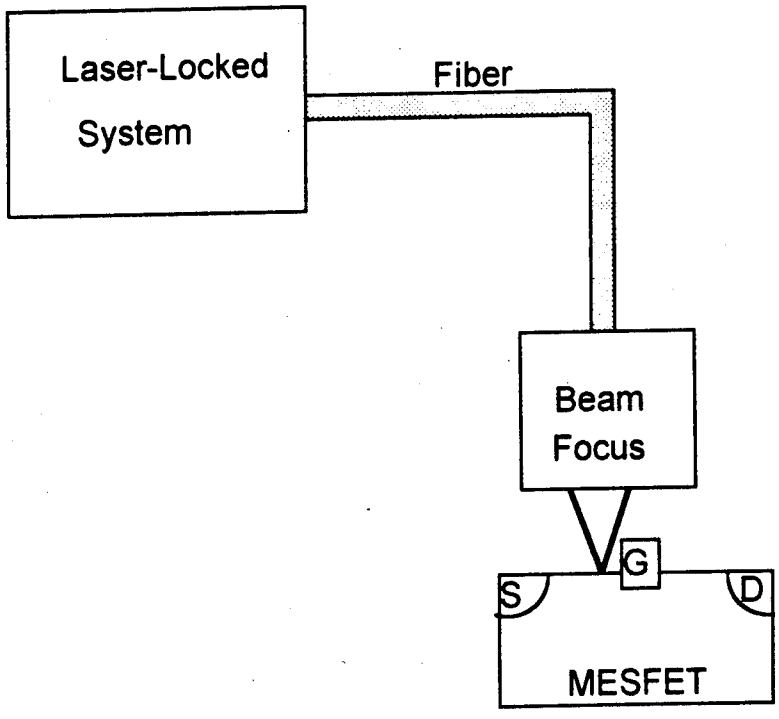

Figure 1 System Overview

1.4 Rationale for Optical-Effects Modeling

The optical-effects description of MESFET physics is necessary to understand the processes that occur under illumination. Under dark conditions, the MESFET is considered a unipolar device which is dominated by field effects in the channel. However, when a MESFET is injected with light, it becomes bipolar. The bipolar nature of an optically injected MESFET was not considered in the standard MESFET device analyses such as the Pucel two section model[1] or the three section model developed by Ki, et al.[2]. The bipolar effect is caused by light induced increases in the free carrier density of the channel. This process originates from the separation and collection of electron-hole pairs along the channel which can be described by the transport dynamics. Therefore, it is vital to consider both electron and hole currents in a physical model of the illuminated MESFET.

To label the optical effect as a photovoltaic or photoconductive process depends on the analysis point of view. Changes in the active channel resistance arise due to increase carrier density when illuminated. This may be termed photoconductive. When carriers are separated due to optical injection, the depeltion region Schottky barrier potential is lowered which in turn widens the active channel. This may be termed photovoltaic. The main point is that minority carriers cause changes in the MESFET.

Using experimental data, the optically induced effects of a microwave amplifier are further explained. Standard coherent detection methods are replaced

by optically injected MESFET circuits which are shown to provide better signal to noise characteristics. These circuits are applied to a viable wavelength division multiplexed (WDM) system. Our work takes advantage of a locked laser subsystem, and therefore, optical mode stability is provided prior to injecting into a MESFET. Analytic results will be discussed and compared with experiment.

The diffusion equation for holes is solved analytically. The hole concentration is used to calculate a voltage via the Schottky diode model. This is done in the field of solar cells, and is applied to the optically injected MESFET in this Thesis. The voltage acts to forward bias the gate junction. This has been shown to account for over 90% of the increase in drain current. The effective gate voltage is the bias plus the Schottky voltage. The effective gate voltage is used in existing MESFET models with reasonable results. 5% of the optical gain is due to the transport of the photo-generated carriers.

The framework for the transit time analysis begins with the current density and current continuity equations along with Poisson's equation. After solving these equations simultaneously, substitutions for injected phenomenon are developed, and the resultant coupled system of equations can be solved. In developing the solutions, expressions result mathematically which are exactly the definitions for transit time and relaxation time. In the mathematics, we find the elegant description of the bipolar transport dynamics of the MESFET. Transit time analysis of devices is not a new field[3,4,5]. Transit time analysis does provide insight into the device physics particularly when illuminated but accounts for less than 5% of the optical effect in the MESFET.

1.5 Benefits of Optically Injected MESFET

Optical injection of microwave active devices (e.g., MESFETs) is analogous to adding an extra terminal to a device through which the optical input can control the output of the MESFET.

The MESFET, used as an optically sensitive microwave element, is an effective way to exploit the benefits of low loss, high bandwidth, electromagnetically immune single mode fiber. Using the MESFET as an optical receiver replaces the standard receiver subassembly (e.g., photodetector plus pre-amplifier) in a system and additionally, is a part of the operating circuit. Therefore, integration of the optical receiver and microwave circuit is achieved which enables system miniaturization, reduced system noise, and immunity from electromagnetic interference.

Direct electrical connections are the conventional methods to control a microwave MESFET. Many electrical connections cause interference and noise problems as well as the difficulty of physically providing the electrical connection. Lightweight, high bandwidth optical fibers can be used to distribute the signal. Fibers are excellent system components particularly in airborne applications where weight is a design parameter and for parallel computer architectures that require many connections. Distribution of signals via fiber can greatly reduce the cost and enhance the performance of such complicated systems. Direct optical control of MESFETs can result in frequency control of microwave oscillators, gain control of

amplifier circuits, lower overall signal to noise characteristics, immunity from electromagnetic interference and electrical isolation.

The benefits of the MESFET as an optically sensitive element are well suited as a low-noise receiver, for distribution and recovery of clock signals, transmission of control signals for phased array antennas, and coherent demodulation.

1.5.1 Limitations and Solutions

Although the limitations of optically injected MESFETs are relatively poor coupling efficiency between the beam and the active device region and the maximum modulation frequency of available semiconductor diode lasers is several GHz, both limitations can be overcome.

Efficiency can be increased by fabricating a microlens structure at the end of optical fibers[6] to focus the beam and then to attach the fiber and microlens to the device in the manner that is currently used in pigtailing LEDs and PINs. By applying semiconductor laser diode technology to the coupling problem, fabrication of an etched optical window on the MESFET is also possible to enhance coupling efficiency. Windows were constructed on IMPATT diodes without any RF performance degradation [7]. Both a flip chip (junction side down) and a top mounted IMPATT were studied[8]. These are discussed in Chapter 5.3.2 Coupling Enhancements.

Subharmonic injection locking can overcome the laser modulation limitation. However, the locking range decreases as the frequency ratio of the fundamental and subharmonic increases. Excellent results have been achieved by using heterodyned locked laser signals to subharmonically inject the MESFET because the locked laser system provides excellent frequency stability and low signal noise.

With the coupling enhancements and heterodyne locked lasers, it is possible to directly inject MESFET with greater efficiency and overall performance than indirect methods (PIN detection followed by pre-amplification). This is in contradiction to a study done by Herczfeld, et.al.,[9] but this work did not address methods of improving coupling or ways to extend the maximum modulation frequency.

HEMT devices can further lower signal-to-noise because the high mobility of the electrons in the active channel of the heterojunction gives rise to high velocity. The high velocity of the electrons in the active channel is related to the cutoff frequency which is inversely related to the noise figure through Fukui's equation[10]. The characteristics of the illuminated HEMTs were analyzed by Simons [11] in 1987 which was followed by their application to an oscillator and amplifier system by deSalles in 1991[12,13].

1.6 References - Chapter 1

[1] R.A. Pucel, H.A. Haus, and H. Statz, "Signal and Noise Properties of GaAs Microwave Field-Effect Transistors", Advances in Electronic and Electron Physics, edited by L.Marton, Academic Press, vol.38, 1975, pp.195-265.

[2] H.C. Ki, S.H. Son, K. Park, and K.D. Kwack, "A Three-Section Model for computing I-V Characteristics fo GaAs MESFET's", *IEEE Transactions on Electron Devices*, vol. ed-34 no.9, September 1987, pp. 1929-1933.

[3] J.G. Ruch, "Electron Dynamics in Short Channel Field-Effect Transistors", *IEEE Transactions on Electron Devices*, vol. ed-19, May 1972, pp. 652-654.

[4] Kjell Blotekjaer,, "Transport Equations for Electrons in Two-Valley Semiconductors", *IEEE Transactions on Electron Devices*, vol. ed-17, no. 1, January 1970, pp.38-47.

[5] R.B. Darling, "Transit-Time Photoconductivity in High-Field FET Channels", *IEEE Transactions on Electron Devices*, vol. ed-34, no.2, Fegruary 1987, pp.433-443.

[6] Kung S. Lee and Frank S. Barnes, "Microlenses on the end of single mode optical fibers for laser applications", *Applied Optics*, vol.24, no. 19, pp.3134-3139, October 1, 1985.

[7] A. Schweighart, H.P. Vyas, J.M. Borrego, and R. Gutmann, "Avalance diode Structures Suitable for Microwave-Optical Interactions", *Solid-State Electronics*, vol.21, no.9, September 1978, pp. 1119-1121.

[8] A. Schweighart, H.P.Vyas, J.M. Borrego, and R. Gutmann,"Effect of Hole versus Electron Photocurrent on Microwave-Optical Interactions in IMPATT Oscillators", *IEEE Transactions on Electron Devices*, vol. ed-26, no. 3, March 1979, pp.232-234.

[9] A.S. Daryoush, P. Wahi, P.R. Herczfeld, and Z. Turski, "Comparison of Indirect Optcial Injection Locking Techniques of Multiple X-Band Oscillators", *IEEE MTT-S Digest*, June 1986, pp.615-618.

[10] H. Kukui, "Optimal Noise Figure of Microwave GaAs MESFET's",*IEEE Transactions on Electron Devices*, vol.ED-26, no.7, July 1979, pp. 1032-1037.

[11] R.N.Simons, "Microwave Performance of an OPtically Controlled AlGaAs/GaAs Hiegh Electron Mobility Transistor and GaAs MESFET", *IEEE Transactions on Microwave Theory and Techniques*, vol.MTT-35, no.12, December 1987, pp.1444-1455.

[12] A.A. DeSalles, and M.A. Romero, "AlGaAs/GaAs HEMT's Under Optical Illumination", *IEEE Transactions on Microwave Theory and Techniques*, vol. 39, no.12, December 1991, pp.2010-2017.

[13] A.A. DeSalles, "Optical Effects in HEMTs", *Microwave and Optical Technology Letters*, vol.3, no.10, October 1990, pp.350-354.

CHAPTER 2

LASER SPECTRUM

2.1 Introduction

Two concepts are investigated in detail in this chapter; injection locked lasers and laser modulation characteristics. One of the applications investigated in *Chapter 9* is a laser communications system using wavelength division multiplexing (WDM). The injection locked laser system provides the necessary mode stability to make WDM viable. Furthermore, the modulation characteristics of lasers are important for systems at RF (1-5 GHz) as well as typical digital frequencies (2-250 MHz). Therefore, this chapter studies locked and unlocked effects of RF modulation as well as square, sawtooth, lower speed sine, and pulsed RF laser modulation, and AM and FM at gigahertz carrier frequencies.

A brief history is given in the next section. In 2.3 Injection Locked Lasers, the system is described in detail. The theory of laser injection locking overlaps with the theory of microwave oscillator locking (*Chapter 7*) and therefore, is treated together in detail in *Chapter 4*. Because the study of RF laser modulation is a key component of the injection locked laser system, it was necessary to identify the maximum RF frequency to produce a laser response. Experiments were conducted

to identify the relaxation oscillation frequency of the semiconductor lasers used in this Thesis (2.4.1 Relaxation Oscillation).

To use injection locked lasers for WDM applications, it was necessary to quantify the changes in the spectrum and linewidths under various modulation conditions. The injection locked system is described in 2.3 Injection Locked Lasers. RF modulation (2.4.3 Single Laser RF Response) produces the microwave subcarrier frequency bands to which the information channels are locked. The information is modulated at slower speeds and is representative of digital bit stream. Pulse trains of square, sawtooth (triangle) and sine waves at 20 MHz are used to modulate the slave lasers both with and without laser injection locking (2.4.4 Pulse Modulated Response). The response of a single laser to an RF pulse modulated laser is investigated in 2.4.5 Pulsed RF Response. In Section 2.4.6, a laser response to a square wave at 250 MHz is obtained to identify any differences in higher speed modulation. Amplitude and frequency modulation of an RF carrier are presented in 2.5 AM and FM Laser Characteristics. Spectral broadening can limit the useable bandwidth of a single mode fiber due to dispersion, and therefore, FM characteristics are an important consequence of laser communication systems. Theoretical description of the modulation properties of injection locked semiconductor lasers is presented in 2.6. Conclusions are drawn in the final section.

2.2 Background

Adler's theory of electrical injection was published in 1946 [1]. He-Ne lasers were injection locked by Stover and Steir and were proven to behave according to Adler's theory[2]. Injection locking has been used to perform conversion from frequency to phase modulation[3], to study optical phase locked loops[4], optical FSK modulation[5,6], to design multi-frequency laser transmitters[7], and to investigate lasers free from electrical bandwidth constraints[8]. Heterodyne detection techniques receive information from coherent optical transmission systems where optical phase or frequency carries the information. The advantages of injection locked lasers include reduction of frequency chirp[9,10,11], suppression of partition noise and mode hopping[12], and linewidth reduction[13,14]. Mode hopping occurs due to temperature and current fluctuations and also, due to spontaneous emission.

Frequency chirp occurs due to gain induced variations of the refractive index in the range up to a few hundred megahertz[15]. Direct current modulation produces the desired modulation of the optical power and also, the wavelength. Chirp is generally larger for square wave than for sine wave modulation due to the sharp edges. Pulse shaping of digital square wave is a mechanism for decreasing the chirp effects by smoothing the rise and fall times[16]. In 2.4.4 Pulse Modulated Response, it is shown that the locked laser system reduces the chirp.

Fluctuations in the phase and intensity of the optical field produce changes in the laser linewidth because carrier density varies with changes in the real refractive index. As the laser reverts back to steady state, the imaginary and real part of the

refractive index changes which cause additional phase fluctuations and line broadening[17]. The process of injection locking dampens instantaneous phase changes caused by spontaneous emission, which subsequently reduces linewidth broadening and shapes the structure of the laser power spectrum[18].

Optimally, the injected frequency should coincide with the resonance frequency which is downshifted by the injection. When injected, the light output increases causing the excited carrier density to decrease. Thus, the refractive index increases which subsequently, lowers the cavity resonance frequency[19]. Also, the stability of the locking and the locking range sets the amount of detuning for an optimal lock. Locking bandwidth and relaxation oscillation of injection locked lasers have been studied since the early 1980's with the work by Kobayashi and Kimura which reported 500 MHz optical locking bandwidth[20].

2.3 Injection Locked Lasers

Injection locked lasers provide several advantages over a single modulated laser. These include reduction of frequency chirp, suppression of partition noise and mode hopping, and linewidth reduction. In this chapter, evidence of the improved spectral characteristics of injection locked lasers under various modulation conditions is presented. In *Chapter 5.3*, the experimental details of injection locked laser system and the variation of laser wavelength with drive current and temperature are discussed. In Figure 1, an overview of the injection system is given.

The Reference is injected into the RF modulated Master laser. The Master is then injected into the slave (S1-Sn) lasers which carry the lower frequency information. The lasers are directed into fibers and coupled in 3 dB optical couplers. The outputs of the couplers are transmitted to the microwave MESFET circuits and to diagnostic equipment.

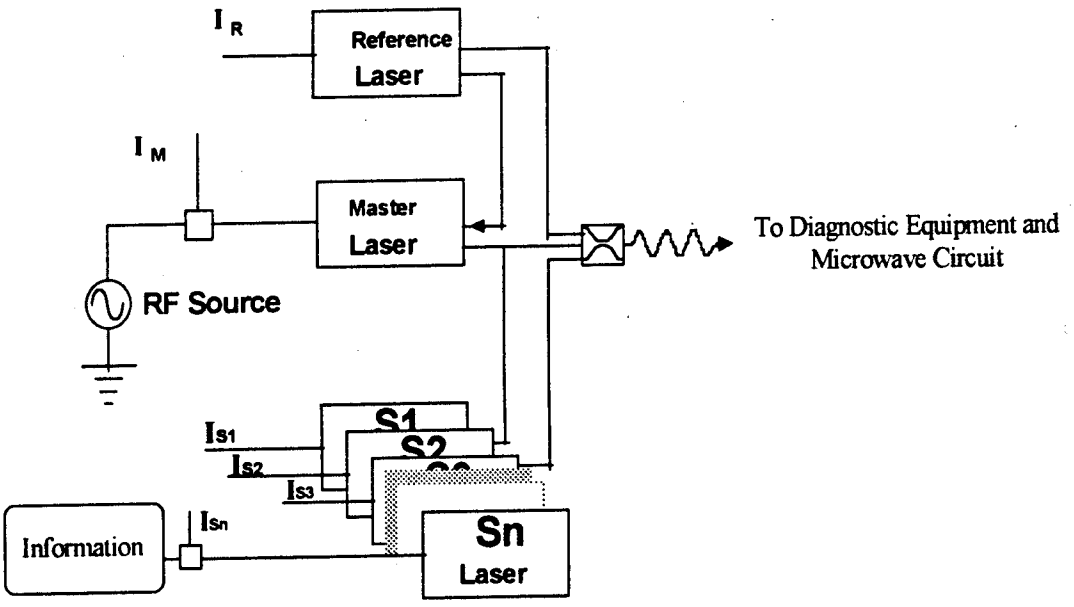

Figure 1 Overview of Injection Laser System

2.3.1 Laser Mode Stability

Mode hopping occurs due to temperature and current fluctuations and also, due to spontaneous emission. In WDM schemes, many channels of information are multiplexed onto one fiber. If the channels modes shift during transmission, the receiver may not know which mode to identify with a given channel. Therefore, the channel information will be routed to an

incorrect destination. Controlling the mode of a laser is necessary to implement WDM schemes. Laser locking provides mode stability relative to the reference laser. Other methods, such as automatic frequency control (AFC) systems, (Figure 2) are possible. AFC methods use a control loop to adjust the temperature of the laser cavity since one of the strongest influences on a laser mode is the temperature[21] . However, AFC methods do not offer the added benefits of reduced linewidth from an injection locked laser system. Another disadvantage is that there is a finite response time associated with the driving electronics of AFC methods.

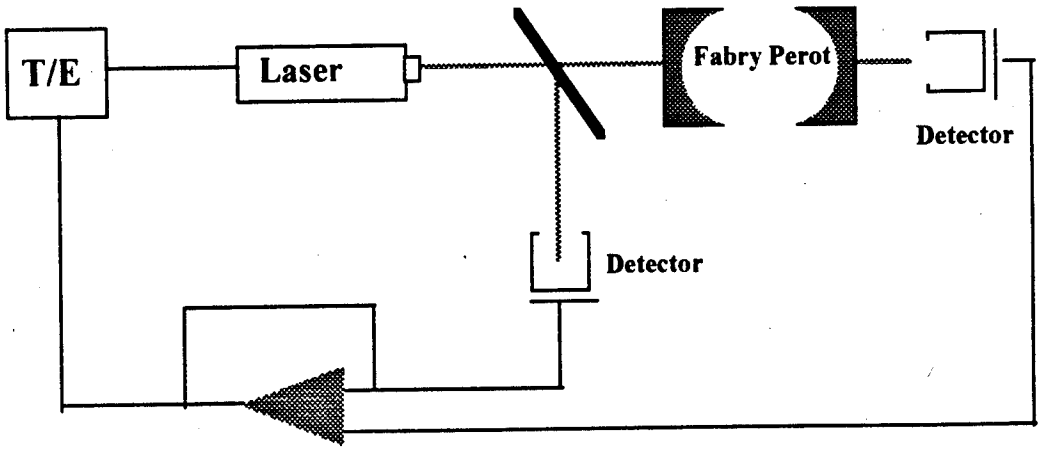

Figure 2 Automatic Thermoelectric Frequency Control System

The information capacity of a fiber transmission system is increased by multiplexing more information onto one fiber. In Figure 3, the frequency relationships between the Reference, Master, and Slave lasers is given. When the Master is modulated at an RF frequency, f, equally spaced sidebands are produced each of which locks to a Slave. Each Slave can also be modulated at digital rates indicated by the box about the frequency line. The maximum information per channel (Slave) is limited by the spacing of the Master sidebands.

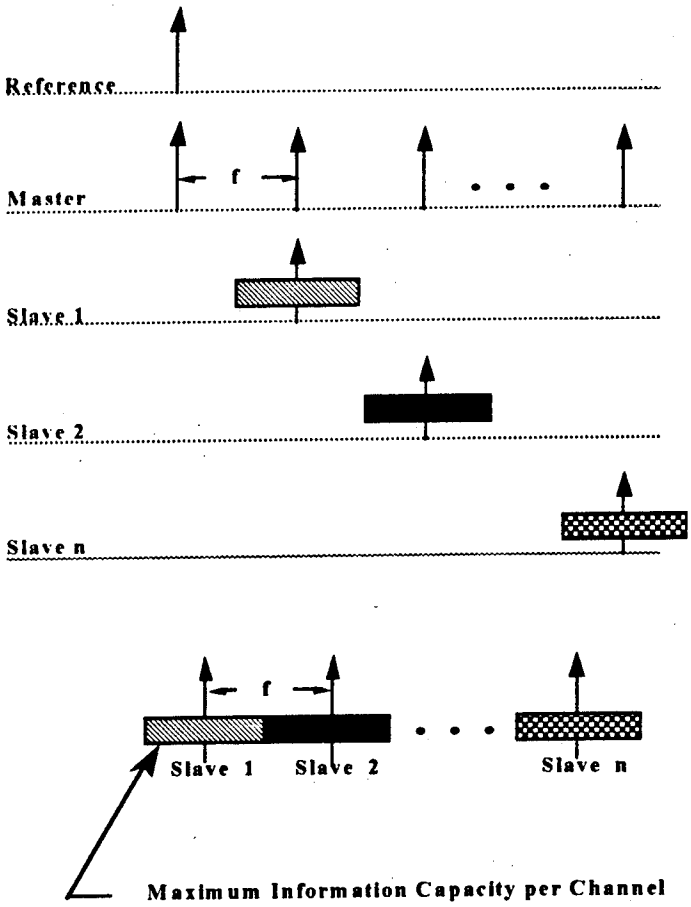

Figure 3 Frequency relationships between lasers

2.3.2 Injection system

The laser injection system is shown in Figure 4 Detailed Laser Injection System. The rationale for each component in the system is given in significant detail in *Chapter 5.3*. The Reference injects the Master, and the Master injects the Slaves. The optical isolators and waveplates prevent self locking and prevent reverse injection. Each laser is directed into a single mode fiber which has polarization controllers attached as shown in Figure 5. Fiber couplers are used to combine the three optical signals. The coupler outputs are transmitted to diagnostic equipment and to the MESFET circuit. When the Reference and Slave are combined,

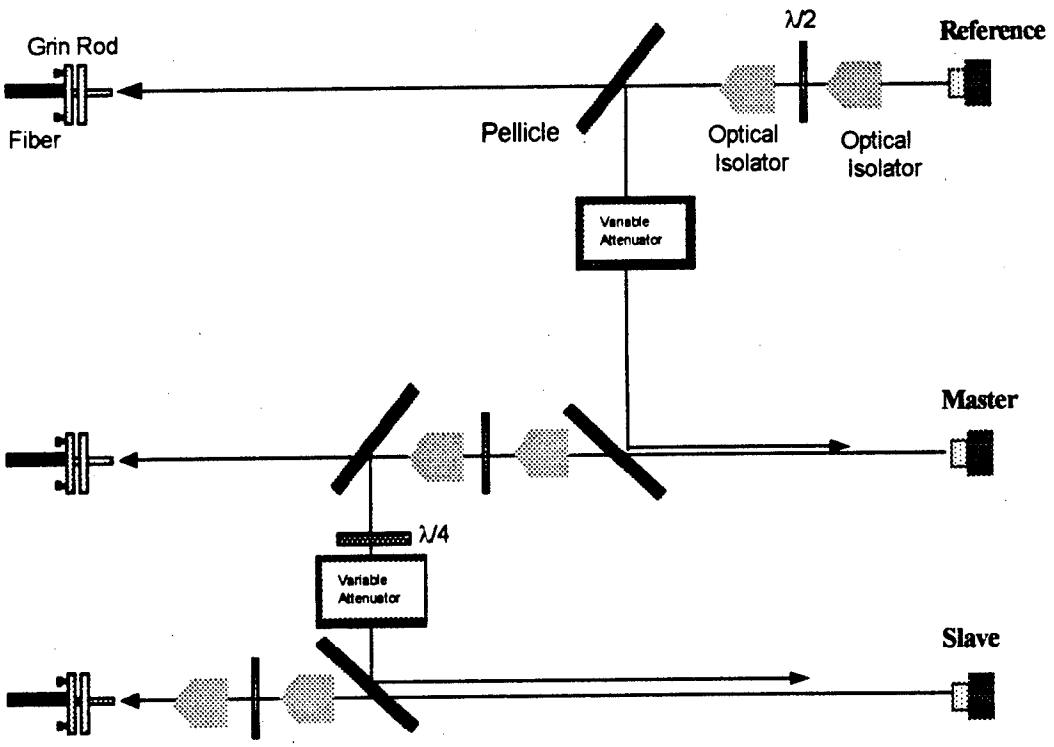

Figure 4 Detailed Laser Injection System

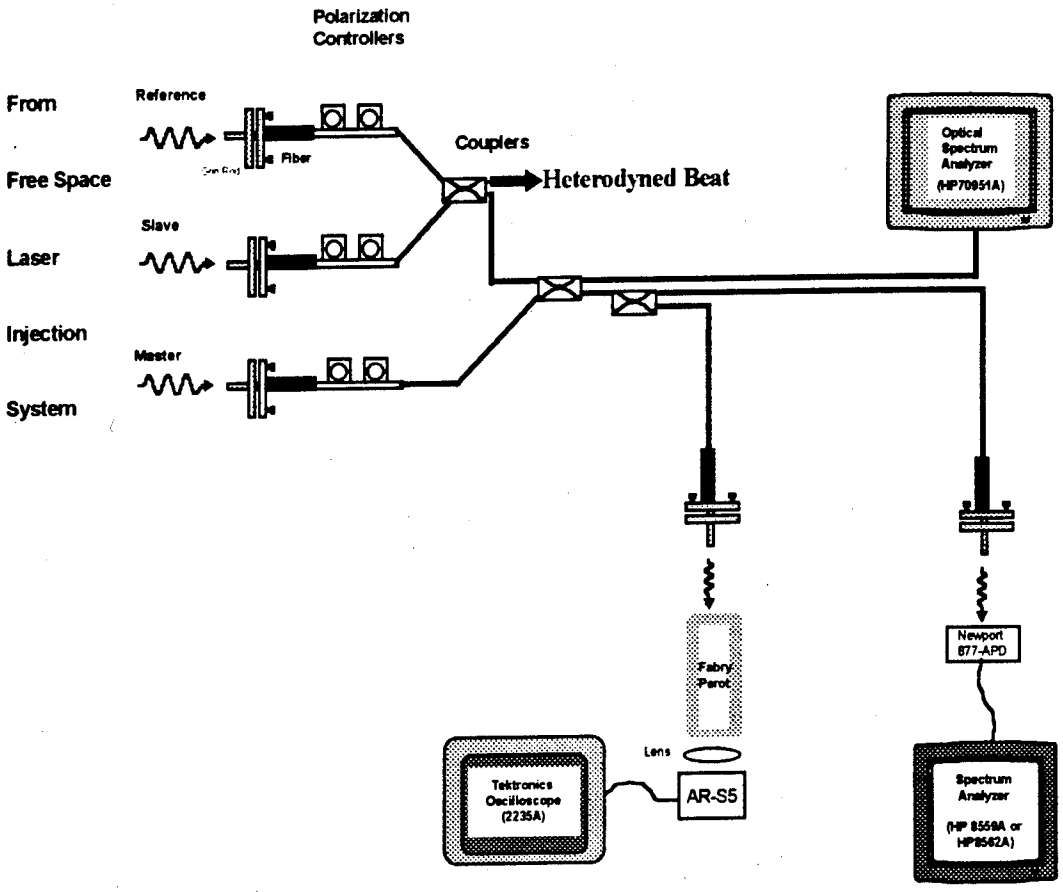

Figure 5 Heterodyne Generation and Diagnostic Setup

the output is the heterodyned beat note between the two lasers at the microwave frequency, f, of the modulated Master. Although the maximum achievable emitted power is 30 mW for the Mitsubishi lasers, the total amount of power available prior to the fiber was 10 mW for high values of laser bias current because there was an experimental tradeoff between optical power coupling and collimation of the laser beam. However, with the best collimation and alignment of all components, only 10% of the original is available at the output of the couplers as shown in Figure 6.

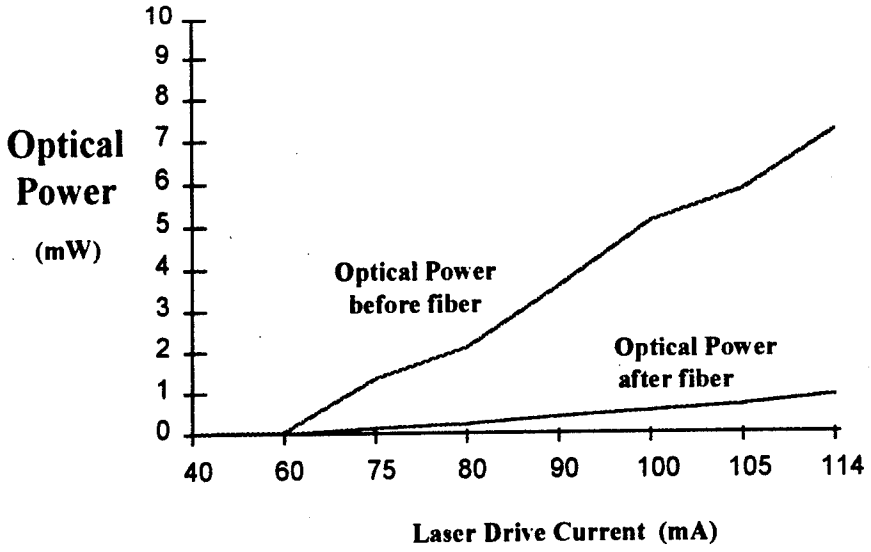

Figure 6 Optical Power vs. Laser Drive Current

2.4 Characteristics of Modulated Lasers

The characteristics of modulated lasers (locked and unlocked) is presented in this section. The reduction of the laser linewidth and reduction of frequency are proven in the following sections. The relaxation resonance is experimentally derived in the first section. The spectrum and linewidths of RF modulated lasers under lock are given in 2.4.2. The overall RF response of the lasers is in next section which is followed by the response to pulse trains of squares, sawtooths, and sinusoids in 2.4.4. The laser response to a pulse modulated RF sinusoid is given in 2.4.5 which is followed by a fast digital square wave modulation at 250 MHz.

2.4.1 Relaxation Oscillation

The small amplitude quasi-sinusoidal exponentially damped oscillations about the steady state amplitude are termed relaxation oscillations. This occurs when a continuously operating laser is slightly disturbed or if recovery time of the excited state population inversion is substantially longer than the laser cavity decay time. A linearized small signal analysis gives analytic solutions for the relaxation oscillation frequency and damping rate[22]. The equations for the photon number n(t) in the oscillating mode and the population inversion N(t) are given below:

$$\frac{dn(t)}{dt} = KN(t)n(t) - \gamma_c n(t)$$
$$\frac{dN(t)}{dt} = R_p - \gamma_2 N(t) - KN(t)n(t)$$

The atomic decay rate is γ_2, and the pumping rate for the laser inversion is R_p. The coupled nonlinearity is a result of KN(t)n(t). The photon decay due to cavity losses plus output coupling is represented by γ_c. K is the coupling constant of the rate equation which includes a Lorentzian lineshape dependence on ω. The steady state solutions are used to produce the linearized small signal form of the rate equations which can be solved analytically to produce the relaxation frequency:

$$\frac{\omega_{osc}}{2\pi} = \sqrt{\frac{r-1}{\tau_c}\frac{1}{\tau_2}}$$

where r is the amount of pump above threshold, τ_c is the cavity life time, and τ_2 is the upper level lifetime of the inverted population in the p-n junction ($\tau_2 = 1/\gamma_2$).

With a cavity lifetime of 1 ps, an upper life time of 1.2 ns, and the GaAs pumped to 1.75 times threshold, the relaxation frequency is 3.99 GHz. As demonstrated in Figure 8 Measured Laser Relaxation Oscillation, this compares favorably to the experimentally derived value of 4.2 GHz since the exact laser parameters are not known for this particular device.

Experimentally, the laser relaxation frequency is determined by driving the laser with an ultra-fast rise time pulse. In Figure 7, a Picosecond Pulse Generator (PSPL-4050B) in conjunction with the fast pulser head (PSPL-4050-RPH) was used to drive the laser with a 1 ns duration. The bias tee used is PSPL 5550B (t_{rise} = 20 ps). The laser output was detected by a Silicon avalanche photodiode (Si-APD) which is rated for rise time maximum of 90 ps. The data was observed on an Hewlett Packard (HP) Digital scope with synchronization provided by the PSPL 4050B trigger output.

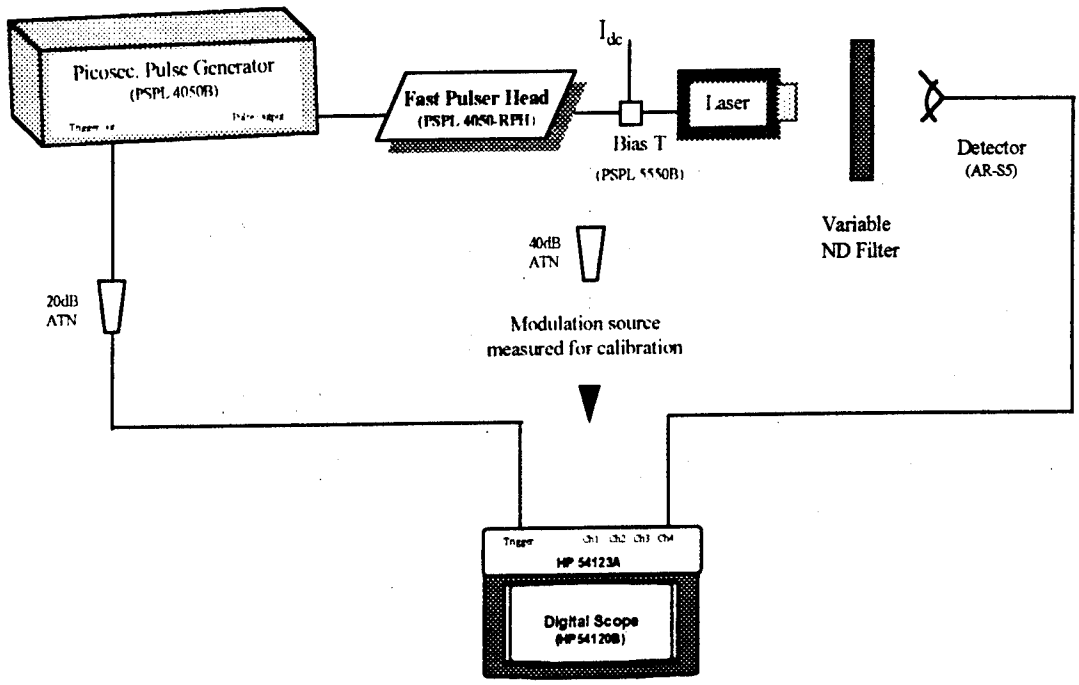

Figure 7 Experiment to measure Relaxation Oscillation

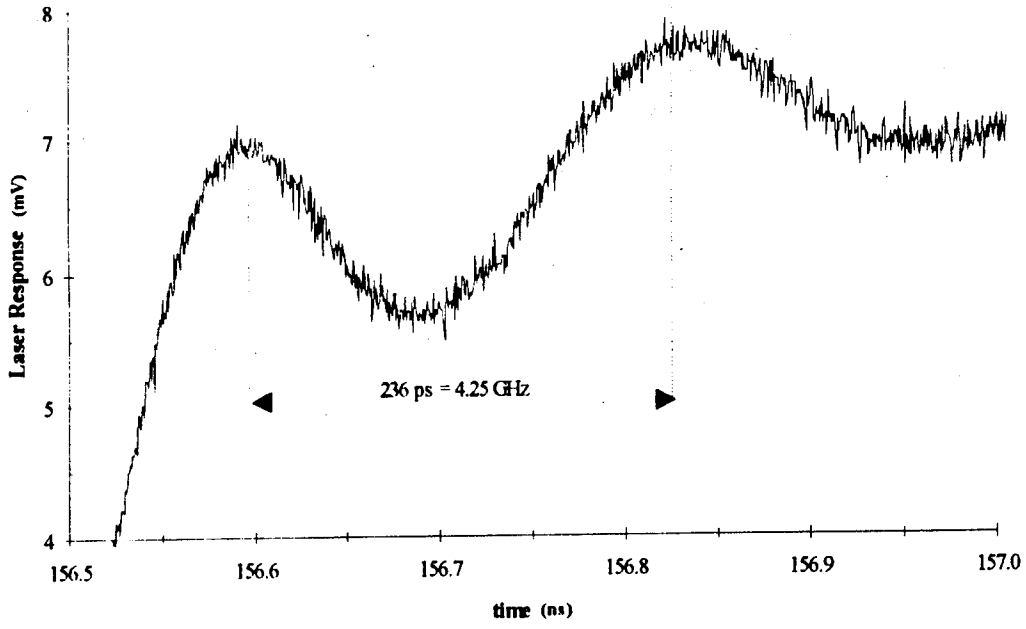

Figure 8 Measured Laser Relaxation Oscillation

2.4.2 RF Modulated Locked Lasers

In this section, the Master laser was modulated at RF frequencies. The optical spectrum was obtained by using an optical spectrum analyzer (OSA) and a Burleigh Fabry Perot Etalon detected and displayed on an oscilloscope. The linewidth of the lasers (unmodulated, modulated, and locked heterodyne beat) are also presented. Figure 9 shows the equipment used to modulate the Master. The RF amplifier was needed to experiment with the modulation power versus the locking bandwidth and the stability of the lock.

The HP optical spectrum analyzer was set to receive all three lasers via one fiber from the 3 dB couplers as shown in Figure 10. The OSA was used to adjust the wavelength to within 0.01 nm. At this point, the etalon output was used for final locking verification. The optical spectrum of all three unlocked lasers is shown in Figure 12 (a), the modulated Master is locked to the reference in Figure 12 (b) while the Slave is free running, and Figure 12 (c) shows the final step when the Slave is injection locked to the Master. The span is 10 nm, the resolution and video

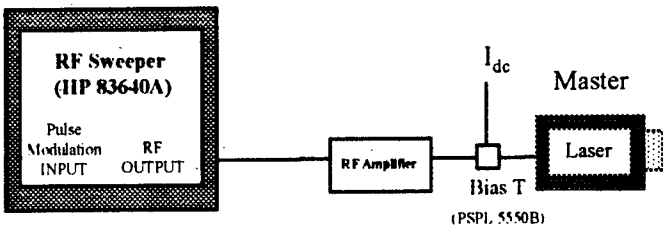

Figure 9 RF Modulation to Characterize locked vs. unlocked linewidths and spectra

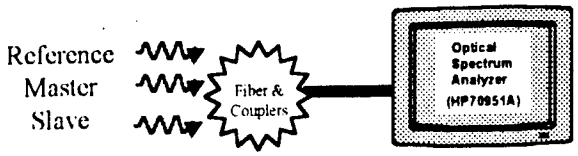

Figure 10 Optical Spectrum Analyzer used to Determine Laser Spectrum

bandwidths are 0.1 nm and 100 KHz respectively, the sweep time is 50 msec, the scale is 10 dB/vertical division, the reference level is -9.46 dBm, the marker position is placed on the Reference spectrum at wavelength of 822.76 nm. Observe the modes progressively merge as each laser is locked. In the 1 nm band to the left of the marker, the unlocked to locked spectral content is reduced by 15 dBm.

Three measurements of linewidth were observed: unmodulated, modulated, and locked heterodyne beat. In Figure 11, the linewidth was measured by allowing two lasers to beat together and direct detecting the output on a Newport 877 APD which fed a HP8559A Spectrum Analyzer.

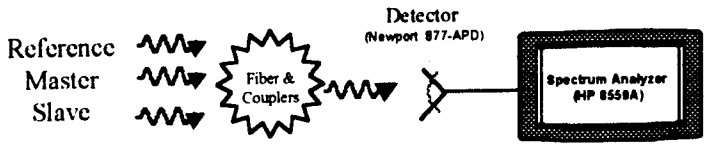

Figure 11 Direct Detection of Linewidth with HP8559A Spectrum Analyzer

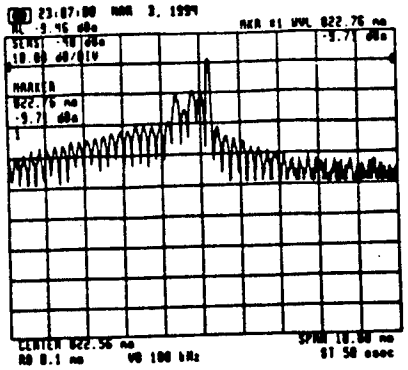

a. All three free running lasers

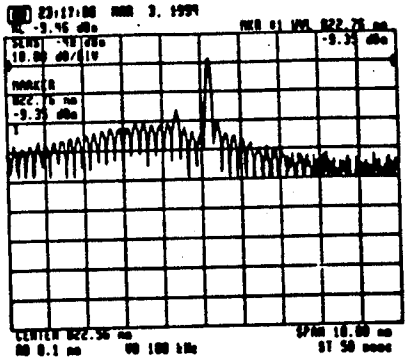

b. Master Locked to Reference
Slave Unlocked

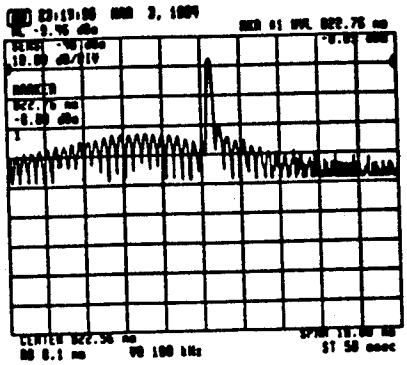

c. Master Locked to Reference
Slave Locked to Master

Figure 12 Comparison of Laser Spectrum with RF Modulated Master

The linewidth results are in Figure 13 where each vertical division is 10 dB. The unmodulated Master is not injected with the Reference, but the two beat together to produce the unmodulated linewidth in Figure 13 (a). In Figure 13 (b), the Master is modulated at 3 GHz and heterodyned with the Reference without locking to measure the modulated linewidth. The modulated linewidth is broader because of the additional frequency components in the spectrum due to the modulation. The optical gain varies with the carrier density causing the number of lasing modes and hence the width of the spectral envelope to increase[23]. Finally, the lasers are locked, and the heterodyned beat between the Reference and the Slave is captured exactly at 3 GHz on the horizontal scale (Figure 13 c). The Newport 877 has a specified unity gain only up to 1.7 GHz, but at 3 GHz , the 877 output power specified at -6 dB (25%). Therefore, the decrease in linewidth amplitude can be attributed to the equipment. Note that the heterodyne linewidth is exactly 6 dB below the unmodulated line. The linewidth narrows from 20 MHz in Figure 13 (a) to 200 KHz in Figure 13 (c). For each measurement in Figure 13, the vertical is 10 dB per division, the span is 20 MHz, the resolution bandwidth is 3 MHz, reference level is 12 dBm, and the attenuation level is 0 dBm.

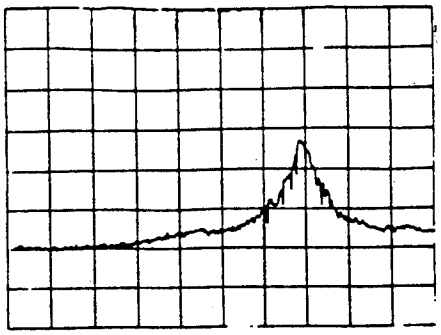

a. Unmodulated Linewidth

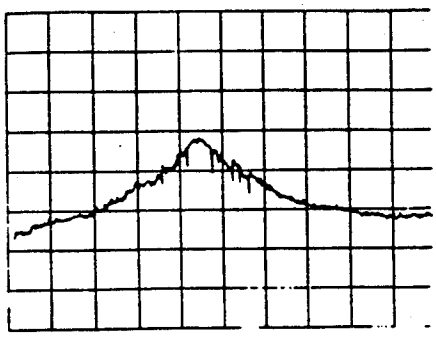

b. Modulated Linewidth

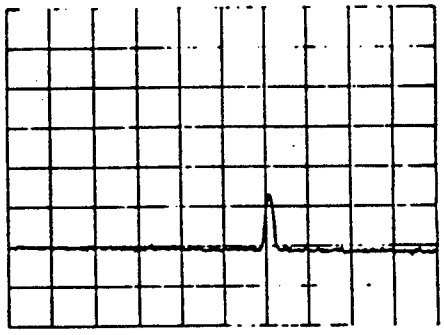

c. Heterodyned and Locked Linewidth

Figure 13 Comparison of Laser Linewidth

2.4.3 Single Laser RF Response

The response of a single modulated laser is measured in this section. Measurements of the spectrum from a Fabry Perot interferometer and direct intensity detection in time and frequency are presented.

The Fabry Perot had 100-150 GHz free spectral range across one sweep depending on the cavity spacing. This means 10-15 GHz per division which was sufficient to see the RF sidebands greater than 2 GHz. However, due to the periodic nature of the etalon, aliasing occurs, and therefore, the spectrum viewed on the scope may be separated by a multiple of 100-150 GHz relative to one another. If the spectra viewed from the Fabry Perot was within one free spectral range, then a beat note on the spectrum analyzer existed or the OSA showed the lines close in absolute wavelength. In Figure 14, the experiment for the detection of the Fabry Perot spectra is given. The scanning electronics of the Fabry Perot provided the trigger for the oscilloscope.

The results in Figure 15 were downloaded from an HP Digital scope. However, during most of the experimental stages, an analog Tektronics scope was used. During the experiment, a change from Hitachi to Mitsubishi lasers was made (rationale in *Chapter 5*). The Hitachi lasers exhibited relaxation at approximately 5 GHz. However, the Mitsubishi lasers showed relaxation near 4 GHz. In Figure 15, the RF modulation frequency is labeled on each graph (f_{RF}). The resolution of the Fabry Perot was inadequate to see the sidebands at 1 GHz but are clearly visible at 2 and 3 GHz. Comb generation at 4 GHz and basically no response at 5 GHz is a

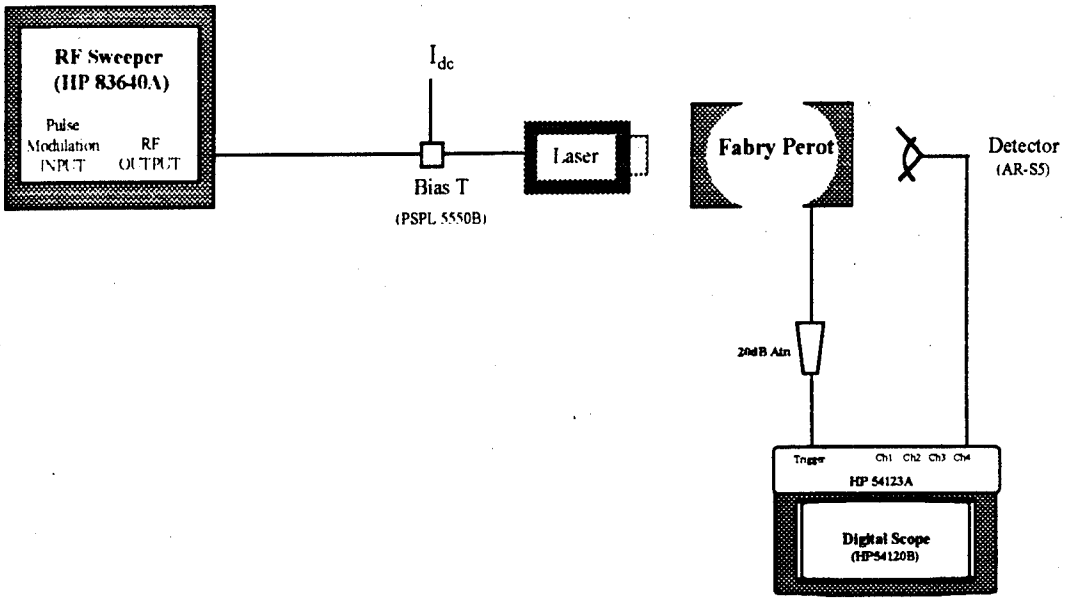

Figure 14 Direct Detection of RF Frequency Spectrum from Fabry Perot Etalon

clear indication of relaxation. The relaxation oscillation was measured and calculated in 2.4.1 Relaxation Oscillation to be 4.2 GHz which agrees with the spectral results of Figure 15.

To facilitate diagnostics and for injecting the MESFET circuits, it was necessary to have the best laser frequency response. At 3 GHz, the sideband is easily distinguished and the power level is adequate. The results in Figure 16 were obtained by photographing the display of a Tektronics 2235A analog scope which replaced the HP digital scope shown in Figure 14.

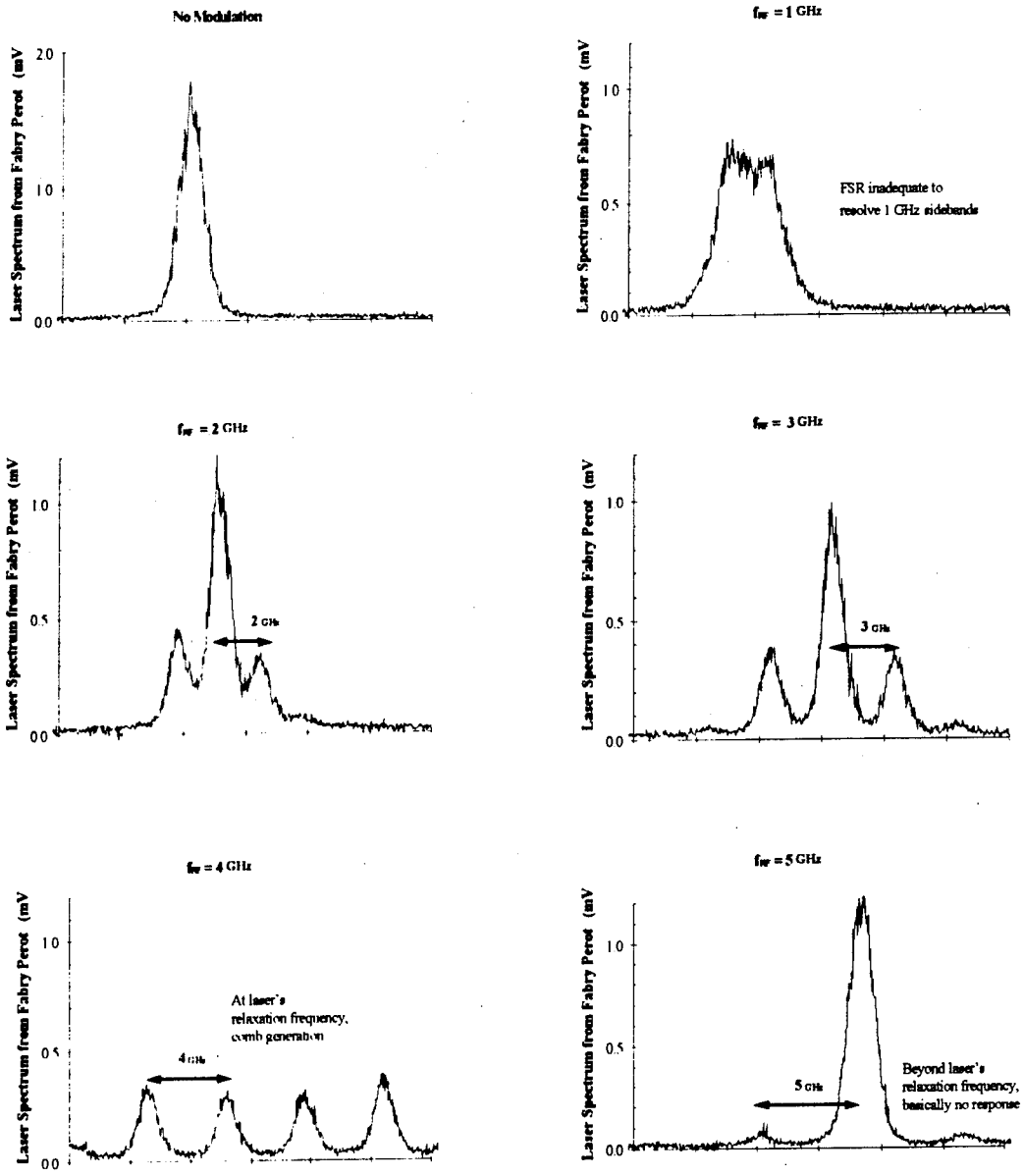

Figure 15 Laser response to RF Modulation before and after relaxation oscillation (horizontal graticules are identical)

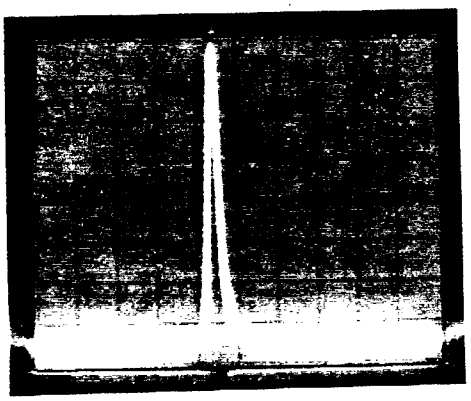

a. No modulation

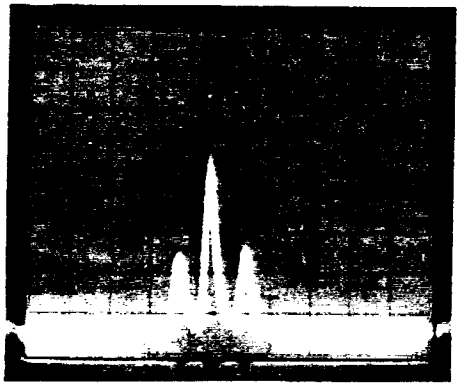

b. RF modulation @ 2.9 GHz

Figure 16 Single Laser Direct Intensity Modulated

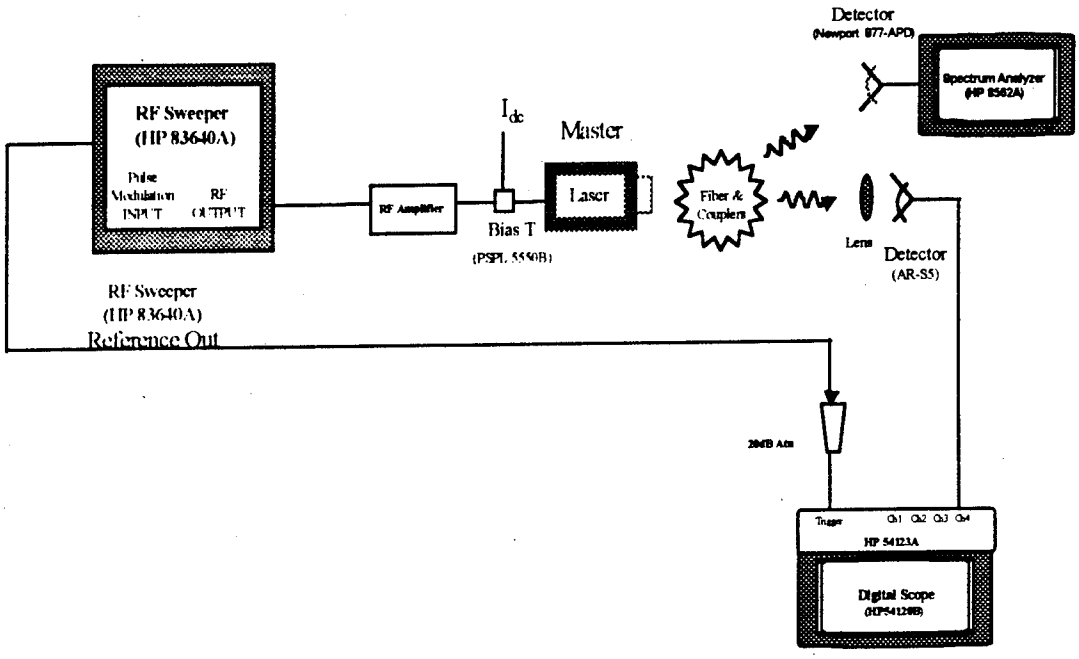

Figure 17 Single Laser Modulation and Direct Detection

Due to equipment limitations, the maximum RF to which AM or FM can be superimposed is 1 GHz. Therefore, for completeness the laser response to 1 GHz RF sinusoidal modulation was necessary. The experimental arrangement is shown in Figure 17. Because the Fabry Perot and the OSA are not able to distinguish a 1 GHz signal easily, the digital scope was used to directly detect the 1 GHz sine wave in time (Figure 18) while the electrical spectrum analyzer was used to detect the frequency spectrum of the detected laser signal (Figure 19).

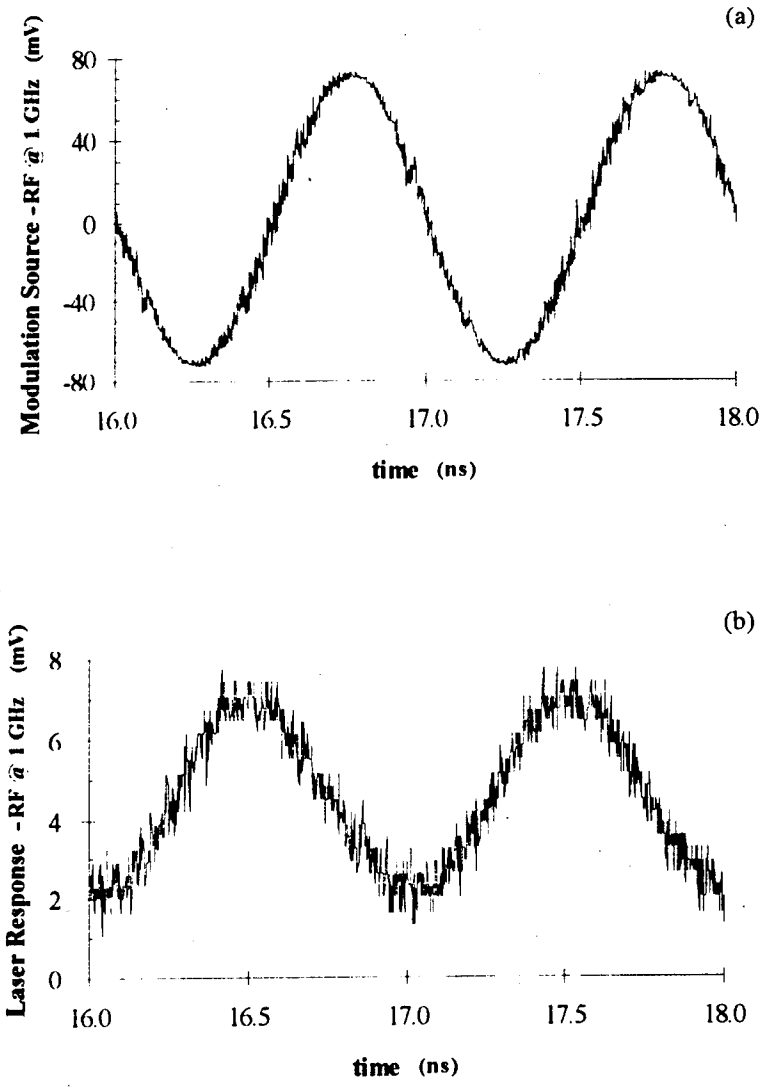

Figure 18 RF Modulation @ 1 GHz; a) Source, b) Laser Response

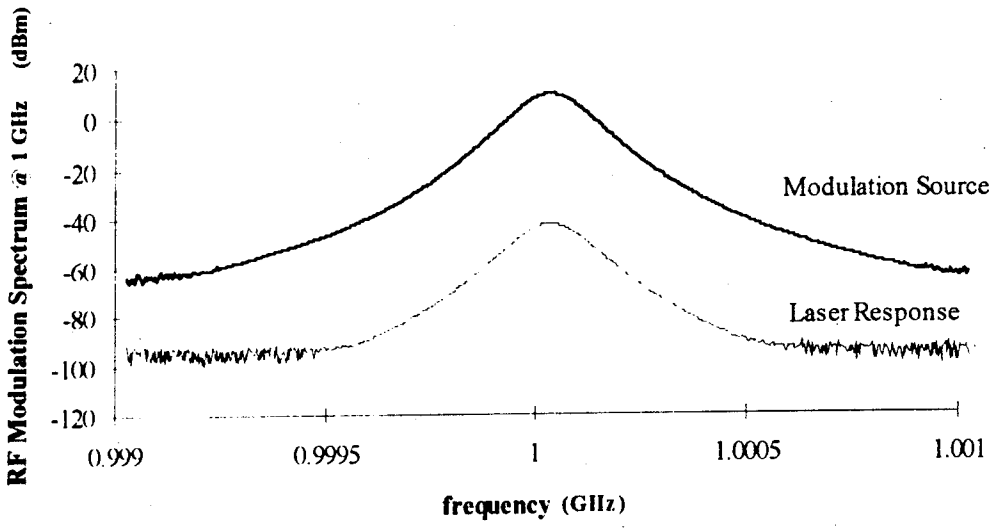

Figure 19 RF Frequency Response @ 1 GHz

2.4.4 Pulse Modulated Response

In this section, the locked laser response to three waves (sinusoid, square, triangle) at 20 MHz repetition rate is determined. The laser spectrum and linewidths are compared for free running laser modulation and for the locked laser cases. The HP Pulse Function Generator (HP8111A) provided the modulation (Figure 20). All three lasers were coupled together. The output of the Fabry Perot was photographed from the Tektronics display (Figure 21).

In Figure 23, Figure 25, Figure 26 are the Fabry Perot response to square, sawtooth, and sinusoid wave at 20 MHz respectively. In each figure, the unlocked laser line is shown in (a) and the modulated Master laser is locked to the Reference

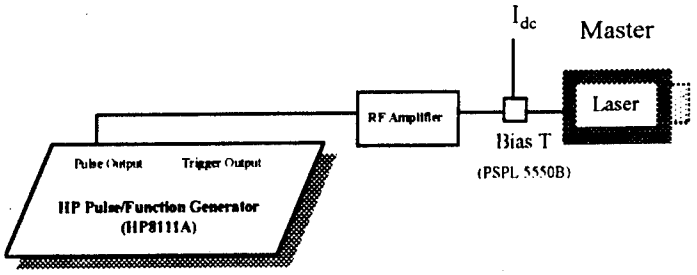

Figure 20 Pulse Modulated Setup

in (b). Since the resolution of the etalon is at best 0.5-1 GHz which is not sufficient for low frequency of 20 MHz, the information extracted is a comparison between the unlocked and locked signals and not a 20 MHz frequency discriminator . Due to equipment availability, higher modulation rates with these types of pulses were not possible at the time the experiments were conducted. An exception is the unlocked laser response to a 250 MHz square wave presented in 2.4.6 Moderate rate Square Wave Modulation. However, it was important to understand the locked laser behavior compared to the unlocked. These experiments show that the frequency content of the locked laser is greatly enhanced over that of the unlocked. This reduction of harmonic spreading under locking condititons is predicted by the theory presented in 2.6 Theory of modulation properties of injection locked lasers.

Figure 24 shows the Slave also locked to the first visible sideband which produces an asymmetric power distribution due to the power contributed by the Slave.

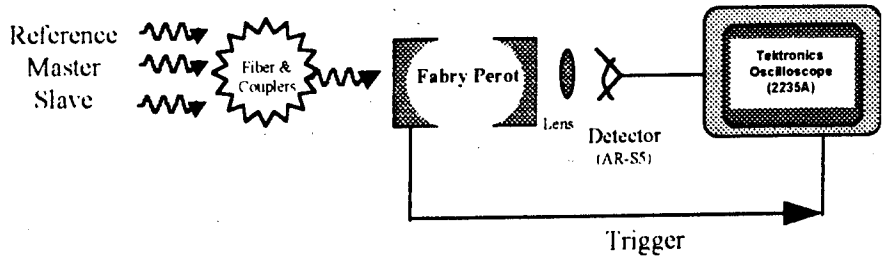

Figure 21 Fabry Perot modes photographed from Oscilloscope display

The linewidths were also measured by detecting the combined laser signals and viewing on an electrical spectrum analyzer (HP8559A) as shown in Figure 22. In Figure 27, Figure 28, Figure 29, the laser linewidths were measured by combining the single modulated Master laser with the Reference without any locking (a), the heterodyned beat note between the Reference and the Slave without locking (b) and with locking (c). The Slave locking took place at the first visible sideband from the Fabry Perot peak. This frequency was found to be 2 GHz by observation on the spectrum analyzer. Particular interest is the striking result for the sine wave in Figure 29 because of perfect beat note when locked (c).

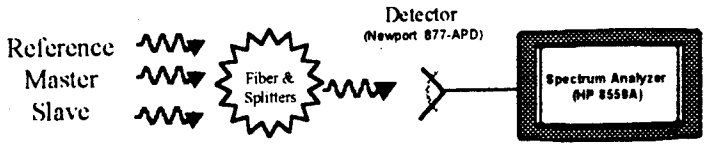

Figure 22 Laser Linewidth Detection

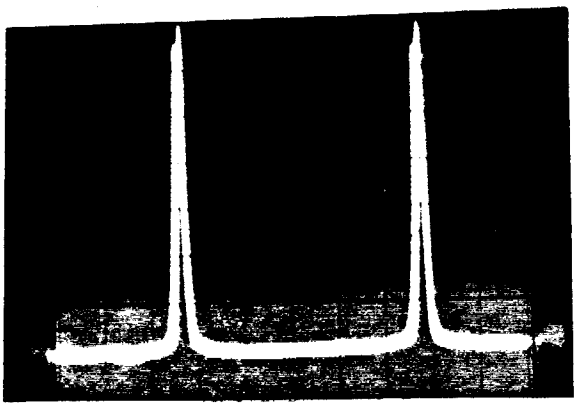

a Unlocked

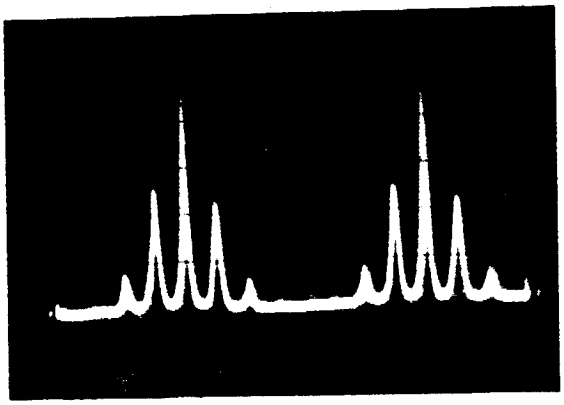

b Master Locked to Reference

Figure 23 Laser Spectrum with Square Wave Modulation @ 20 MHz

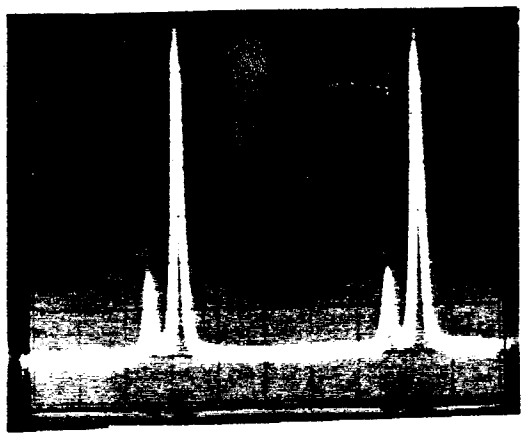

a. Unlocked

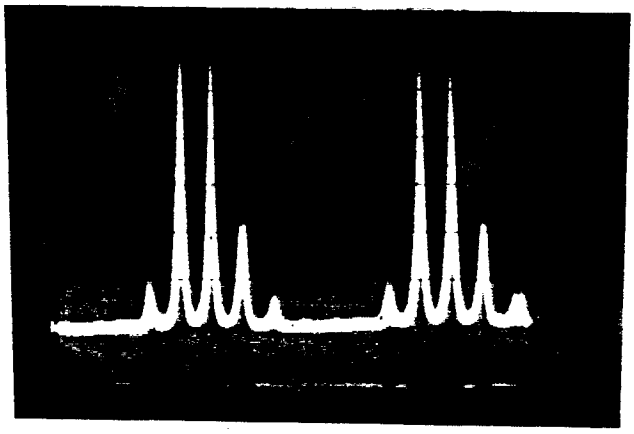

b. Master Locked to Reference

Slave Locked to Master

Figure 24 Laser Spectrum with Square Wave Modulation @ 20 MHz

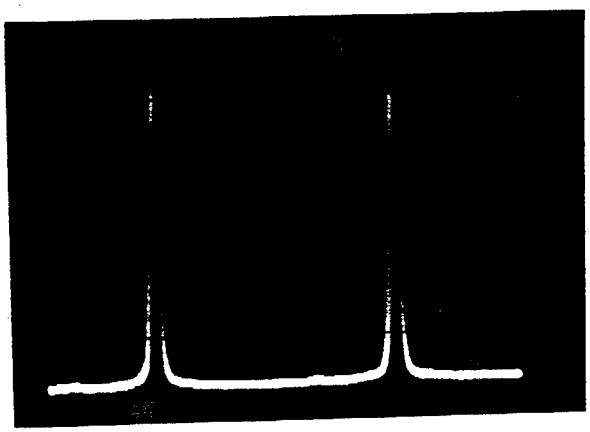

a. Unlocked

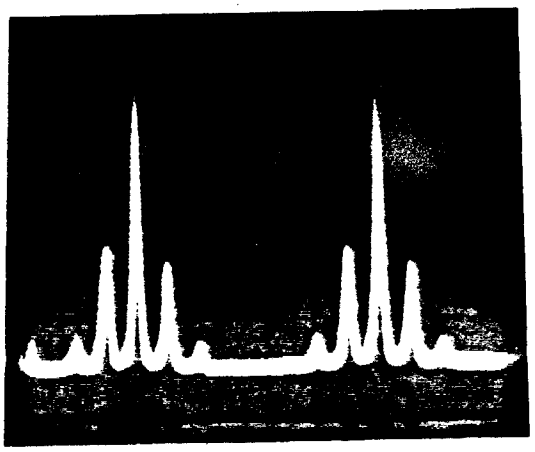

b. Master Locked to Reference

Figure 25 Laser Spectrum with Triangle Wave Modulation @ 20 MHz

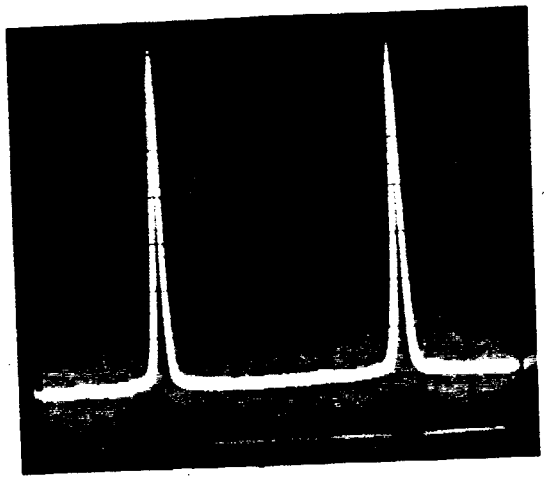

a. Unlocked

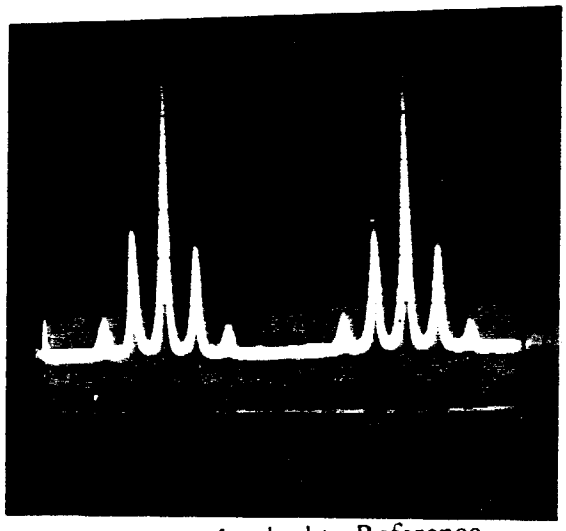

b. Master Locked to Reference

Figure 26 Laser Spectrum with Sine Wave Modulation @ 20 MHz

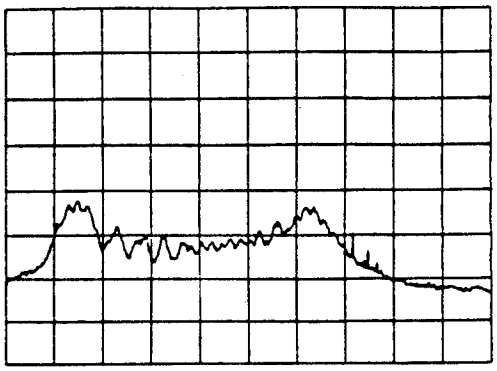

a. Single Laser

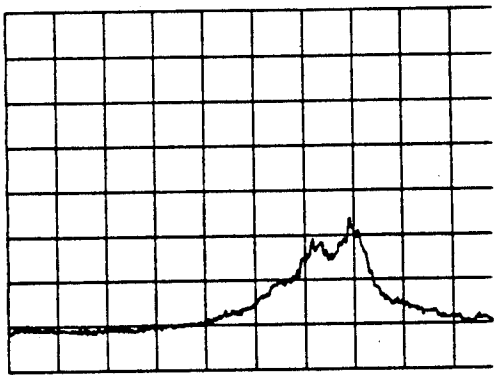

b. Heterodyned and Unlocked

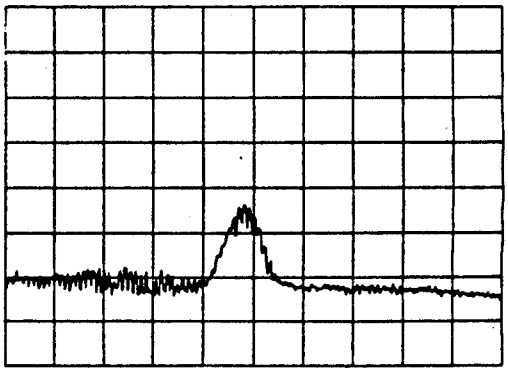

c. Heterodyned and Locked

Figure 27 Laser Linewidth with Square Wave Modulation @ 20 MHz

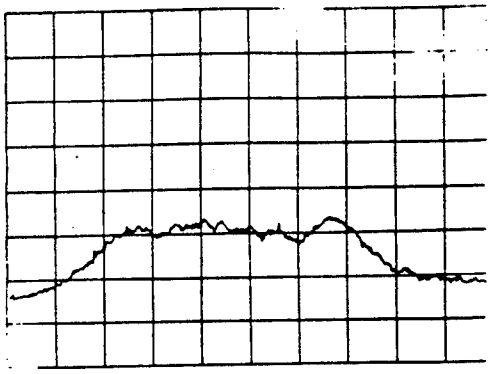

a. Single Laser

b. Heterodyned and Unlocked

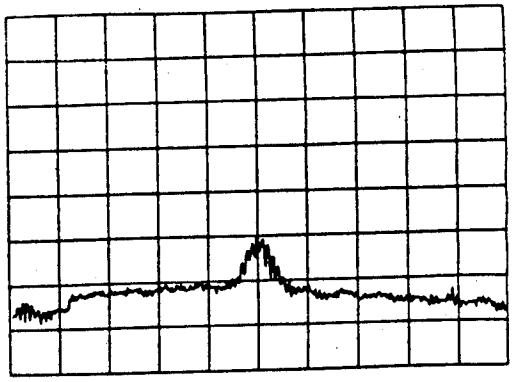

c. Heterodyned and Locked

Figure 28 Laser Linewidth with Triangle Wave Modulation @ 20 MHz

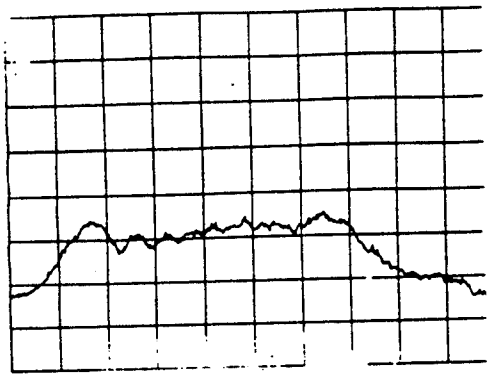

a. Single Laser

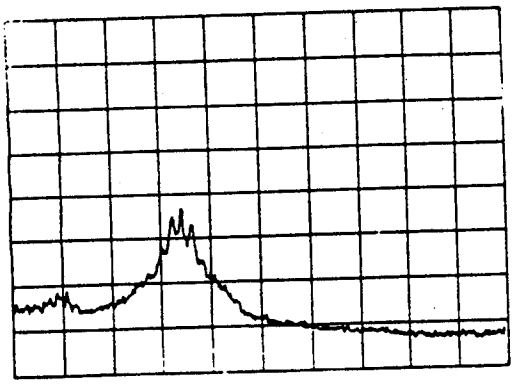

b. Heterodyned and Unlocked

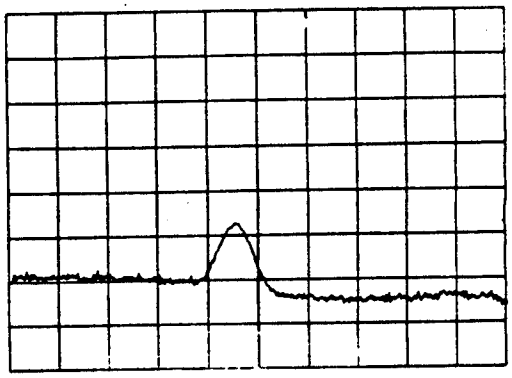

c. Heterodyned and Locked

Figure 29 Laser Linewidth with Sine Wave Modulation @ 20 MHz

2.4.5 Pulsed RF Response

This section builds from the RF and Pulse modulation responses in the two previous sections. The laser is modulated with a pulsed-RF signal. The 2.9 GHz RF sinusoid is enabled during pulse train (square, sinusoid and triangle) at 2 MHz frequency. No locking experiments were conducted with the pulsed RF modulation.

The RF sweeper (HP83640A) at 2.9 GHz was pulsed by the function generator (HP8111A) at a rate of 2 MHz nominally as shown in Figure 30. The modulation source and the laser response are shown in Figure 31, Figure 32, Figure 33 for square, triangle and sinusoid respectively. The modulation source was observed electrically at the output of the pulse generator and at the output of the sweeper (a). The detected laser output was captured with a digital scope (b). The trigger output of HP8111A was used to synchronize the scope.

Figure 34 is the frequency response of the RF (3 GHz) pulse modulated at 2.06 MHz. Experiments were conducted at pulse frequency up to 10.9 MHz, but these results are not presented here because of the lack of added information. The frequency was detected and viewed on an HP8562A spectrum analyzer. The frequency components are present at 2.06 MHz intervals.

The laser output spectrum was photographed detected etalon output as shown in Figure 21 Fabry Perot modes photographed from Oscilloscope display. However, the Fabry Perot did not have enough frequency resolution to identify the frequency spectrum clearly. Given the equipment available and schedule, it did not make sense to purse these experiments any further or to present the results here

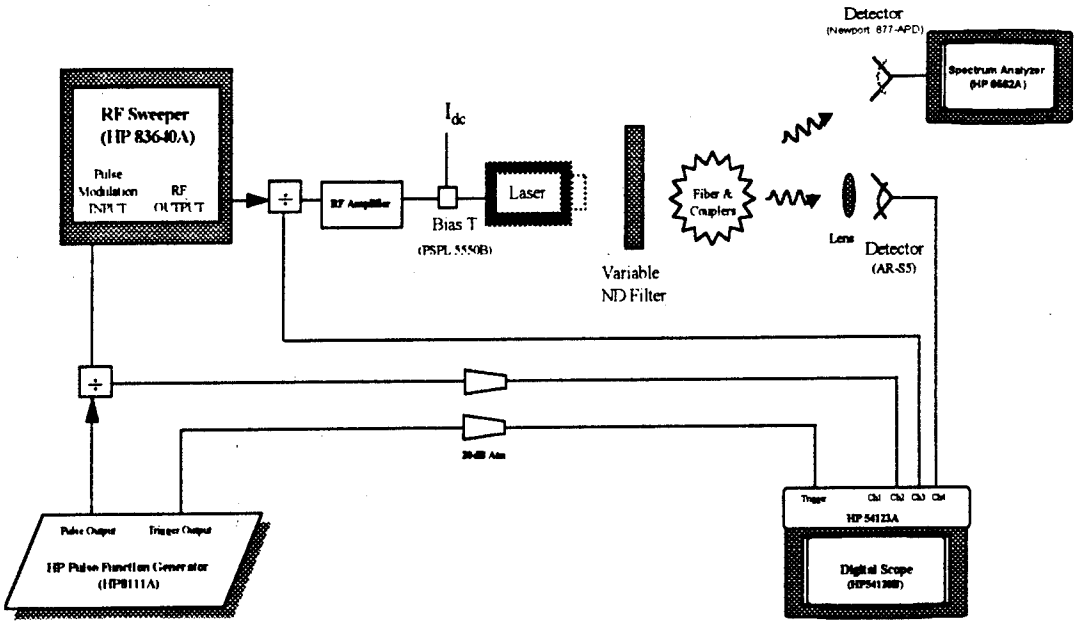

Figure 30 Pulsed RF Experiment

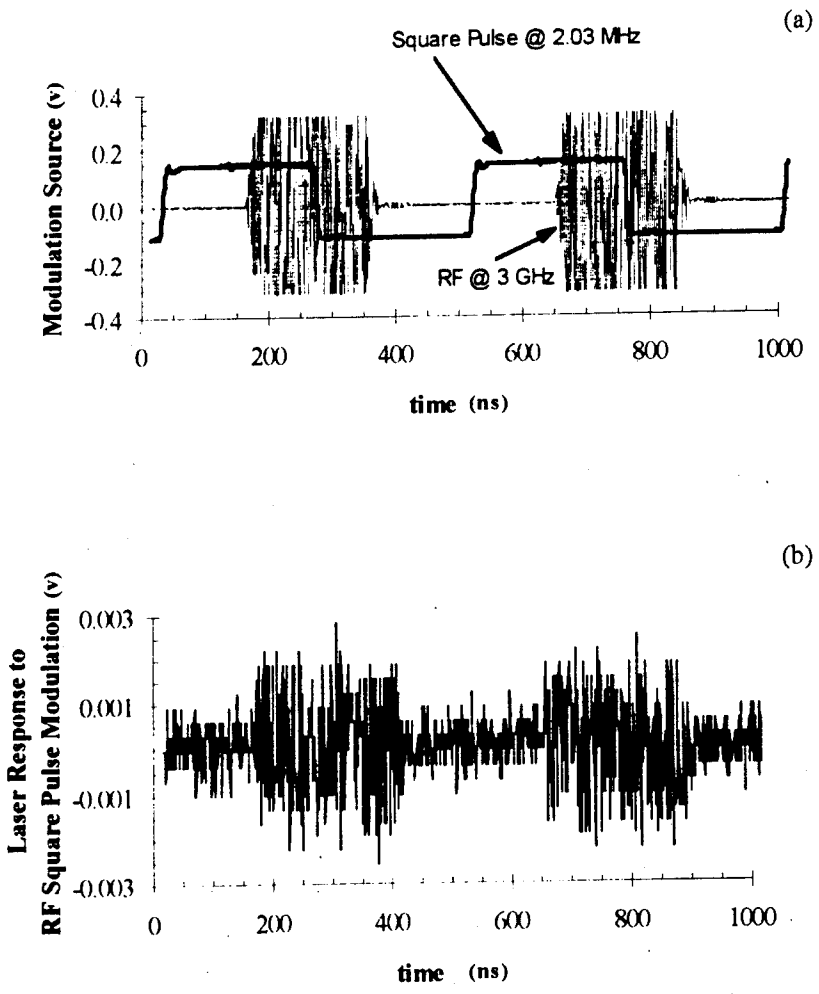

Figure 31 RF Pulsed with Square Wave; a) Source, b) Laser Response

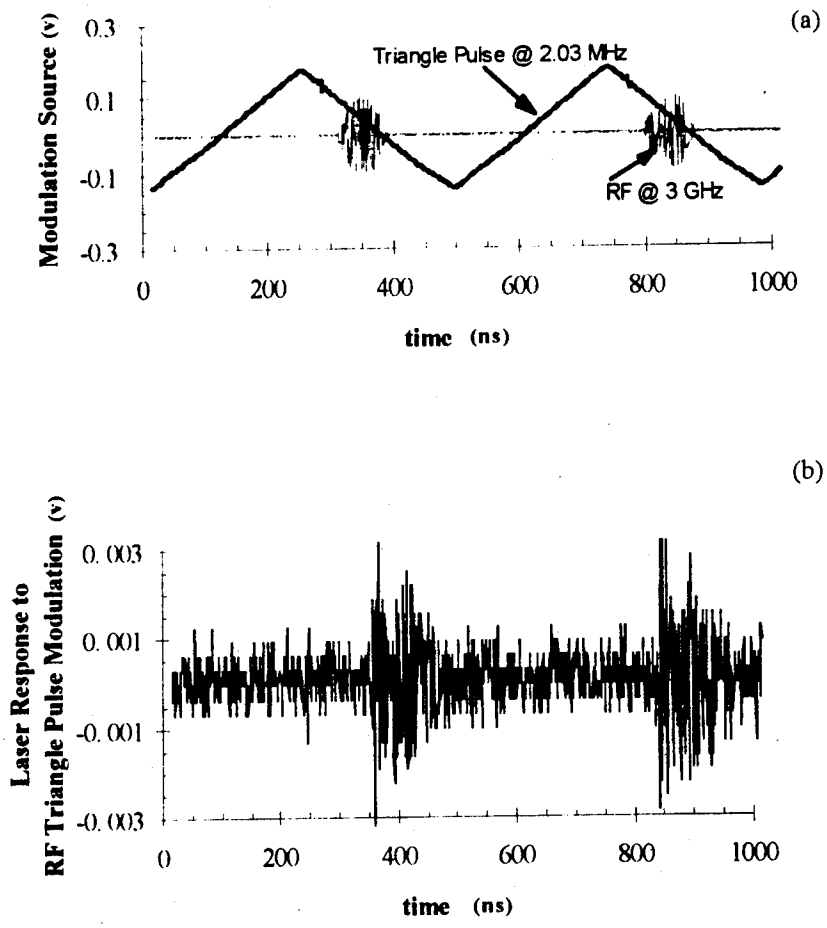

Figure 32 RF Pulsed with Sawtooth (triangle) Wave; a) Source, b) Laser Response

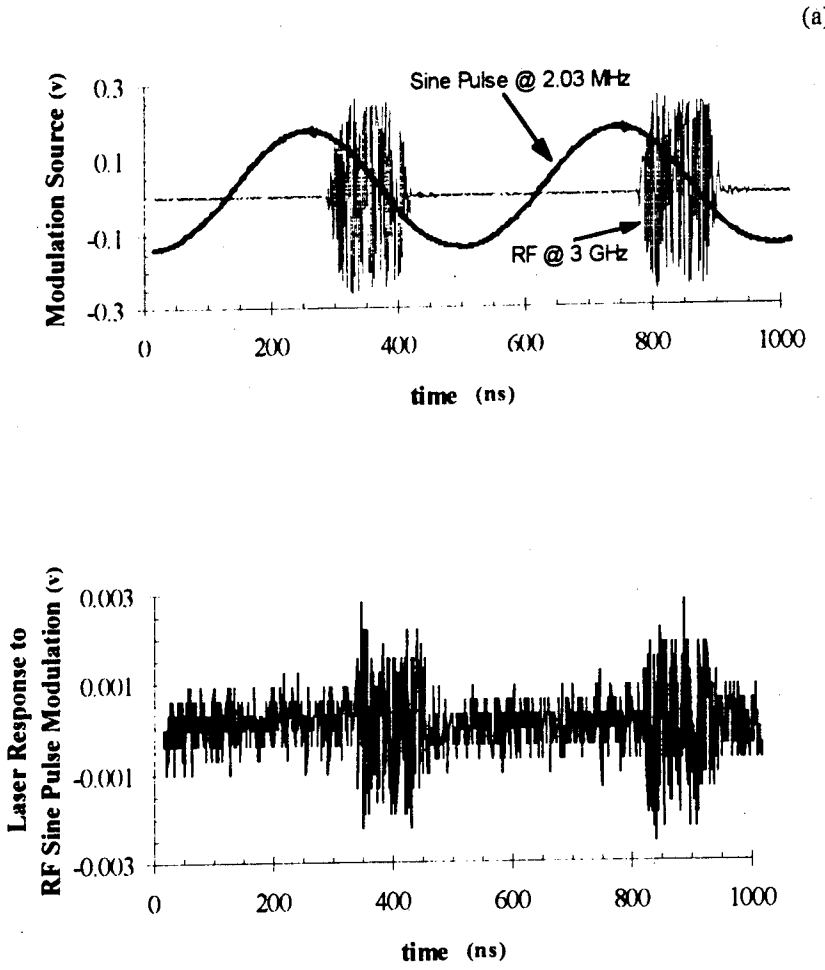

Figure 33 RF Pulsed with a Sine Wave; a) Source, b) Laser Response

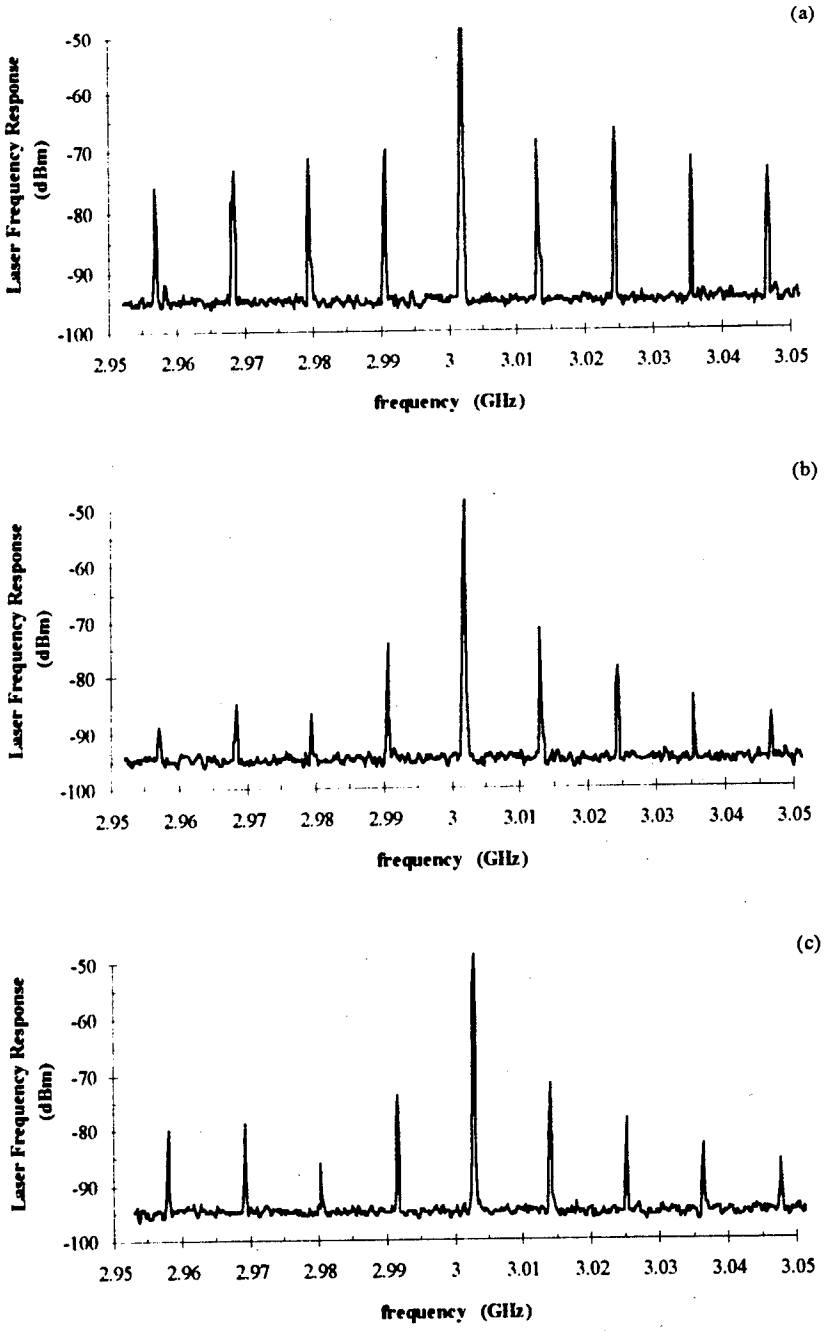

Figure 34 RF Pulse Modulation Frequency Response; a) Square, b) Triangle, c) Sine

2.4.6 Moderate rate Square Wave Modulation

The purpose of this section is to prove that the laser can respond to sharp edges of a square wave at the modulation rates to 250 MHz. For WDM applications, digital information may be clocked at significant rates above 20 MHz (2.4.4). The square wave generator modulated the laser at 250 MHz as shown in Figure 35. The detected laser output was viewed in time on the digital scope (Figure 36) and in frequency on a spectrum analyzer (Figure 37). The HP 8082A square wave generator was not available during the laser locking experiments.

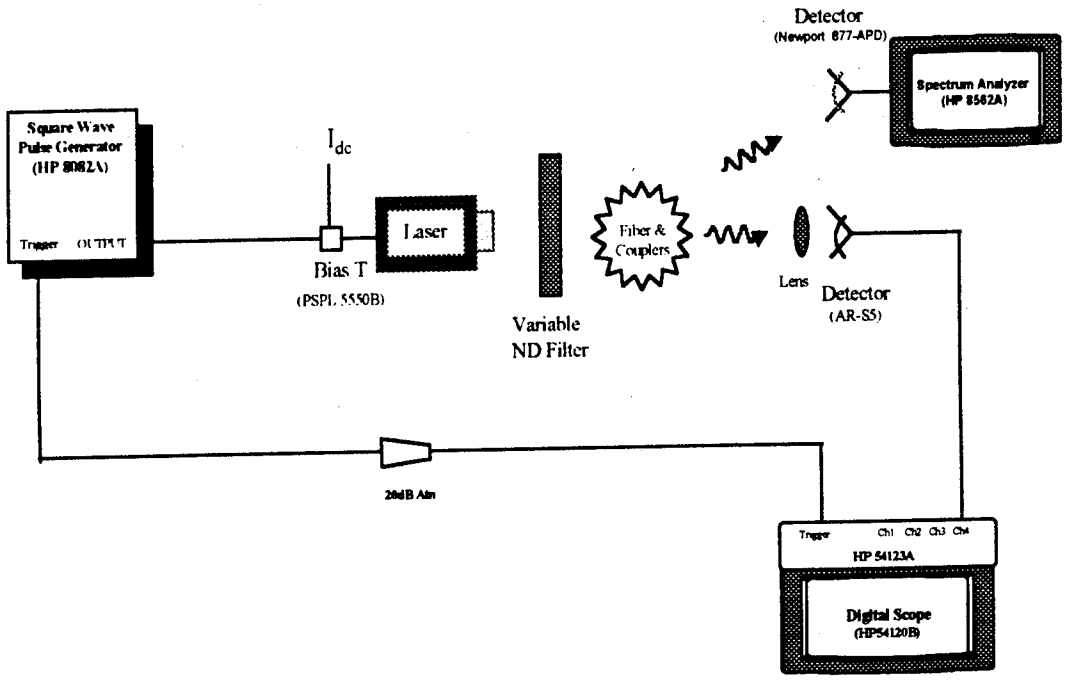

Figure 35 Direct and Frequency Spectrum Detection of 250 MHz Square Wave

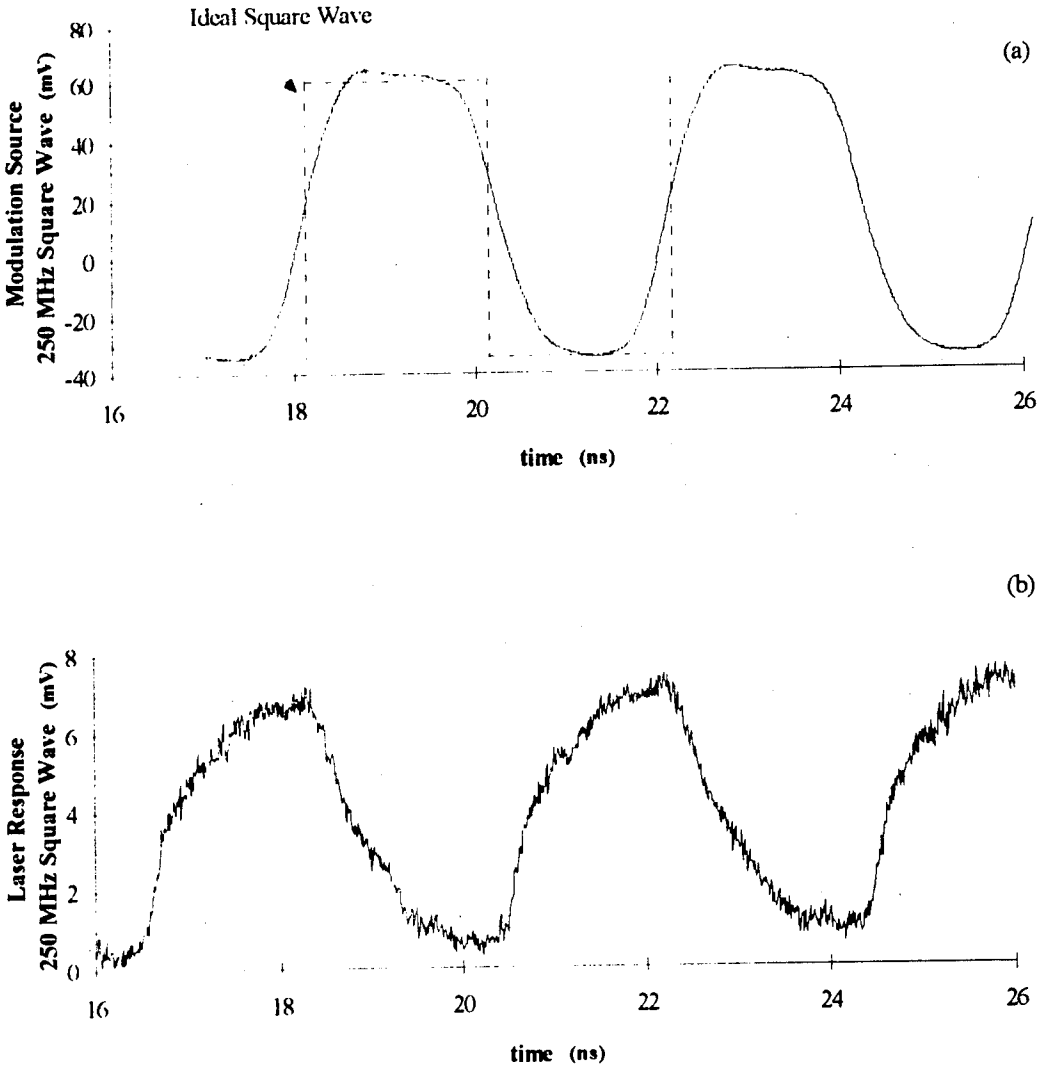

Figure 36 Square Wave Modulation @ 250 MHz; a) Source, b) Laser Response

Because the source limit was 250 MHz (Figure 36), therefore, the source and laser response to the 250 MHz wave are not exactly square. For reference, the ideal square wave is drawn as a dotted line. The laser frequency response follows the source perfectly.

(a)

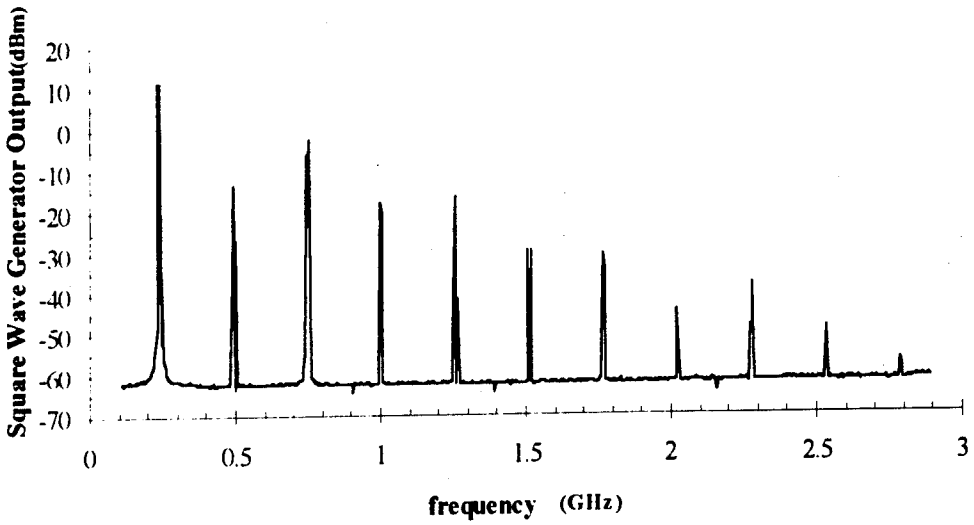

(b)

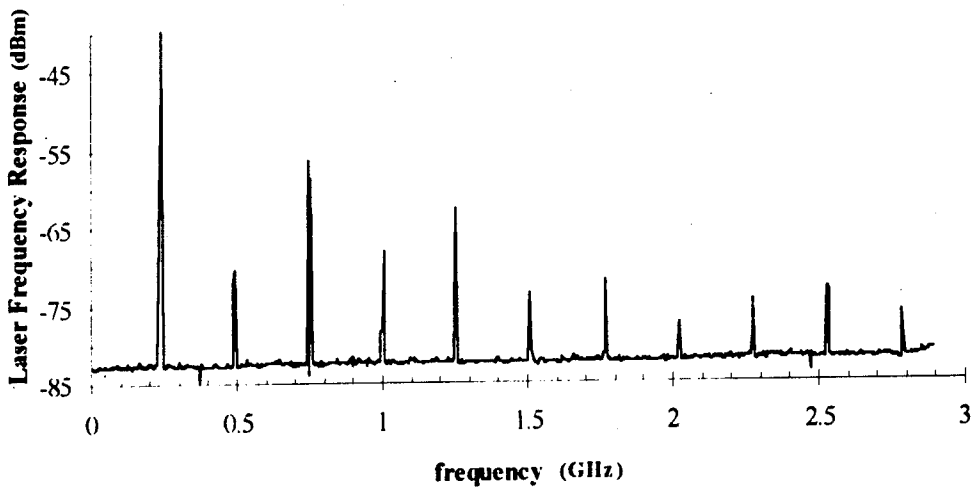

Figure 37 Square Wave Frequency Spectrum @ 250 MHz; a) Source, b) Laser Response

2.5 AM and FM Laser Characteristics

The laser modulation response at 1 GHz RF with 50% and 2% AM, and with 1 KHz deviation FM is presented in this section. Also, the frequency response and the frequency composition of the unlocked and the locked heterodyned beat were measured.

The Fluke 6061A sweeper provides internal source for AM and FM generation at a maximum RF frequency of 1 GHz (Figure 38). The output of the Fluke and the detected laser output were measured in time on the HP42123A and in frequency on the HP8562A. The time response of 50% AM and 1 KHz deviation FM signals are reported in Figure 39 and Figure 40 respectively. The frequency responses for the fundamental and the second harmonic of a 50% AM are figure and Figure 42.

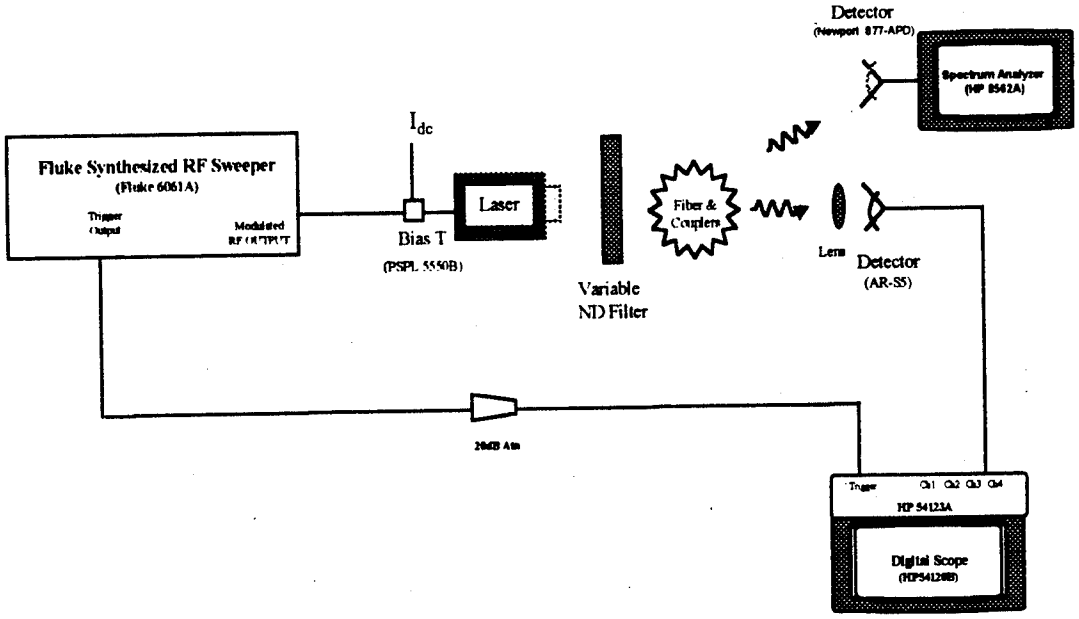

Figure 38 AM & FM Experimental Setup

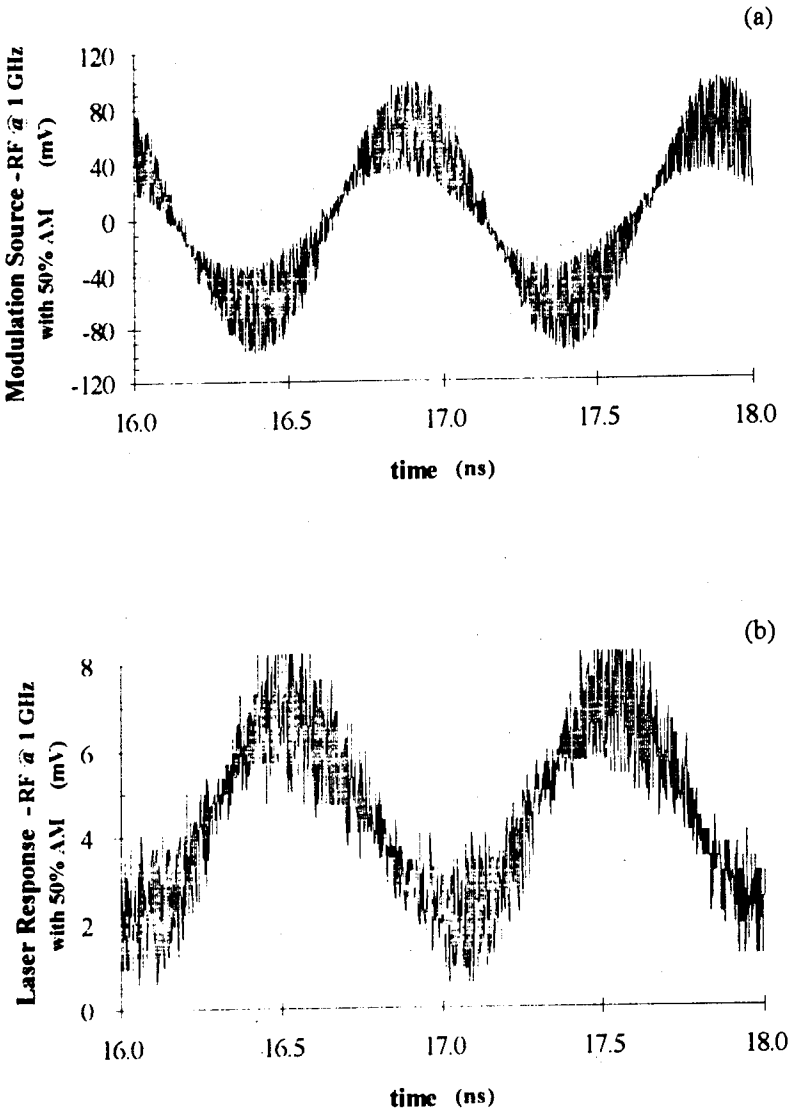

Figure 39 Amplitude Modulation of 50% @ 1 GHz; a) Source, b) Laser Response

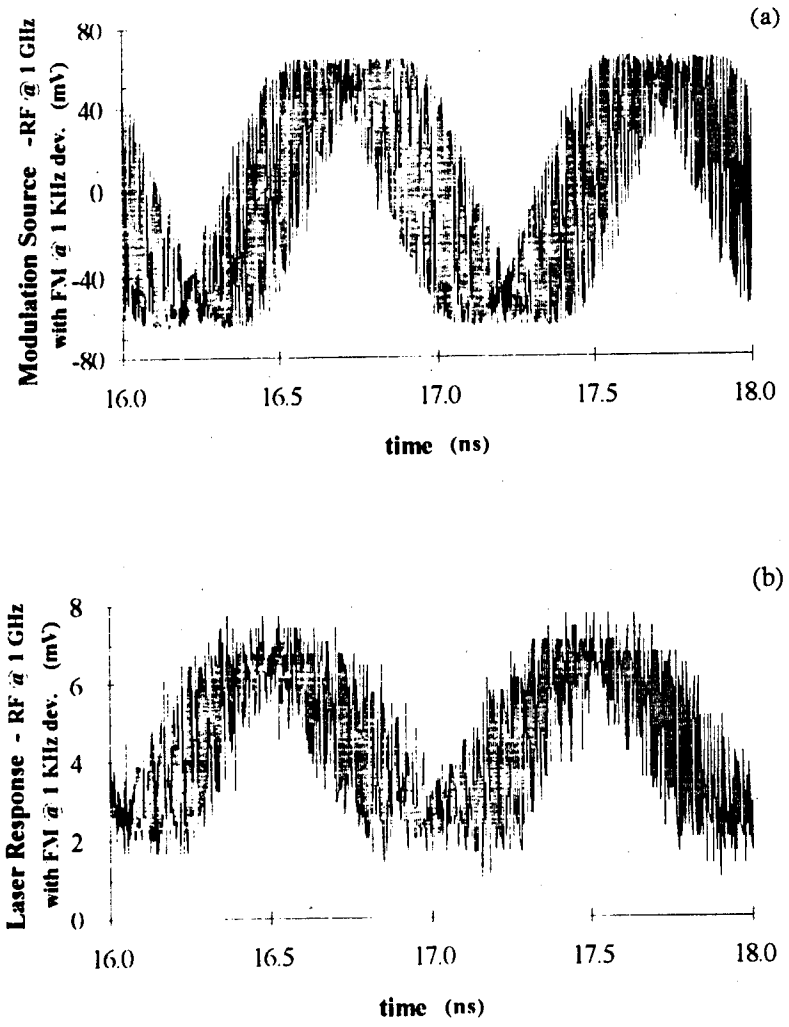

Figure 40 FM modulation at 1 KHz and RF at 1 GHz; a) Source, b) Laser Response

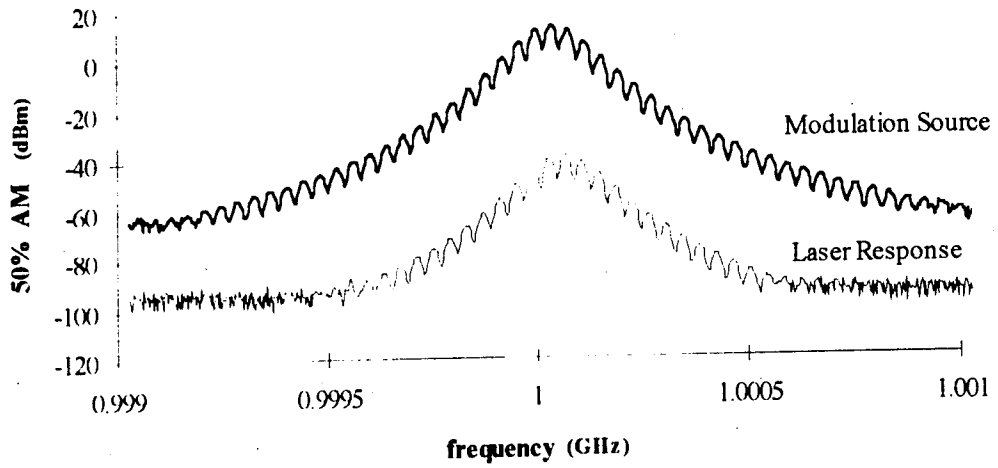

Figure 41 Frequency Response of RF @ 1 GHz with 50% AM

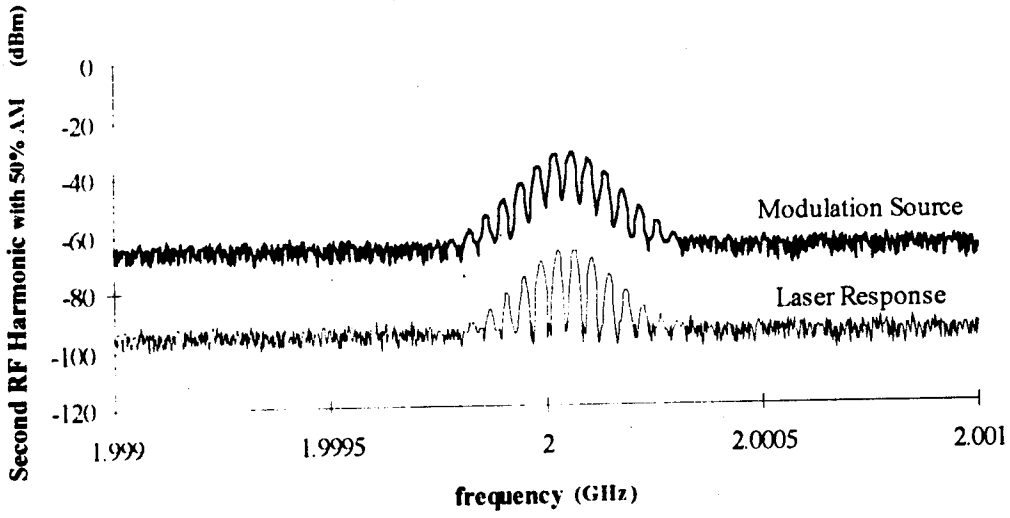

Figure 42 Second Harmonic of RF @ 1 GHz with 50% AM

The amplitude modulation index, m, can be measured directly from the HP8562A. The degree of modulation is calculated as follows:

$$m = \frac{E_{USB} - E_{LSB}}{E_c}$$

The upper and lower sideband amplitudes are E_{USB} and E_{LSB}, and the carrier is represented by E_c. Since amplitude modulation is symmetrical E_{USB} equals E_{LSB} and the modulation index can be re written as follows with amplitude conversion to dB:

$$E_{LSB} - E_c = 20\log\frac{m}{2}$$

The modulation index, measured from the frequency response in Figure 41 and Figure 42 and using the above formula, is 50% as expected for both the source and the laser responses. Both harmonics were not captured together so that the incidental FM can also be observed by using a narrower span at the sideband of interest.

Figure 43 is the frequency response for 50% (a) and 2 % (b) AM signals. The two curves per graph represent the unlocked modulated single laser (lighter line) and the locked heterodyned beat (darker line).

FM modulation index is related to the modulation frequency and the peak to peak frequency deviation (Δf_{peak}).

$$m_{FM} = \frac{\Delta f_{peak}}{f_m}$$

When the bandwidth is greater than the modulation frequency (RBW > fm) so that the scan width and the bandwidth are wide enough to cover significant sidebands, the modulation bandwidth can be calculated from one measurement of $2\Delta f_{peak}$.

Twice the deviation is the distance across a constant horizontal line as shown in Figure 44 (at f_m = 1 KHz , $2\Delta f_{peak}$ =1750 Hz, therefore, m = 0.875).

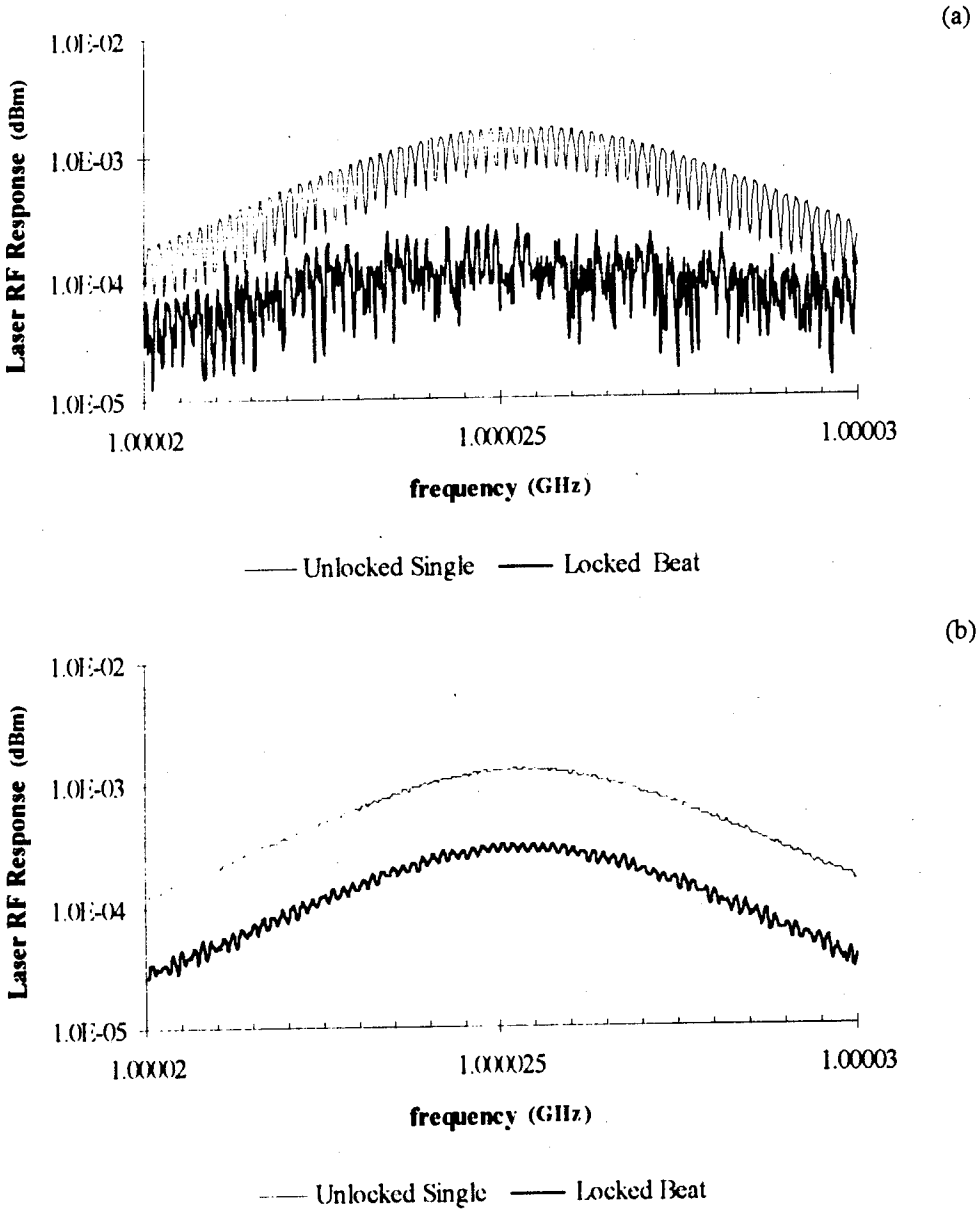

Figure 43 AM @ 1 GHz RF under locking conditions; a) 50 %, b) 2%

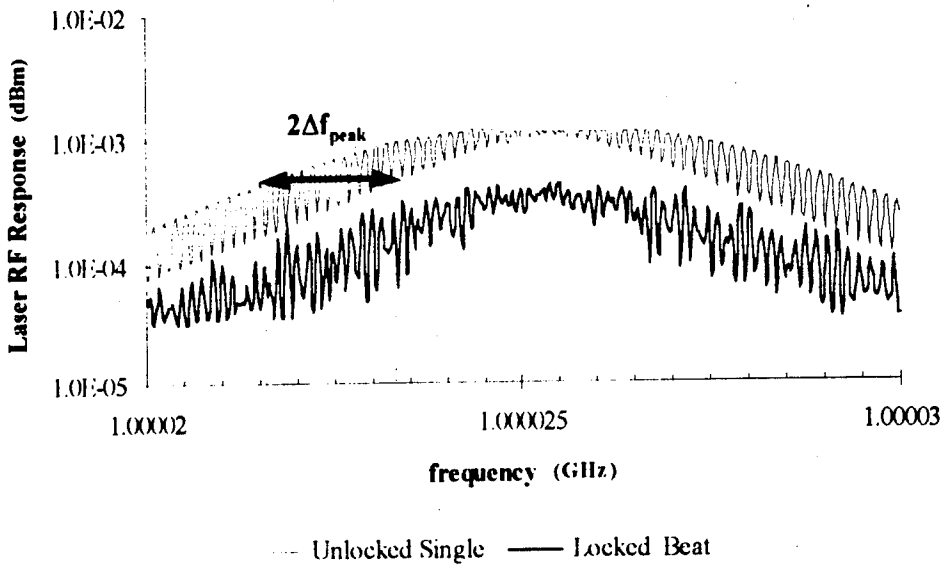

Figure 44 FM with 1 KHz deviation @ 1 GHz RF and under locking conditions

2.6 Theory of modulation properties of injection locked lasers

The modulation frequency response of a modulated injection locked laser is presented in this section. The analysis presented is based on separate works completed by Lidoyne and Gallion[24], Agrawal[25], and Henry[26,27]. The work completed by Kobayshi and Kimura were improved upon by including amplitude-phase coupling, stability, and relaxation effects[28]. Since the frequency range of interest exceeds several megahertz, thermal effects are neglected[29].

The analysis begins with the semiconductor laser rate equations expressed in terms of the photon number P, the phase of the optical field of the modulated laser

Φ, and the carrier number in the semiconductor active volume N as follows:

$$\frac{dP}{dt} = \left(G - \frac{1}{\tau_p} + \frac{v_g}{L}\sqrt{\frac{P_{inj}}{P}}\cos(\theta) + \frac{R}{P} \right) P$$

$$\frac{d\Phi}{dt} = (\omega_s - \omega_o) + \frac{v_g}{2L}\sqrt{\frac{P_{inj}}{P}}\sin(\theta)$$

$$\frac{dN}{dt} = -\frac{N}{\tau_e} - GP + J$$

The gain is G, the cavity loss rate is τ_p^{-1}, the lifetime of the carriers is τ_e, θ is the phase difference between the two lasers, the group velocity is v_g, the cavity length is L, the spontaneous emission rate is denoted by R, the carrier injection rate is represented J, ω_s is the resonant frequency of the cavity, ω_o is the stationary value of the optical field equal to the injection frequency.

Assuming direct current modulation of the laser, the current modulation is represented by f(t) which is included as an AC component of J.

$$J(t) = J_o + \Delta J_m f(t)$$

Jo is the DC value and $\Delta J_m f(t)$ is the AC.

The rate equation linearization proceeds as described by Agrawal for small signals which have a modulation index less than 0.3 [30]. The rate equations are linearized by equating the time derivatives to zero. Next, the values are expanded around their steady state values.

$$P(t) = P_o + \Delta p(t)$$
$$N(t) = N_o + \Delta n(t)$$
$$\Phi(t) = \Phi_o + \Delta\Phi(t)$$

where the o-subscript denotes the steady state and Δ represents the deviation about steady state. The gain G and resonant frequency ω_s are expanded via Taylor's series to include the linewidth enhancement factor α. Because the linewidth enhancement factor is directly related to the carrier induced change in the refractive index, direct modulation of the laser causes indirect frequency modulation. Therefore,the modulation properties of the laser are significantly effected by α [31].

$$G = G_o + \Delta n \frac{\partial G}{\partial N} + \Delta p \frac{\partial G}{\partial P}$$

$$\omega_s = \omega_{os} + \frac{\alpha}{2} \Delta n \frac{\partial G}{\partial N} + \Delta p \frac{\partial \omega_s}{\partial P}$$

Furthermore, the differential gain terms are represented by shorthand notation as follows:

$$G_n = \frac{\partial G}{\partial N}$$

$$G_p = \frac{\partial G}{\partial P}$$

The dependence of the resonant frequency ω_s on the photon number is neglected since the gain change has symmetry about the laser line which forces the transform to be nearly zero[32].

The time derivatives of the steady state are obviously equal to zero. Also, the steady state gain minus the loss is zero ($G_o - \tau_p^{-1} = 0$). Ignoring all effects beyond the first order, the rate equations are as follows:

$$\frac{\partial \Delta p(t)}{\partial t} = \Delta p(t)\left(P_o G_p - \frac{R}{P_o} - \frac{v_g}{2L}\cos(x)\sqrt{\frac{P_{inj}}{P_o}} \right) + \frac{v_g}{2L} P_o \Delta\Phi(t)\sin(x) + P_o G_n \Delta N(t)$$

$$\frac{\partial \Delta\Phi(t)}{\partial t} = \frac{\alpha}{2} G_n \Delta N(t) - \Delta p(t)\frac{v_g}{4P_o L}\sin(x)\sqrt{\frac{P_{inj}}{P_o}} - \Delta\Phi(t)\frac{v_g}{2L}\cos(x)\sqrt{\frac{P_{inj}}{P_o}}$$

$$\frac{\partial \Delta N(t)}{\partial t} = \Delta J - \Delta p(t)(Go + P_o G_p) - \Delta N(t)\left(\frac{1}{\tau e} + P_o G_n \right)$$

where:

$$\theta = \Phi + \Delta\Phi - \phi_{inj} = x + \Delta\Phi$$

$$x = \Phi - \phi_{inj}$$

The radical was expanded, and the fact that $\frac{\Delta p}{P_o} << 1$ was used in the approximation. After substituting for the steady state and differential phase $\Phi+\Delta\Phi(t)$ in the argument of the cosine and sine, the trigonometric identities for sum and difference were used. Also, the approximation for cosine and sine with small arguments were applied to the first order.

$$\cos(x + \Delta\Phi) = \cos x \cos\Delta\Phi - \sin x \sin\Delta\Phi$$
$$\approx \cos x - \Delta\Phi \sin x$$

$$\sin(x + \Delta\Phi) = \sin x \cos\Delta\Phi + \cos x \sin\Delta\Phi$$
$$\approx \sin x + \Delta\Phi \cos x$$

After Fourier transform, the photon number and optical phase can be written as a modulation transfer function times the Fourier transfer of the modulation f(t).

$$\Delta p(\omega) = H_p(\omega)\ \Delta J_m F(\omega)$$
$$\Delta\Phi(\omega) = H_\Phi(\omega)\Delta J_m F(\omega)$$

The transfer functions are represented as follows:

$$H_P(\omega) = \frac{P_o z\, \alpha G_n \sin x + G_n P_o (\, i\omega + z\cos x)}{\chi(\omega)}$$

$$H\Phi(\omega) = \frac{\frac{\alpha}{2} G_n\left(i\omega + z\cos x + \frac{R}{P_o} - P_o G_P\right) - \frac{G_n}{2} z\sin x}{\chi(\omega)}$$

where the denominator $\chi(\omega)$ is :

$$\chi(\omega) = \left[\left(i\omega + z\cos x + \frac{R}{P_o} - P_o G_P\right)\left(i\omega + \frac{1}{\tau_e} + G_n P_o\right) + G_n P_o\left(G_o + G_P P_o\right)\right]$$
$$\bullet\left(i\omega + z\cos x\right) + (z\sin x)^2 \bullet \left(i\omega + \frac{1}{\tau_e} + G_n P_o\right)$$
$$+\left(G_o + G_P P_o\right) P_o z\, \alpha G_n \sin x$$

A substitution for the radical term has been made for simplification:

$$z = \frac{vg}{2L}\sqrt{\frac{P_{inj}}{P_o}}$$

The spontaneous emission rate R is related to the spontaneous emission factor n_{sp} and the gain ($R = G_o/n_{sp}$). The cavity loss α_a , group index n_g and the facet reflectivity R_m are used to calculate τ_p and the steady state gain G_o.

$$\tau_p = \frac{n_g}{c}\left(\alpha a + \frac{1}{L}\log(\frac{1}{Rm})\right)^{-1}$$

$$G_o = \frac{1}{\tau_p}$$

The constants used are as follows:

$G_p = 1.8 * 10^4$

$G_n = 5.75 * 10^3 s^{-1}$

$\Delta J_m = 2mA$

$\alpha = 5$

$\tau_c = 2.2 * 10^{-9} s$

$\alpha_a = 45cm^{-1}$

$Rm = 0.31$

$n_{sp} = 0.26$

$L = 300\mu m$

$Volume = 1.2 * 10^{-10} cm^3$

$n_g = 4.3$

$v_g = \frac{c}{n_g}$

The resultant transfer functions are plotted in Figure 45 Photon Number Transfer Function and Figure 46 Phase Transfer Function of the optical field for free running modulated laser and for injection locked laser with phase detuning, x, of +10 °, 0°, -10°, and -50° and injection level, P_{inj} / P_o ,equal to -40 dB. Given this power level, the edge of the stable locking range corresponds to approximately 10°.

At 0° lock is guaranteed, and the detuning response is flat and the maximum output power is reached. Therefore, injection locking is a mechanism to smooth out the frequency response of a modulated semiconductor laser diode. The chirp to power ratio may be obtained from the ratio of the phase and photon number (intensity) modulation responses. Chirp to power ratios are routinely used in evaluation of FSK systems.

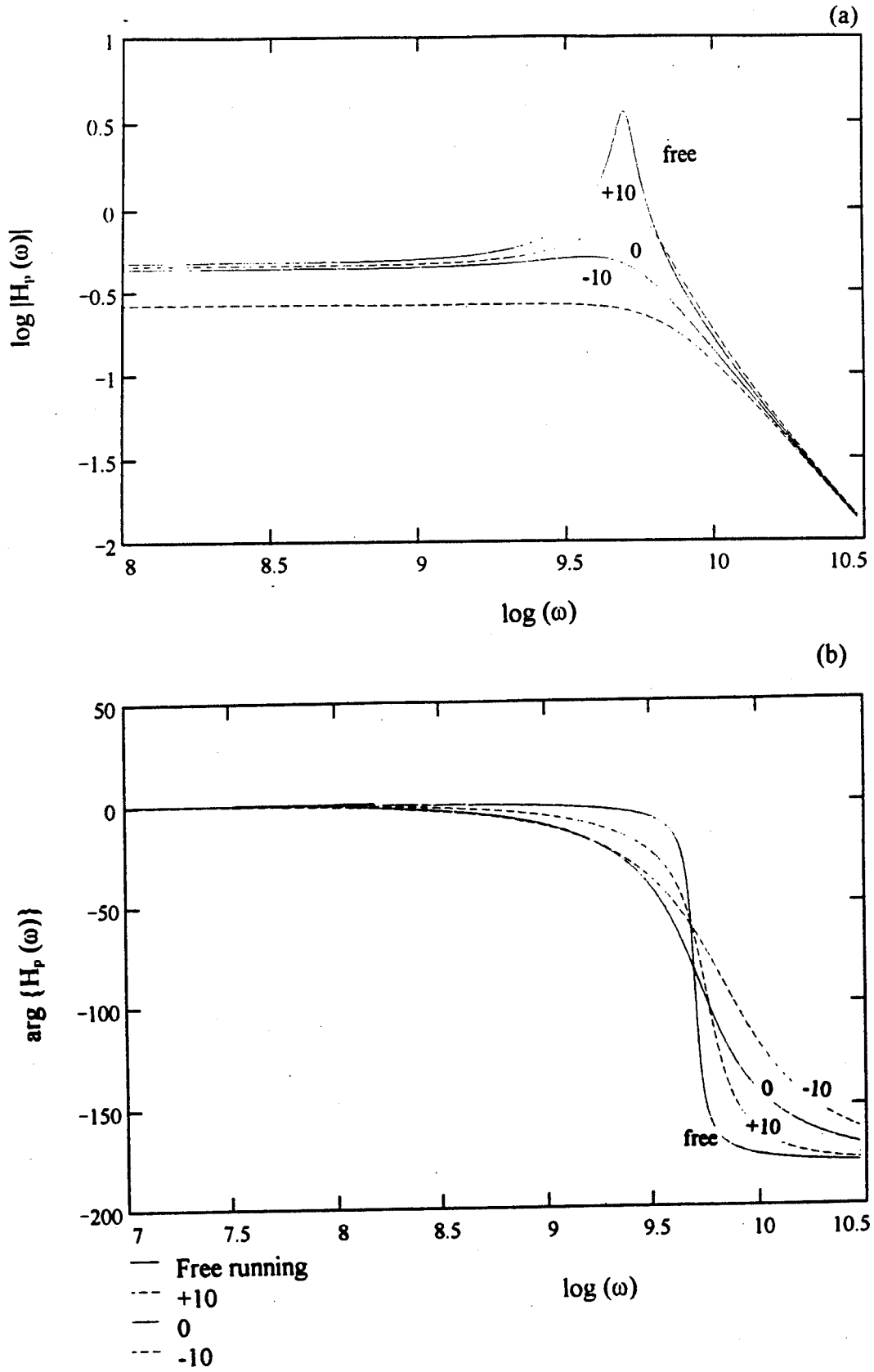

Figure 45 Photon Number Transfer Function

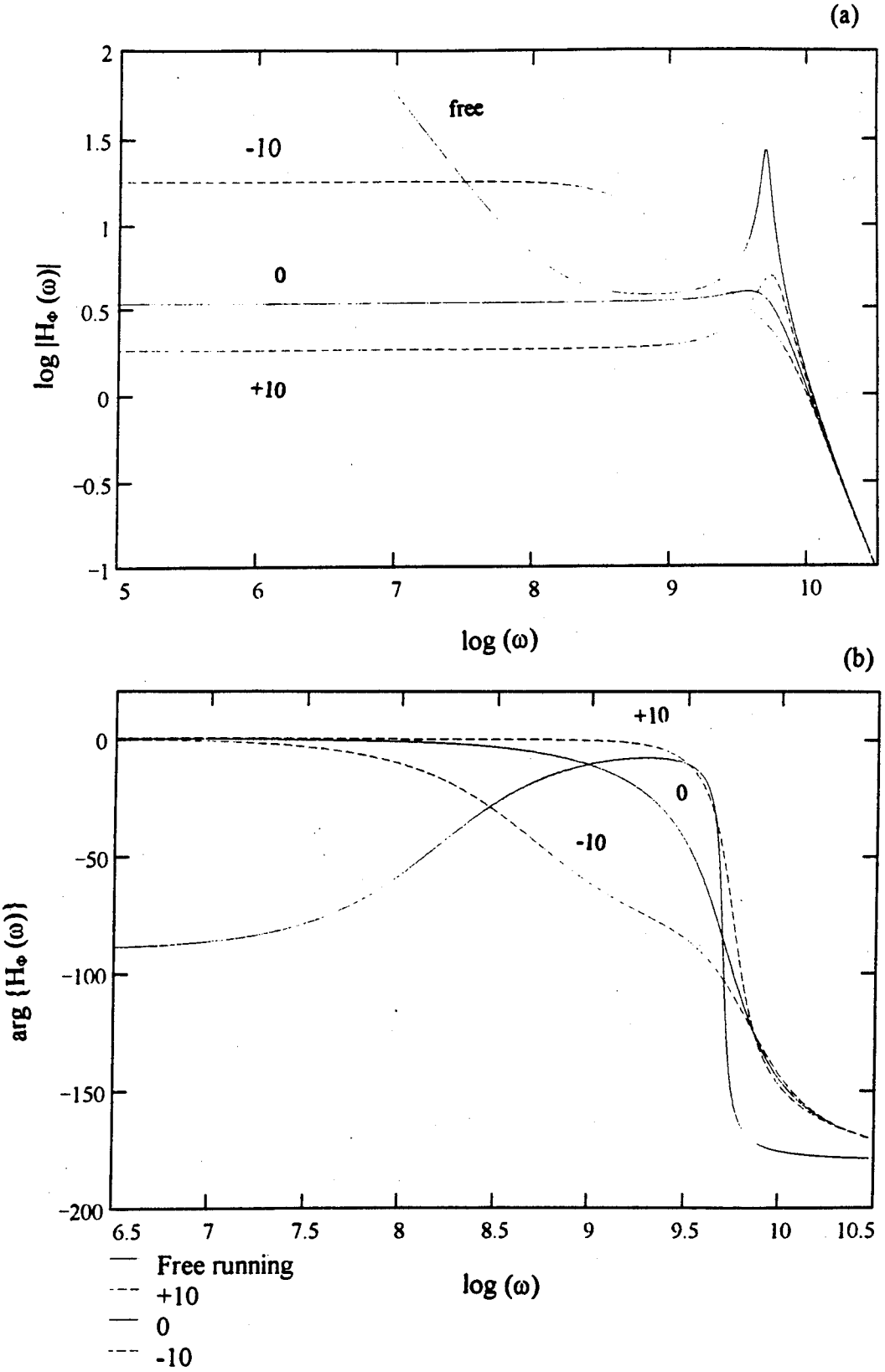

Figure 46 Phase Transfer Function of the optical field

The power density spectrum $S_f(\omega)$ can be written in terms of the output y(t) and subsequently, in terms of the Fourier transform function $Y(\omega)$ using Parseval's Theorem.

$$S_f(\omega) = \frac{1}{2\pi}\int_{-\infty}^{\infty}|y(t)|^2 dt = \frac{1}{2\pi}\int_{-\infty}^{\infty}|Y(\omega)|^2 d\omega$$

$$= \frac{1}{2\pi}\int_{-\infty}^{\infty} S_y(\omega) d\omega$$

Defining $Y(\omega)$ in terms of a transfer function $H(\omega)$ and an input frequency response $F(\omega)$,

$$|Y(\omega)|^2 = |H(\omega)|^2 |F(\omega)|^2$$

the output power density function $S_y(\omega)$ can be rewritten as $S_y(\omega) = |H(\omega)|^2 |F(\omega)|^2$. The integration can be performed numerically to obtain the total power spectrum. The power spectrum represents the Fabry Perot experimental results in the previous sections. A deterministic expression for the power density is possible by expanding the time domain response in a Fourier series representation, performing the autocorrelation of the field, and then computing, the average power spectrum via a Fourier Transform kernel[33].

Harmonic spreading is significantly reduced when the modulated laser is injection locked as predicted by the theoretical expression for the power density and as shown in the experimental results of this Chapter.

2.7 Conclusion

The locked laser frequency response depends on the phase detuning between the modulated laser and the injected laser field, the injected power levels and the type and frequency of the direct current modulation. Under strong injection conditions within the stability regime, an injection locked laser exhibits a flat frequency response as compared to the free running laser response. Under locking conditions, the flat transfer function contributes to the reduction of harmonic spreading; thus, the laser responds with enhanced signal content at the modulation frequency.

Experimental results have been presented to characterize the laser response to RF modulation and to lower frequency square, triangle, and sine waves and to pulsed, amplitude modulated and frequenc modulated RF signals. The model presented in Section 2.6 shows the flattening of the laser transfer function as the laser approaches lock. Compared to the free running modulated laser response, the locked laser response is enhanced which is imperative for high speed communications , and also, the optical mode is stabilized which makes WDM viable.

2.8 References - Chapter 2

[1] Robert Adler, "A study of Locking Phenomena in Oscillators", *Proceedings of IRE and Waves and Electrons*, vol. 34, 1946, pp.351-357.

[2] H.L. Stover, and J. Steir, "Locking of Laser oscillators by light injection," *Applied Physics Letters*, vol.8, pp.91-93, February 6, 1966.

[3] S. Kobayashi, andT. Kimura, "Optical Phase Modulation in an Injection Locked AlGaAs Semiconductor Laser", *IEEE Journal of Quantum Electronics*, vol.QE-18, no.10, October 1982, pp.1662-1669.

[4] K Kikuchi,., T. Okoshi, M. Nagamatsu, and N. Henmi, "Degradation Of Bit-Error Rate In Coherent Optical Communications Due To Spectral Spread Of The Transmitter And The Lockal Oscillator," *Journal of Lightwave Technology*, vol. LT-2, pp.1024-1033, 1984.

[5] Bernard G. Glance, "An optical Heterdoyne Mixer Providing Image-Frequency Rejection", *IEEE Journal of Lightwave Technology*, vol.LT-4, no.11, November 1986, pp.1722-1725.

[6] Robert Olshansky, Vincent Lanzisera, and Paul Hill, "Wideband Modulation of Semiconductor Lasers for Microwave-Multiplexed Lightwave Systems", *11th IEE International Semiconductor Laser Conference*, August 29-Sept 1, 1988, pp.52-53.

[7] P. Russer, and G. Arnold, "Direct Modulation of Semiconductor Injection Lasers", *IEEE Transactions on Microwave Theory and Techniques*, vol.30, no.11, November 1982, pp.1809-1821.

[8] Isabelle Petitbon, Philippe Gallion, Guy Debarge, and Claude Chabran, "Locking Bandwidth and Relaxation Oscillations of Injection-Locked Semiconductor Laser", *IEEE Journal of Quantum Electronics*, vol. 24, no. 2, February 1988, pp. 148-154.

[9] G.P. Agrawal, and T.M. Shen, "Pulse-Shape Effects on Frequency Chirping in Single-Frequency Semiconductor Lasers Under Current Modulation", *Journal of Lightwave Technology*, vol.-LT-4, no.5, May 1986, pp.497-503.

[10] A.S. Sudbo, "The Frequency Chirp of Current Modulated Semiconductor Diode Lasers",*IEEE Journal of Quantum Electronics*, vol.QE-22, no.7, July 1986, pp.1006-1008.

[11] G.P. Agrawal, N.K. Dutta, and N.A. Olsson, "Reduced Chirping in Coupled-cavity-semiconductor Lasers", *Journal of Applied Physics*, vol.45, no.2, July 15, 1984, pp.119-121.

[12] K. Iswashita, and K. Nakagawa, "Suppression Of Mode Partition Noise By Laser Diode Light Injection," *IEEE Journal of Quantum Electronics*, vol. QE-18, pp.1669-1674, 1982.

[13] G.P. Agrawal, R. Roy, "Effect of Injection-Current Fluctuations on the Spectral Linewidth of Semiconductor Lasers", *Physical Review*, vol.37, no.7, April 1, 1988, pp.2495-2501.

[14] R. Olshansky, and D. Fye, "Reduction of Dynamic Linewidth in Single-Frequency Semiconductor Lasers", *Electronics Letters*, vol.20, no., 22, October 25, 1984, pp.928-929

[15] A.S. Sudbo, "The Frequency Chirp of Current Modulated Semiconductor Diode Lasers",*IEEE Journal of Quantum Electronics*, vol.QE-22, no.7, July 1986, pp.1006-1008.

[16] G.P. Agrawal, and T.M. Shen, "Pulse-Shape Effects on Frequency Chirping in Single-Frequency Semiconductor Lasers Under Current Modulation", *Journal of Lightwave Technology*, vol.-LT-4, no.5, May 1986, pp.497-503.

[17] Charles H. Henry, "Theory of Linewidth of Semiconductor Lasers", *IEEE Journal of Quantum Electronics*, vol. QE-18, no.2, February 1982, pp. 259-264.

[18] Charles H. Henry,., "Theory of the Phase Noise and Power Spectrum of a Single Mode Injection Laser", *IEEE Journal of Quantum Electronics*, vol. QE-19, no.9, September 1983, pp.1391-1397.

[19] Lang Roy, "Injection Locking Properties of a Semiconductor Laser", *IEEE Journal of Quantum Electronics*, vol. QE-18, no. 6, June 19882, pp.976-983.

[20] S. Kobayashi, and T. Kimura, "Injection Locking Characteristics of an AlGaAs Semiconductor Laser", *IEEE Journal of Quantum Electronics*, vol.QE-16, no.9, September 1980, pp.915-917.

[21] S. Kobayashi, and T. Kimura, "Automatic Frequency Control in a Semiconductor Laser and an Optical Amplifier", *Jourant of Lightwave Technology*, vol.LT-1, no.2, June 1983, pp.394-402.

[22] Anthony E. Seigman, Lasers, University Science Books, California, 1986, pp.954-972.

[23] Roy Lang, and Kohroh Kobayshi,"Suppression of the Relaxation Oscillation in the Modulated Output of Semiconductor Lasers", *IEEE Journal of Quantum Electronics*, vol.12, no. 3, March 19??, pp.194-199.

[24] O. Lidoyne, Philippe B. Gallion, and Erasme, D., "Modulation Properties of an Injection-Locked Semiconductor Laser", *IEEE Journal of Quantum Electronics*, vol.27, no. 3, March 1991, pp.344-351.

[25] Agrawal, G.P., Intensity Dependence of the Linewidth Enhancement Factior and Its Implications for Semiconductor Lasers, *IEEE Photonics Technology Letters*, vol.1, no.8, August 1989, pp. 212-214.

[26] C.H. Henry, "Theory of phase noise and power spectrum of a single-mode injection laser, *IEEE Journal of Quantum Electronics*, vol. QE-19, pp.1391-1397, 1983.

[27] C.H. Henry, "Theory of linewidth of semiconductor lasers," *IEEE Journal of Quantum Electronics*, vol. QE-18, pp.259-264, 1982

[28] S. Kobayashi, and T. Kimura, "injection Locking in AlGaAs Semiconductor Laser", *IEEE Journal of Quantum Electronics*, vol.QE-17, no.5, Mya 1981, pp.681-689.

[29] A. Sudbo, and L. Hafskjaer, "Modeling of the Frequency Modulation Response of Semiconductor Diode Lasers", *IEEE Journal of Quantum Electectronics*, vol.24,no.4, April 1988, pp.625-634.

[30] G.P. Agrawal, "Power spectrum of directly modulated single mode semiconductor lasers:, *IEEE Journal of Quantum ELectronics*, vol.QE-21, pp.680-698, 1985.

[31] C.H. Henry, "Theory of Phase Noise And Power Spectrum of a Single-Mode Injection Laser," *IEEE Journal of Quantum Electronics*, vol. QE-19, pp.1391-1397, 1983

[32] D. Welford, "A Rate Equation Analysis for the Frequency Chirp Modulated Pwoer Ratio of Semiconductor Diode Laser," *IEEE Journal of Quantum Electronics*, vol. QE-21, pp.1749-1751, 1985.

[33] O. Lidoyne, Philippe B. Gallion, and D. Erasme, "Modulation Properties of an Injection-Locked Semiconductor Laser", *IEEE Journal of Quantum Electronics*, vol.27, no. 3, March 1991, pp.344-351.

CHAPTER 3

OPTICAL PROCESSES in the MESFET

3.1 Introduction

In this Chapter, optically induced effects in GaAs MESFETs are explored. Following a historical review of research in the area, the physics of photo-induced effects is discussed. The concept of photoconductivity and gain are presented to explain why more than one electron is collected at the MESFET contacts for every one photon injected. Schottky barrier lowering is the major contributor to the increase in drain current.

Solving Poisson's equation with the current continuity and current density equations gives an analytical tool to discuss the perturbations in the MESFET channel when injected. Because the MESFET used in this Thesis is a commercially available device, details of the process and structure are unknown. Therefore, detailed solutions to the diffusion equation provide us with understanding but questionable accuracy. Also, the results of the derivation is a coupled system of equations that is analogous to the laser rate equations. These theoretical results are given here and a large signal circuit model with experimentally derived parameters is given in Chapter 6.

3.2 Background

In this section, the history of MESFETs are followed by a review of photoconductivity research. Optical effects is discussed in the final subsection.

3.2.1 Semiconductors and Transistors

The first bipolar transistor was invented in 1947 at Bell Laboratories. The major results in the research of semiconductors and transistor theory were published in the 1950's. In 1950, Shockley published Electrons and Holes in Semiconductors[1] . Carrier recombination and lifetime established by the efforts of Hall[2] and Shockley[3] , and Stevenson and Keyes[4] . The FET (and MESFET) is based on a current path whose conductance is modulated by the application of an electric field transverse to the direction of current conduction. The field-effect transistor (FET) was initially described by Shockley[5] where majority carrier flow rather than bipolar flow is required for transistor action.

A compilation of the physics of semiconductor devices was written by S.M.Sze of Bell Labs[6] . During the 1960's and early 1970's, Van der Ziel[7] and Baechtold[8] , Klassen[9] analyzed the noise characterization of FET devices. Van Der Ziel considered small signal high frequency behavior of FET[10] . Grebene and Ghandhi created a device oriented model of the FET beyond pinchoff.[11] . It provides a qualitative and quantitative description of current conduction mechanism. In 1970,

Lehovec and Zuleeg took the FET analysis into the hot electron range[12]. The area of velocity saturation and field dependent mobilities are also represented in the model. Statz, Haus and Pucel developed a comprehensive model for the FET by assuming two regions in the FET: ohmic and velocity saturation[13]. In 1987, H.C.Ki, et al., extended this work to a three section model for GaAs MESFET operation[14]. Chang and Day[15] reported a two dimensional analytic solution to Poisson's equation by considering a three region model of the MESFET channel. It was the first work in thirty years which produced an analytic 2-D solution in the high-field region of FET's.

Large signal modeling of GaAs MESFETs began to appear in the literature in the early 1980's. The well known Curtice Model was established to facilitate the design of GaAs integrated circuits. Transit time effects where neglected. The parameters of the model were evaluated in part from experiment or device analysis. The usefulness of the Curtice model is that it could be integrated in conventional time-domain circuit simulation programs (e.g., SPICE) with minimal computational complexities. The Statz-Raytheon model refined the original Curtice model to include better modeling of saturation phenomenon. The Statz model is used in this Thesis. Curtice extended his modeling work in 1985 to FET operation from DC-to-RF domain. This nonlinear model was developed using measurements and the method of harmonic balance[16]. This nonlinear model boasts good results compared to 2-D models in the time domain with the added benefit of less computational power required. To derive the model parameters, experimental techniques were established. Determination of device parameters were required. (Fukui method)[17].

3.2.2 Photoconductivity

The first report of photoconductivity was by Willoughby Smith in 1873[18] when he noticed a difference in resistance of a selenium resistor in the day versus the dark hours. In 1955, A. Rose analyzed the photoconductors in a phenomenological way whereby the conductivity of the material is increased with illumination[19]. In 1960, R.H. Bube published his work in Photoconductivity in Solids. Bube's book establishes a mathematical analysis and a conceptual framework to discuss photoconductivity phenomena. The concept of photoconductivity implies an electric conductivity associated with the absorption of photons (i.e., absorption of energy from particles which changes the conductivity). Bube's follow up book provides the fundamentals of photoelectronic properties and is a comprehensive publication of research in the field of photoconductivity.

3.2.3 Optical Effects in Semiconductors

The light sensitive properties GaAs MESFET have been researched with several different areas of emphasis. During the last decade, work has been conducted on injecting MESFETs with light and describing the effects in the device.

Gammel and Ballantyne published some of the earliest results in 1978. A pulsed 15 ps optical signal was detected which was generated by a mode-locked dye laser. The main optically sensitive mechanism was described by a change in the

device transconductance (photoconductive)[20]. To improve coupling efficiency the gate metal was replaced with a waveguide which was the first integrated FET structure to take advantage of its optical properties[21]. The first analytical model of photo-changes in the circuit parameters (g_m, C_{gs}, C_{gd}) was published in 1979. In this model and supporting data, the illumination is said to cause carrier generation apart from equilibrium which forces a voltage to be developed (See Section 3.5.2 Optically Generated Minority Carriers and Induced Voltage)[22]. This photo-voltage adds to the existing Schottky barrier potential which lowers the effective barrier height. After detailed analyses of the MESFET under illumination, the changes in the Schottky barrier have been found to be the major contributor to the measured photo-effects (with the exception of external circuit conditions). Common source and common drain MESFET oscillator configurations were studied

In 1982, the photosensitivity of GaAs FET was studied using optical and also electron beam stimulation by Noad[23]. The electron beam injection was used to take advantage of the narrow spot sizes of tens of nanometers. The small spot sizes helped to isolate the photosensitive device area. The influence of the e-beam voltage was mapped out from the source contact to the active region across the gate metal, active channel and to the drain contact. The e-beam voltage of 10kV produced current changes only when focused on the active channel region. With 15KV, the beam was shown to penetrate the gate metalization which produced bulk effects. Carriers are generated from the absorption of energy into the semiconductor material. With appropriate field conditions within the device, the generated carriers are swept into the channel and contribute directly to the established current.

In 1983, DeSalles characterized the RF optical effects in MESFETs , adapted existing MESFET models to include light injection and proposed several applications for their use[24] . The gain of the device was controlled optically and the fundamental device parameters were measured. The same year, Mizuno published experimental MESFET measurements of RF parameters with similar results[25] .

The photo-induced changes in the depletion region width which give rise to changes in the device impedance. The most dramatic device changes are optically sensitive transconductance, g_m, and capacitance, C_{gs}, C_{ds}, which directly influence the operating frequency and output power[26] . As the depletion region width changes with optical injection, the effective space charge density increases. The majority of the studies on optical effects on devices has concentrated on approximations to calculate the photovoltaic effect at the gate. DeSalles built from the work of Lehovec and Zuleg[27] , Grebene and Ghandi[28] , and Pucel, Haus and Statz[29] , which collectively establish dark MESFET theory of operation. These theories were modified to include the characteristics of the illuminated MESFETs[30] . Without resorting to complete two-dimensional numeric methods, the continuity equations were solved with photo injection terms included by R.B. Darling[31],[32] . The continuity equations describe in detail all the photo-effects in a semiconductor regardless of their magnitude. This method provides a means to include transit time effects into the optical model and to determine an analytical expression for the optical gain. The optical gain characteristics from a carrier transport viewpoint is the primary emphasis of the work completed by Darling[33] .

Analytical work by Simons and Bhasin have described the physical effects of optically injected MESFET devices[34,35]. The Simons work has some encouraging results but does show serious discrepancy between the computed and the measured values of C_{gs} and g_m which he attributes to the inclusion of several simplifying assumptions in the model[36]. In 1992 Madjar, Herczfeld and Paolella analyzed the MESFET by solving the diffusion equation in each MESFET region that is illuminated[37]. This links an illuminated MESFET model with the actual device physics. This analysis is in a convenient form for integration into circuit models because the resultant currents can be represented as sources around the intrinsic MESFET model. Further work by the same researchers in 1994, modeled optical switching of MESFETs using Schottky barrier effects.[38]

3.3 Classification of Optical Processes

There are three major classes of optical processes in semiconductor materials. For the GaAs MESFET, these optical processes are related to variations in the parasitic elements of the MESFET, to photoconductive processes, and to photovoltaic processes. The main optical effect is the generation of minority carriers. The way in which the minority carrier ultimately changes the MESFET operation is the "process".

Changes to the parasitics are considered to be separate effects beyond the intrinsic device operation. Increases in the conductivity of the substrate, drain and

source contacts, and other parasitic parts of the structure are attributed to photoconductive processes. In general, these changes in conductivity occur independent of the "intrinsic" MESFET operation and are presented with the circuit model in Chapter 6. The discussion of the illumination perturbations to the device parasitics will follow closely the work of Simons[39] and DeSalles[24].

Optical energy separates electron-hole pairs. The transport dynamics of the carriers is directly influenced by the photoconductivity. Photoconductive processes arise from photogenerated electron-hole pairs along the longitudinal direction of the channel which depend strongly on V_{ds} not V_{gs}. The longitudinal electric field profile of the channel, which is determined mainly by V_{ds} for a given V_{gs}, determines the transport dynamics of the generated carriers . Therefore, the photoconductive optical gain is controlled by the longitudinal electric field which is most strongly effected by V_{ds}.

Photovoltaic processes are due to the collection of photogenerated carriers in the high electric field of a space-charge region. Voltage develops due to changes in the carrier concentration. It is well known that changes in bias effect the channel thickness of MESFET devices under dark conditions. Bias changes ultimately effect the electrostatic potential profile of the channel which modulates the channel thickness. When a MESFET is illuminated, the photogenerated carriers are collected in the high electric field of the space charge region. This is transverse to the channel. Therefore, an additional voltage, termed photovoltage, is developed across the space charge region. Analogous to dark conditions, the additional photovoltage will modulate the conductivity-effective channel thickness of the dark

MESFET. The additional photovoltage is developed across the transverse direction to the channel. In steady state, photovoltaic processes can be reduced to an effective change in Vg-to-substrate. The photovoltaic contribution to optical gain will be shown to be independent of V_{ds}. The gain is independent of V_{ds} because the V_{ds} potential is primarily due to the development of the transverse field but dependent on V_{gs} which is longitudinal to the channel. It has been found that major contributor to the measured changes in the drain current is due to the photovoltage which subsequently forward biases the gate depletion region, lowers the Schottky barrier and causes the channel width to widen.

Under dark conditions, the channel current is essentially unipolar. Generation (G), recombination and injection have negligible effect on the terminal characteristics of the MESFET. Under illumination, current flow becomes bipolar with electron-hole pairs are generated, separated, and recombining both inside and outside of the channel. The main effect is the increase in Vg-to-substrate which effectively lowers Schottky barrier potential. These processes will alter the channel carrier densities via transit-time photoconductivity. Also, the high electric field of any depletion region adjacent to the channel will separate any photogenerated carriers and inject one polarity type into the channel. The effect of transverse channel injection can also alter equilibrium of the depletion region and depletion width. Therefore, the channel thickness can be modulated by the light. The photogenerated carriers are separated and collected by the electric field of the MESFET channel. The change in the space-charge density will increase the electric

field at each boundary. This perturbation of the field will tend to inject electrons into the channel from the source and holes in from the drain.

An incident optical beam may generate electron-hole pairs in only a portion of the photoconductive channel and the response then depends on the location of the excitation. For completeness, a model of optical injection should allow for position dependence. Also, high field causes saturation of the photocurrent. The response then becomes strongly nonlinear with electrical bias. The generated carriers may become heated by the field which implies that the carrier mobilites become field dependent. This is a lower bound on the carrier transit time through the channel. Both position and field dependent mobility can be modeled by a complete solution to coupled differential equations derived from Poisson's equation and current continuity and density equations. The transit time solution has been found by other authors to produce 5% of the total drain current change[40].

In summary, changes in the channel current are from photogenerated electron-hole pairs. The minority carrier generation is the primary effect. The transport of these carriers are secondary. The transition rate of photon absorption and the electron ionization from the valence to the conduction band provides the coupling between the electron and photon transport. The generation rate represents this phenomenon.

3.4 Photoconductivity

Electrons and holes are distributed throughout the energy levels. The mobility μ of these carrier is related to the material's conductivity σ.

$$\sigma = q\{ n\mu_{no} + p\mu_{po} \}$$

Photoconductivity is a combination of optical excitation and transport phenomena. When illuminated, the concentration of free carriers changes by an amount $\Delta\sigma$; this is photoconductivity. The initial carrier concentration and the mobilities have an added component due to the optical perturbation. Replacing n with $n_o+\Delta n$ and p with $p_o+\Delta p$, the conductivity becomes:

$$\sigma + \Delta\sigma = q\{ (n_o + \Delta n)(\mu_{no} + \Delta\mu_n) + (p_o + \Delta p)(\mu_{po} + \Delta\mu_p)\}$$

Therefore, the photoconductive component $\Delta\sigma$ is

$$\Delta\sigma = q\{\mu_{no}\Delta n + \mu_{po}\Delta p + (n_o + \Delta n)\Delta\mu_n + (p_o + \Delta p)\Delta\mu_p\}$$

The change in carrier concentration is related to the lifetime τ and the generation rate G via:

$$\Delta n = G\tau_n$$
$$\Delta p = G\tau_p$$

Generation rate of electron hole pairs is related to the absorption coefficient of the material and the reflectivity times the photon energy absorbed:

$$G = \eta \frac{\Gamma P_{opt}}{h\nu} e^{-\alpha d}$$

where η is the efficiency, Γ is the transmissivity of the surface, P_{opt} is the optical power, α is the absorption coefficient of the material, and d is the depth inside the

material. In Table 1, the absorption coefficients and bandgap energies of several semiconductor materials are given for reference. Rewriting the photoconductivity:

$$\Delta\sigma = q(\mu_{no}\tau_n + \mu_{po}\tau_p) + q(n\Delta\mu_n + +p\Delta\mu_p)$$

where $n_o+\Delta n$ and $p_o+\Delta p$ were replaced with n and p respectively. There are three types of effects represented in the latter equation: (1) increase in carrier density with constant lifetime τ, (2) increase in carrier density with photo-excitation dependent lifetime $\tau(G)$, and (3) increase in carrier mobility. For this study, we are assuming

Table 1 Semiconductor bandgap energy

Semiconductor Material	*Absorption Coefficients* α *(cm^{-1})*	*Bandgap @ 300 °K (eV)*
Si	10^3	1.12
Ge	$8x10^5$	0.66
GaAs	10^4	1.42

that the lifetime is a constant. Mobility changes can be attributed to scattering by charged impurities and excitation of carriers from one energy band to another that means the mobility of each band is different.

In GaAs, the mobility is field dependent which gives rise to velocity saturation of the carriers at high enough values of the field. This will be considered in solving Poisson's equation in the Supplement . For semiconductors, the change in carrier concentration (Δn, Δp) is much less than the initial carrier concentration (n_o, p_o). With $\Delta n << n_o$ and $\Delta p << p_o$, the change in conductivity is written as follows:

$$\Delta\sigma = q(\mu_{no}\tau_n + \mu_{po}\tau_p) + q(n_o\Delta\mu_n + +p_o\Delta\mu_p)$$

3.5 Optical Gain

It has been found that both I_S and I_D increase significantly more than 100 times I_G ($\Delta Ig << \Delta Id - \Delta Is$)[41]. Therefore, the photo-process is not simply a sweep out of photogenerated carriers. This means there is an optical gain mechanism. More than one carrier pair is generated for each absorbed photon. In this section, the origins of the optical gain are discussed. Expressions are developed which describe the gain mechanism in semiconductors. Five possible causes of the phenomenon are developed in the sub-sections based on the origins of the gain.

The process of optically generated carriers is discussed now. Free carrier pairs are optically generated if the energy of the photon ($h\nu$) is greater than the GaAs bandgap. If the depletion region were illuminated, electron-hole pairs are generated here. The electrons are swept out of the depletion region by the electric field. The holes are emitted through the gate metal. In the undepleted material, carriers are also photo-generated. The holes (minority carriers in n-type GaAs) diffuse into the junction before recombining if they are within a diffusion length to the junction. The separation of the carriers causes a space charge to be created. The photo-induced carriers produce a voltage. The effect of the minority carriers generated outside of the depletion region but in the semiconductor has been found to be significant.

Carriers are generated in the n-type GaAs material from light illuminating the active area between the gate metal and source and/or between the gate metal and drain. The absorption of the photon energy occurs in the active region, buffer and

substrate (when $h\nu \geq E_g$ = band gap of GaAs). In Figure 1, V_{bi} is the built-in barrier voltage, V is the bias voltage (forward bias is -V, reverse bias is +V). E_c, E_v, E_F, are the conduction and valence band, and the Fermi energy levels. E_g is the energy gap. Uncompensated charge is changed by optical energy. The number of positive charges decreases because they are excited from the valence band to empty donor levels or increases by exciting deep donors to the conduction band. The concentration of negative charges decreases by exciting acceptors to the conduction band or increases by exciting from the valence band to empty acceptors . Under the assumption of complete sweep efficiency (all are swept out), no recombination occurs. The photo-generated carriers give rise to photoconductive effects which are changes in the resitivity of the regions of the device, and cause the metal-semiconductor depletion region and the channel-substrate depletion widths to

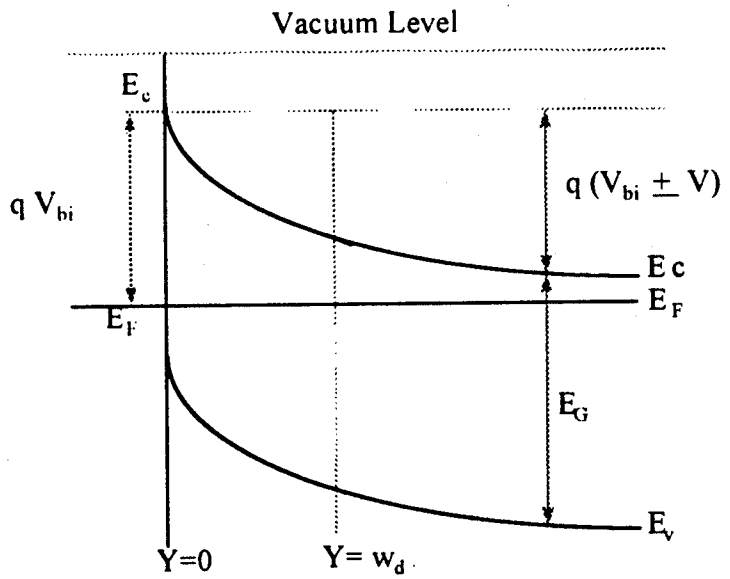

Figure 1 Energy band diagram

change. The photon absorption and the generated carriers are primary effects while the transport details of the photo-generated carriers is secondary.

The hole diffusion is governed by the following equation:

$$\frac{d^2}{dy^2}p - \frac{1}{D_p \cdot \tau_p}\cdot p = -\alpha \cdot P_{opt} \cdot \Gamma \cdot \frac{\lambda}{h \cdot c} \cdot e^{-\alpha \cdot y}$$

which can be solved analytically as a function of the depth (y) into the n-type GaAs:

$$p = \tau_p \cdot \alpha \cdot P_{opt} \cdot \Gamma \cdot \frac{\lambda}{h \cdot c} \cdot \left[e^{-\alpha \cdot d} \cdot \cosh\left(\frac{a - y}{L_p}\right) - \alpha \cdot L_p \cdot e^{-\alpha \cdot a} \cdot \sinh\left(\frac{y - d}{L_p}\right) - e^{-\alpha \cdot y} \right] \cdot \frac{1}{\cosh\left(\frac{a - d}{L_p}\right) \cdot \left(\alpha \cdot L_p\right)^2 - 1} \qquad (3\text{-a})$$

where a is the depth of the epitaxial layer and d is the depletion region depth (w_d from this point). The diffusion length $L_{n,p}$ is related to the diffusion coefficient $D_{n,p}$ and the lifetime τ by $L_{n,p} = \sqrt{D_{n,p}\tau_{n,p}}$. Equation (3-1a) will be used in the following sections to derive optically generated hole currents. The change in hole concentration in the channel is related to the integral of the optical generation rate:

$$\begin{aligned} p = \Delta p &= \int_0^a -\frac{\tau P_{opt} \Gamma}{a\, h\nu} e^{-\alpha y} dy \\ &= \frac{\tau}{a}\left(\frac{-P_{opt}\Gamma}{h\nu}\right)(1 - e^{-\alpha a}) \approx \frac{\tau}{a}\left(\frac{-P_{opt}\Gamma}{h\nu}\right)\alpha a \end{aligned} \qquad (3\text{-1b})$$

In p-n junction or a metal-semiconductor junction, a barrier is produced with a built-in potential due to the ionized atoms and the internal electric field. The potential barrier is produced by the migration of holes and electrons at the junction which causes a space charge field to be set up. The space charge field stops more carriers from leaving . When forward biased, the carriers are injected across the junction which lowers the barrier. Under reverse bias, the barrier gets larger by the

junction which lowers the barrier. Under reverse bias, the barrier gets larger by the amount of the bias and only saturation currents exist. n-type GaAs semiconductor acts as a rectifying Schottky barrier. When illuminated, the barrier conducts with electrons. If we consider complete sweep-out, the hole charges must decay through metal, and the electrons must drift into the channel.

In the depletion region, the carriers which have now been separated by the field, reduce the barrier potential by an amount V_{ph} . V_{ph} adds to the gate potential in the forward bias direction. This is the so-called photovoltaic effect. When the free carriers move in response to local fields and accumulate to produce space charge regions, a photovoltage is developed because thermal equilibrium has been disturbed[42].

The carriers are collected by the gate electrode and the source and drain contacts. The holes are collected by emission into the gate metalization after they are generated and separated from electrons in the gate and surface depletion regions. The electrons and holes from the active channel are collected by the drain and source contact respectively. If optical power is injected, there is an increase in the drain and source currents ΔI_d -ΔI_s which are bounded by the total gate current I_G.

It has been found that both I_S and I_D increase significantly more than 100 times I_G ($\Delta I_G << \Delta I_d - \Delta I_s$). Therefore, the photo-process is not simply a sweep out of photogenerated carriers from the depletion regions. This means there is an optical gain mechanism. The separation and transport of photo-generated carrier pairs must give rise to more than one pair collected at the device contacts. Optical gain is defined as the number of charges collected in the external circuit for each photon

absorbed. If the lifetime of a carrier is greater than its transit time, it traverses the material several times before exiting at the ohmic contacts. Bube defined gain as the ratio of lifetime to transit time.

$$\text{Gain} = (\tau_n \mu_n + \tau_p \mu_p)\frac{\phi}{d^2}$$

where τ_n, τ_p are the lifetimes of the electrons and holes respective and μ_n and μ_p are the mobilities of the carries and ϕ is the potential, and d is the depth. Using the definition of the conductivity σ:

$$\text{Gain} = \sigma\frac{\phi}{d^2}$$

When bias is applied, the transit time of the carriers decreases which then increases the gain. However, the contacts are ohmic which cause space charge limited current injection when voltages are applied. Gain values greater than one require the presence of ohmics, but in competition with this requirement is the fact that the voltage on the contact develops a space charge limited injection. The tradeoff between the decrease in carrier transit time and the space charge created at the ohmic gives rise to a maximum achievable optical gain[43-46]. The maximum gain occurs when the injected charge from the ohmics is equal to the photo-excited charge. The dielectric relaxation time τ_{dr} is the minimum value of the transit time τ before space-charge injection from the ohmics dominates. The dielectric relaxation time is related to the reciprocal of the mobility. Therefore, the gain is proportional to the following:

$$\text{Gain}_{max} \propto \frac{\tau}{\tau_{dr}}$$

If the ohmic contacts are for both holes and electrons, the gain is

$$\text{Gain} = \frac{\tau_n}{\tau_{dr\ n}} + \frac{\tau_p}{\tau_{dr\ p}}$$

If the hole contact is not ohmic and the electron contact is ohmic or if the operation is mainly unipolar as in the dark MESFET operation, the hole leaves the material but is not replaced. Therefore, effective hole lifetime is the hole transit time. Since the hole has not been replaced, the electron does not need to be replaced by the contact, and so, the electron lifetime is also the hole transit time. The gain then becomes:

$$\text{Gain} = \frac{\tau_{dr\ p}}{\tau_{dr\ n}} + \frac{\tau_{dr\_p}}{\tau_{dr\_p}} = \frac{\tau_{dr\ p}}{\tau_{dr\ n}} + 1 = 1 + \frac{\mu_n}{\mu_p}$$

There are five possible causes of the optical gain phenomenon: (1) gate currents[44], (2) transverse channel injection, (3) voltage drops across gate resistances from the supply to the MESFET gate metal[45], (4) photo-carrier induced voltages, and (5) transit time effects[46]. The gate diode currents are at least an order of magnitude too small to cause optical gain. The gate circuit voltage drops produce significant gain when the gate resistance R_g is large (i.e., gate is essentially open circuited), but if the R_g is less than 1-3 KΩ the gain is too small to account for the photo-induced changes. Transverse channel injection produces a maximum gain of one. Transit time effects in the channel account for 5% of photo-induced changes in the drain current. The photo-carrier induced voltages are shown to be the major contributor to the gain mechanism. These are discussed in the following sections.

3.5.1 Gate Currents

The depletion region under the gate metal is shown in Figure 4. The carriers photo-generated in the depletion region produce a gate current I_g. However, as shown in Chapter 5, practically all of the optical signal is reflected off of the metalized gate. Therefore, most of the depletion region is unilluminated, and the carrier generation is zero with the exception of the carriers from depletion region tails. The tails of the depletion region extend past the gate electrode and are illuminated (Figure 2). However, this effect is small and at least an order of magnitude too small to contribute to gain mechanism. The carriers, photogenerated in the undepleted regions, may diffuse into the depletion region (Figure 3). Since dark MESFET operations is mostly unipolar and assuming 100% sweep-out of the carriers, the main effect at the gate diode is the ionized donor charge.

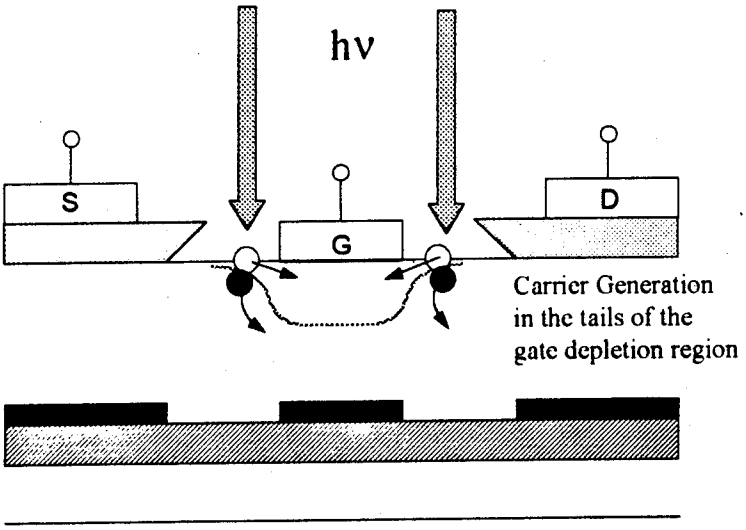

Figure 2 Carrier generation in the Depletion Region Tails

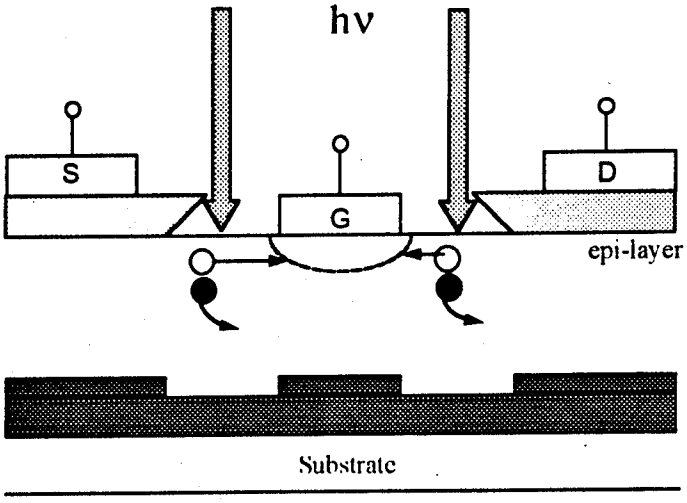

Figure 3 Photo-carriers diffuse into gate depletion region

Carriers are generated in the surface depletion regions close to the gate metal. The holes are added to the gate current through emission to the gate metal. Figure 4 shows schematically the surface depletion regions. The contributions to the total gate current I_G from the surface depletion regions and the gate depletion region are shown. The hole currents generated on the source and drain sides in the surface depletion region are I_{sD_G} and I_{dD_G} respectively.

The hole current generated in the tails of the Schottky gate depletion region is I_g.

The overall gate photo-current is given by

$$I_G = I_g + I_{sD\_G} + I_{dD\_G}$$

The hole currents generated inside the surface depletion regions (I_{sD_G}, I_{dD_G}) are given by

$$I_{dD\_G} = \int_0^d q \frac{\alpha}{h\nu} P_{opt} \Gamma e^{-\alpha} dy$$

$$I_{sD\_G} = \int_0^s q\frac{\alpha}{h\nu}P_{opt}\Gamma e^{-\alpha y}dy$$

where d and s are the depth of the surface depletion region on the drain and source sides respectively and Γ is the surface transmissivity.

The photo-current I_g is the sum of holes generated from absorbed photons in the depletion region I_{L_abs} and holes generated in the undepleted material that diffuse into the depletion region I_{g_inj}. Excess carriers, generated in the undepleted regions, may diffuse into the gate depletion region if they are within a diffusion length and are separated as shown in Figure 3. The electric field at the depletion region separates the electron-hole pair. The exact calculation of these currents depends on the device geometry, but simplifications will be shown that are reasonably accurate are discussed in Section 3.7-Supplement .-A The hole current that is generated in the undepleted material and diffuses into the depletion region I_{g_inj} is:

$$I_{g\_inj} = q\frac{P_{opt}\Gamma_u}{h\nu}A\left(\frac{(\alpha L_p)^2(a-w_d)e^{-\alpha w_d}}{(\alpha L_p)^2-1}\right)$$

where Γ_u is the transmissivity of the channel surface. If there were significant illumination of the gate depletion region or if the depletion tails were illuminated, the hole current generated from absorbed photons in the depletion region I_{L_abs} is:

$$I_{L\_abs} \approx -qA\frac{P_{opt}\Gamma_{g.u}}{h\nu}\alpha w_d$$

where Γ_g is the gate transmissivity. If Γ_g is essentially zero, the absorbed photons in the depletion tails are still represented with the surface transmissivity Γ_u. Assuming

the Γ_g is zero but the depletion tails are illuminated. with the surface transmissivity Γ_u written as Γ, the total photo-current emitted from the gate depletion region I_g is :

$$I_g = I_{g\ inj} + I_{L\ abs} \approx q\frac{P_{opt}\Gamma}{h\nu}A\left(\frac{(\alpha L_p)^2(a - w_d)e^{\alpha w_d}}{(\alpha L_p)^2 - 1} + \alpha w_d\right)$$

The overall gate current I_G ($I_G = I_g + I_{sD\_G} + I_{dD\_G}$) is small and on the order of a few micro-Amps. Therefore, I_G is ignored in the optical effects model of this Thesis.

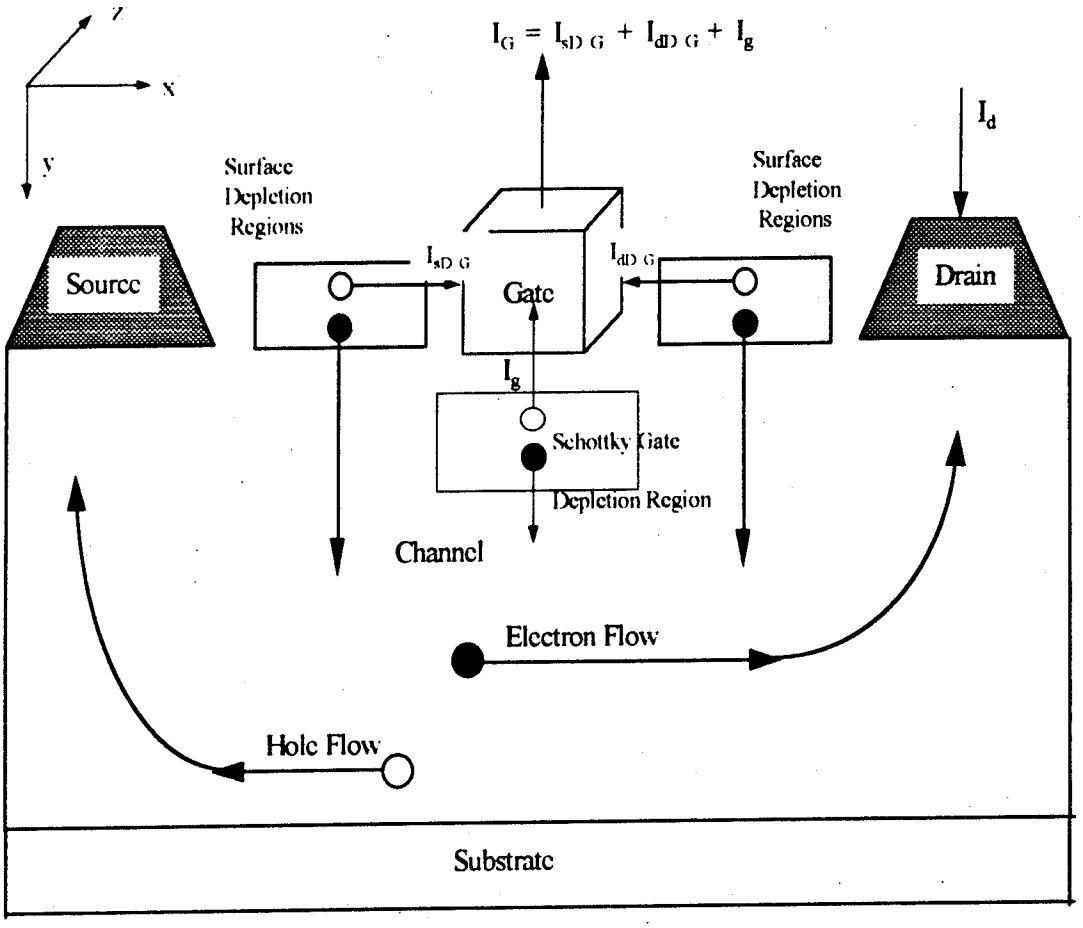

Figure 4 Carrier Injection into the Channel

3.5.2 Optically Generated Minority Carriers and Induced Voltage

In this section, the photo-generated minority carriers are shown to produce a voltage. This is the major optical effect in the MESFET. The change in voltage subsequently modifies the channel width and other MESFET model parameters. As shown in Chapter 5, virtually all of the optical power incident on the gate metal is reflected off of the surface. Therefore, the major optical effect is generated between the gate metal and the source contact and between gate and drain contacts. The carriers are generated in the undepleted regions and effect the barrier height by producing a voltage.

Voltage develops due to changes in the carrier concentration. It is well known that changes in bias effect the channel thickness of MESFET devices under dark conditions. Bias changes ultimately effect the electrostatic potential profile of the channel which modulates the channel thickness. When a MESFET is illuminated, the photogenerated carriers are collected in the high electric field of the space charge region. This is transverse to the channel. Therefore, an additional voltage is developed across the space charge region. This voltage effect is lumped together as one photovoltage which is superimposed on the gate bias. The magnitude of this effect is on the order of milli-Amps and is only surpassed by the gate bias circuitry photo-effects.

When illuminated , the concentration of minority carriers is much greater than under dark conditions. Therefore, the change in electrons traversing the junction is negligible in comparison to the change in holes.

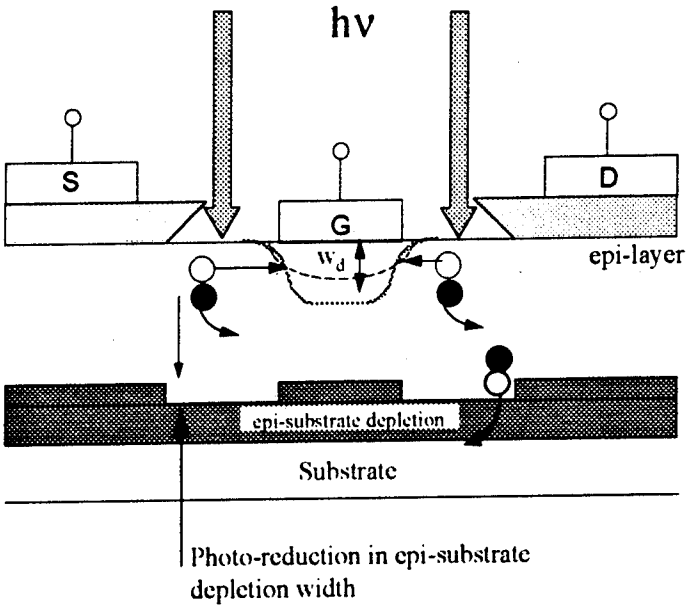

Figure 5 Carrier induced changes in the depletion region width

Excess carriers, generated in the undepleted regions, may diffuse into the gate depletion region and are separated as shown in Figure 5. The electric field at the depletion region separates the electron-hole pair. The electrons move to n-type material where they are the majority carrier. Similarly, the holes migrate to where they are majority. This sets up a field because there are excess carriers on opposite sides of the junction. This is analogous to a charged parallel plate capacitor. The electrons move to the n-type active layer which causes the region to become negatively charged. The junction is forward biased by this amount which then causes the Schottky barrier height to decrease.

The depletion region between the channel (epitaxial layer) and the substrate exists which is created by the abrupt differences in the doping concentrations of the two regions. The carrier pairs are generated form the absorbed light in the depletion

region. The carriers are swept out in opposite directions by the existing electric field. Since the substrate is highly resistive, an equivalent open circuit voltage is developed across the substrate to epilayer barrier[47]. The barrier potential is forward biased by the amount of this photovoltage, and therefore, the width of the depletion region decreases. Thus, the channel is wider.

Both depletion widths (directly under the gate and at the epi-substrate barrier) are reduced due to the production of free carriers in these regions as shown in Figure 5. The channel to substrate interfacial barrier depletion region and the gate depletion region are discussed from the viewpoint of Schottky diode. A more detailed analysis of the photo-voltage has also been calculated[48]. However, many details of the MESFET structure are necessary to calculate the integrals of the excess carrier density. Because of errors would be introduced by assuming the structure of the MESFET, the usefulness of this more exact model was not apparent for use in this Thesis. We have found that a good approximation (as shown below) is the Schottky diode open circuit voltage. With the increase in hole concentration is given by equation 3-1b, the photovoltage V_{ph} can be calculated from the Schottky diode equation.

The amount of V_{ph} is calculated by using a Schottky diode model to represent the region. Since the substrate has a high resistance, the open circuit diode equation can be used. Crowell and Sze [49,50] as well as R.H.Bube[51] have developed models of the current in Schottky barrier and will be used in the following analysis.

The total current though the "diode" is the dark current plus the contribution from the light effects ($I = I_{Dk} - I_L$). In terms of densities, the dark diode current density is

$$J_{Dk} = J_{ss}\left(e^{\beta V} - 1\right)$$

which represents the diffusion limited Schottky equation where β is $q/kT\eta$, and η is the ideality factor, and J_{ss} is the reverse saturation current density of the diode. Substituting for the reverse saturation current to get an expression containing the built in potential of the barrier:

$$I_{Dk} = \kappa e^{\beta V_{bi}}\left(e^{\beta V} - 1\right)$$

where V_{bi} is the barrier height of the junction and κ is a constant proportional to the electronic charge q and the doping concentration N_d.

The total current density is

$$J = J_{Dk} - J_{ph}$$

Under short circuit, V=0,

$$J_{sc} = J_{ss} - J_{ph}$$

With J=0, the open circuit photovoltage of a solar cell is given by[52]

$$V_{oc} = \eta \frac{kT}{q} Ln\left(\frac{J_{sc}}{J_{ss}}\right)$$

where J_{sc} is the short photo-current density and J_{ss} is the reverse saturation current density. Using this expression for the photovoltage and equation 3-1b, the photovoltage can be rewritten as

$$V_{ph} = \eta \frac{kT}{q} Ln\left(\frac{p_o + \Delta p}{p_o}\right) \qquad (3\text{-}2)$$

where $p_n = \frac{n_i^2}{N_d}$. This has been experimentally proven to provide excellent results.

The calculated carrier concentration is in Figure 6 and the corresponding voltage in Figure 7. The experimental values of the photovoltage were obtained by measuring the voltage drop across the gate with a large (59.7KΩ) in series with the applied V_{gs} with the drain opened. The large resistor essentially open circuits the gate circuit, and therefore, the measured value is V_{ph}. The gate current was measured as a function of applied V_{gs} with illumination. From the data, the zero current crossing V_{gs} was extrapolated which is V_{ph}. Both experiments gave the same result. However, the current is so small it was difficult to measure accurately. The changes in the gate current magnitude were 1-2 μA. Therefore, the data given in the Figure 7 is from the voltage measurement technique.

In Supplement A, more information on the carrier generation is given. However, the simple expression of 3-1b and 3-2 gave reasonable results. In Chapter 6 and 8, the photovoltage V_{ph} is superimposed onto the gate bias in existing MESFET models to predict drain current changes and other circuit effects. These calculation match well with experiment.

Because the MESFET may be imbedded in a gate circuit which is not an open circuit (i.e., R_g large), the approach taken here must be emphasized. The photovoltage is due to carrier generation into both gate and barrier depletion regions. The total photovoltage (gate + barrier depletion) is the open circuit voltage. The gate photovoltage may be zero depending on external circuit resistances. However, the substrate region is a high resistance (R = large) and

therefore, the voltage developed here is always accurately described by V_{ph}. Therefore, an additional voltage, that is developed across the space charge region, is accurately described by V_{ph}. Furthermore, experimentally, it is impossible to measure the voltage across the barrier. However, as described above, the gate open circuit voltage can be measured at the device terminals.

The voltage (V_{ph}) developed is the total photovoltage developed from the surface to the substrate Vg-to-substrate and is given by KVL as:

$$V_{ph} = V_{epi\_sb} + V_{gate\ depl}$$

V_{ph} is superimposed onto the existing internal gate bias v_{gs} and creates a bias V_{gs_eff}:

$$V_{gs\_eff} = v_{gs} + V_{ph} = V_{gss} - V_{Rg} + V_{ph}$$

The power supply bias V_{gss} is reduced by the amount of voltage drop across any existing gate resistance V_{Rg} (See Section 3.5.3). Using this superposition method, excellent results have been achieved. With increasingly positive gate voltage, the depletion width contracts which allows more current to flow in the channel. The depletion region width changes because of the addition of the photo-voltage,

$$w_d(y) = \left(\frac{2\varepsilon\varepsilon_o V_{bi}}{qN_d}\right)^{\frac{1}{2}} \left(1 + \frac{V_{gs} + V_{ph} - V(y)}{V_{bi}}\right)^{\frac{1}{2}} = w_o \left(1 + \frac{V_{gs} + V_{ph} + V(y)}{V_{bi}}\right)^{\frac{1}{2}} \quad (3\text{-}3)$$

where V_{gs} is the bias voltage and is a negative quantity, and the photovoltage is V_{ph} is a positive number and is mainly a function of the optical intensity, and the potential V(y) is the channel potential with respect to the source. V(y) is V_s at the source side and V_d at the drain side of the depletion region respectively. The larger V_{ph} is the more forward biased the junction becomes, and subsequently, the

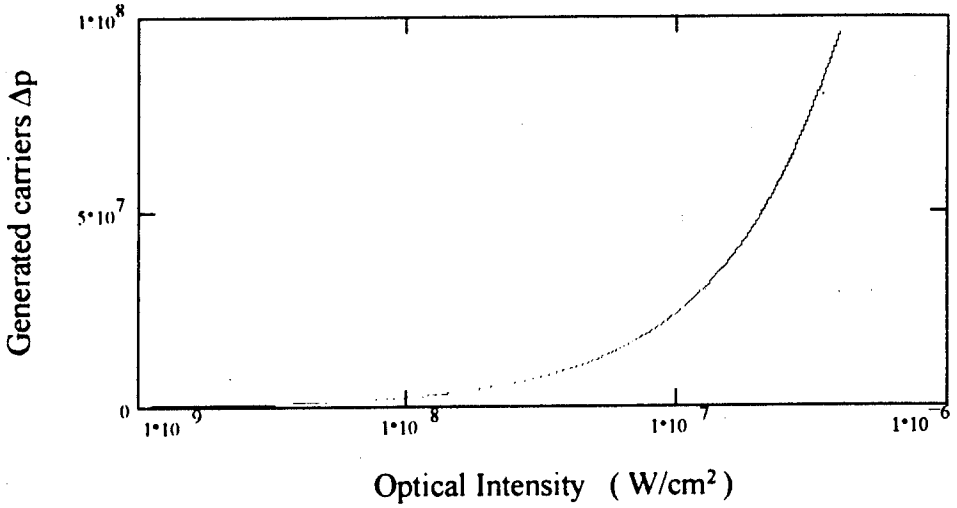

Figure 6 Generated Minority Carriers vs Optical Intensity

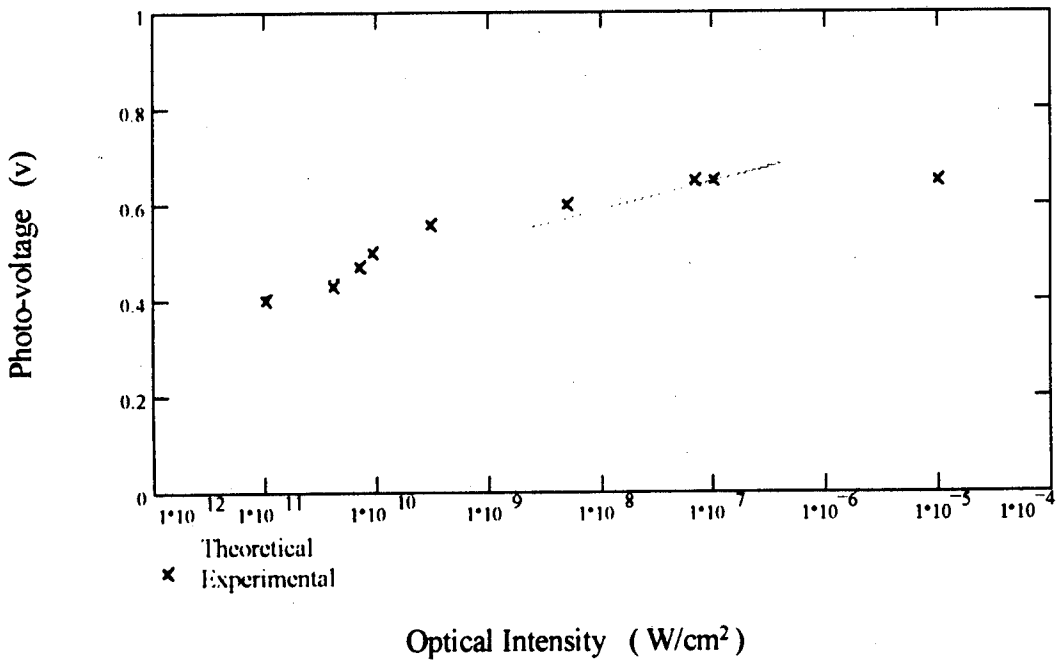

Figure 7 Theoretical and Measured Photo-Voltage vs Optical Intensity

depletion width gets smaller. A smaller depletion width means a larger active channel. Therefore, there is an increase in the conductivity as well as an increase in the channel width. In Chapter 6, additional MESFET model parameters are given with the photo-voltage superimposed.

3.5.3 Gate Bias Circuitry

The effect of the gate circuitry is now discussed. The photo-generated holes which add to the gate current, cause a voltage drop across any gate resistance. This voltage forward biases the gate electrode away from the supply bias voltage. This gate circuitry effect can be significant. When the resistance is high ($R_g > 10\ K\Omega$), these changes are on the order of the photo-induced increases in the drain current, but for lower resistances, this does not accurately model the photo-effects. This effect can be viewed as an external photovoltaic effect since the gate bias circuitry is not an intrinsic MESFET effect.

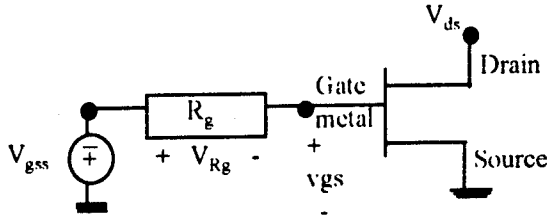

Figure 8 Gate circuitry

Holes in the tails of the gate depletion region or in the surface depletion regions manifest themselves as reverse bias gate current as discussed in Section 3.5.1. Although these are small quantities (micro-Amps), their effect is tremendous when in series with a large gate resistance R_g. Figure 8 is a schematic of the MESFET with external supply V_{gss} and gate resistance R_g shown. The hole currents in turn produce a voltage drop V_{Rg} across resistive elements R_g on the gate side:

$$V_{gss} + V_{Rg} = v_{gs} = R_g(I_{G\,Dk} + I_L) \tag{3-4}$$

where V_{gss} is the bias and is a negative quantity as indicate by its polarity in Figure 8 , v_{gs} is the voltage at the gate metal contact, $I_{G\,Dk}$ is the dark gate current, and I_L is the photo-induced current. The following expression from Section 3.5.1 is rewritten for convenience:

$$I_G = I_{G\,Dk} + \{ I_{g\_inj} + I_{L\,abs} + I_{sD\_G} + I_{dD\_G} \}$$

where the dark current is

$$I_{G\,Dk} = I_{ss} \left(e^{\beta V} - 1 \right)$$

where the reverse saturation current I_{ss} is related to V_{bi} is the barrier height of the junction and the electronic charge q and the doping concentration N_d as described in the previous Section. Therefore, the bias seen at the gate metal v_{gs} is the power supply bias V_{gss} forward biased by V_{Rg}. Rewriting the voltage drop across the gate resistance:

$$V_{Rg} = V_{gss} - v_{gs} = R_g I_{ss} (e^{V_{gss} \frac{q}{\eta kT}} - 1) - R_g I_L \tag{3-5}$$

With the bias supply is fixed V_{gss}, the actual voltage at the gate metal v_{gs} has increased by the amount of the V_{Rg}. With increasingly positive gate voltage, the

depletion width contracts which allows more current to flow in the channel. Now, the depletion region width changes because of the changed voltage at the gate metal V_{Rg}. The depletion region width is given by 3-3. The larger V_{ph} is the more forward biased the junction becomes, and subsequently, the depletion width gets smaller. A smaller depletion width means a larger active channel. Therefore, there is an increase in the conductivity as well as an increase in the channel width.

Under essentially open gate conditions (Rg>>>1) the gate current is nearly zero, and the voltage at the gate contact becomes:

$$vgs = \eta \frac{kT}{q} Ln\left(\frac{I_{ss} + I_L}{I_{ss}}\right) \tag{3-6}$$

The depletion region *edge* is pinned to this value. This sets the maximum amount of voltage drop V_{Rg}.

When the gate resistance is less than a few KΩ, the diode description fails. Particularly, if R_g is zero, there is no additional current. The photo-effects of Section 3.5.2 will represent the MESFET. In Chapter 6, experimental data is given that agrees well with the photo-voltage arguments presented here.

3.5.4 Transverse Channel Injection

In the gate and surface depletion regions, photo-generated electron-hole pairs are separated. Through emission, the holes are collected by the gate metal, while the electrons are swept out and are injected into the channel. In Figure 4, the electron injection into the channel from the surface depletion regions and Schottky gate depletion region is shown. The channel current is assumed to absorb the electrons via current continuity.

First, the total increase in gate current must equal the amount collected at the source and drain contacts ($I_S + I_G = I_D$). Because the optical energy is almost entirely reflected off of the gate metallization (Gate metal reflectivity = 96%. See Chapter 5.), the gate current increase is small due to the hole current from the gate depletion region I_g . In addition the surface depletion regions are small, and therefore, increases in the source side depletion region to the gate I_{sD_G} and drain side depletion region to the gate t $I_{dD\ G}$ hole currents are small.

Although the magnitude of the photo-generated carriers is not large, the important concept is that one carrier pair is generated for each one photon absorbed. The optical gain is one due to these effects and can be written as the ration of the change in current ΔI to the absorbed optical energy:

$$\text{Gain} = \frac{\Delta I_G + \Delta I_S + \Delta I_d}{\frac{q\eta}{h\nu} \sum_{\substack{\text{Gate,} \\ \text{Source,} \\ \text{Drain}}} \int P_{opt} \Gamma}$$

The denominator can be integrated across the lateral dimensions x, z and summed for each of the regions (gate, source and drain). The maximum gain at the drain is related to the absorption coefficient of the channel and is approximately equal to one:

$$Gain\_d = 1 - e^{-\alpha d} \approx 1$$

In terms of an increase in current magnitude, the transverse channel injection terms contribute to the overall current. In terms of a gain quantity, the maximum gain from these injected electrons is one. The transit of the channel photo-carriers and the effect on the channel conductivity are discussed in the next section.

The drain current as a result of the excess carriers in the channel is

$$I_{d\ inj} = \int_{d}^{a} p(y)\, q\, w \left(\frac{\tau_n}{\tau_{tn}} v_n + v_p\right) dy$$

where the limits of integration are given by the dimensions of the device, and w is the width of the channel and where the velocity of the majority carriers has been written in terms of its lifetime and transit time as follows:

$$n v_n + p v_p = p \left(\frac{\tau_n}{\tau_{tn}} v_n + v_p\right)$$

The hole density p(y) is given by 3-1a which is re-written below:

$$p \quad \tau_p \cdot \alpha \cdot P_{opt} \cdot \Gamma \cdot \frac{\lambda}{h \cdot c} \cdot \left[\frac{e^{\alpha \cdot d} \cdot \cosh\left(\frac{a - y}{L_p}\right) \quad \alpha \cdot L_p \cdot e^{\alpha \cdot a} \cdot \sinh\left(\frac{y - d}{L_p}\right)}{\cosh\left(\frac{a - d}{L_p}\right)} - e^{-\alpha \cdot y} \right] \cdot \frac{1}{(\alpha \cdot L_p)^2 - 1}$$

The photo-generated current $I_{d\ inj}$ is on the order of a tenth of a μAmp and is neglected.

3.5.5 Carrier Transit Time

The concept of lifetime is important to describe the carrier effects of an optically injected semiconductor material. If the lifetime of the carrier is longer than its transit time, the carrier will make several passes through the material. The increase in carrier concentration is the change in channel conductivity. Although this effect contributes only 5% or less to the photo-induced increase in drain current, the analysis is instructive, and the resultant coupled system of equations is analogous to the laser rate equations as discussed in Chapter 4.

Substituting current density equations into current continuity equations , eliminating the gradient of the carrier density by neglecting the longitudinal diffusion term, and phenomenonlogically adding the transverse injection terms (Kn, Kp) into the resulting set of equations, we can solve for the electron and hole current derivatives. These equations are a dynamic set of coupled equations for the electron current, hole current, and electric field. The full derivation is given in Supplement . The coupled matrix equation is as follows:

$$\frac{d\underline{\xi}}{dx} = \underline{\underline{M}} * \underline{\xi} + \underline{K}$$

where the matrices are defined as

$$\underline{\xi} = \begin{bmatrix} \Delta I_n \\ \Delta I_p \\ \Delta E \end{bmatrix}$$

$$\underline{K} = \begin{bmatrix} qAG + K_n^* \\ qAG + K_p^* \\ 0 \end{bmatrix}$$

$$\underline{\underline{M}} = \begin{bmatrix} 0 & \frac{-1}{\tau_p \mu_p E_{bias}} & 0 \\ 0 & \frac{1}{\tau_p^* \mu_p E_{bias}} & 0 \\ \frac{1}{\varepsilon A \mu_n E_{bias}} & \frac{-1}{\varepsilon A \mu_p E_{bias}} & \frac{-q}{\varepsilon E_{bias}} \left(\frac{\Delta\mu_n n_o}{\mu_n} + \frac{\Delta\mu_p p_o}{\mu_p} \right) \end{bmatrix}$$

with the electron lifetime approaching infinity and the hole concentration approaching zero in the n-type GaAs.

3.6 Conclusion

The MESFET under optical illumination has been studied in this Chapter. The effects of optical injection have been described by carrier generation in various regions of the device. Optical gain exists which means more than one electron-hole pair is generated for each photon absorbed. The five origins of optical gain have been explored. External gate circuitry has been shown to significantly effect the MESFET operation when illuminated. Internal to the MESFET, carrier generation sets up a charge distribution similar to a parallel plate capacitor. The additional potential across the distribution reduces the width of the depletion region. For the intrinsic MESFET, this photo-effect is the major cause of the optical gain. The development of optical gain phenomenon and the transport equations (3.5.5) is used in Chapter 4 because of its analogy to the laser rate equation.

3.7 Supplement A - Carrier distribution

When illuminated the hole and electron current densities from the absorbed photons in the depletion region are:

$$J_n(y) = Js\,(e^{\beta(Vg-V)} - 1) - q\,P_{opt}\,\Gamma\,\frac{\lambda}{hc}(1 - e^{-\alpha y})$$

$$J_p(y) = -qP_{opt}\,\Gamma\frac{\lambda}{hc}\,(e^{\alpha y} - e^{\alpha w_d})$$

w_d is the depletion depth, and Js is the reverse saturation current. The total current is

$$\begin{aligned} J &= J_n(y) + J_p(y) \\ &= Js\,(e^{\beta(Vg-V)} - 1) - q\,P_{opt}\,\Gamma\,\frac{\lambda}{hc}(1 - e^{\alpha w_d}) \\ &= J_{Dk} - J_L \end{aligned}$$

Alternatively, the light current density could have been expressed without considering the electron and hole currents separately:

$$I_{L\_abs} = A\int_0^{w_d} -q\frac{P_{opt}\Gamma_g}{h\nu}e^{\alpha y}\,dy = qA\frac{P_{opt}\Gamma_g}{h\nu}(e^{\alpha w_d} - 1) \approx -qA\frac{P_{opt}\Gamma_g}{h\nu}\alpha w_d \qquad (3\text{-}7a)$$

where the exponent was expanded via Taylor Series and A is the effective area.

The hole currents that diffuse into the gate depletion region from the undepleted channel are given by

$$I_{g\_inj} = A\int q\,D_p\,p(y)\,w\,dy$$

In the above, the diffused hole concentration p(y) is given in equation 3-1a. If the thickness of the undepleted region (a) is small versus the hole diffusion length L_p, then the hyperbolic sine terms go to zero and the hyperbolic cosine go to unity ($\sinh\{a/L_p\}=0$ and $\cosh\{a/L_p\}=1$). Also, the velocity of the holes divided by the

hole diffusion constant can be neglected compared to α. Since $\alpha w_d << 1$ and $\alpha(a-w_d) << 1$, the exponential terms can be expanded via Taylor series ($e^{-b} \approx 1 - b$). The integrated result for the short circuit current is then:

$$I_{g\ inj} = q\frac{P_{opt}\Gamma_u}{h\nu}A\left(\frac{(\alpha L_p)^2(a-w_d)e^{\alpha w_d}}{(\alpha L_p)^2-1}\right) \qquad (3\text{-}7b)$$

Combining 3-7a and 3-7b to get the complete photo current:

$$I_L = q\frac{P_{opt}\Gamma}{h\nu}A\left(\frac{(\alpha L_p)^2(a-w_d)e^{\alpha w_d}}{(\alpha L_p)^2-1}+\alpha w_d\right)$$

The total Schottky junction current is $I = I_{ss}\left(e^{\beta V}-1\right) - I_L$

3.8 Supplement B- Transport equations

Starting from the current density, current continuity equations for electrons and holes and using longitudinal Poisson self-consistency in the one dimension we can describe the carrier transport effects. Carrier transport is described via two current density equations, two current continuity, and Poison's equation.

Current density equations:

$$I_n \equiv J_n A = q\,\mu_n\, nAE + qAD_n \nabla n \approx q\,\mu_n\, nAE$$
$$I_p \equiv J_p A = q\,\mu_p\, pAE - qAD_p \nabla p \approx q\,\mu_p\, pAE$$

Poisson's equation

$$\frac{\partial^2 \Psi}{\partial x^2} = \frac{\partial E}{\partial x} = \frac{q}{\varepsilon}\left\{p(x) - n(x) + N_d(x) - N_a(x)\right\}$$

Current Continuity

$$\frac{\partial n(x)}{\partial t} = G_n(x) - U_n(x) + \frac{1}{q}\nabla \bullet J_n$$
$$\frac{\partial p(x)}{\partial t} = G_p(x) - U_p(x) - \frac{1}{q}\nabla \bullet J_p$$

Substituting current density equations into current continuity equations , eliminating the gradient of the carrier density by neglecting the longitudinal diffusion term, and phenomenonlogically adding the transverse injection terms (Kn, Kp) into the resulting set of equations, we can solve for the electron and hole current derivatives.

$$\frac{\partial I_n}{\partial x} = qA(x) * \left\{G_n(x) - U_n(x) - \frac{\partial n(x)}{\partial t}\right\} - K_n(x)$$
$$\frac{\partial I_p}{\partial x} = qA(x) * \left\{G_p(x) - U_p(x) - \frac{\partial p(x)}{\partial t}\right\} - K_p(x)$$

These equations are used with current density and Poisson's equation to form a dynamic set of coupled equations for the electron current, hole current, and electric field. External excitation from optical injection Δ or electrical injection Θ are substituted in these equations. Also, the coupled equations are linearized to first order in Δ or Θ because the order of the electric fields and carrier densities are approximately equal.

The coupled system of differential equations is given below:

$$\frac{d\underline{\xi}}{dx} = \underline{\underline{M}} * \underline{\xi} + \underline{K}$$

where:

$$\underline{\xi} = \begin{bmatrix} \Delta I_n \\ \Delta I_p \\ \Delta E \end{bmatrix}$$

$$\underline{K} = \begin{bmatrix} qAG + K_n^* \\ qAG + K_p^* \\ 0 \end{bmatrix}$$

$$\underline{\underline{M}} = \begin{bmatrix} \frac{-1}{\tau_n^* \mu_n E_{bias}} & \frac{-1}{\tau_p \mu_p E_{bias}} & \frac{qA}{E_{bias}}\left(\frac{\Delta\mu_n n_o}{\tau_n^* \mu_n} + \frac{\Delta\mu_p p_o}{\tau_p \mu_p}\right) \\ \frac{1}{\tau_n \mu_n E_{bias}} & \frac{1}{\tau_p^* \mu_p E_{bias}} & \frac{-qA}{E_{bias}}\left(\frac{\Delta\mu_n n_o}{\tau_n \mu_n} + \frac{\Delta\mu_p p_o}{\tau_p^* \mu_p}\right) \\ \frac{1}{\varepsilon A \mu_n E_{bias}} & \frac{-1}{\varepsilon A \mu_p E_{bias}} & \frac{-q}{\varepsilon E_{bias}}\left(\frac{\Delta\mu_n n_o}{\mu_n} + \frac{\Delta\mu_p p_o}{\mu_p}\right) \end{bmatrix}$$

$$\frac{1}{\tau_n^*} = \frac{1}{\tau_n} + j\omega_i$$

$$\frac{1}{\tau_p^*} = \frac{1}{\tau_p} + j\omega_i$$

ω_i is the injected frequency and the differential field dependent mobility is $\Delta\mu_{n,p} \quad \mu_{n,p}(\Delta E)$. The differential carrier mobility is a result of substituting $E = E_{bias} + \Delta E_{opt}$ into the coupled equations to represent the injection and maintaining that the mobilities are a function of electric field.

$$\mu(E) = \mu(E_{bias} + \Delta E) = \mu(E_{bias}) + \mu(\Delta E)$$

In general the recombination rates for a single level recombination are a function of electron capture, electron emission, hole capture, and hole emission. If thermal equilibrium is assumed, the expressions for $U_n(x), U_P(x)$ simplify greatly. Further simplification is possible when conditions for low injection are satisfied. This occurs if the injected carriers ($\Delta n \approx \Delta p$) are much fewer than the majority carriers. Based on low level injection and the previous assumption the combined recombination term is now given by:

$$U = \frac{\Delta p}{\tau_p} + \frac{\Delta n}{\tau_n}$$

$U(x)$ will now represent the total recombination term in the system of differential equations.

3.8.1 Optical Injection

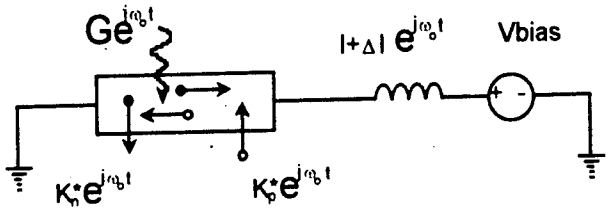

Optical injection does not alter the channel bias ($\Delta V=0$). Carriers are produced within the channel with the same optical frequency and with phase delay equal to the transverse transit time. The transverse injection term, therefore, is a complex quantity and is related to the current density in the y-direction (i.e., transverse to the channel) [53] .

$$G \neq 0$$

$$K_n \neq 0$$

$$K_p \neq 0$$

$$K_{n.p} \Rightarrow K^*_{n.p} = (J_{n.p.y1} + J_{n.p.y2})Wdx$$

3.8.2 Electrical Injection

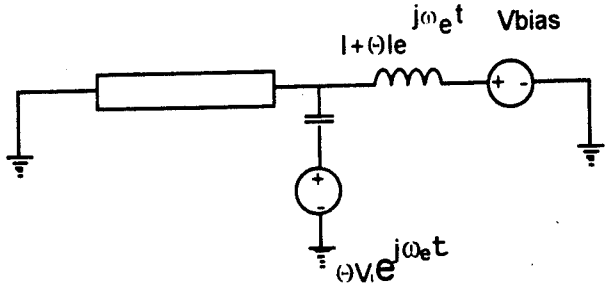

Under electrical excitation conditions, $\underline{K} = \underline{0}$ because of carriers are not generated (G=Kn=Kp=0) and the potential boundary values change and vary with electrical excitation frequency:

$$\Theta V \neq 0 = V_e e^{(j\omega e t)}$$

3.8.3 DC Injection Case

For DC injection conditions, there is no injection frequency(ω_i =0). Also, for n-type GaAs MESFETs, the electron lifetime goes to infinity:

$$p_o \rightarrow 0 \quad \text{and} \quad \frac{1}{\tau_n} \rightarrow 0 \qquad \text{Subsequently,} \quad \frac{1}{\tau_n \cdot} \rightarrow 0$$

Hence, the matrix becomes:

$$\underline{\underline{M}} = \begin{bmatrix} 0 & \frac{-1}{\tau_n \mu_p E_{bias}} & 0 \\ 0 & \frac{1}{\tau_p^* \mu_p E_{bias}} & 0 \\ \frac{1}{\varepsilon A \mu_n E_{bias}} & \frac{-1}{\varepsilon A \mu_p E_{bias}} & \frac{-q}{\varepsilon E_{bias}} \left(\frac{\Delta \mu_n n_o}{\mu_n} + \frac{\Delta \mu_p p_o}{\mu_p} \right) \end{bmatrix}$$

The system is decoupled and solutions may be written analytically. First, the integrating factors will be calculated. The system will be then be rewritten in terms of the integrating factors. The boundary conditions will be discussed and applied to determine the analytic solution for the DC steady state case.

3.8.4 Integrating Factors

The integrating factors for the electron and hole current under DC injection conditions are the same form. The difference is a minus sign in the exponent and the effective hole lifetime, τ^*_p, in the hole equation. For the hole current:

$$f(x) = \exp\left\{\int_x^{x'} \frac{1}{\tau_p^* \mu_p E} dx'\right\} = \exp\left\{\int_x^{x'} \frac{1}{\mu_p E}\left[\frac{1}{\tau_p} + j\omega_i\right] dx'\right\}$$

$\omega_i = 0$ for DC

τ_p = hole lifetime

Using the definition for the hole transit time:

$$\tau_{tp}(x, x') = \int_x^{x'} \frac{1}{\mu_p E} dx'$$

Therefore,

$$f(x, x') = \exp\left\{\frac{-\tau_{tp}}{\tau_p}\right\}$$

The definition of transit time under low injection follows that of Sze[54].

The integrating factor for the electric field equation:

$$g(x) = \exp\left\{\int_{x'}^{x} \frac{1}{\mu_n E} dx'\right\}\left(\frac{1}{\varepsilon} q\mu_n(\Delta E) n_o\right)$$

Using the definition for the electron transit time:

$$\tau_{tn} = \int_x^{x'} \frac{1}{\mu_n E} dx'$$

Using the defintion of the dielectric relaxation time:

$$\tau_i = \frac{\varepsilon}{q\mu_n(\Delta E) n_o}$$

Therefore,

$$g(x) = \exp\left\{\frac{-\tau_{tn}}{\tau_i}\right\}$$

3.8.5 Rewritten equations

The solutions can now be written in terms of the integrating factors.

The solution for the hole current:

$$\Delta I_p(x) = \frac{1}{f(x)}\left[\int_x^L f(x, x')\{qAG + K^*_n\} dx' + C\right]$$

If we know boundary condition for the hole current, then the latter equation can be written as:

$$\Delta I_p(x) = \Delta I_p(L) f(x, L) + \left[\int_x^L f(x, x') \{ qAG + K^*_n \} dx' \right]$$

The total channel current is the sum of both the electron and hole currents. Therefore, solution for the hole current can be used to solve for the electron current at a point, x, along the channel given the initial boundary value of the electron current , $\Delta I_n(0)$, the hole current at x=x, and at x=0, and phenomenonlogically adding in the transverse injection currents.

$$\Delta I = \Delta I_n + \Delta I_p$$

$$\Delta I_n(x) + \Delta I_p(x) = \Delta I_n(0) + \Delta I_p(0) - \int_0^x (K^*_n + K^*_p) dx'$$

Substituting for ΔI_p.

$$\Delta I_n(x) = \Delta I_n(0) - \frac{1}{f(x)} \left[\int_x^L f(x, x') \{ qAG + K^*_n \} dx' \right] + \frac{1}{f(0)} \left[\int_0^L f(0, x') \{ qAG + K^*_n \} dx' \right] - \int_0^x (K^*_n + K^*_p) dx'$$

The electric field equation is rewritten below in terms of its integrating factor, g(x):

$$\Delta E(x) = \frac{1}{g(x)} \left[\int_0^x g(x', x) \left\{ \frac{\Delta I_n}{\mu_n} - \frac{\Delta I_p}{\mu_p} \right\} \frac{dx'}{\varepsilon A E_{bias}} \right]$$

If we know boundary condition for the electric field, then the latter equation can be written as:

$$\Delta E(x) = \Delta E(0)g(0,x) + \left[\int_0^x g(x',x)\left\{\frac{\Delta I_n}{\mu_n} - \frac{\Delta I_p}{\mu_p}\right\}\frac{dx'}{\varepsilon A E_{bias}}\right]$$

3.8.6 Boundary Conditions

1. From the perturbed electric field and negligible longitudinal diffusion:

a. $\Delta I_n(0) = \Delta E(0)/Z_n(0)$

b. For strongly n-type channel, $p^*=0$, and, therefore,

$$\Delta I_p(L) = qA\mu_p(\Delta E)\tilde{p}_o\Delta E(L) = 0$$

For n - type, $\tilde{p}_o \approx 0$

2. For the case of optical injection, the electrical bias is fixed. Therefore, the boundary condition is Vds equal to a constant. or

$$\Delta Vds = 0 = \int_0^L \Delta E(x)dx$$

The impedances seen by the electrons and holes in the channel are directly related to the perturbational electric field because the photovoltaic effect results in changes to the channel dimensions which effects the channel impedance From the current density equations, the channel impedances can be expressed as follows:

$$\Delta I_p(L) = qA\mu_p(\Delta E)p_o\Delta E(L) = 0 = \frac{\Delta E(L)}{Z_p(L)}$$

$$\Rightarrow \lim_{x \to L} Z_p(x) \to \infty$$

$$\Delta I_n(0) = qA\mu_n(\Delta E)n_o\Delta E(0) = \frac{\Delta E(0)}{Z_n(0)}$$

$$\Rightarrow Z_n(x) \propto \frac{\Delta E(x)}{\Delta I_n(x)} \propto \int g(x,x')\frac{1}{\varepsilon A\mu_n E}dx'$$

3.8.7 Solution

Using Green's Function analysis, it is possible to determine an analytic solutions to the equations. The general method is to let the integrating factors equal shifted delta functions and solve the equations. The true solution then can be calculated with the aid of delta function properties.

3.9 References - Chapter 3

[1] W.Shockley, Electrons and Holies in Semiconductiors, Van Norstrand, Princeton, N.J., 1950.

[2] R.N.Hall "Electron-hole Recombination in Ge", *Phys. Rev.*, vol.87, 1953, p.387.

[3] W.Shockley, and W.T.Read, "Statisitics of Reocombination of Holes and electrons", *Phys. Rev.*, vol. 87, 1952, p.832.

[4] D.T.Stevenson, and R.J. Keyes, "Measurement of Carrier Lifetime in Ge and Si", *J.Applied Phys*, vol26, 1955, p.190.

[5] W.Shockley, *Proc.IRE*, vol.40, pp.1365-1376, 1952.

[6] S.M.Sze, Physics of Semicondcutor Devices, John Wiley& Sons, New York, first edition 1969.

[7] A. Van der Ziel, "Gate Noise in Field Effect Transistors at Moderately High Frequencies", *Proc. of IEEE*, 1963, pp.461-467.

[8] W. Baechtold, "Noise Behavior of Schottky Barrier Gate Field-Effect Transistors at Microwave Frequencies", *IEEE Transactions on Electron Devices*, vol.ED-18, No.2, February 1971, pp. 97-104.

[9] Francois M. Klassen, "On the Influence of Hot Carrier Effects on the Thermal Noise of Field-Effect Transistors", *IEEE Transactions on Electron Devices*, vol.ED-17, no.10, October 1970, pp.858-862.

[10] A Van der Ziel, "Small-signal, High-frequency Theory of Field-Effect Transistors", *IEEE Transactions of Electron Devices*, vol. 11, 1964, pp.128-135.

[11] A.B. Grebene, and S.K. Ghandhi, "General Theory for Pinched Operation of the Junction-Gate FET", *Solid State Electronics*, Pergamon Press 1969, vol.12, pp.573-589.

[12] K. Lehovec, and R. Zuleeg, "Voltage-Current Characteristics of GaAs J-FETs in the Hot Electron Range", *Solid State Electronics*, Pergamon Press 1970, vol.13, pp.1415-1426.

[13] H. Statz, H.A. Haus, and R.A. Pucel, "Noise Characteristics of Gallium Arsenide Field-Effect Transistors", *IEEE Transactions on Electron Devices*, vol.ED-21, No.9, September 1974, pp.549-562.

[14] H.C. Ki, S.H. Son, , K. Park, and K.D. Kwack, "A Three-Section Model for computing I-V Characteristics fo GaAs MESFET's", *IEEE Transactions on Electron Devices*, vol. ed-34 no.9, September 1987, pp. 1929-1933.

[15] C. Chang, and D.S. Day, "Analytic Theory for Current-Voltage Characteristics and Field Distribution of GaAs MESFET's", *IEEE Transactions on Electron Devices*, vol. 36, no.2, Februrary1989, pp.269-280.

[16] W.R. Curtice, and M. Ettenberg, "A Nonlinear GaAs FET Model for use in the Design of Output Circuits for Power Amplifiers", *IEEE Transactions on Microwave Theory and Techniques*, vol. MTT-33, no. 12, December 1985.

[17] H. Fukui, "Determination of the Basic Device Parameters of a GaAs MESFET", *Bell System Technical Journal*, vol.58, no.3, March 1979, pp.771-797.

[18] W.Smith, Nature, vol.7, p.303, 1837.

[19] A Rose, "Performance of Photoconductors", *Proceedings of the IRE*, December 1955, pp. 1850-1869.

[20] J. C. Gammel and J. M. Ballantyne, "The OPFET: A new high-speed optical detector, " *Proc. IEDM*, pp.120-123, 1978.

[21] J.C. Gammel and J.M. Ballantyne, "Integrated photoconductive detector and waveguide structure", *Applied physuics Letters*, vol36, no.2, Janurary 15, 1980, pp.149-151.

[22] J. Graffeuil, P. Rossel, and H. Martinot, "Light-induced effects in GaAs FETs," *Electron Lett.*, vol. 15, pp. 439-441, 1979.

[23] J.P. Noad, E.H. Hara, R.H. Hum, and R.I. Macdonald, "FET Photodectors: A Combined Studing Using Optical and Electron-Beam Stimulation", *IEEE Transactions on Electron Devices*, vol. ed-29, no.11, November 1982, pp.1792-1797.

[24] A. A. DeSalles, "Optical control of GaAs MESFETs", *IEEE Trans. Microwave Theory and Tech.*,vol. MTT-31,pp.812-820, 1983.

[25] H. Mizuno, "Microwave characteristics of an optically controlled GaAs MESFET", *IEEE Trans. MTT*, vol.MTT-31, no.7, July 1983, pp.596-599.

[26] A. Madjar, P. R. Herczfeld, and A. Paolella, "Analytical model for optically generated currents in GaAs MESFETs", *IEEE Trans. Microwave Theory and Tech.*, vol.40, pp.1681-1691, 1992.

[27] K. Lehovec, and R. Zuleeg, "Voltage-Current Characteristics of GaAs J-FETs in the Hot Electron Range", *Solid State Electronics*, Pergamon Press 1970, vol13, pp.1415-1426.

[28] A.B. Grebene, and S.K Ghandhi, "General Theory for Pinched Operation of the Junction-Gate FET", *Solid State Electronics*, Pergamon Press 1969, vol.12, pp.573-589.

[29] R.A. Pucel, H.A. Haus, and H. Statz, "Signal and Noise Properties of GaAs Microwave Field-Effect Transistors", Advances in Electronic and Electron Physics, edited by L.Marton, Academic Press, vol.38, 1975, pp.195-265.

[30] A.A. DeSalles, "Optical Control of GaAs MESFETs", *IEEE Transactions on Microwave Theory and Techniques*, vol.mtt-31, no.10, October 1983, pp.812-820.

[31] R.B. Darling, "Analysis of Microwave Characteristics of Photoconductive IC Structures", *IEEE Journal of Lightwave Technology*, vol. LT-5, no. 3, March 1987, pp.325-339.

[32] R.B. Darling, "Transit-Time Photoconductivity in High-Field FET Channels", *IEEE Transactions on Electron Devices*, vol. ed-34, no.2, February 1987, pp.433-443.

[33] R.B. Darling, "Optical Gain and Large-Signal Characteristics of Illuminated GaAs MESFET's", *IEEE Journal of Quantum Electronics*, vol. QE-23, no.7, July 1987, pp.1160-1171.

[34] R.N. Simons, and K.B. Bhasin, "Analysis of Optically Controlled Microwave-Millimeter-Wave Device Structures", *IEEE Transactions on Microwave Theory and Techniques*, vol. MTT-34, no.12, December 1986, pp.1349-1355.

[35] R. N. Simons and K. B. Bhasin, "Analysis of optically controlled microwave/millimeter wave device structures", *IEEE MTT-S Digest*, pp.551-554, 1986.

[36] R. N. Simons and K. B. Bhasin, "Analysis of optically controlled microwave/millimeter wave device structures", *IEEE MTT-S Digest*, pp.551-554, 1986.

[37] A. Madjar, P.R. Herczfeld, and A. Paolella, "Analytical Model for Optically Generated Currents in GaAs MESFETs", *IEEE Transactions on Microwave Theory and Techniques*, vol.40, no.8, August 1992, pp.1681-1691.

[38] A.Madjar, A.Paolella, P.Herczfeld, "Modeling the Optical Switching of MESFET's Considering the External and Internal Photovoltaic Effects", *IEEE Transactions on Microwave Theory and Techniques*, vol.42, no.1, January 1994, pp.62-67.

[39] R.N. Simons, and K.B. Bhasin, "Analysis of Optically Controlled Microwave-Millimeter-Wave Device Structures", *IEEE Transactions on Microwave Theory and Techniques*, vol. MTT-34, no.12, December 1986, pp.1349-1355.

[40] R.N. Simons, and K.B. Bhasin, "Analysis of Optically Controlled Microwave-Millimeter-Wave Device Structures", *IEEE Transactions on Microwave Theory and Techniques*, vol. MTT-34, no.12, December 1986, pp.1349-1355.

[41] J.C. Gammel, and J.M. Ballantyne,"The OPFET: A New High Speed Optical Detector", *Proc. IEDM*, 1978, pp.120-123."

[42] Jacques I. Pankove, Optical Processes in Semiconductors, Dover Publications, Inc., New York, pp.170-174, 202, 302-336.

[43] R.H.Bube, Photoconductivity of Solids, John Wiley & Sons, Inc., 1960, pp.60-84, 126-128.

[44] R.H.Bube, Photoelectronic properties of semiconductors, Cambridge University Press, 1992, pp.1-45, pp.118-124.

[45] A.A. DeSalles, "Optical Control of GaAs MESFETs", *IEEE Transactions on Microwave Theory and Techniques*, vol.MTT-31, no.10, October 1983, pp.812-820.

[46] R.B. Darling, "Transit-Time Photoconductivity in High-Field FET Channels", *IEEE Transactions on Electron Devices*, vol. ed-34, no.2, Fegruary 1987, pp.433-443.

[47] A.Madjar, A.Paolella, P.R.Herczfeld, "Modeling the Optical Switching of MESFETs Considering the External and Internal Photovoltaic Effcts", *IEEE Transactions on Microwave Theory and Techniques*, vol. 42, no.1, January 1994, pp.62-67.

[48] A.Madjar, A.Paolella, P.R.Herczfeld, "Modeling the Optical Switching of MESFETs Considering the External and Internal Photovoltaic Effcts", *IEEE Transactions on Microwave Theory and Techniques*, vol. 42, no.1, January 1994, pp.62-67.

[49] C.R. Crowell and S.M.Sze, "Current Transport in Metal-Semiconductor Barriers," *Solid State Electron.*, vol.26, pp.705-709, Nov./Dec. 1966.

[50] S.M.Sze, Physics of Semiconductor Devices, John Wiley & Sons, NY, 1981, pp.820-825.

[51] R.H.Bube, R.H.Bube, Photoelectronic properties of semiconductors, Cambridge University Press, 1992, pp.1-45, pp.244-261.

[52] H.J.Hovel, "Solar Cells", Semiconductor and Semimetals, Academinc Press, 1975.

[53] A. Madjar, P.R. Herczfeld, and A. Paolella, "Analytical Model for Optically Generated Currents in GaAs MESFETs", *IEEE Transactions on Microwave Theory and Techniques*, vol.40, no.8, August 1992, pp.1681-1691.

[54] S.M.Sze, Physics of Semiconductor Devices, John Wiley & Sons, NY, 1981, p.620.

CHAPTER 4

THEORY OF OSCILLATION AND LOCKING

4.1 Introduction

In this Chapter, the theory of oscillation phenomenon is discussed. The goal is to represent the laser and microwave oscillator in the same way. In microwave oscillators, it is well known that the current of the active element is the sum of the incoming and outgoing wave amplitudes. Through a quantum mechanical Langevin treatment, the laser oscillations will be treated in this manner and will use the well established microwave oscillator theory by Kurokawa[1].

The reservoir theory of a semiconductor laser is used to establish a link from the laser rate equations to a description of the system in terms of an electrical terminology. A laser is a non-equilibrium open system. In this system, the ordering force is gain saturation and the fluctuating forces are from external reservoirs. The macroscopic coherence of light and matter is established by the balance between the gain saturation and the external reservoirs.

In Chapter 2, the laser rate equations were used analyze injection locking phenomenon of direct current modulated lasers. In Chapter 7, an equivalent circuit is used to represent a microwave oscillator which is locked to an external signal. It is the purpose of this Chapter to demonstrate the overlap between both oscillatory

devices. The motivation for the treatment is the existence in this Thesis of both laser and microwave oscillators. Once the analogy between the electrical and laser oscillator theories is completed, representation of injection phenomenon is developed.

The analysis begins with the development the laser rate equations in terms of the field amplitude. In Chapter 2, the laser rate equations were established in form of the photon number (intensity). Next, quantum mechanical Langevin treatment field fluctuations of a laser are established via reservoir theory[2,3]. The inherent difficulties of the quantum mechanical approach are overcome by modeling the laser in terms of electrical circuit connected to an infinite transmission line as first described by Lax[4]. The laser is viewed with an output coupling mirror followed by free space. These theoretical developments are linked to the theory of electric oscillations. Once the theory for the free running oscillator is developed, the injection locked case is analyzed.

Microwave circuit models of semiconductor lasers exist which treat the laser as a two port equivalent circuit and includes package parasitics[5]. However, in the development presented here, the link to gain saturation and the carrier equation is clear. Also, this work allows a one to one correspondence between the electrical oscillator and the coupled laser rate equations.

The laser and electrical oscillator theory is compared. The semiclassical rate equations are shown to support both the laser and the microwave oscillator. Given the comparison is accurate, it is then possible to model either injection locked oscillatory system.

4.2 Laser Rate Equations

The wave equation is solved for the n^{th} eigenmode solution of an undriven field inside a laser cavity. The solution to the wave equation for the electric field inside a laser cavity is given as follows where the field is assumed to be quasi-sinusoidal with slowly varying amplitude and phase referenced to a carrier frequency ω.

$$\tilde{E}(t) = \frac{1}{2}\left(E(t)\, e^{j\omega t} + c.c.\right)$$

The slowly varying envelope (SVE) approximation supposes that the time variations of the phasor amplitudes is slow compared to the optical carrier ω and that the cavity decay rate g and the linewidth $\Delta\omega_a$ are also so small. The resultant magnitudes permit all second order and higher terms to be dropped. After substituting back into the wave equation, retaining only $e^{j\omega t}$ terms and invoking the SVE, the field amplitude E(t) for a semiconductor laser is written as follows:

$$\frac{dE(t)}{dt} = [\, j\omega + \frac{1}{2}(\hat{G} - \gamma)\,]\, E(t) \qquad (4\text{-}1)$$

The loss γ is related to the photon life time τ_p ($\gamma = \frac{1}{\tau_p}$). The complex gain $\hat{G}$ is expanded:

$$\hat{G} = G_o + G_N \Delta N(1 + j\alpha) + G_S \Delta S$$

Above threshold, the dc gain equals the loss ($G_o = \frac{1}{\tau_p}$).

Next, assuming sinusoidal steady state, the electric field amplitude may be written as

$$E(t) = E_o(t)\, e^{j\omega t} \tag{4-2}$$

Furthermore, noting that the photon number S is related to the square of the field amplitude and eliminating higher order terms of the fluctuations, we can write

$$S_o + \Delta S = (E_o + \Delta E)^2 \approx E_o^2 + 2E_o \Delta E$$
$$So = E_o^2$$
$$\Delta S \approx 2E_o \Delta E$$

Substituting the derivative of (4-2) into (4-1) and separating the magnitude and phase parts, the field $E_o(t)$ and the phase $\phi(t)$ equations are obtained

$$\frac{dE_o(t)}{dt} = [\frac{1}{2}(G_N \Delta N + 2\, E_o \Delta E G_S)\ ]\ E_o(t)$$

$$\frac{d\phi(t)}{dt} = \frac{\alpha}{2} G_N \Delta N$$

The carrier equation is

$$\frac{dN}{dt} = J - \frac{N}{\tau_s} - E_o^2(G_o + G_N \Delta N + G_s 2E_o \Delta E) \tag{4-3}$$

where the gain term for the carrier does not include the linewidth enhancement factor and is written as

$$G = G_o + G_N \Delta N + G_S \Delta S$$

Next the fluctuation about steady state are evaluated by defining the steady state components and their time dependent fluctuations:

$$E = E_o + \Delta E$$
$$N = N_o + \Delta N$$
$$J = J_o + \Delta J$$

All higher order terms of the perturbations are dropped, thus

$$\frac{d\Delta E(t)}{dt} = \frac{1}{2}(G_N\,\Delta N\,E_o + 2\,E_o^2\,\Delta E G_S)$$

$$\frac{d\phi(t)}{dt} = \frac{\alpha}{2} G_N\,\Delta N$$

$$\frac{d\Delta N}{dt} = \Delta J - \frac{\Delta N}{\tau_s} - E_o^2 G_N \Delta N - (G_o + G_s E_o^2) 2E_o \Delta E \qquad (4\text{-}4)$$

4.3 Langevin Equations for the Internal Field

The Langevin equation for the field b(t) will be derived by treating the empty laser cavity from a reservoir theory standpoint which analyzes the round-trip gain and loss of a field within the cavity (Figure 2). The photon field leaks into an external reservoir via the output coupling mirror. The reservoir theory considers the photon field inside the cavity, the population inversion and dipole moment as the system[6]. The reservoir is constructed with the external fields (vacuum fields), carriers, and pump source as the fluctuating forces (Figure 1). The system dissipates to the reservoir while the fluctuations of the reservoir quantities perturb the system.

In the case of microwave oscillators, Kurokawa couples the external field to the internal field in the cavity. This must be done in this laser analysis in order to develop the same model for the electrical and laser oscillators. Because conventional laser reservoir theory ignores the external field coupling, the theoretical development of the quantum mechanically self consistent theory, used here, is a modification of the conventional approach. The analysis starts with the results of the quantum mechanical treatment of the internal and external laser field fluctuations[7].

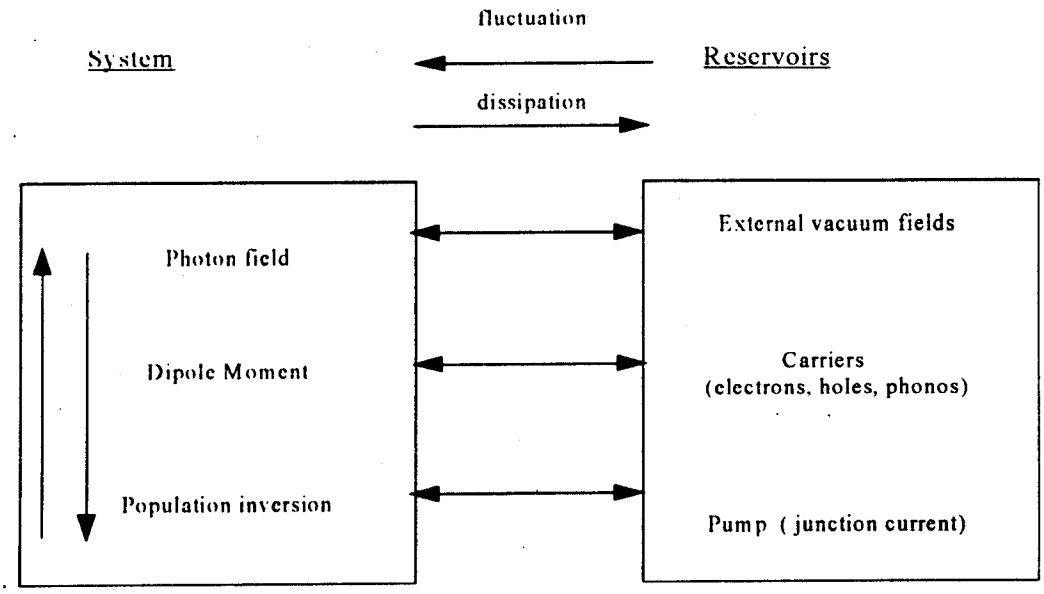

Figure 1 Laser System Viewed from Reservoir Theory

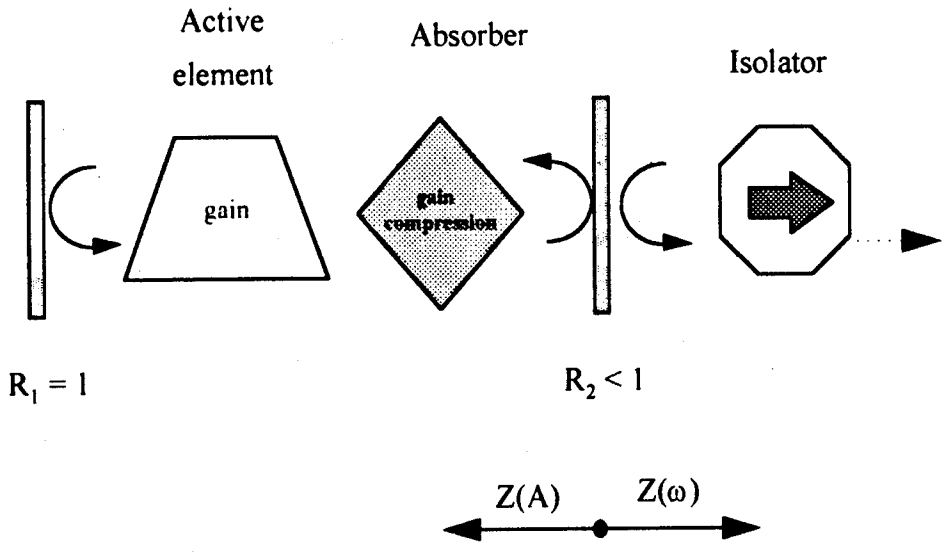

Figure 2 Laser model

In Figure 2, the cavity is shown as well the "impedance" terms that will ultimately be related to the laser system in the next Section. The external and internal loss are included as reflections from the mirrored endfaces. The active gain is included.

$$\frac{d\hat{b}(t)}{dt} = -\frac{1}{2}\left[R_1 + R_2 + \Gamma_c - g\frac{c}{2n_o}\right]\hat{b}(t) + \hat{F}_b(t)$$

$$= -\frac{1}{2}\left[\frac{\omega}{Q_{int}} + \frac{\omega}{Q_{ext}} - \left(\Gamma_c + g\frac{c}{2n_o}\right)\right]\hat{b}(t) + \hat{F}_b(t)$$

Γ_c is the term associated with the absorber which represents gain compression. This gain saturation term is a negative quantity; it is a reduction in the existing level of gain. The gain compression is a function of the field intensity S(i.e., the square of the field). This term is not inlcuded in the quoted work of Yamamoto. g is the complex gain per unit length inside the cavity.

$$g\frac{c}{n_o} = \frac{\omega}{\mu^2}(\chi_i + j\chi_r)$$

Gain saturation has been shown to occur, and therefore, the compression term is included in the complex gain equation rather than with the cavity loss. The complex Langevin gain $\hat{G}_L$ is identified as follows:

$$\hat{G}_L = \frac{\omega}{\mu^2}(\chi_i + j\chi_r) + \Gamma_c$$

$\hat{F}_b(t)$ is the noise operator plus the contribution due to radiation under thermal equilibrium. R_1 and R_2 are the mirror reflectivities which represent loss each time the field contacts it. As shown, the reflectivities can be written in terms of the cavity Q. Q_{ext} is due to the coupling to the external field at the output mirror R2. Q_{int} is the internal loss due to the rear mirror R1. The following approximation is used:

$$R = e^{-\frac{\omega}{Q}\tau} \approx 1 - \frac{\omega}{Q}\tau$$

The total loss $\gamma_{\perp}$ in the cavity is photon decay rate.

$$\gamma_{\perp} = \frac{\omega}{Q_{int}} + \frac{\omega}{Q_{ext}} = \frac{1}{\tau_p}$$

Assuming quasi-sinusoidal field and substituting the latter definitions, the semi-classical field equation becomes:

$$\frac{db(t)}{dt} = \left[j\omega + \frac{1}{2}\cdot\left(\hat{G}_{\perp} - \gamma_{\perp}\right)\right] b(t) + F_a(t) \qquad (4\text{-}5)$$

The total number of excited carriers is described from the equation of motion for the carrier number N(t). The electron system is given by :

$$\frac{dN(t)}{dt} = P - \langle R_{st} \rangle - \frac{N(t)}{\tau_{sp}} - \frac{\omega}{\mu^2}\chi_i S(t) + F_c(t)$$

where N(t) is the carrier rate, P is the pump rate, R_{st} is the stimulated emission rate, τ_{sp} is the lifetime, photon number is S(t), $\frac{\omega}{\mu^2}\chi_i$ is the gain, and $F_c(t)$ is the Langevin noise term. The carrier pump and stimulated emission rate are related to the current density J. Assume the noise term is not present and re-writing the carrier equation in terms of the later definitions:

$$\frac{dN(t)}{dt} = J - \frac{N(t)}{\tau_{sp}} - GS(t) \qquad (4\text{-}6)$$

From the laser rate equation development in the previous section, the field equations, (4-1)and (4-5), and the carrier equations, (4-3) and (4-6), are the same.

When the complex gain factor is expanded, the linewidth enhancement factor α_L is identified. First, expansion about the steady state gain:

$$\chi_i = \langle \chi_{io} \rangle + \Delta N(t) \frac{d\langle \chi_{io} \rangle}{dN_o}$$

$$\chi_r = \langle \chi_{ro} \rangle + \Delta N(t) \frac{d\langle \chi_{ro} \rangle}{dN_o}$$

The mean value, denoted by $< >$, and the time dependence of the fluctuations are implied from this point further. Next, expanding the gain term:

$$\hat{G}_L = \frac{\omega}{\mu^2}\left[\chi_{io} + j\,\chi_{ro} + \Delta N \frac{d\chi_{io}}{dN_o}\left(1 + j \frac{d\chi_{ro}}{dN_o} \Big/ \frac{d\chi_{io}}{dN_o} \right) \right] + \Gamma_c \Delta S$$

The deviation of the real part of the susceptibility divided by the imaginary part is as α_L and represents the linewidth enhancement of semiconductor lasers.

$$\hat{G}_L = \frac{\omega}{\mu^2}\left[\chi_{io} + j\,\chi_{ro} + \Delta N \frac{d\chi_{io}}{dN_o}(1 + j\alpha_L) \right] + \Gamma_c \Delta S$$

The steady state gain equals the loss, and therefore, we can write

$$G_o - \gamma = 0 = \frac{1}{2}(\chi_{io} + j\,\chi_{ro}) - \frac{1}{\tau_p}$$

The Langevin internal field equation b(t) is used to derive the quasi-linearized operator Langevin equations for time derivatives of the perturbed quantities of field $\Delta b(t)$, phase $\Delta\phi(t)$, and carrier $\Delta N(t)$.

$$b(t) = [\, B_o + \Delta B(t) \,]\, e^{j\Delta\phi}$$

$$N(t) = N_o + \Delta N(t)$$

Noting the expansion for the intensity S yeilds:

$$S = B_o^2$$

$$\Delta S \approx 2B_o \Delta B$$

Next, expand around B, use the fact that the steady state derivatives equal zero, and separate into magnitude and phase. The internal field , phase and carrier equations in terms of the semi-classical parameters are:

$$\frac{d\Delta B}{dt} = \frac{\Delta N}{2}\frac{\omega}{\mu^2}\frac{d\chi_i}{dN_o}B_o + 2B_o\Delta B\Gamma_c + \hat{H}_r(t)$$

$$\frac{d\Delta\phi}{dt} = \frac{\alpha}{2}\Delta N\frac{\omega}{\mu^2}\frac{d\chi_i}{dN_o} + \hat{H}_i(t)$$

$$\frac{d\Delta N}{dt} = \Delta J - N\left(\frac{1}{\tau_{sp}} + \frac{\omega}{\mu^2}\frac{d\chi_i}{dN_o}B_o^2\right) - \frac{\omega}{\mu^2}\chi_i 2B_o\Delta B + F_c(t)$$

The Hermetian noise operators are included ($\hat{H}_r, \hat{H}_i$ and $F_c(t)$) for completeness but are not used in this Chapter. With these identifications, the quantum mechanical approach is reconciled to the laser field equations of the previous section..

$$\frac{d\Delta B}{dt} = \frac{\Delta N}{2}G_N B_o + 2B_o\Delta B\Gamma_c + \hat{H}_r(t)$$

$$\frac{d\Delta\phi}{dt} = \frac{\alpha}{2}\Delta N G_N + \hat{H}_i(t)$$

$$\frac{d\Delta N}{dt} = \Delta J - \Delta N\left(\frac{1}{\tau_{sp}} + G_N B_o^2\right) - 2B_o\Delta B G_{oi} + F_c(t)$$

4.4 Electric Oscillator Theory

The electric oscillator is described by an active element with the external circuit connected through a circulator Figure 3. In this section, the electric oscillation equations are developed by modeling the laser as an active element (gain) between two reflective walls (Figure 2). The end result is that the terms in the microwave oscillator are related to the laser rate equation parameters through the Langevin field and carrier equations. The case of injection locking is then discussed. The carrier equations are shown to couple to the field equation through the complex impedance term Z(A) which contains a complex gain factor.

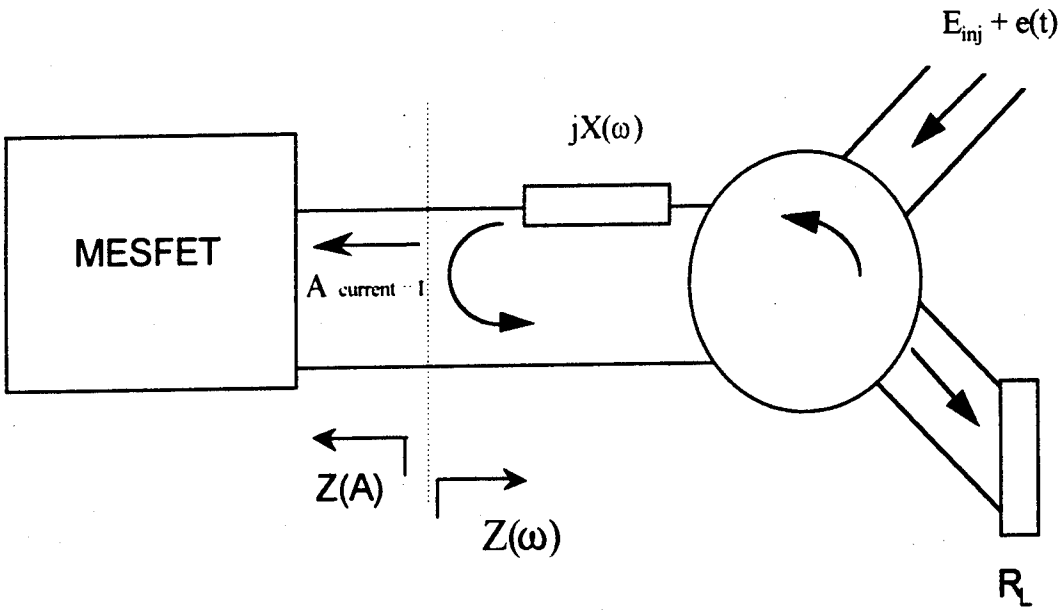

Figure 3 Equivalent microwave oscillator circuit

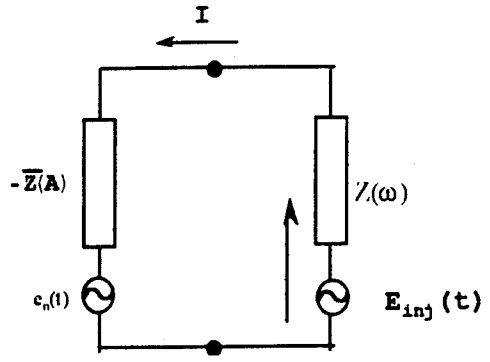

Figure 4 Circuit Model

For an undriven oscillator, the injection term $E_{inj}(t)$ is zero in Figure 4. For now, also assume the noise $e_n(t)$ is not present. Kurokawa writes the necessary condition for oscillation as.

$$A\left[Z(\omega) - Z(A)\right] = 0 \qquad (4\text{-}7)$$

where Z(A) is a function of the current amplitude A, and Z(ω) is a function of frequency. The real part is the internal loss minus the negative resistance which is the gain

$$Z(A) = R(A) - jX(A)$$
$$R(A) = \gamma_{int} - G = R_a - R_i(A)$$

$$G = R_i(A)$$
$$\gamma_{int} = R_a$$

In Chapter 3, the optical gain of the MESFET was shown to be $\text{Gain} = 1 + \frac{\mu_n}{\mu_p}$. The mobilities are related to the susceptibility of the laser equations in Section 4.3.

The real part of $Z(\omega)$ is the external loss or load resistance

$$Z(\omega) = R_L + jX(\omega)$$
$$\gamma_{ext} = R_L$$

Separating real and imaginary parts of $Z(\omega)$-$Z(A)$, and using (4-7):

$$R_L - R(A_o) = 0 \qquad (4\text{-}8)$$

$$X(\omega_1) + X(A_o) = 0 \qquad (4\text{-}9)$$

For an electrical oscillator circuit the reactance is modeled as an inductance and capacitance in series. Therefore, $X(\omega)$ becomes:

$$X(\omega) = \omega L - \frac{1}{\omega C} \approx 2L(\omega - \omega_{LC})$$
$$\omega_{LC} = \frac{1}{\sqrt{LC}}$$

Expanding the complex impedance via Taylor's expansion:

$$\begin{aligned} Z(A) &= Z(A_o) + \Delta A \frac{\partial Z(A)}{\partial A} \\ &= R(A_o) + \Delta A \frac{\partial R(A)}{\partial A} - j\left(X(A_o) + \Delta A \frac{\partial X(A)}{\partial A}\right) \\ &= R(A_o) + - jX(A_o) + \Delta A \frac{\partial R(A)}{\partial A}\left(1 - j\frac{\frac{\partial X(A)}{\partial A}}{\frac{\partial R(A)}{\partial A}}\right) \\ &= \left(R_a - R_1(A)\right) - j\,X(A_o) + \Delta A \frac{\partial\left(R_a - R_1(A)\right)}{\partial A}(1 + j\alpha) \\ &= - (G - \gamma_{int}) - j\,X(A_o) - \Delta A \frac{\partial R_1(A)}{\partial A}(1 + j\alpha) \end{aligned}$$

where α is given the ratio of deviation of $X(A)$ to $R(A)$:

$$\alpha = -\frac{\frac{A}{R(A)}\frac{\partial X(A)}{\partial A}}{\frac{A}{R(A)}\frac{\partial R(A)}{\partial A}} \tag{4-10}$$

At microwave frequencies, the effect of the linewidth enhancement α is generally too small to consider. However, to draw the analogy between the laser and microwave oscillator theory, it is necessary to include α. Using the sinusoidal steady state representation and including the deviation ΔA,

$$A = \mathrm{Re}\left\{(A_o + \Delta A)e^{j(\omega_1 t + \phi + \Delta\phi)}\right\}$$

Combining with the original circuit equation

$$[\,Z(\omega) - Z(A)](A + \Delta A)e^{j(\omega_1 t + \phi + \Delta\phi)} = 0$$

After substitution, and equating the sum of the real parts of the impedances to zero for oscillation to occur via (4-8)

$$R_L - R(A_o) = (R_L + R_a) - R_1(A_o) = 0$$

Rewriting in terms of gains and losses:

$$(\gamma_{int} + \gamma_{ext}) - G = 0$$

Furthermore, the imaginary part must be related through (4-9),

$$X(\omega_1) = -X(A_o)$$

In the laser equations, the external and internal loss are related through the lifetime

$$\gamma_{ext} + \gamma_{int} = (R_L + R_a) = \left(\alpha_1 - \frac{1}{\ell}\ln(\Gamma)\right)^{-1} \equiv \frac{1}{\tau_p}$$

where ℓ is the cavity length and Γ is the reflectivity. Substituting,

$$X(\omega) + X(A_o) = X(\omega) - X(\omega_1) \approx 2L(\omega - \omega_{LC} - \omega_1 - \omega_{LC}) = 2L(\omega - \omega_1)$$

Recombining,

$$[Z(\omega) - Z(A)] = j2L\,(\omega - \omega_1) + \Delta A \frac{\partial R_1(A)}{\partial A}(1 + j\alpha) \qquad (4\text{-}11)$$

Finally, the current amplitude times the impedance difference must be zero for oscillation:

$$[Z(\omega) - Z(A)]A = \left[j\,2\,L\,(\omega - \omega_1) + \Delta A \frac{\partial R_1(A)}{\partial A}(1 + j\alpha) \right] A = 0 \qquad (4\text{-}12)$$

4.4.1 The Driven Oscillator - Injection Phenomenon

The driven oscillator is represented by adding driving terms to the right hand side of (4-12). An injected signal $E_{inj}(t)$ and/or a noise source $e_n(t)$ are included:

$$[Z(\omega) - Z(A)]A = \left[j\,2L\,(\omega - \omega_1) + \Delta A \frac{\partial R_1(A)}{\partial A}(1 + j\alpha) \right] A = \eta E_{inj}(t) + e_n(t)$$

The injected signal may be an electrical or optical signal. Since some percent of the field may be reflected due to impedance mismatches in the electrical case or due to surface reflections in the optical case, the injected field coupling factor is represented by η. For the straightforward case of an electrical injection, $E_{inj}(t)$ represents the electrical field. For optical signal injection, $E_{inj}(t)$ is most simply the Schottky photovoltage developed from the generation of minority carriers. In Chapter 3, the photo-induced carrier generation is described as well as other secondary light induced effects.

4.4.2 Coupling to the Carrier Equation

In this section, the carrier equation is shown to couple to the field equation. Rewriting the carrier equation here for convenience:

$$\frac{dN(t)}{dt} = J - \frac{N(t)}{\tau_{sp}} - GS(t)$$

Assume a two level system, and describing the gain G as $\kappa\Delta N=(N_2-N_1)\kappa$ where κ is a constant. Rewriting in terms of ΔN.

$$S\kappa(N_2 - N_1) = J - \frac{N_2}{\tau_{sp}} - \frac{dN_2}{dt}$$

Using the stationary form of the latter carrier equation with J constant

$$(N_2 - N_1) = \frac{-1}{1 + S\kappa\tau_{sp}} N_1$$

and therefore,

$$\frac{\partial(N_2 - N_1)}{\partial S} = \frac{S\kappa\tau_{sp}}{\left(1 + S\kappa\tau_{sp}\right)^2} N_1$$

Define a intermediate saturation parameter s_i as

$$s_i = \frac{-A}{R_i}\frac{\partial R_1}{\partial A}$$

The amplitude A is equal to the field amplitude E for the laser development. Note that the photon number S is E^2 and the gain term G must be proportional to $R_i(A)$ as discussed earlier. Therefore,

$$R_1(A) = G_0 = (N_2 - N_1)\kappa$$

and the fluctuation of the photon number:

$$\frac{\partial S}{\partial E} = \frac{\partial E^2}{\partial E} = 2\frac{\partial E}{\partial E}$$

This yields the photon number fluctuation in terms of the amplitude ($\partial S = 2\partial E$).

Re-substituting in s_i,

$$s_i = \frac{-A}{R_i}\frac{\partial R_i}{\partial A} = \frac{-2\sqrt{S}}{(N_2 - N_1)} \cdot \frac{\partial (N_2 - N_1)}{\partial S}$$

Therefore,

$$s_i = \frac{2}{1 + \frac{1}{S\kappa\tau_{sp}}}$$

The overall saturation parameter is defined as follows:

$$s = \frac{-A}{R(A)}\frac{\partial R(A)}{\partial A} = \frac{-A}{R(A)}\frac{\partial (R_i - R_a)}{\partial A} = \frac{-A}{R_i - R_a}\frac{\partial R_i}{\partial A}$$

The load resistance R_L must equal R_i minus R_a because the real parts of the impedances must be equal and opposite in order to establish oscillation (4-8).

Regrouping the denominator and using latter definition of R_L:

$$\frac{1}{R_i - R_a} = \frac{1}{R_i}\left(1 + \frac{R_a}{R_i - R_a}\right) = \frac{1}{R_i}\left(1 + \frac{R_a}{R_L}\right)$$

The internal loss R_a is a constant function of amplitude A; however, R_i is not constant. The overall saturation parameter is now equal to

$$s = \frac{-A}{R_i}\frac{\partial R_i}{\partial A}\left(\frac{R_L + R_a}{R_L}\right) = s_i\left(\frac{R_L + R_a}{R_L}\right)$$

Equation 4-10 defined the linewidth enhancement factor α which is now re-written in terms of s. This will allow us to explicitly couple to the carrier equation. Let α now equals:

$$\alpha = \frac{\begin{matrix} A & \partial X(A) \\ R(A) & \partial A \end{matrix}}{\begin{matrix} -A & \partial R(A) \\ R(A) & \partial A \end{matrix}} = \frac{\begin{matrix} A & \partial X(A) \\ R(A) & \partial A \end{matrix}}{s_1 \begin{pmatrix} R_L + R_a \\ R_L \end{pmatrix}} \tag{4-13}$$

With another change of variables,

$$\alpha = \frac{r}{s_1 \begin{pmatrix} R_L + R_a \\ R_L \end{pmatrix}}$$

where r is the numerator of (4-13). The gain's dependence on the complex susceptibility is very important at laser oscillation frequencies. However, it is generally small term in the microwave oscillator cases, and is therefore, excluded. This allows us to couple the carrier equation to the field equation, and also, to use the microwave oscillator model of Kurokawa to describe laser action. Repeating the original carrier equation,

$$\frac{d\Delta N}{dt} = \Delta J - \frac{\Delta N}{\tau_s} - E_o^2 G_N \Delta N - (G_o + G_s E_o^2) 2E_o \Delta E$$

Therefore,

$$\kappa(N_2 - N_1)S \propto -E_o^2 G_N \Delta N - (G_o + G_s E_o^2) 2E_o \Delta E$$

4.5 Comparison of Laser and Electrical Oscillator Theory

The development for microwave oscillators is analogous to the theory for laser oscillation. In this section, the results of the semi-classical laser rate equations are equated to the microwave oscillator complex impedance representations.

Furthermore, the necessary condition for laser oscillation is shown to support the same requirement as for microwave oscillators.

The development begins with the definition of a complex function of frequency $Z(\omega)$ in Langevin rate equation terminology. Let the complex impedance which is a function of frequency be equal to a loss plus a complex saturation term as follows:

$$Z(\omega) = \frac{\omega}{Q_{ext}} + j\,(\omega - \omega_o)$$

The next step is to define a term that is a function of the amplitude E and is the source of the negative resistance which is necessary to start oscillation:

$$Z(E) = \left(\frac{\omega}{\mu^2} \chi_i(E) + \Gamma_c - \frac{\omega}{Q_{int}} \right) - j \frac{\omega}{\mu^2} \chi_r(E)$$

where Γ_c is a function of the field squared. The internal and external loss are equal to the photon decay rate:

$$\frac{\omega}{Q_{int}} + \frac{\omega}{Q_{ext}} = \frac{1}{\tau_p}$$

The complex equation for the field amplitude is

$$[Z(\omega) - Z(E)]E = \left[j\,(\omega_o - \omega) + \frac{1}{\tau_p} - \frac{\omega}{\mu^2} \left(\chi_i(E) - j\chi_r(E) \right) - \Gamma_c \right] E = 0$$

Converting the $j\omega_o$ to the time derivative of the electric field:

$$\frac{dE}{dt} = \left\{ j\,\omega + \left[\frac{\omega}{\mu^2} \left(\chi_i(E) - j\chi_r(E) \right) + \Gamma_c - \frac{1}{\tau_p} \right] \right\} E$$

Substituting for the terms in the square brackets from the semi-classical equations,

$$\frac{dE(t)}{dt} = [\, j\omega + \frac{1}{2}(\hat{G} - \gamma) \,] E(t)$$

Therefore, the original laser field equation (4-1) has been derived from oscillator theory. Noise e(t) and injected field Einj(t) terms may be included as follows:

$$[Z(\omega) - Z(E)]E = \left[j(\omega_o - \omega) + \frac{1}{\tau_p} - \frac{\omega}{\mu^2}\left(\chi_i(E) - j\chi_r(E)\right) - \Gamma_c \right] E = e(t) + E_{inj}(t)$$

Now the laser terminology is completely related to a microwave oscillator. Table 1 Relationship between Electrical and Laser Oscillation Terms gives a comparison between microwave and optical oscillation terminology. Also, Table 2 is a more detailed summary of terms developed in this Chatper.

Table 1 Relationship between Electrical and Laser Oscillation Terms

	Electrical Oscillator		**Laser**		**Relationship**
Oscillator field Strength	Current Amplitude	A	Photon Amplitude	$S=E^2$	$S_o = A\sqrt{\frac{L}{2\hbar\omega}}$
Active Element	Complex Impedance	Z(A)	Complex Gain factor	$G(N,S)=Go-\gamma_{int}$	$G(N,S) = \frac{Z(A)}{L}$
Load	Complex Impedance	$Z(\omega)$	Complex photon decay rate	$G(\omega)= \gamma_{ext} + j(\omega-\omega_o)$	$G(\omega) = \frac{Z(\omega)}{L}$
Stored Energy		$1/2LA^2$		$\hbar\omega S^2$	
Power Flow to a load		$1/2R_LA^2$		$\hbar\omega S^2\gamma_{ext}$	

Table 2 - Summary

		Semi-classical	Electrical Oscillator
Complex Gain $\hat{G}$	$G_o + G_N\Delta N(1+j\alpha) + G_S\Delta S$	$\chi_i + j\chi_r + \frac{\partial \chi_i}{\partial N}\Delta N(1+j\alpha) + \Gamma_c\Delta S$	$R_i(Ao) + \frac{\partial R_i(A)}{\partial A}\Delta A(1+j\alpha)$
Steady State Gain G_o	G_o	$g\frac{c}{n_o} = \frac{\omega}{\mu^2}\chi_o = \chi_{io} + j\chi_{ro}$	$-R_i(A_o)$
G_N	$\frac{\partial G(N,S)}{\partial N}$	$\frac{\omega}{\mu^2}\frac{d\chi_i}{dN}$	$\frac{\partial R_i(A)}{\partial A}$
Gain Compression G_S	$\frac{\partial G(N,S)}{\partial S} \approx \frac{-\kappa}{\tau_p}$	Γ_c	$\frac{\partial Z(A)}{\partial A}$
Linewidth Enhancement Factor α	$\frac{\partial n_r}{\partial n_i}$	$\frac{\partial \chi_{ro}/\partial N}{\partial \chi_{io}/\partial N}$	$\frac{\frac{A}{R(A)}\frac{\partial X(A)}{\partial A}}{s_i\left(\frac{R_L+R_o}{R_L}\right)}$
Loss γ	$\frac{1}{\tau_p} = \gamma_{int} + \gamma_{ext}$	$\frac{\omega}{Q_{int}} + \frac{\omega}{Q_{ext}}$	$R_o + R_L$
Complex function of frequency $Z(\omega)$	$\gamma_{ext} + j(\omega - \omega_o)$	$\frac{\omega}{Q_{ext}} + j(\omega - \omega_o)$	$\frac{\omega}{Q_{ext}} + j\,2L(\omega - \omega_o)$
Complex function of field Z(A)	$\hat{G}(N,S) - \gamma_{int}$	$\left[\frac{\omega}{\mu^2}\chi_i(E) - \frac{\omega}{Q_{int}}\right] - j\frac{\omega}{\mu^2}\chi_r(E)$	$[R_o - R_i(A)] - jX(A)$
Field	$\frac{dE(t)}{dt} = [\,j\omega + \frac{1}{2}(\hat{G} - \gamma)\,]E(t)$	$\frac{dx(t)}{dt} = \left[j\omega - \frac{1}{2}\left[\frac{\omega}{Q_{int}} + \frac{\omega}{Q_{ext}} - g\frac{c}{2n_o}\right]\right]x(t)$	$A[Z(\omega) - Z(A)] = 0$

4.6 Conclusion

The theory of oscillation phenomenon was discussed. The goal to represent the laser and microwave oscillator in the same way was achieved by modeling the laser in terms of Kurokawa's microwave oscillator theory through a quantum mechanical development by Yamamoto and Imoto. The overlap between both the laser and the microwave oscillator devices was given. Once the analogy between the electrical and laser oscillator theories was completed, representation of injection phenomenon was developed. The versatility of these theories allow us to model various injection phenomenon with the same basic equations. These include

- electrical oscillator with electrical injection
- electrical oscillator with optical injection
- injection locked laser

By bridging the gap between the classical theory and the circuit theory, an analysis method has been established that is applicable to both lasers and electrical oscillators under injection locking conditions.

4.7 References - Chapter 4

[1] K. Kurokawa, "Injection Locking of Microwave Solid-State Oscillators", *Proceedings of the IEEE*, vol. 61, no. 10, October 1973, pp.1386-1410.

[2] O. Nilsson, Y. Yamamoto, and S. Machida, "Internal and External Field Fluctuations of a Laser Oscillator: Part II- Electrical Circuit Theory", *IEEE Journal of Quantum Electronics*, vol. QE-22, no.10, October 1986, pp.2043-2051.

[3] Y. Yamamoto, and I. Nobuyuki, "Internal and External Field Fluctuations of a Laser Oscillator: Part I- Quantum Mechanical Langevin Treatment", *IEEE Journal of Quantum Electronics*, vol. QE-22, no.10, October 1986, pp.2032-2042.

[4] M.Lax, "Classical noise Noise in self sustained oscillators,", *Physic Reveiw*, vol.160, pp.290-307, 1967.

[5] R.S. Tucker and D.J. Pope, "Microwave Circuit Models of Semiconductor Lasers", *IEEE Transactions on Microwave Theory and Techniques*, vol.MTT-31, no.3, March 1983, pp.289-294.

[6] Y. Yamamoto, and I. Nobuyuki, "Internal and External Field Fluctuations of a Laser Oscillator: Part I- Quantum Mechanical Langevin Treatment", *IEEE Journal of Quantum Electronics*, vol. QE-22, no.10, October 1986, pp.2032-2042.

[7] Y. Yamamoto, and I. Nobuyuki, "Internal and External Field Fluctuations of a Laser Oscillator: Part I- Quantum Mechanical Langevin Treatment", *IEEE Journal of Quantum Electronics*, vol. QE-22, no.10, October 1986, pp.2032-2042.

CHAPTER 5

FABRICATION AND EXPERIMENT

5.1 Introduction

This chapter describes the experimental systems and the fabrication of the microwave circuits used in this thesis. Certain techniques and equipment, described in this chapter, were of the utmost importance for successfully executing the experiments. Issues, such as radio frequency isolation and polarization, required engineering to overcome. This chapter concentrates, therefore, on engineering solutions that were necessary to explore the science of this Thesis.

An overview of the entire system is given in Section 5.2 The laser locking system is discussed in 5.3 Experimental Laser Injection System. Since laser wavelength and mode structure can vary considerably from one laser to the next, these characteristics of the lasers has been an important aspect of the experiments. The MESFET injection arrangement was designed to balance the need for focused optical power and the need for the experimenter to vary circuits, power and to view the device. Section 5.4 Experimental Free Space Optical System for MESFET Injection addresses these issues and provides analyses that were conducted to design the setup. The design and fabrication of the MESFET microwave circuits (Section 5.7) were completed mostly in the University of Colorado's Transmission

Laboratory and some cases at Ball Aerospace in Broomfield, Colorado. When modulating semiconductor laser diodes at gigahertz frequencies and working with microwave circuits, attention to radio frequency (RF) issues are an important part of each experiment(5.6 RF Considerations). In particular, it is vital to design and build a cable that will minimize the reflections when the laser is biased above threshold. Also, undesirable antenna effects had to be eliminated in the laboratory so that the experiments could be conducted in a controlled scientific manner. 5.5 Experiments Conducted details the experiment matrix that was used. Conclusions are drawn in the final section.

5.2 Experimental System Overview

There are two distinct parts of the experiment: the locked laser design and the MESFET injection setup which is shown in Figure 1 Complete Experimental System. This section gives a brief overview of the entire system. The next sections will provide more detail.

The locked laser system was first used to study the noise properties of injection lasers[1]. Modifications were made to improve the power coupling, beam collimation, and optical isolation, to control the polarization, and to minimize cable reflections when modulating the lasers. The MESFET injection system evolved from a simple setup that brought the beam in contact with the MESFET via a microscope objective and allowed viewing of the MESFET on a CCD to a more refined beam

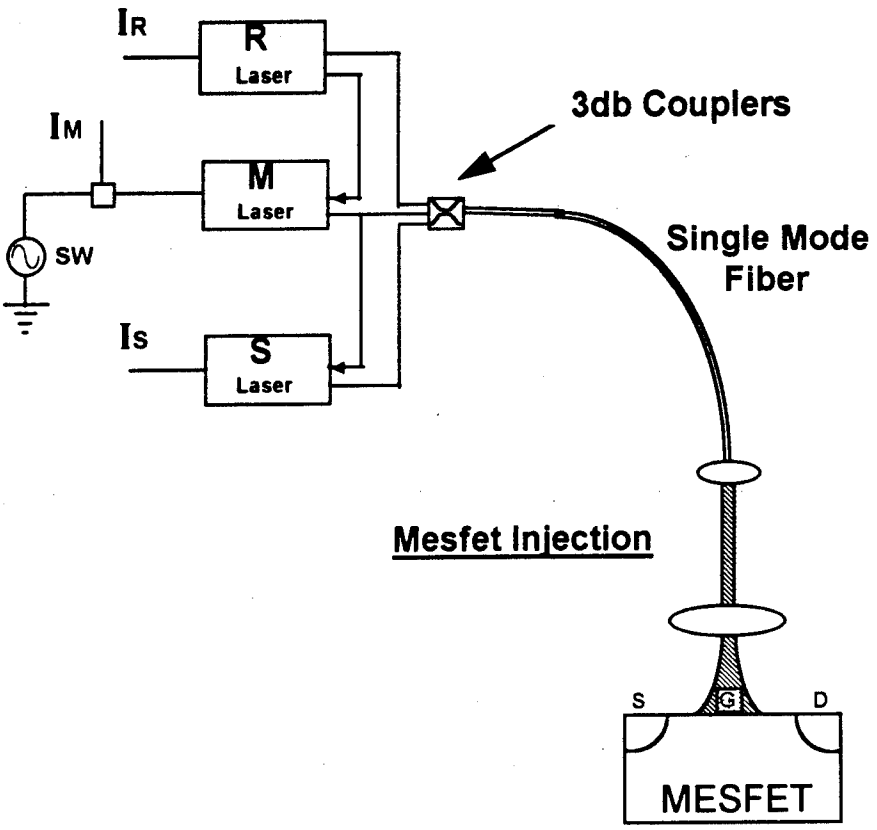

Figure 1 Complete Experimental System

focusing system with micropositioning capability on several stages and variable lens on the CCD camera.

All experiments were conducted on optical tables to minimize vibrational resonances and provide a rigid surface to reliably mount optical components. However, air flow disturbances and acoustic vibrations still created obstacles because thin membrane beam splitters, called pellicles which were needed in locked laser experiments, are extremely sensitive to such disturbances. The heterodyne beat

note which was viewed on an HP Spectrum Analyzer (HP8559A) identified the vibrations when the signal would actually fluctuate until the source was quieted.

Radio frequency from modulation sources, from amplifiers, and from cables were picked up by the spectrum analyzers and microwave circuits. These sources acted like antennas of unwanted RF and were caged to limit the amount of radiation.

The next sections will discuss the experimental systems individually.

5.3 Experimental Laser Injection System

The experimental laser injection system is shown in Figure 2 Injection Laser System. The lasers used in the 5 GHz experiments, completed early in the research, were Hitachi HLP-1600 semiconductor laser diodes. The shelf lives of the lasers were exceeded by several years. Eventually, material in the contacts outdiffuses into the active semiconductor regions and subsequently, deteriorates the modal quality to the point of no lasing action or multimode behavior. After this happened, new lasers had to be used. The majority of the Thesis results (3 GHz) are with Mitsubishi ML5415C AlGaAs semiconductor lasers in the 820-830 nanometer wavelength range . These are stable, single transverse mode lasers which were collimated by Newport F-L40B diode laser objectives. Current was controlled with a Melles-Griot current source (06-DLD-201) which has a noise level of 2μA RMS. Temperature control was provided with a Melles-Griot temperature controller (06-DTC-001) with a thermoelectric sensor (06-DTC-003) which provided stability to 0.005°C.

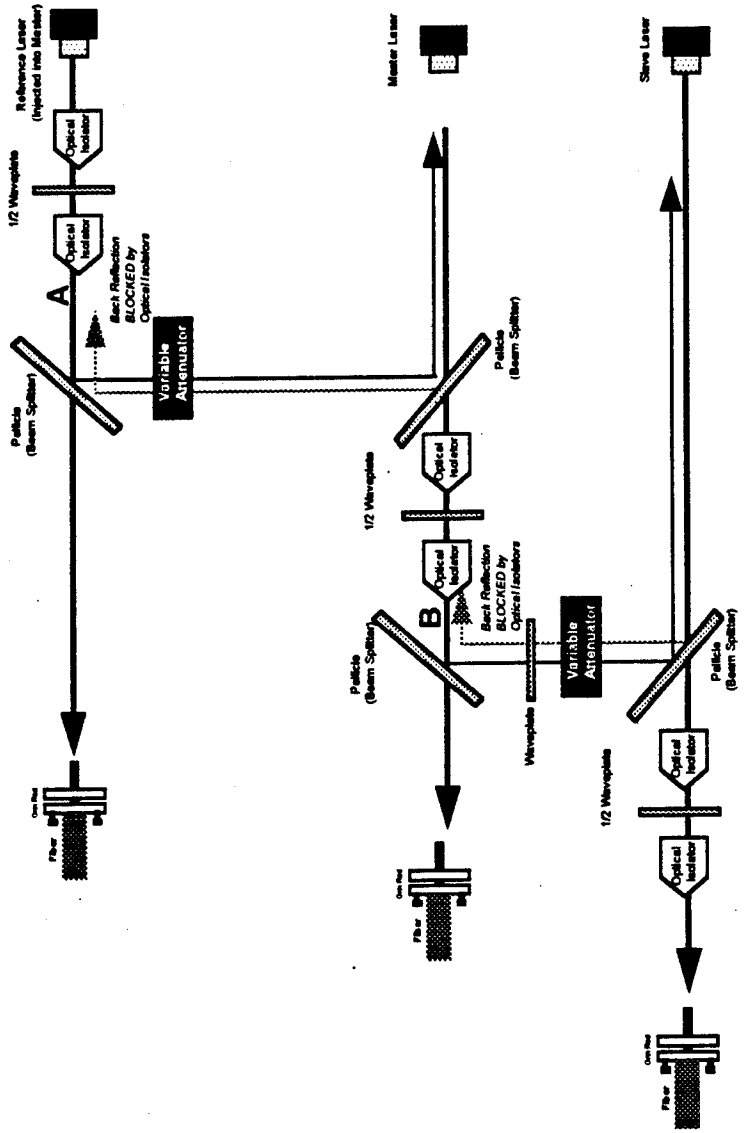

Figure 2 Injection Laser System

When the laser thermal stability fluctuates, the laser wavelength changes. For the Mitsubishi lasers, the rate of change from the shorter wavelength side of a mode to the longer side is 0.20nm/°C, and for the older Hitachi lasers, it is 0.3nm/°C. Coupled with the thermal stability specification (0.005°C), this results in a frequency shift that is on the edge of the locking bandwidth. This fact and the age of the cooling elements created a severe problem when trying to lock the lasers. As with the lasers, the thermoelectric coolers also have a finite shelf life. The TEC life is restricted by the large currents at which they operate. The thermosensors and the cooling elements had to be replaced during the experiment because they could not maintain adequate temperature stability. Also, cooling fans were installed in the power supplies, that drive the elements, to lengthen the life of the electronics. The Melles-Griot product uses an Analog Devices two terminal monolithic integrated circuit temperature transducer (AD592) to provide output current proportional to the absolute temperature. The thermoelectric coolers (TEC) are solid state heat pumps that utilize the Peltier effect. The TEC used was a Marlowe Industries (MI-1023-T-03AC) device. The Peltier effect is a temperature change induced by the flow of current. When current passes through the junction of two different types of conductors, a temperature change results. TEC consists of a p-type and n- type pairs connected electrically and sandwiched between ceramic plates. During operation, DC current flows through the TEC causing heat to be transferred from one side to the other which creates a hot and a cold side. A strip chart recorder was used to trace the current to the TEC from the power supply to assure that the power supply was operating properly and responding to a properly operating sensor.

The cold side of the TEC is in contact with the laser mount which is a 54x38mm plate. Thermal contact is secured with Dow340 thermal grease. The fin on which the plate is attached is used to dissipate the heat to the optical table. This system worked for the older Hitachi 10mW lasers, but with the Mitsubishi 30mW lasers the fin was not adequate to dissipate the heat. Melles Griot acknowledged this as a known problem for the newer lasers. Since the experiment is sensitive to acoustic and wind vibrations, fans were not a solution, and therefore, additional heat sinks were mounted onto the laser mounts. With the room vents off to prevent air disturbances, the room near the lasers routinely warmed to 24°C. The temperature gradient between the heat sinks and the ambient air was nonexistent; there was no heat dissipated when the room warmed. The laser stability was nonexistent when this happened. The inability to remove the heat from the device forced the temperature higher, and then the sensors called for more current to cool the device. The power supply responded with more and more current which in turn heated the electronics. A crude but effective system to cool the air surrounding the lasers was used. To generate a temperature gradient, frozen ice paks were placed close to the fins. This sufficiently cooled the air, surrounding the laser mounts, which allowed the TECs to cool the lasers. Subsequently, the call for current was smooth and bounded. Initially, dry ice was placed in the vicinity of the laser mounts but did not work because it was too cold. The mounts would thermally expand and contract destroying the optical alignment. The combination of properly functioning thermal elements, heat sinks, and the ambient air coolers would allow the lasers to be stable for several hours.

The output of the laser collimator was fed into optical isolators. The Reference laser is split into a path to inject the Master and one to couple into a fiber. Similarly, the Master is split into a path to inject the Slave and one to couple into a fiber. The Slave is required to couple into its fiber. The fibers are connected to Gould 3dB Couplers (22-20685-50-21201) to mix the optical signals and to fan out the resultant beam. The couplers and the FC-type connectors from the original setup were replaced to the specified Gould couplers with ST-type connectors to increase the optical power. The mixed beam was directed via fiber to 4 places:

1. MESFET free space system to inject the devices with the optical signals
2. HP Optical Spectrum Analyzer (HP70951A) to see the absolute wavelength of the lasers to within 0.008 nanometer resolution. Gross tuning of wavelength via current and temperature were completed with this Analyzer.
3. Fabry Perot Etalon to view the optical modes with better resolution than the Optical Spectrum Analyzer (OSA). However, because the etalon is a periodic device, alaising occurs which would distort the actual position of the signals. The modes could be as much as 150 GHz apart and appear to be exactly the same. This is why it was imperative to use the OSA to get the wavelengths to within 0.01 nanometer and then tune using the etalon output. The output was detected by a high speed photodiode (ARS-5) and fed into an oscilloscope.
4. Newport high speed avalanche photodiode(877-APD) which is fed to an HP Spectrum Analyzer (HP8559A) to see the beat note between the optical signals. Locking the lasers means their frequencies are locked and therefore, when

locked, the beat would be extinguished. Also, when we viewed the Reference and Slave signals only, the locked heterodyne beat note is seen at the modulation frequency (5 GHz or 3 GHz).

At point A in Figure 2 Injection Laser System, the Master is transmitted straight through the path and also, reflected onto the Reference injecting path. Similarly, at point B in Figure 2, the Slave is transmitted straight through the path and also, reflected onto the Master injecting path. The unwanted reflections could cause unwanted locking. Optical isolators are used after the laser collimators to extinguish back reflection onto itself and to eliminate unwanted locking from other laser paths. It is possible that the back reflected light, mainly from the grin lens at the fiber input, would cause self locking which would defeat the purpose of the experiment. Also, injection paths from the Master into the Reference or the Slave into the Master could be established without the isolators. The optical isolators are designed to transmit the forward light beam and attenuate the reverse beam. The Hoya M500, used in these experiments, operates on the Faraday effect to rotate the polarization of the incoming beam. It uses paramagnetic glass to achieve more than 30dB isolation. The output of the isolator is passed through a half waveplate to match the input polarization of the next isolator. The combination provides over 70dB of isolation. Due to the cost of the isolators, the Slave path originally had two waveplates in place of the isolators, which did not provide sufficient isolation, because self-locking was observed. Additional isolators fixed this problem.

Thin membrane beam splitters, called pellicles, were needed in the locked laser setup. Pellicles are high tensile strength elastic membranes which are stretched like a drumhead over a frame. The thickness is five microns or less. The ones used in this experiment were coated to enhance the beam splitting properties at 830 nanometer wavelength. The benefits of pellicles over standard beam splitters are chromatic and spherical aberration in converging beams is negligible, absorption is low, ghost image problems are virtually eliminated, and basically no differences of optical path length for coincident beams. However, they are particularly sensitive to acoustical disturbances. Air flow disturbances and acoustic vibrations created obstacles. Examples of the sources of airflow and acoustic disturbances are the overhead vents, humans walking past the table creating a draft, the door opening and closing, talking, electronic fans or power supplies.

The stability, collimination and polarization of the laser beams are critical details in achieving a stable lock. Mechanical stability was achieved by actually gluing the mounting optics to the bases and using magnetic bases in the injection paths. This achieved the stability but at the cost of experimental time. Using magnetic bases instead of micropositioning stages increases the experimental difficulty level greatly particularly when aligning the laser collimating lens. Securing a perfect laser beam collimination is absolutely imperative in order to have enough optical overlap of the two coincident beams. Furthermore, the polarization of the beams must be the same. Because the optical isolators rotate the polarization, it was necessary to add waveplates to the Master injection path which could be adjusted prior to injecting into the Slave laser. If the waveplates were rotated while viewing

the beat on the spectrum analyzer, it was evident that the polarization was causing the beams to lock or not. These solutions were milestones in the experimental process.

It was necessary to control the beam polarization so that the lasers would interfere constructively at the MESFET injection point and at interferometric diagnostic equipment. Fiber polarization control via butterfly-type tension devises were used. Each wing approximated a quarter-wave plate, and two, therefore, would yield all possible points on the Poincare sphere. Because polarized light in fibers becomes depolarized in standard single mode fiber after a few meters, it was necessary to also provide a waveplate in the MESFET injection path to tweak in the polarization. The method was to adjust the polarization with the butterflies at the Fabry Perot Etalon input, and then to tweak the polarization via waveplate in the free space segment of the MESFET path.

5.3.1 Laser Wavelength Tuning

The laser wavelength tunes with temperature and with current. Because the manufacturers specify a range of wavelengths for a given semiconductor laser part number that is typically a 30-50 nm spread, the difficulty is to get all three lasers to lase at virtually the same wavelength ($\leq$0.01nm). Therefore, the Mitsubishi lasers were characterized.

With the use of the HP Optical Spectrum Analyzer set to a span of 10nm, the wavelength at which the optical mode hopped was measured as the temperature and current were varied (Figure 4 Laser Wavelength Characterization). Mode hops are non-continuous changes in the wavelength and are sometimes as much as 2-3nm. The temperatures were nominally 30°C, the highest constant temperature for safe laser operation, 25°C and 20°C. Given the laser power, the TECs could reliably maintain a minimum case temperature of 15°C. The current was varied slowly in steps of less than 0.5mA from threshold, 65mA, to the maximum current of 115mA and when the mode hopped the wavelength was noted. At each step, the temperature was allowed to stabilize before the reading was taken.

The characterization was not exhaustive but did provide adequate information to make an educated laser selection and to fit the data. The data was fitted by a least squares linear fit and was used to project the wavelengths for current and temperature combinations not measured (Figure 3 Calculated & Measured Wavelength vs Current). The 24.95°C calculations perfectly match the experimental data, but the match for the 20.11°C cases did not predict the wavelength steps. The idea was to obtain information to make an educated decision which could minimize the number of passes through the alignment procedure and subsequent locking trials. The data did help to discard the lasers at much higher or lower wavelengths. However, because the tuning is not smooth under all circumstances (i.e., random mode hops exist) and because each laser has definite maximum and minimum wavelength that cannot be changed by current or temperature, several laser

selections were necessary before the final three lasers were able to be tuned within locking range. It must be emphasized that the wavelengths of the lasers must be virtually the same to attempt locking(≤0.01nm). More than ten lasers were characterized out of which three were chosen for Figure 4. In general, the wavelength dependence on current or temperature is a staircase response which is also seen for most of the cases shown in Figure 4.

The current tuning is much stronger than the temperature tuning which means that a current tune will pull and hold the wavelength over a temperature tune. In general, therefore, gross adjustments were made with current and then tweaking is completed via temperature.

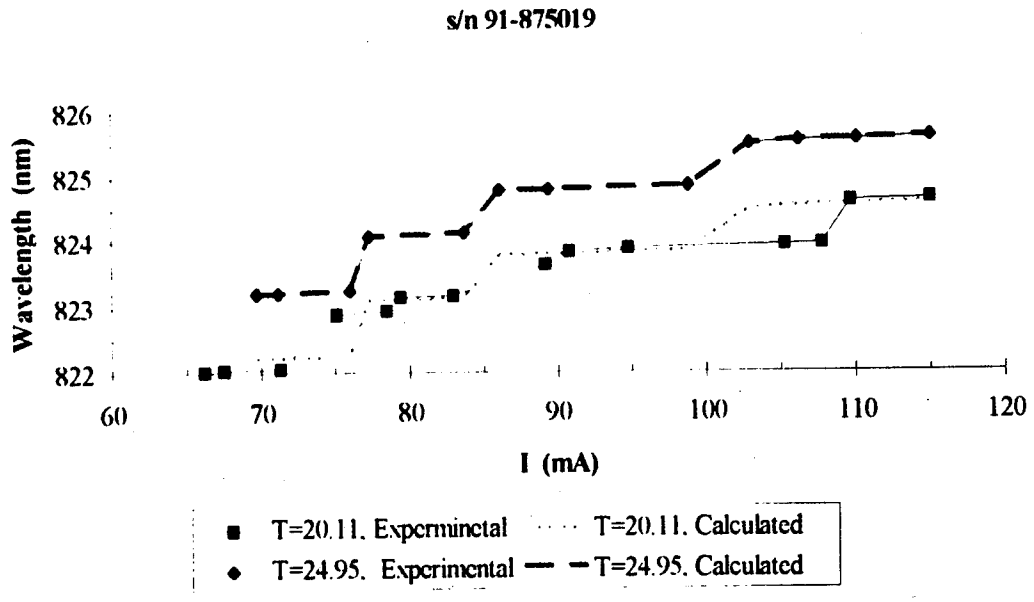

Figure 3 Calculated & Measured Wavelength vs Current

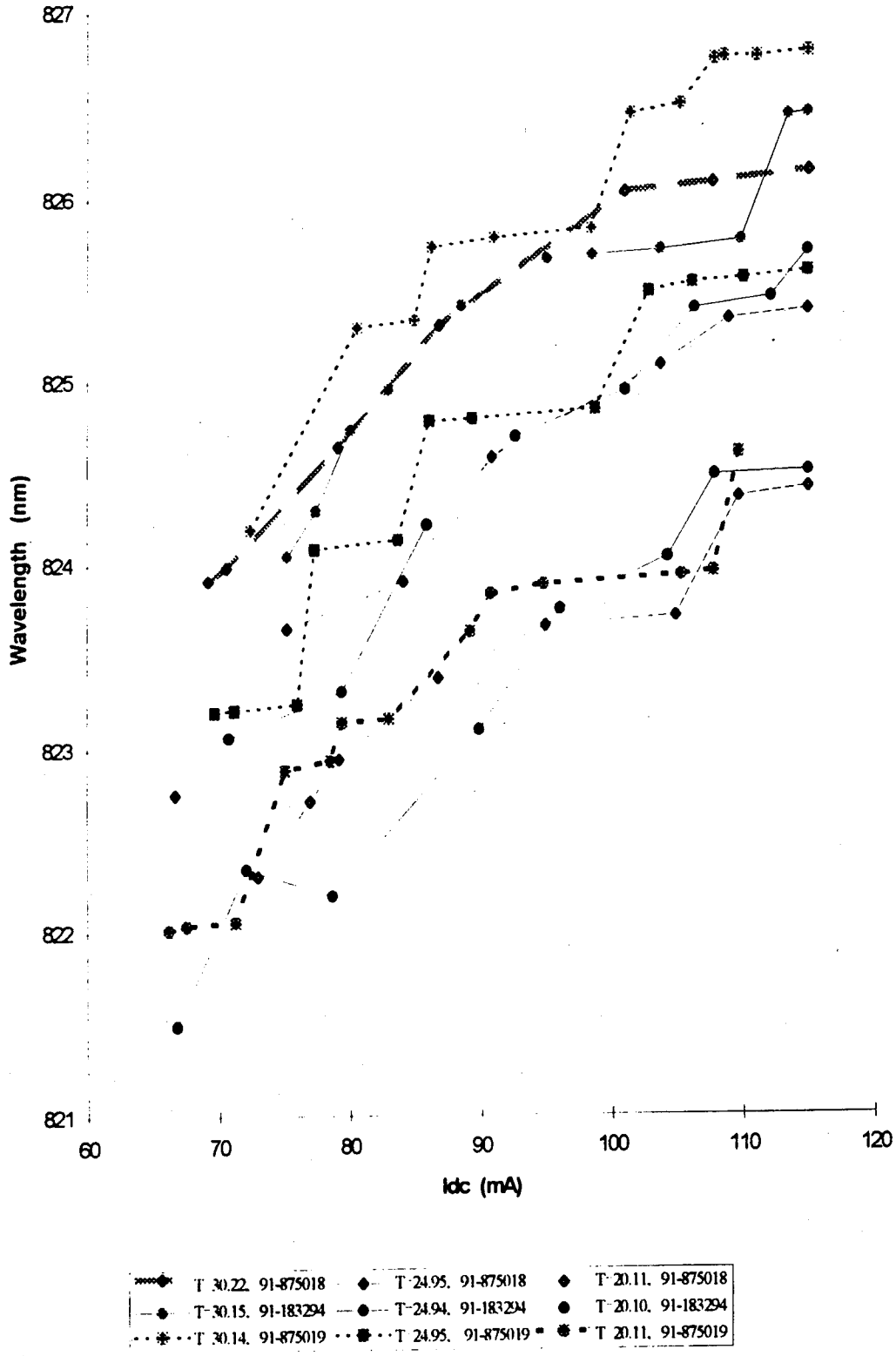

Figure 4 Laser Wavelength Characterization

5.3.2 Optical Alignment

In this section, the optical alignment procedure is discussed with special attention to injection paths alignment.

The laser wavelength tunes with temperature and with current. Temperature changes of 5°C or more caused the laser mount to actually expand or contract, and therefore, the optical alignment is destroyed. Since the average thermal coefficients of expansion of aluminum and most of its alloys is 22μinches per inch–°C, a temperature change of 5°C will yield 5μm over the entire mounting plate in both x and y dimensions. Assuming the expansion is linear, at the midpoint of the y dimension alone, where the laser is mounted, the expansion could be as much as 2.5μm. With fiber radius of 4.5 μm and size of the laser front facet, where the injection takes place, of a similar dimension, the expansion of the mount seriously affects the alignment. Therefore, the alignment and laser tuning process evolved to (1) gross alignments, (2) wavelength tune, (3) precise alignment at the currents and temperatures established in step 2, (4) fine tuning the injection paths using a CCD camera and monitor, and (5) tweak the wavelength, polarization, and power via variable attenuators to establish laser lock.

The injection paths are grossly aligned by using an infrared viewing card. To fine tune the injection paths, the back reflection from the front facet of the laser (to be injected) was imaged into a CCD Camera. Figure 5 Setup to Align the Injection Paths shows the setup for aligning the reference into the master laser. The same

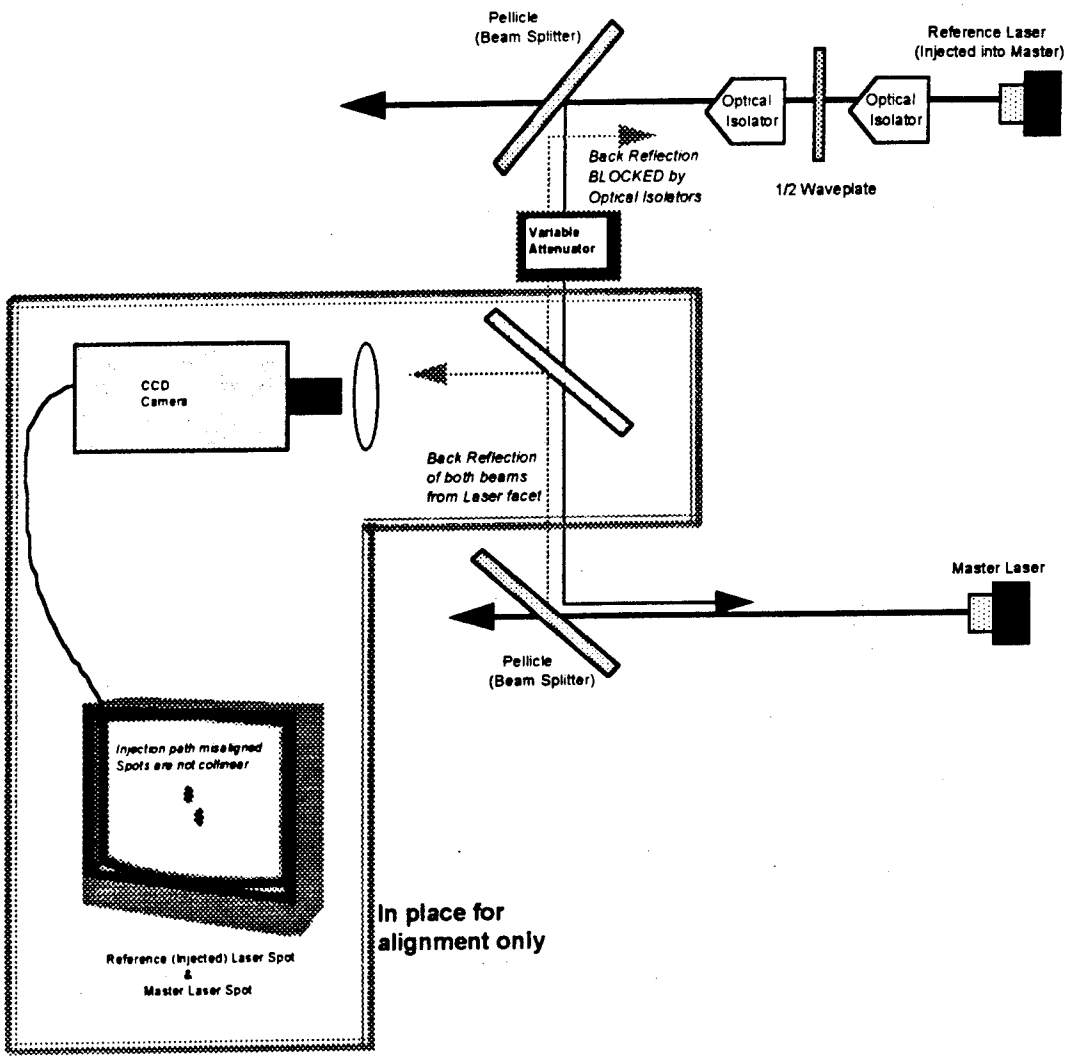

Figure 5 Setup to Align the Injection Paths

procedure was followed for the master into the slave. The back reflection from the master's front facet produces the master spot and the injecting reference laser's spot on the monitor. The straight-through back reflection from the master is blocked by the optical isolators in the reference laser's path. The power of the master is much higher (15-20mW) than the injecting master power (<0.5mW) when driven above

threshold and measured at the master front facet. The CCD is saturated by the power, and therefore, the current on the master must be reduced to approximately 2-3mA to view both spots simultaneously and to not saturate the camera. The pellicles shown have angular adjustments and are used to align the spots. Care must be taken to allow thermal stability after current adjustments or else the alignment will not be accurate.

Once the master and reference are aligned and locked, the alignment procedure for the master into the slave path takes place. The master beam travels through optical isolators and a half waveplate which changes its polarization from that at its front facet. Therefore, in the master into the slave injection path is another waveplate used to match the polarization of the master to the slave for locking.

5.3.3 RF Laser Cable Design

The Master laser was modulated at various frequencies in the gigahertz regime by superimposing the RF onto the laser's direct current drive with a bias T (Picosecond Pulse Labs 5550B). At these frequencies, large reflections are possible if the cables and the laser are not impedance matched, and therefore, the amount of RF that actually gets to the laser is dependent on the laser impedance characteristics. It was not feasible to simply increase the RF power because over 25dBm of power was needed to get a very small modulation index out of the laser. The laser

impedance was measured and a specially designed impedance matched cable was designed and built.

Above threshold with a lead of approximately 2mm, the laser impedance is equal to a series connection of a resistance of 4Ω and an inductance of 3nH. An RF cylindrical resistor of 46Ω was attached to the laser lead with conductive epoxy. Solder could not be used because it would change the inductance and capacitance of the cable to laser system. The other side of the resistor was butted up against a copper coaxial line which was mechanically supported by custom made jig and counterweighted to prevent the weight of the copper from destroying the delicate connections. The cable attached to the laser is shown in Figure 6 Laser RF Modulation Cable. Because the copper ground of the cable was not shielded, it did radiate some RF. Absorbers and metal shields were used during the MESFET injection experiments to limit the radiation from the cable. See 5.6 RF Considerations for other methods enacted to limit the RF from interfering in the MESFET experiments. Also, time domain reflectometry (TDR) measurements were taken of the standard laser cable and compared to the impedance matched cable. The impedance matched cable was a significant improvement over the original design.

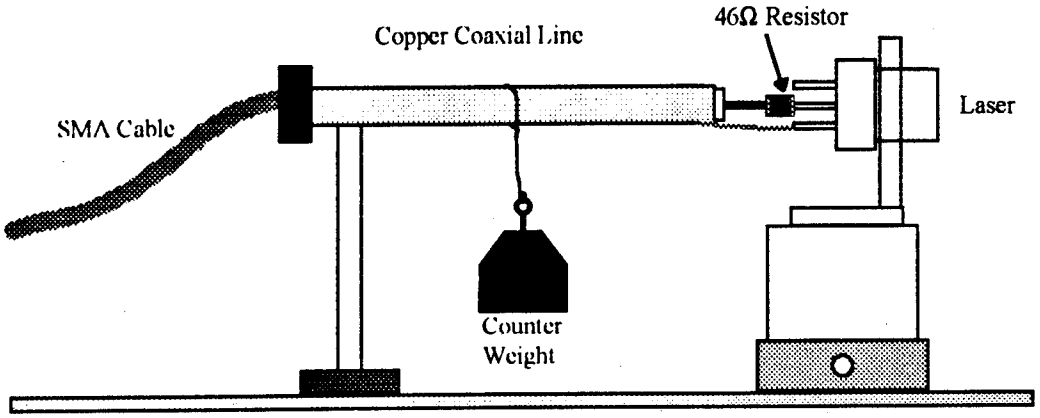

Figure 6 Laser RF Modulation Cable

5.4 Experimental Free Space Optical System for MESFET Injection

The design specifications for the MESFET setup were that the beam must be focused to a spot on the order of 10-30μm radius, the back reflection from the MESFET surface must be viewed via CCD camera to be able to know where the beam was located relative to the active area on the MESFET, interchanging microwave circuits must be convenient. Figure 7 is a schematic of the MESFET injection system.

The optical signal is transmitted to the setup by fiber from the laser system. The free space injection system is a four focal length system consisting of 20x microscope objective (f_{20x}≈9mm), two lens (100 mm and 200 mm), and 10x

microscope objective ($f_{10x} \approx$ 16.9mm). The four focal length system shown is shown Figure 9. The fiber, 20x, 10x and the circuit were mounted on stages that permitted stable x-y-z positioning to fine tune their relative position, thus, giving adequate control on the beam waist size at the MESFET surface. The 100mm and 200mm lens were mounted to the table on magnetic bases because it was impossible to fit micropositioner stages in the limited space. The space was dictated by the available bench space and the focal lengths of the available lens. The microwave circuit jig was secured with posts and supported with steel plates from the back. The surface was illuminated with a variable intensity light source so that the back reflection could be seen on a CCD camera. It was important to have completely separate entry paths for the light source and camera otherwise the camera would be saturated by the reflection of the source from the first beam splitter. The MESFET back reflection to the CCD had to be largeenough to see the device's structure on the monitor. However, if too much amplification occurred the image would be too large to determine what area on the MESFET is in view. The best lens for the back reflected light image was a 10x microscope objective, and therefore, no other lenses could be between the circuit and the camera.

Also, it was necessary to have significant space between the fiber and the circuit to place two beam splitters; one for the light source path and the second for the CCD camera path. Therefore, long focal length lenses were necessary to bring

the beam in focus in the object plane of the 10x. Because a gaussian beam diverges from 3-5μm in the fiber to 60μm at 1 mm from the fiber

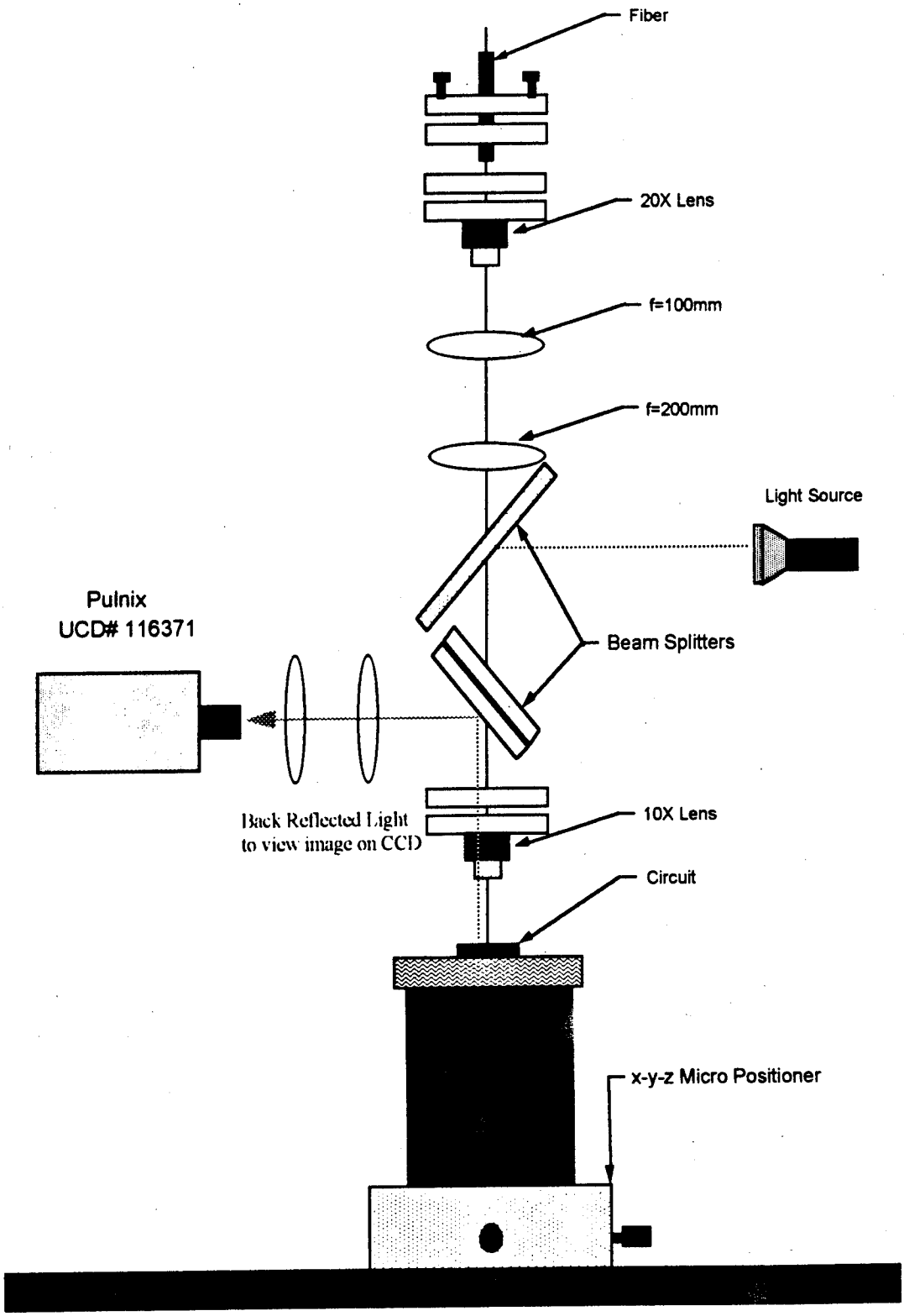

Figure 7 MESFET Injection Setup

(Figure 8 Waist Divergence from Fiber Endface), the selection of the first lens, 20x, was necessary.In the following sections, the gaussian beam studies (5.4.1), used in the design, are presented and the amount of optical power at the MESFET active area is calculated (5.4.2).

5.4.1 Gaussian Beam Analysis

The output of the single mode fiber is focused onto the MESFET active area with a four focal length free space optical system. Assuming a gaussian optical intensity distribution at the planes normal to the propagation direction, z, the solutions to the wave equation can be used to derive the transformation (ABCD) law of a gaussian beam

$$\frac{1}{q} = \frac{1}{R} - j\frac{\lambda}{\pi\omega(z)} = \mathrm{Re}\left\{\frac{1}{q}\right\} - \mathrm{Im}\left\{\frac{1}{q}\right\} = \frac{C + D\left(j\frac{\lambda}{\pi\omega^2(z)}\right)}{A + B\left(j\frac{\lambda}{\pi\omega^2(z)}\right)}$$

$$\omega(z) = \left(j\frac{\lambda}{\pi\,\mathrm{Im}\left\{\frac{1}{q}\right\}}\right)$$

and relate it to the complex beam radius, q(z), the beam spot size, $\omega(z)$, and the radius of curvature of the wave, R(z).

With these relationships, the beam waist divergence as a function of position can be calculated for any optical system which can be specified by an ABCD transformation matrix. The ABCD matrices of several media can be simply multiplied together to obtain the overall equivalent matrix for the entire system. The following are the unit cells for a lens (f) sandwiched between two distances of free space ($l1$, $l2$)

$$\begin{bmatrix} A & B \\ C & D \end{bmatrix} = [\text{free space}] \bullet [\text{lens}] \bullet [\text{free space}]$$

$$= \begin{bmatrix} 1 & l_2 \\ 0 & 1 \end{bmatrix} \bullet \begin{bmatrix} 1 & 0 \\ \frac{1}{-f} & 1 \end{bmatrix} \bullet \begin{bmatrix} 1 & l_1 \\ 0 & 1 \end{bmatrix}$$

The equivalent ABCD matrix is used in the equations for the complex beam radius, the beam spot, and the radius of curvature. Figure 8 is a graph of the beam waist divergence as the distance from the end of the fiber increases. At 1mm, the beam waist is at 60μm which is twenty times the fiber core radius. The radius of the first lens (i.e., numerical aperture) must be large enough to collect the beam. The numerical aperture multiplied by the focal length must be greater than radius of the beam, or equivalently, the radius of the lens must be greater than the radius of the beam. When all distances are exactly at the focal planes of the lenses, the overall minification or magnification is give by the following ratio:

$$\frac{\omega_4}{\omega_0} = \frac{f_2 \; f_4}{f_1 \; f_3}$$

For the system components in this design, this ratio was computed to be nearly one for exact placement of the lenses which means the beam radius was nearly 4.5μm.

In practice, it could be possible to get close to this ideal if all the components were mounted on micropositioning stages. However, it was possible to mount the fiber, 20x, 10x and the circuit on micropositioning stages while the 100 and 200 mm lenses were mounted on magnetic bases. It was impossible to fit five micropositioner

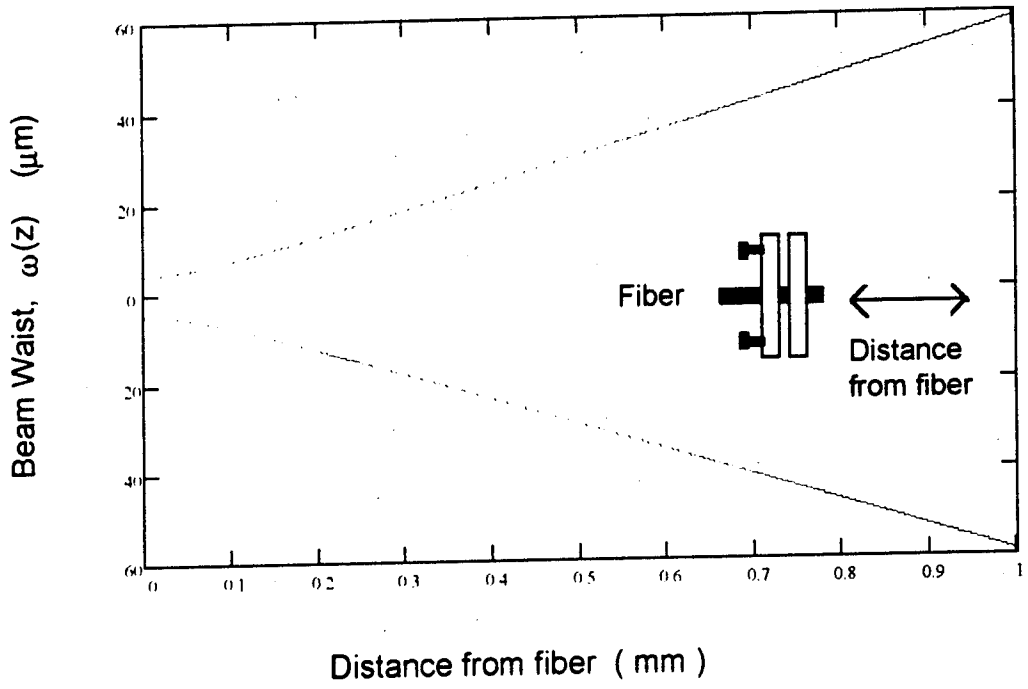

Figure 8 Waist Divergence from Fiber Endface

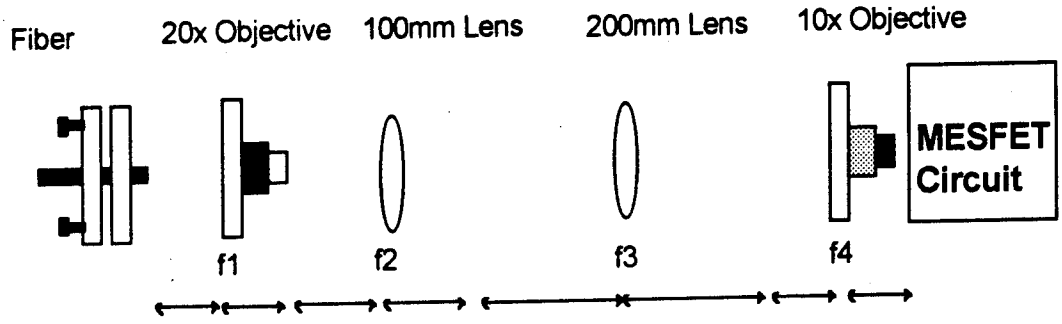

Figure 9 4-f System

stages in the limited space dictated by the available bench space and the focal lengths of the available lens.

The actual beam size was measured by comparing it to the distance from the drain to source contacts and was equal to 9-14 μm. The distance from drain to source contacts was measured with a high power calibrated microscope and was equal to $4\frac{2}{1}$ μm. When the beam was compared to this distance, it was roughly twice to three times this measurement which means the beam size was 9-14μm. The difference between the measured and exact radius was due to inability to obtain precisely the exact alignment of all 4 lenses.

The most sensitive alignment was found to be the 20x objective position. Figure 10 shows the calculated values of the beam radius as the distance from the 20x is varied. The beam diverges rapidly from perfect focus. At twice the focal length of the lens, the beam is 500μm. In comparison, the position of the 200mm lens (or the 100mm) is less sensitive to variation. Figure 11 shows the beam variation when the 200mm lens position is varied. Therefore, the 200mm and 100mm lenses were mounted on magnetic bases while the others were micropositioners.

The overall system ABCD matrix was calculated by multiplying the individual matrices that correspond to the four focal length system used in this experiment:

$$M_{Equivalent} = (L_{4b}\, M_{10x}\, L_{4a})\,(L_{3b}\, M_{200}\, L_{3a})\,(L_{2b}\, M_{100}\, L_{2a})\,(L_{1b}\, M_{20x}\, L_{1a})$$

In the above , matrices for free space distances before and after the lenses are represented by L, and the lenses are given by M. When computing $M_{Equivalent}$ for Figure 10 and Figure 11, the corresponding L matrices were functions of position.

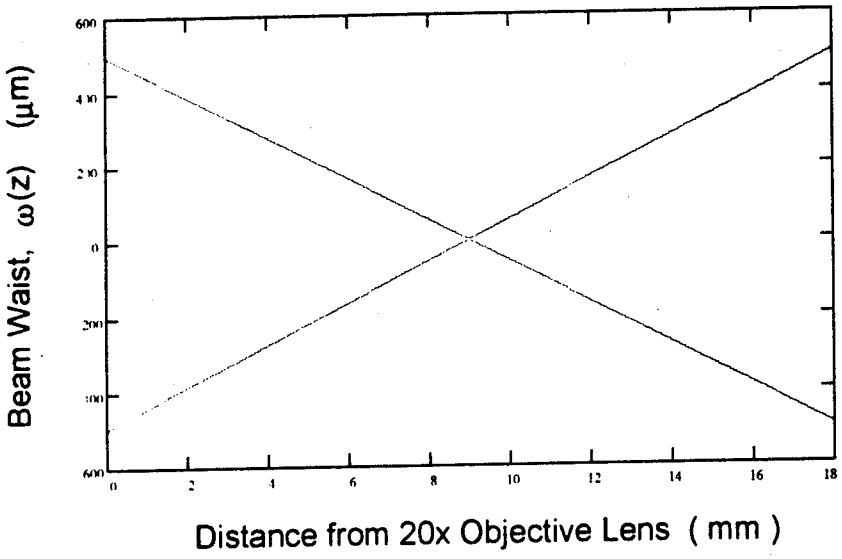

Figure 10 Waist Divergence as a function of the distance from 20x

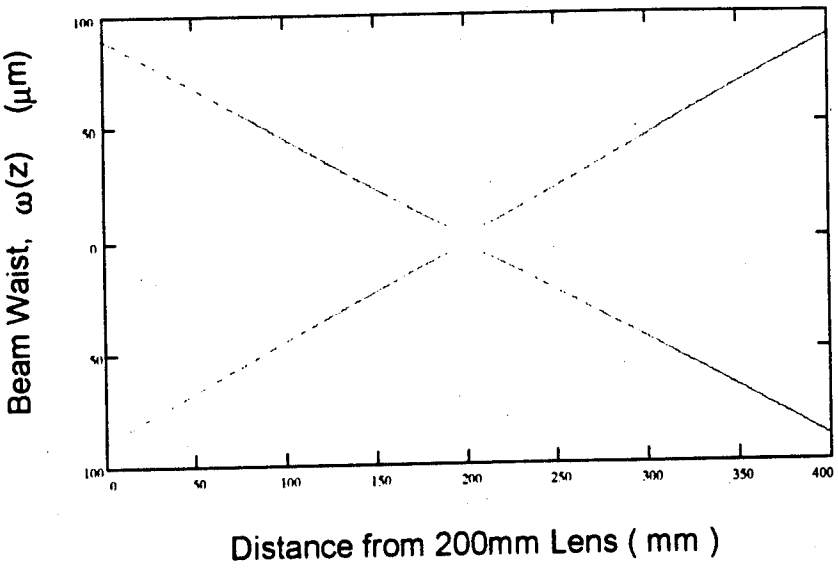

Figure 11 Waist Divergence as a function of the distance from 200mm Lens

5.4.2 Optical Power Transmitted through MESFET Surface

The number of optical components in the path, the MESFET dimensions, the optical power per area based on a gaussian distribution, and the reflectivity of the multilayer are combined to compute the amount of optical power transmitted to the active MESFET area in GaAs material.

In the experimental setup (Figure 7), there are six surfaces before the MESFET. For each surface, approximately 96% of the optical power is transmitted for a total of 78% (=$\{96\%\}^6$). The measured size of the drain to source line was 2μm which is 14-20% times the size of the beam computed in the previous section (9-14μm). Accounting for the surface reflections and the beam size, the power at the MESFET surface is 10.9% (= 78% x 14%)the original power level at the fiber

output. The gate metal reflects 96% of the optical signal for all realistic gate depths x_{Au}. The passivation layer reflects 20-35%. The theory of stratified media and the results of the calculations for these cases is given in 5.4.3 Multilayer Analysis. Since the beam is focused between the source and drain, the passivation layer transmitance is the number of concern. The total is 2.2-3.8% (=10.9% x 20-35%) of the original power level gets to the GaAs. The absorption coefficient α_{GaAs} of the GaAs is 10^4 cm^{-1}. The amount of power that is absorbed, $P_{absorbed}$, is related exponentialliy to α_{GaAs}:

$$P_{absorbed} = P_{optical} e^{\{-\alpha d\}}$$

For a depth of 0.5μm, the exponential term is 0.61. Therefore, the total optical power absorbed by the GaAs is 1.3-2.3% of the original power at the fiber output.

5.4.3 Multilayer Analysis

The theory of stratified media is used analyze the reflectivity of the MESFET[2]. Two areas are considered; the gate metallization and the passivation layer (SiO_2 or Si_3N_4). The multilayers are shown pictorially with the calculation results in Figure 12 for both cases: 1) Air, gold, GaAs, and 2) Air, passivation layer, GaAs. The gate metal reflects 96% of the optical signal for all realistic gate depths x_{Au}. The passivation layer reflects 20-35%.

Because these MESFETs are commercial devices, the passivation layer composition is an educated guess. Si_3N_4 was used in this analysis. The field propagation in each of successive material layers are represented by a matrix. The matrices are multiplied in order to obtain an equivalent matrix whose elements are related to the reflectance of the total stack of material given by the following:

$$R = \frac{A^2 + B^2}{C^2 + D^2} \qquad T = \frac{n3}{n1}\left(\frac{E^2 + F^2}{C^2 + D^2}\right)$$

In these equations, the 1 subscripts correspond to air, 2 refers to the middle layer of gold or Si_3N_4 and 3 is the GaAs material. The refractive indices, n, are given by Born and Wolf for a wavelength of 871nm at room temperature[3].

$$n1 = 1$$
$$n\_Si_3N_4 = 3.1 + i0$$
$$n_{gate\ metal} = 0.161 + i5.140$$
$$n3 = 3.606 + i0.0359$$

In the equations the propagation constant is given by k ($k_0=2\pi/\lambda$). The direction of propagation is represented by x. 5.9 Supplement contains details of the required substitutions into the reflectance and transmitance equations.

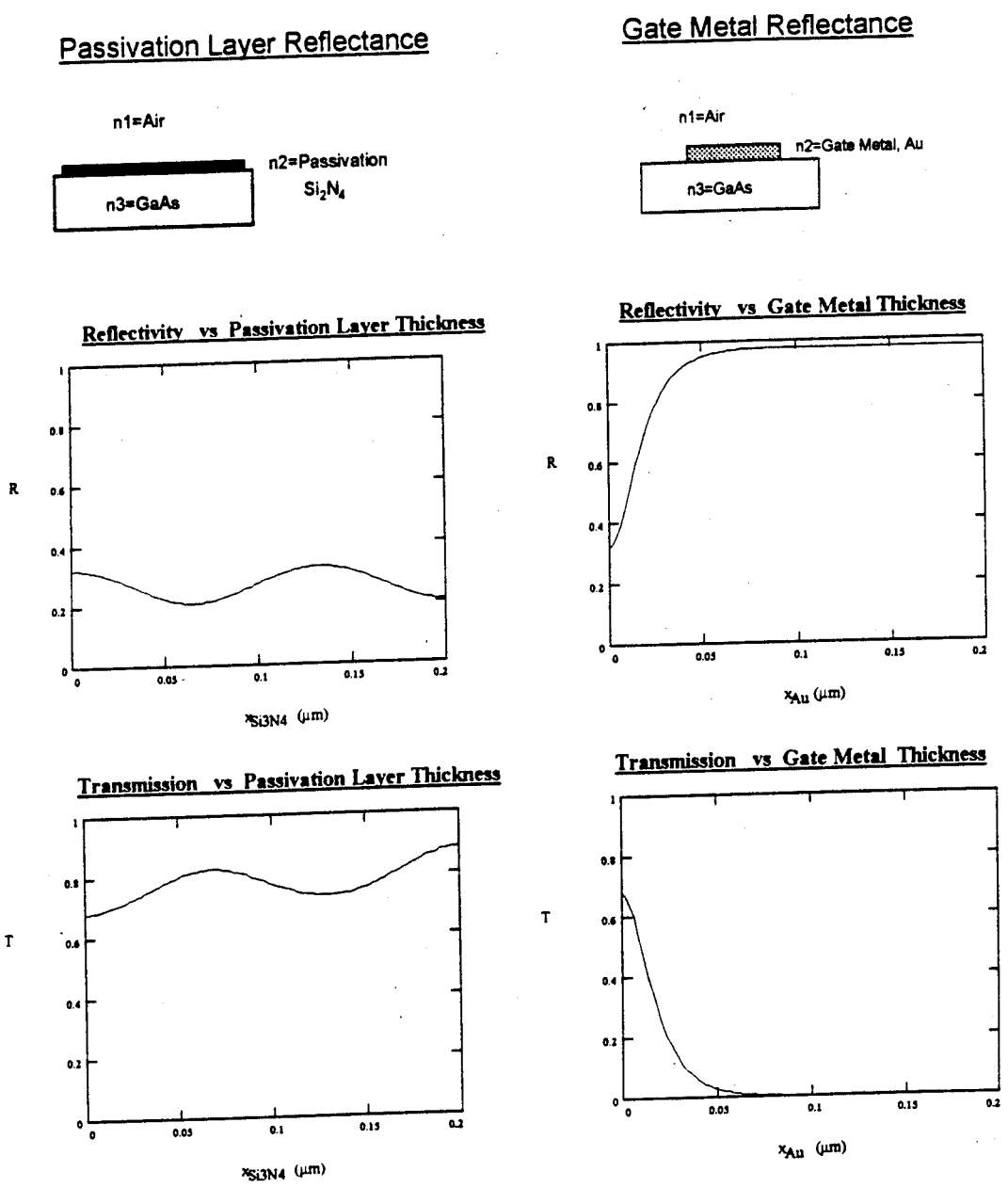

Figure 12 Reflectance of MESFET Surface

5.4.4 Coupling Enhancements

The experimental system in Section 5.4 Experimental Free Space Optical System for MESFET Injection had to be robust to conveniently change the circuits and did not specifically address methods to enhance optical coupling that could be used in non-experimental systems. There are reliable methods for securing the optical beam to the MESFET active area which may be used separately or in some combination. These include the following:

1. Mounting the fiber directly onto the MESFET using the same methods that are used in fiber pigtailing lasers and detectors as shown in Figure 13 MESFET with Fiber Pigtail.

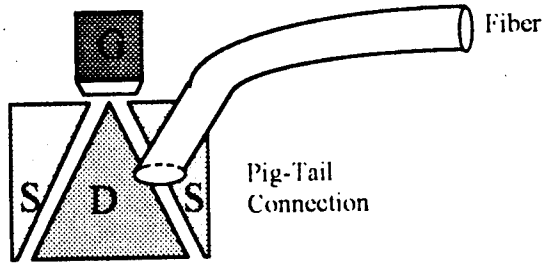

Figure 13 MESFET with Fiber Pigtail

2. Growing windows over the active region which can be easily etched by standard photolithographic processes which would provide a strong focus of an incoming beam which is presented in Figure 14 MESFET with Etched Lens Windows.

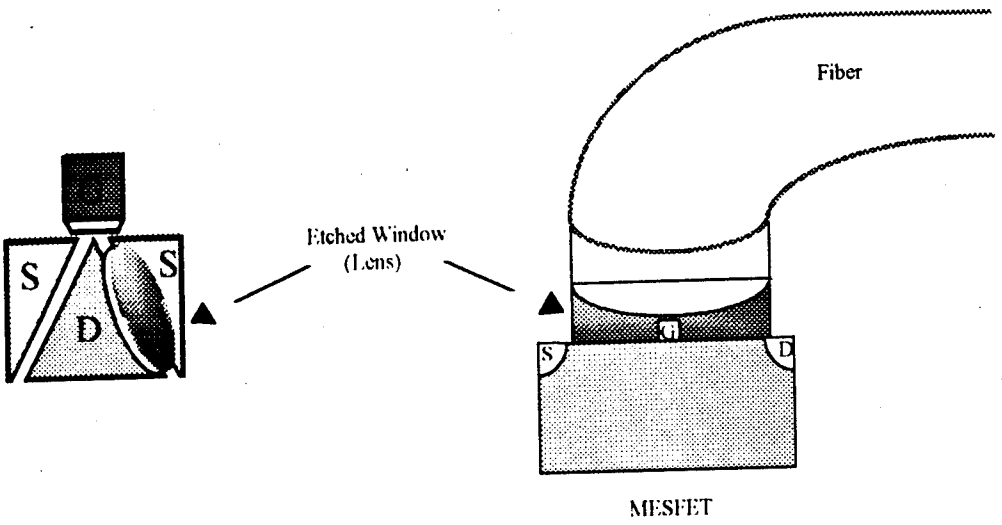

Figure 14 MESFET with Etched Lens Windows

3. Growing a microlens on the end of a single mode fiber is a possible way to enhance the optical coupling into the MESFET for non-experimental systems. A microlens is shown in Figure 15 Microlens grown on fiber endface. The beam divergence as a function of distance from the end of the microlens was calculated for lens radii of 3, 6 and 9 μm.

4. Figure 16 shows these calculations for a fiber radius of 3μm, index of refraction equal to 1.55, and wavelength of 830nm. The distance before the lens is zero (L1=0) since the lens is grown from the fiber's endface and the distance after the lens, L2, is varied in the calculations. Since the focal length of a lens is related to its radius and refractive index, the minimum beam waist occurs at almost 3, 6 and 9 μm.

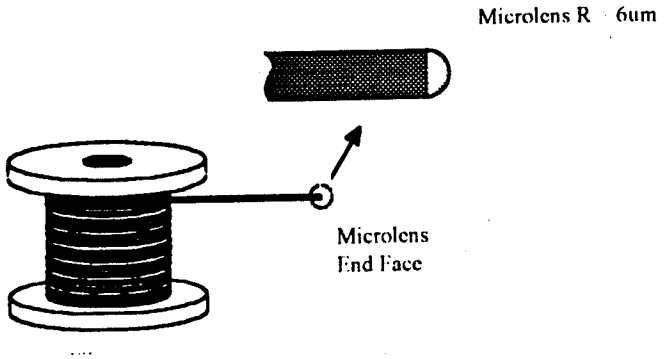

Figure 15 Microlens grown on fiber endface

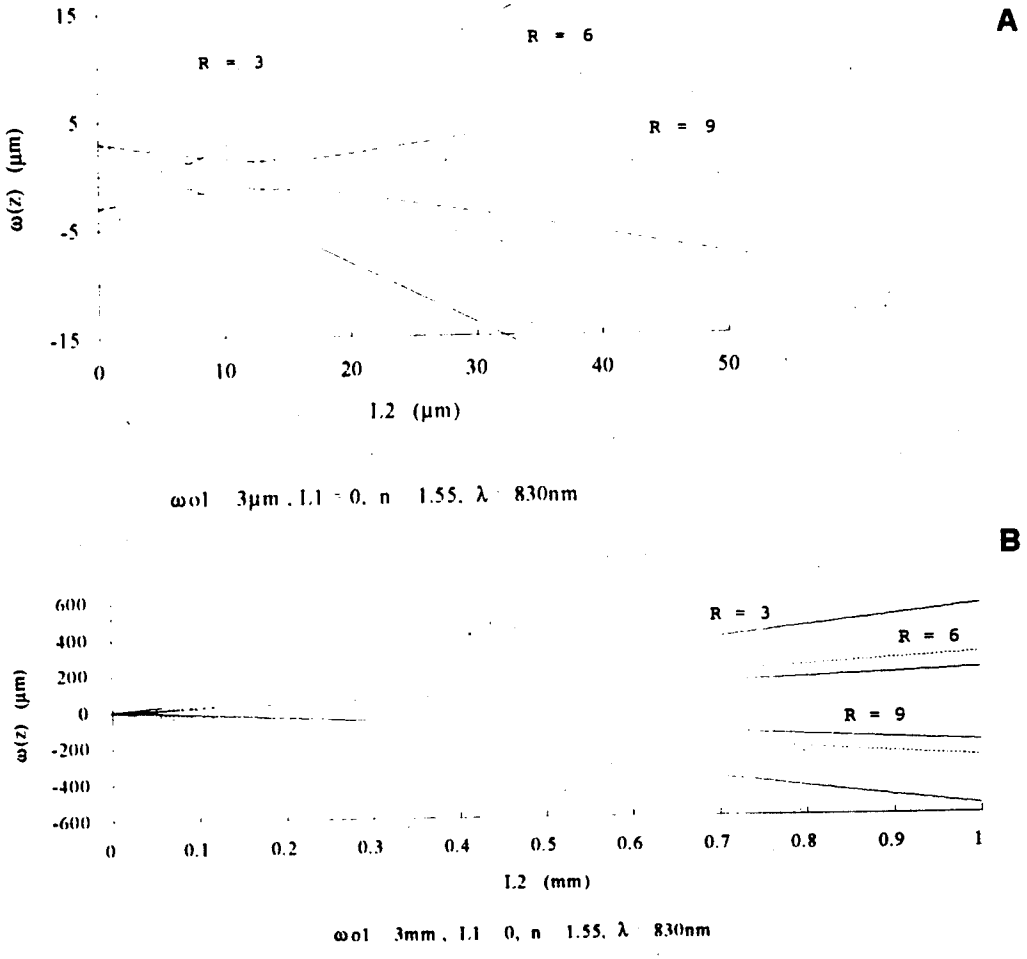

Figure 16 Beam Waist Divergence propagation from Microlens

5.5 Experiments Conducted

In this section, the observation matrix that was used to design the set of experiments, presented in this Thesis, is discussed. The experiments and the results are fully described in the referenced Chapters.

A pictorial description of the type of laser injection used throughout the Thesis is given Figure 17 Optical Signal Configurations used in the Experiments. Table 1 is a summary of the laser modulation experiments given in *Chapter 2*. The Square Wave @ 250MHz and the Low Frequency square, sine, triangle modulated waves are the types of signals that would be used in a digital application. Many slave lasers, modulated with these types of signals, could be locked to a sideband of the Master and then multiplexed onto a single fiber. The locked versions of these signals are much cleaner than the unlocked cases. The AM and FM experiments are used to compare the optical signal detected via customary means with the cases when they are injected into the MESFET amplifier.

Table 2 is a summary of the experiments in the oscillator section (*Chapter 7*). Table 3 is a summary of the experiments in the amplifier and standalone MESFET sections (*Chapter8 and Chapter 6*).

Table 1 Optical Configurations and Types of Modulation

Type of Modulation	Optical Signal Configuration				
	No Injection	Single Unlocked	Single Locked	R&S Unlocked	R&S Locked
RF					
1 GHz	√	√	√		
3 GHz	√	√	√	√	√
5 GHz	√	√	√	√	√
RF with Pulse Modulation (f_{RF} = 3 GHz)					
Pulse Source @ f_{pulse} = 2 MHz					
Square	√	√			
Sine	√	√			
Triangle	√	√			
1 ns Square Pulse	√	√			
Square Wave Train (f = 250 MHz)	√	√			
Amplitude Modulation (f =1 GHz, 50% AM)	√	√			
Frequency Modulation (f=1 GHz, 1 KHz dev)	√	√			
Low Frequency Modulation (f =20 MHz)					
Square	√	√	√	√	√
Sine	√	√	√	√	√
Triangle	√	√	√	√	√

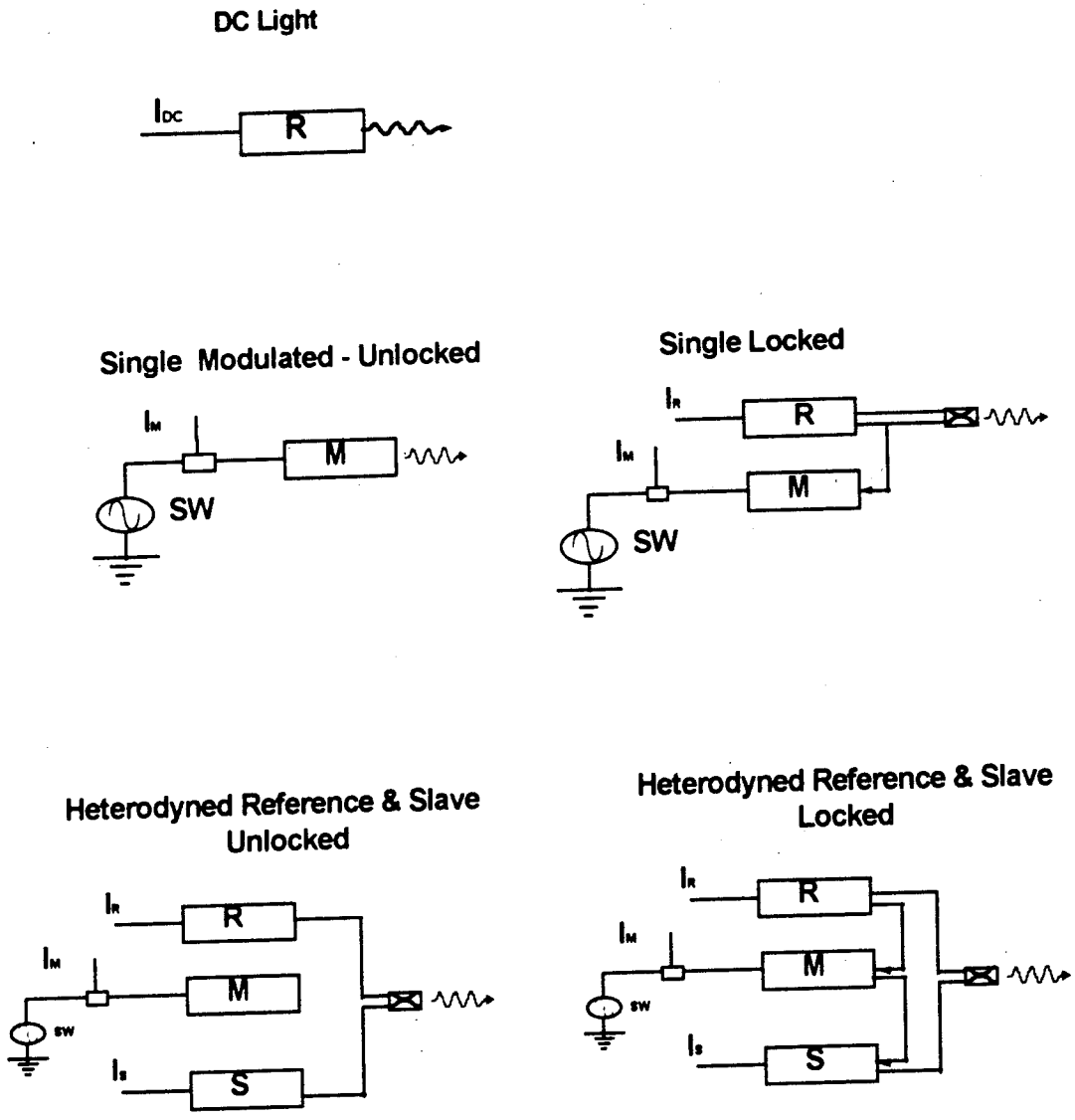

Figure 17 Optical Signal Configurations used in the Experiments

Table 2 Oscillator Experiments

Type of Injection	Oscillator Nominal Free Running Frequency					
	5 GHz			3 GHz		
	Spectrum	Phase Noise	I-V Curves	Spectrum	Phase Noise	I-V Curves
No Injection (dark)	√		√	√	√	√
Electrical				√		
DC Laser Light	√		√	√	√	
Single Modulated Laser light	√		√	√	√	
Single Laser locked to Reference	√		√	√	√	
Unlocked heterodyned beat (R&S)				√	√	
Locked heterodyned beat (R&S)				√	√	

Table 3 Amplifier & MESFET Experiments

Measurement	Device	
	Amplifier	MESFET
S-Parameters		
No Injection	√	√
DC Light	√	√
Single Unlocked (f = 2 GHz, 2.5 GHz)	√	√
R&S Locked (f = 2 GHz, 2.5 GHz)	√	√
Y-Parameters		
No Injection	√	√
Single Unlocked (f = 2.5 GHz)	√	√
Noise		
No Injection	√	√
Single Unlocked (f = 2.5 GHz)	√	√
ΔGain		
Electrical Signal on Gate (P_{RF}=-10 dBm, f_{RF}=2.0 GHz)		
No Injection	√	
DC Light	√	
Electrical Signal on Gate (P_{RF}=-30 dBm, f_{RF}=2.0 GHz)		
No Injection	√	
DC Light	√	
RF Modulated Signal Reception		
Single Unlocked	√ Signal level too low	√
R&S Locked		√
AM Signal Reception (f = 1 GHz, 50% AM)		
Electrical Signal	√	
Single Laser Unlocked	√	
FM Signal - Reception (f = 1 GHz, 1 KHz dev.)		
Electrical Signal	√	
Single Laser Unlocked	√	
Schotky Photo-Voltage Experiments		
(Derived from I- V Characteristics)		
No external Gate Resistior		Dark 5 DC Optical Power levels
R_{GATE_EXT} = 59.6 KΩ		Dark 5 DC Optical Power levels
R_{GATE_EXT} = 597 Ω		Dark 5 DC Optical Power levels

5.6 RF Considerations

Gigahertz frequencies were used to modulate the laser, were amplified by the amplifier, and were the center frequency of the designed oscillators, and required several RF issues to be addressed. Radiating RF fields were picked up by the microwave MESFET circuits and were disturbing the experimental results. It was impossible to distinguish between the actual optically induced effects in the MESFET and the fields that were picked up from radiation. Equipment grounding and shielding were necessary.

First, the laser cable radiated RF power because it had no shielding. Absorbers and metal plates were used to shield most of the emitted power. Section 5.3.3 RF Laser Cable Design has more details on this effort.

Next, the contact of the duroid ground planes to the jig ground had to be guaranteed. The jigs used flat head screws to press the copper plate in contact with the duroid ground plane (Figure 18 Circuit Jig). If the screws were tightened too much, the duroid would bow against the stress of the plate and the contacts and cause less ground plane connection. The best possible connections were made and then the plate was grounded to the same reference as the power supplies that provided the bias. In the oscillator case circuit, it was necessary to also use conductive epoxy between the plate and the ground plane because the circuit was large (2"x2").

Equipment grounds were checked and fixed where necessary for all RF equipment that includes HP Sweeper, HP RF Amplifier, MITEQ mixers. Also,

special cages were built and grounded to contain additional radiation from equipment.

Finally, while using an RF mixer to measure the oscillator's phase noise, there was leakage from one mixer arm into the other that distorted the results. Even though the specification of the mixer was within a few tenths of a decibel, the experiment proved higher leakage which could be due to the age of the mixer. To circumvent this problem, a different measurement procedure was used.

5.7 Microwave Circuit Fabrication

The microwave circuits designed were two 2"x2" oscillators, operating at 5 GHz and 3 GHz nominal frequency (5.7.1 Oscillator), a 1"x1" amplifier with response from 1 GHz to 3 GHz (5.7.2 Amplifier), and a standalone MESFET embedded in 50Ω microstrip lines (5.7.3Standalone MESFET Duroid Circuit).

The circuits were designed and built on microstrip in the Transmission Laboratory at the University of Colorado. Since the MESFET active region had to be exposed to inject the optical signal, a series of devices were built with unpackaged MESFET chips. The raw chips had to be wire bonded from their contacts to the duroid lines. The contacts required 1.0 mil and 0.75 mil gold wire. The wire bond machines at the University supported 1.5 mil wire which was twice the size needed. Dave Panenen at Ball Aerospace in Broomfield, Colorado, graciously helped with the use of Ball's bonder. After several design iterations and

experimental problems, the available raw chips were scarce, and it became inconvenient to go to Ball to re-fabricate the circuits. Packaged devices were available which were carefully dismantled to expose the active region. This art speeded up the fabrication processes significantly.

The microwave circuits, designed for this system, used the Fujitsu FSC11x GaAs MESFET. The MESFET gate is $.4x500\ \mu m$ with source to drain separation of $10\ \mu m$. To assure the focusing calculations were correct the beam size was visually compared to the size of the gate electrode which is $20x70\mu m$. A high power microscope photo with calibrated scale was taken to measure the size of the active region of the actual devices being used in the experiments.

The oscillator is designed on a microstrip (Duroid, ε=2.2) subcircuit using PUFF a microwave CAD program. The gate and drain bias supplies are connected with a bias tee. When optically injected, the MESFET impedance changes in the same way that the impedance changes with bias. It is possible that the originally designed impedance match circuit will not be impedance matched when the MESFET is optically injected. An external stub tuner should be used to impedance match the original microwave circuit when injected. However, tuners at the frequency of interest were not available during the experiments. The impedance mismatch is discussed during the interpretation of the results and did not change the over all operation of the circuit (i.e., the oscillator continued to oscillate)..The circuit is mounted in a microwave test jig (Figure 18) which works fine but does present

slight problems establishing a good ground plane and providing a constant temperature via heat sink.

The connections from the metal plate to the duroid ground plane are established by pressing a copper plate with flat head screws against the bottom of the duroid circuit (i.e., ground plane) and abutting the gold RF signal connectors to the top of the circuit (i.e., signal lines). If the screws were tightened too much, the duroid would bow against the stress of the plate and the contacts and cause less ground plane connection. The ground plane connections for the 1"x1" amplifier and standalone MESFET were not difficult to achieve, but the larger 2"x2" oscillator needed to be epoxied to the copper plate to maintain an adequate ground. Ground planes and RF considerations are discussed more fully in 5.6 RF Considerations.

The details of each of the circuits are presented in the following sections.

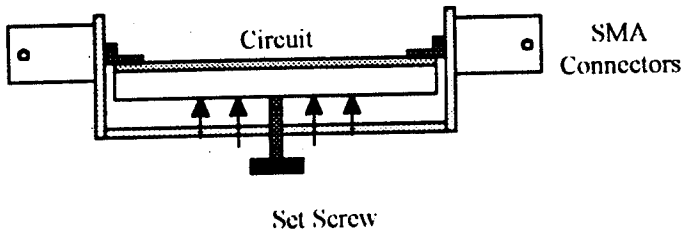

Figure 18 Circuit Jig

5.7.1 Oscillator Design

Two oscillator designs were needed to provide frequencies at 5 GHz and 3 GHz which were dictated by the frequency response of the semiconductor laser diodes.

The initial sets of experiments were conducted with Hitachi lasers which had a relaxation oscillation just beyond 5 GHz while the majority of the results were completed with Mitsubishi lasers which had a measured relaxation at 4.2 GHz. Also, diagnostic equipment frequency limits existed. The Newport 877 avalanche photodiode, which was used to detect the heterodyned beat on the spectrum analyzer, has a unity gain frequency response to 2ghz, a -8db (0.16 mW) response at 3 GHz, and virtually no response at 5 GHz. Although the ARS-5 detector, used to detect the output of the Fabry Perot, has fast enough response to be used with the 5 GHz signals, it was an experimental disaster to move the Fabry Perot each time it was necessary to view the beat spectrum, and it was also necessary to view both the interferometer output simultaneously with the beat spectrum to assure a stable laser lock was established.

The oscillators were designed with the aid of a microwave circuit design program called PUFF. Figure 19 Oscillator Schematic shows the circuit layout and its connections to diagnostic equipment. Bias is provided on the gate and drain, and the source is terminated into a 50Ω load to ground. The impedances and resultant S-parameters are given for both oscillators in Parameters.

Bias T's are used on the drain to measure oscillator output characteristics and on the gate to superimpose the electrical RF signal during the electrical injection experiments. The output of the drain is fed into the spectrum analyzer, and the drain and gate bias lines were connected to multi-meters to read current and voltage. This is depicted in Figure 19 Oscillator Schematic.

Table 4 Oscillator Design Parameters

	Oscillator Nominal (design) Frequency	
	3 GHz	**5 GHz**
Circuit Impedance		
Z_0	50Ω	50Ω
Z_{G1}	50Ω, 78^{Eo}, 15.749mm	50Ω, 60^{Eo}
Z_{G2}	50Ω, 75^{Eo}, 15.143mm	50Ω, 60^{Eo}
Z_D	50Ω	50Ω
Z_S	50Ω, 80^{Eo}, 16.153mm	50Ω, 60^{Eo}
S-Paramters @ f		
S_{gg}	9.58 dB, -91.6^{Eo}	
S_{dd}	12.9 dB, -57.5^{Eo}	1.6 dB, -38.6^{Eo}
S_{ss}	-10.69 dB, -105.0^{Eo}	-8.34 dB, -170.6^{Eo}
S_{ds}	13.94 dB, -114.6^{Eo}	
S_{gs}	-0.82 dB, -98.9^{Eo}	
S_{sg}	9.93 dB, 177.0^{Eo}	
S_{dg}	25.16 dB, 58.0^{Eo}	
S_{gd}	-2.33 dB, -44.0^{Eo}	
S_{sd}	-3.72 dB, 50.1^{Eo}	

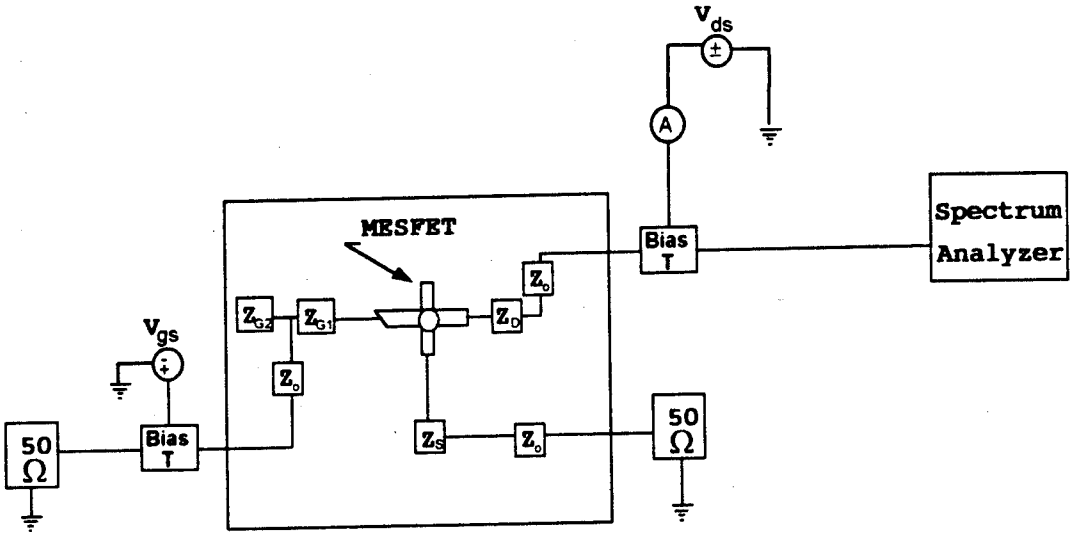

Figure 19 Oscillator Schematic

5.7.2 Amplifier Design

The amplifier was designed to work at *2-3 GHz* but also had some gain at 1 GHz. The original reason for a 3 GHz amplifier was based on the laser locking system.. We wanted to put the Master laser into relaxation oscillation and lock the Slave to various sidebands. The relaxation frequency was 5GHz for the Hitachi and 3GHz for the Mitsubishi. However, the amplifier modulation experiments were more interesting because we already had proved subharmonic laser locking independently of the MESFET experiments and because it was no consequence if the amplifier was injected with a subharmonic optical signal or the first sideband locked optical signal. The modulation experiments required the use of a FLUKE Synthesized Sweeper which provides excellent AM and FM signals up to 1 GHz. Also, to get at the base circuit responses under illumination, we needed to get

S-Parameter measurements for the amplifier and the standalone MESFET. The HP8702B has a frequency response to 3 GHz . Since the oscillator frequency was out of range of the HP8702B Network Analyzer, it became an important constraint in the amplifier design.

The amplifier was designed with the aid of a microwave circuit design program called PUFF. Bias is provided on the gate and drain, and the source is grounded. The two source leads are connected to ground by drilling a hole through the duroid substrate and soldering a short lead to sources and to the ground plane. Figure 20 Amplifier Schematic shows the circuit layout and its connections to diagnostic equipment.

Bias T's are used on the drain to measure amplifier output characteristics and on the gate to superimpose the electrical RF signal during the baseline amplifier experiments. The output of the drain is fed into the spectrum analyzer, and the drain and gate bias lines were connected to multi-meters to read current and voltage.

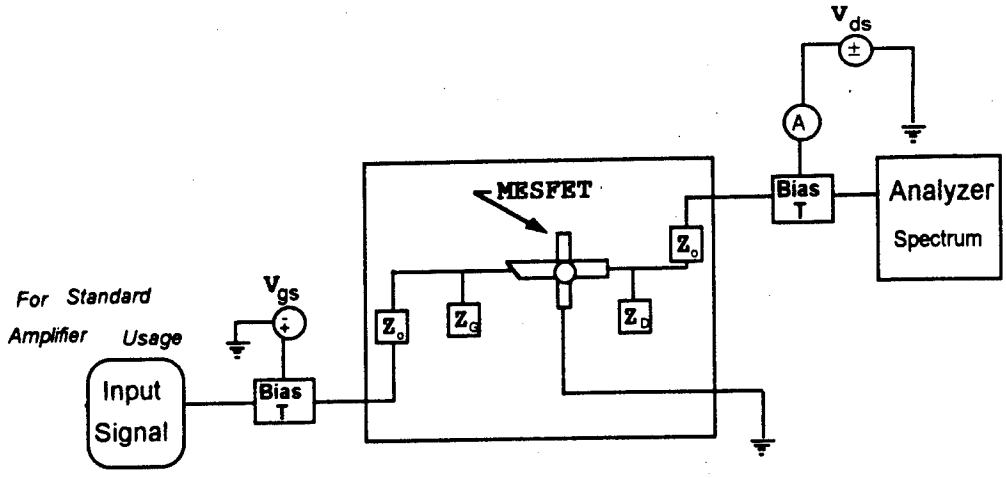

Figure 20 Amplifier Schematic

5.7.3 Standalone MESFET Duroid Circuit

To understand the effect of light injection on circuit model parameters, a single MESFET in a common source (CS) configuration was used with the gate and drain simply connected to 50Ω microstrip lines and the source grounded as shown in Figure 21 DC MESFET Schematic. The output of the drain is fed into the spectrum analyzer, and the drain and gate bias lines were connected to multi-meters to read current and voltage.

Because of the characteristics of the Fujitsu FSC11x MESFET, this configuration had more gain at 1 GHz than the amplifier since the amplifier was designed for maximum gain at 3GHz. These results shown in *Chapter 8* along with the amplifier results.

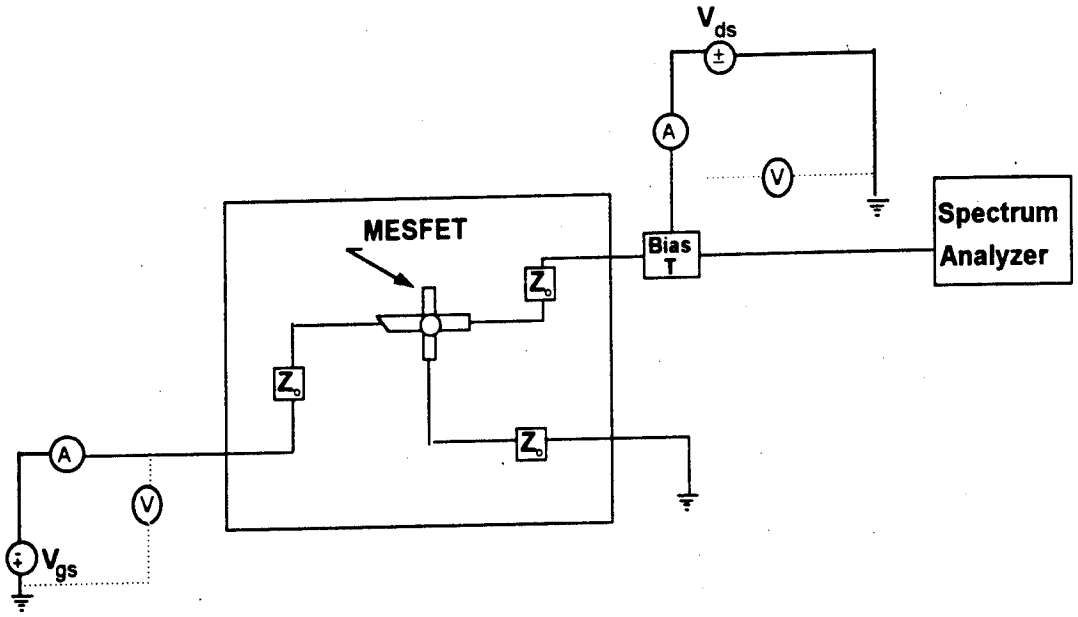

Figure 21 DC MESFET Schematic

5.8 Conclusion

The design of the experimental systems for both laser and MESFET injection was a significant portion of the effort necessary to achieve the results described in this Thesis. The beam focusing system in the MESFET injection path was used to obtain the smallest optical beam and still maintain the ability to view the device via CCD camera. The total optical power reaching the GaAs layer of the MESFET is 2.2-3.8% of the original power. At a depth of GaAs of 0.5μm, the total optical power absorbed by the GaAs is 1.3-2.3% of the original power at the fiber output. Microwave circuit design and fabrication was arelatively simple aspect of this project, but removing the MESFET lids was certainly an art. Improvements in

the original laser injection system included power optimization, thermal fixes, polarization control, optical isolation and RF laser cable design. Crucial engineering solutions to less than exciting but formidable obstacles were used to overcome RF considerations, thermal stability problems, wavelength mode instability, and alignment concerns.

5.9 Supplement

The following are the substitutions made in the reflectance and transmitance equations in 5.4.3 Multilayer Analysis:

$A \quad n1 \cdot q1 \quad n2 \cdot q2 + k2 \cdot q4$ $\qquad$ $D \quad n1 \cdot q3 + n2 \cdot q4 + k2 \cdot q2$

$B \quad n1 \cdot q3 \quad n2 \cdot q4 \quad k2 \cdot q2$ $\qquad$ $E \quad 4 \cdot n1 \cdot n2 \cdot q5 - 4 \cdot n1 \cdot k2 \cdot q6$

$C \quad n1 \cdot q1 + n2 \cdot q2 \quad k2 \cdot q4$ $\qquad$ $F \quad -4 \cdot n1 \cdot n2 \cdot q6 + 4 \cdot n1 \cdot k2 \cdot q5$

$$q1 \quad \left| n2 + n3 \cdot (n2 \quad n3) \cdot \cos(\phi) \cdot e^{\alpha 2 \cdot x} \right| \quad (k2 \quad k3) \cdot \sin(\phi) \cdot e^{-\alpha 2 \cdot x}$$

$$q2 \quad n2 + n3 \quad (n2 \quad n3) \cdot \cos(\phi) \cdot e^{\alpha 2 \cdot x} + (k2 \quad k3) \cdot \sin(\phi) \cdot e^{-\alpha 2 \cdot x}$$

$$q3 \quad k2 \cdot k3 + (k2 \quad k3) \cdot \cos(\phi) \cdot e^{\alpha 2 \cdot x} + (n2 \quad n3) \cdot \sin(\phi) \cdot e^{-\alpha 2 \cdot x}$$

$$q4 \quad k2 + k3 \quad (k2 \quad k3) \cdot \cos(\phi) \cdot e^{\alpha 2 \cdot x} \quad (n2 \quad n3) \cdot \sin(\phi) \cdot e^{-\alpha 2 \cdot x}$$

$$q5 \quad \cos(k0 \cdot (n2 \quad n3) \cdot x) \cdot e^{(k0 \cdot (k2 \quad k3) \cdot x)}$$

$$q6 \quad \sin(k0 \cdot (n2 \quad n3) \cdot x) \cdot e^{(k0 \cdot (k2 \quad k3) \cdot x)}$$

$$\alpha 2 \quad 2 \cdot k0 \cdot k2$$

$$\phi \quad 2 \cdot k0 \cdot n2 \cdot x$$

5.10 References - Chapter 5

[1] Marc R. Surette, "Noise Properties of Injection Locked Semiconductor Lasers: Application to Optically Driven Phased Array Antennas", Ph.D. Thesis, University of Colorado, 1991.

[2] Alan Mickelson, Physical Optics, Van Norstrand, N.Y., 1992.

[3] Max Born and Emil Wolf, Principles of Optics, Pergamon Press, 1989, pp.34-70, pp.612-613.

CHAPTER 6

DC MESFET INJECTION

6.1 Introduction

In this Chapter, optically induced effects in semiconductors are calculated and experimental data is presented. This Chapter is largely dependent on the ideas presented in Chapter 3. Based on the results of Chapter 3, the major optical effect that can be measured at the device terminal is a carrier induced photo-voltage V_{ph}. This voltage is added to the gate bias to model the DC optical effects in the MESFET. The same photo-generated carriers are modeled as an RF modulated source added to a SPICE model of a FET based oscillator in Chapter 7 and to a FET based amplifier in Chapter 8.

A large signal model is used to analyze the optically injected MESFET circuits used in this Thesis. The model is based on the Statz-Raytheon large signal model. A common source MESFET was measured for its DC operating characteristics as well as its S-Parameters. These measurements are shown to fit well with the approximate Statz model derived in this Thesis. The effect of carrier density changes on the parasitic resistances is shown to be a decrease of 10-15% when illuminated.

6.2 Small Signal Model

The dark and illuminated drain current may be calculated using an existing MESFET small signal model by Pucel, et.al[1]. The photo-effects are modeled by superimposing V_{ph} onto the gate bias V_{gs} in all the circuit element equations. In the next section, a large signal approach is considered because in Chapters 7 and 8 the MESFET is used in oscillator and amplifier circuits. It is the use of the MESFET as a circuit element rather than a standalone element that this Thesis is concerned.

6.3 Optically Induced Effects On Circuit Parameters

In this section the photo-effects on the MESFET circuit parameters are discussed. Based on the results of Chapter 3, the major optical effect that can be measured at the device terminal is a carrier induced photo-voltage V_{ph}. This voltage is added to the gate bias to model the DC optical effects in the MESFET. The same photo-generated carriers are modeled as an RF modulated source added to a SPICE model of an FET based oscillator in Chapter 7 and to a FET based amplifier in Chapter 8. In this Chapter, a circuit model approach is taken to model the illuminated MESFET (Figure 1). Measurements of the DC MESFET S-parameters are presented.

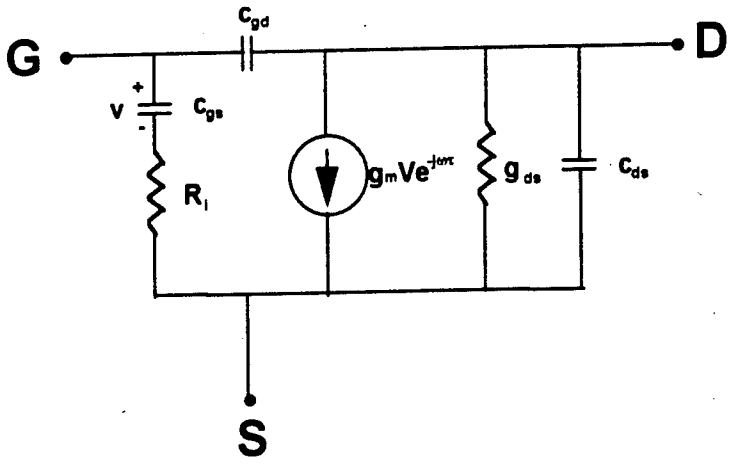

Figure 1 MESFET Circuit Model

6.3.1 Large Signal Characteristics

The large signal Statz Raytheon model describes the drain source current as

$$I_{ds} = I_{dss}\,\frac{\beta(V_{gs}-V_{to})^2}{1+\sigma(V_{gs}-V_{to})}\,(1+\kappa V_{ds})\,\tanh(\alpha V_{ds})$$

The model parameters have been found to be α=2.5, κ=0.25, β=1.25, and σ=0.2. V_{TO} is the pinchoff potential equal to 1v. The transconductance is found from the derivative of Ids with respect to V_{gs} and holding V_{ds} a constant:

$$g_m = \frac{\partial I_{ds}}{\partial V_{gs}} = I_{dss}\,\frac{\beta(V_{gs}-V_{to})(2+\sigma(V_{gs}-V_{to}))}{\left(1+\sigma(V_{gs}-V_{to})\right)^2}\,(1+\kappa V_{ds})\,\tanh(\alpha V_{ds})$$

It is our goal to approximate the Statz model by a third order polynomial in order to isolate the optically induced effects:

$$I_{ds\ m} = I_{dss}\left(s_0 + s_1 V_{gs} + s_2 V_{gs}^{\ 2} + s_3 V_{gs}^{\ 3}\right)$$

$$g_{m\ m} = I_{dss}\left(s_1 + 2\,s_2 V_{gs} + 3\,s_3 V_{gs}^2\right)$$

Expanding via series expansion to the third order, the coefficients of the Ids and gm equation are as follows:

$$s_0 = \frac{\beta V_{to}^2}{(1-\sigma\ V_{to})}\,(1+\kappa V_{ds})\ \tanh(\alpha V_{ds})$$

$$s_1 = \frac{-\beta V_{to}}{(1-\sigma V_{to})}\left(2+\frac{\sigma V_{to}}{(1-\sigma V_{to})}\right)(1+\kappa V_{ds})\ \tanh(\alpha V_{ds})$$

$$s_2 = \frac{\beta}{(1-\sigma V_{to})}\left(1+\frac{\sigma V_{to}(2-\sigma\,\mathrm{Vto})}{(1-\sigma\ V_{to})^2}\right)(1+\kappa V_{ds})\ \tanh(\alpha V_{ds})$$

$$s_3 = \frac{-\beta\sigma}{(1-\sigma\ V_{to})^4}\,(1+\kappa V_{ds})\ \tanh(\alpha V_{ds})$$

The coefficients are graphed in Figure 3 and Figure 4.

In Chapter 3, it was shown that the Schottky barrier is lowered by a potential equal to the photovoltage V_{ph}. This potential is a positive number. The power supply setting of the gate bias V_{gs} is a negative number. The superposition of V_{ph} onto V_{gs} creates an intrinsic bias level that is more forward biased than the power supply setting. Also, in Chapter 3, it was shown that the gate circuitry may cause additional voltage drops by the amount across an existing resistance V_{Rg}. To consider either case our model can be written with a superimposed voltage V in the following manner:

$$I_{ds}(v_{gs}+V) = \begin{bmatrix} s_0 + s_1 V + s_2 V^2 + s_3 V^3 \\ s_1 + 2s_2 V + 3s_3 V^2 \\ s_2 + 3s_3 V \\ s_3 \end{bmatrix} \begin{bmatrix} 1 \\ v_{gs} \\ v_{gs}^2 \\ v_{gs}^3 \end{bmatrix} I_{dss}$$

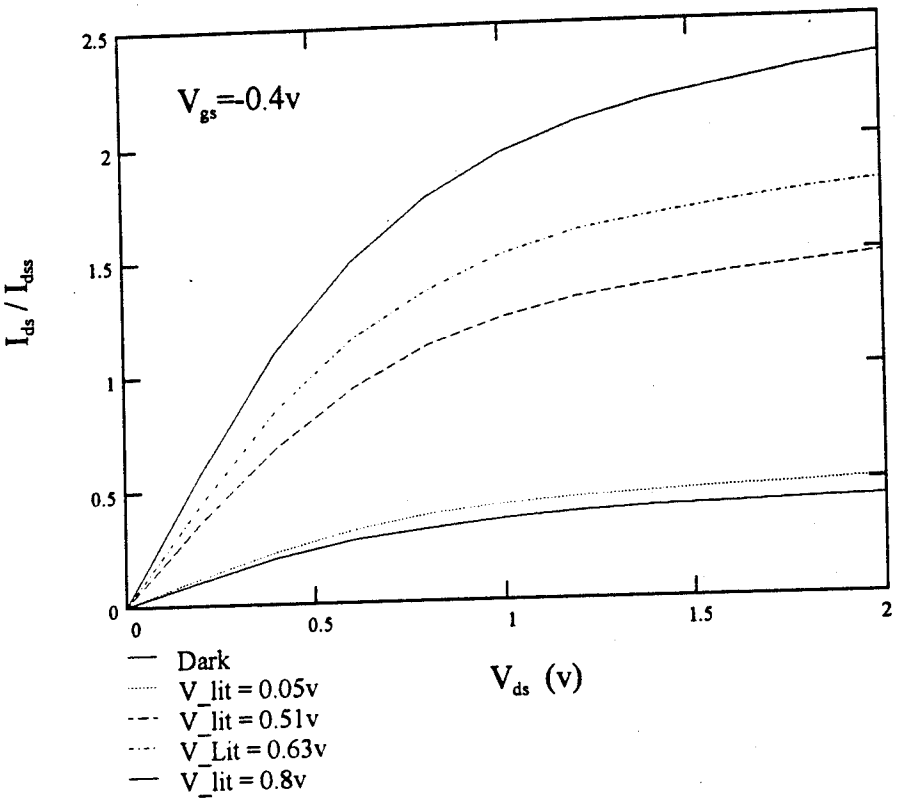

Figure 2 Photo-induced Changes in I_{ds} vs. V_{ds}

$$g_m(v_{gs}+V) = \begin{bmatrix} s_1 + 2s_2V + 3s_3V^2 \\ 2(s_2 + 3s_3V) \\ 3s_3 \end{bmatrix} \begin{bmatrix} 1 \\ v_{gs} \\ v_{gs}^2 \end{bmatrix} I_{dss}$$

The coefficients of the $I_{ds}(v_{gs}+V)$ matrix are graphed in Figure 3 and Figure 4 for V equal to 0v, $\pm$0.2v, $\pm$0.4v.

I_{ds} is given below as an expansion on V_{ds} to calculate the drain conductance g_d. The hyperbolic tangent provides the necessary saturation in the original Statz

equation, and in the following expansion it was necessary to go to the fourth order to get reasonable results.

$$I_{ds} \quad \frac{\beta \cdot (V_{gs} - V_{to})^2}{1 + b \cdot (V_{gs} - V_{to})} \cdot \begin{vmatrix} 0 & 1 \\ \alpha & Vds \\ \lambda \cdot \alpha & Vds^2 \\ \frac{1}{3} \cdot \alpha^3 & Vds^3 \\ \frac{1}{3} \cdot \lambda \cdot \alpha^3 & Vds^4 \end{vmatrix}$$

Changes in I_{ds} are delayed by the electron transit time (τ = channel length/drift velocity when changes in the gate bias voltage V_{gs} take place. Curtice showed a method for modeling the time delay (10ps) in circuit analyis programs[2]:

$$I_{ds}[V_{gs}(t-\tau), V_{ds}(t)] \approx I_{ds}[V_{gs}, V_{ds}] - \tau \frac{\partial I_{ds}}{\partial V_{gs}} \frac{dV_{gs}}{dt}$$

The second term is the first term of the expansion of $I_{ds}(t-\tau)$.

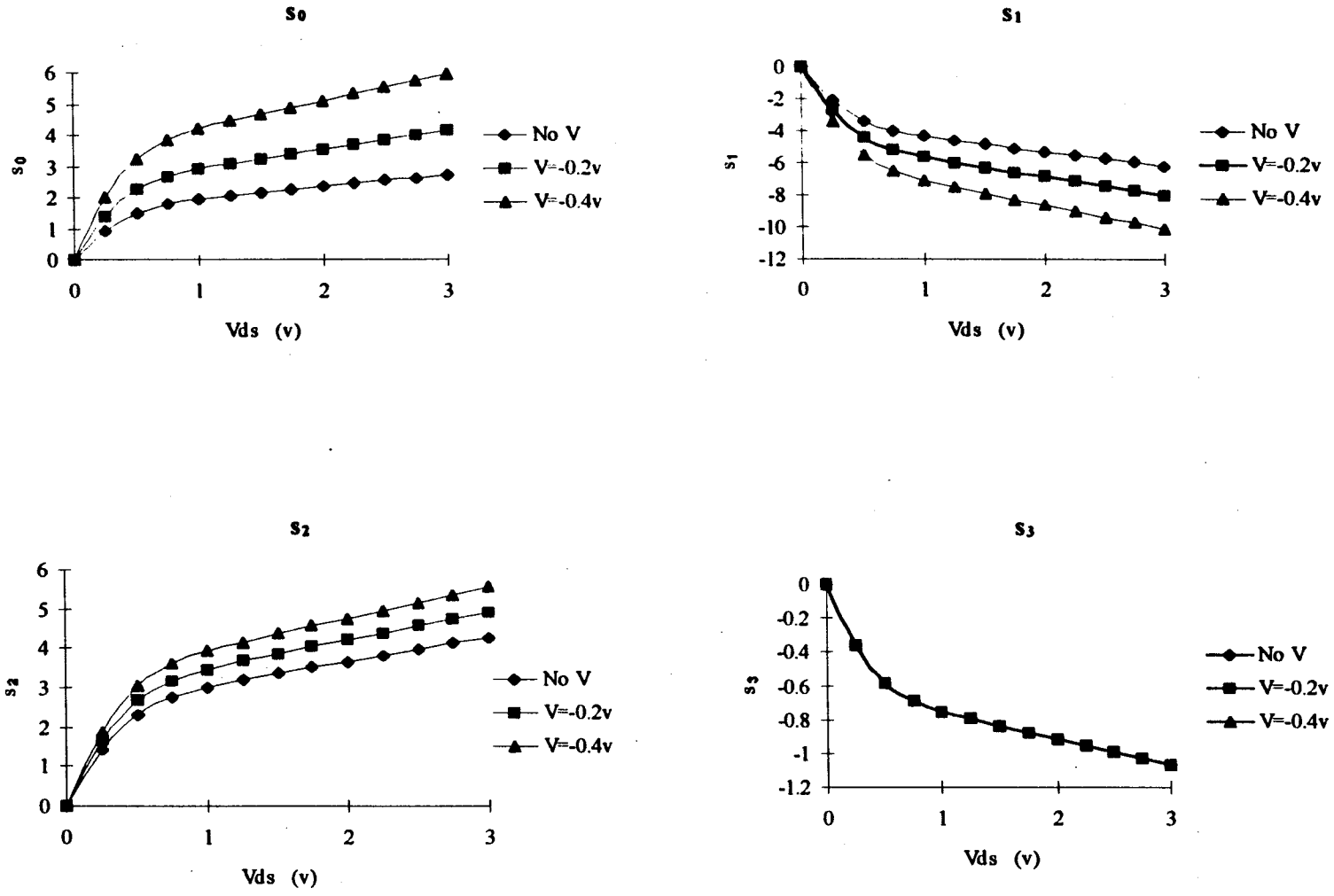

Figure 3 Model Coefficients for negative V

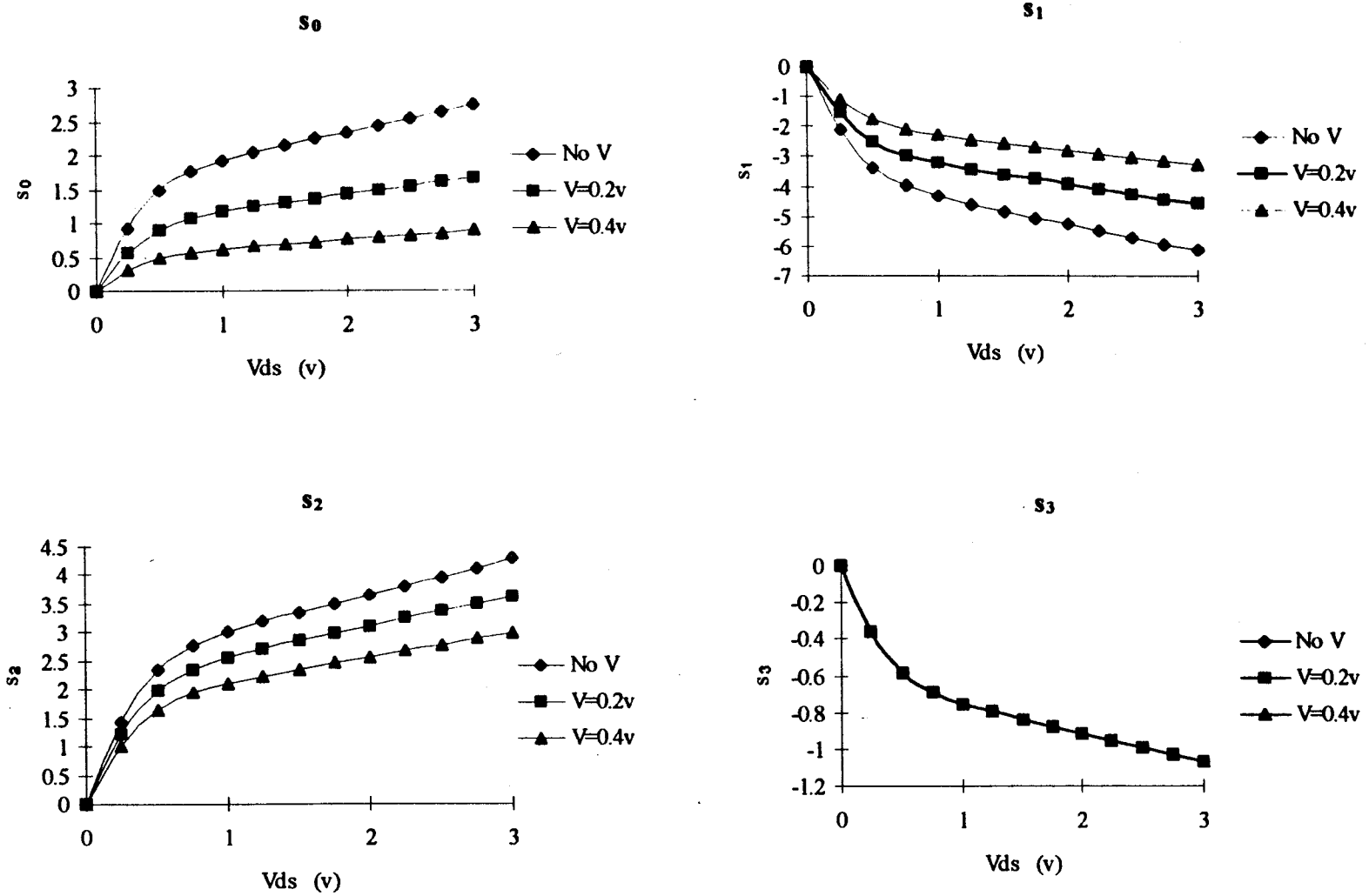

Figure 4 Model Coefficients for positive V

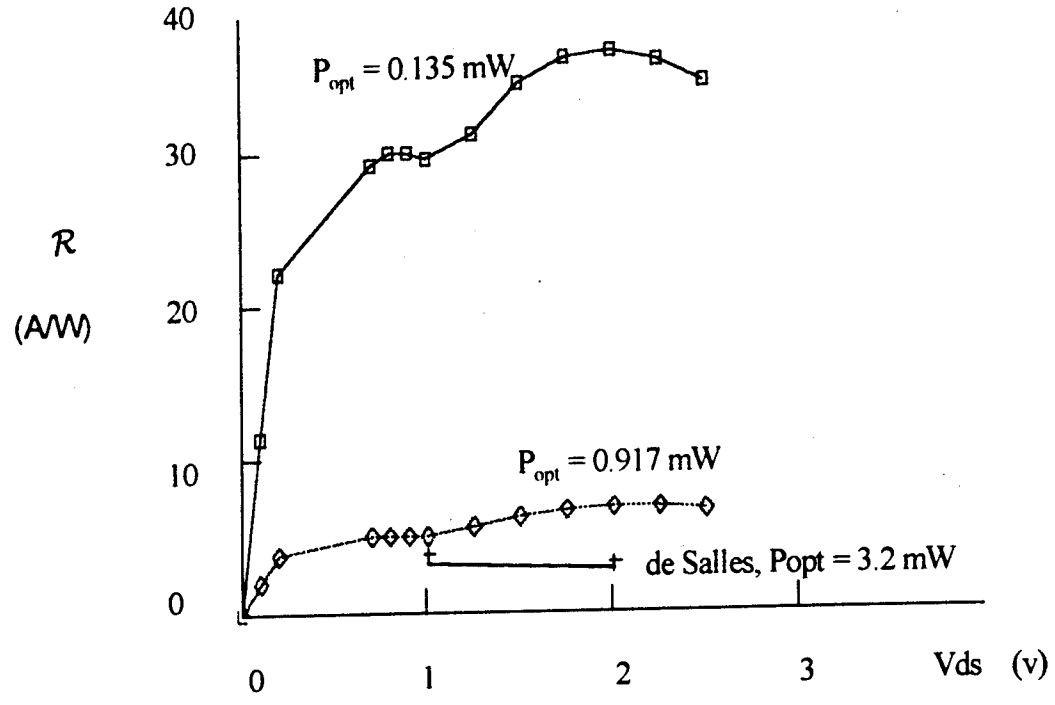

Figure 5 Responsivity vs. V_{ds}

In Figure 5, the responsivity in Amps per Watt of the MESFET has been calculated from measured values of the drain current for optical power of 0.135 mW and 0.917 mW. Also, two points have are shown on the graph from the DeSalles work for an optical power of 3.2 mW. In comparison, photodiode (p-i-n) detector at wavelength of 1.3μm may have a responsivity of 0.56 A/W. The MESFET is as much as 54 times better than the p-i-n detector. This is due to the optical gain effect described in detail in Chapter 3.5. The optical gain is analogous to the gain mechanism in an avalanche photodiode.

Figure 6 is the modeled drain current normalized by I_{dss} for several values of photovoltage (shown in the legend as V_{lit}). Figure 7 and Figure 8 show the device transconductance g_m versus V_{ds} for V_{gs} =-0.4v and versus V_{gs} for V_{ds}=1.5v respectively. Figure 9 is the drain conductance g_d calculated from derivative of I_{ds} with respect to V_{ds} and with V_{gs} fixed at -0.4v.

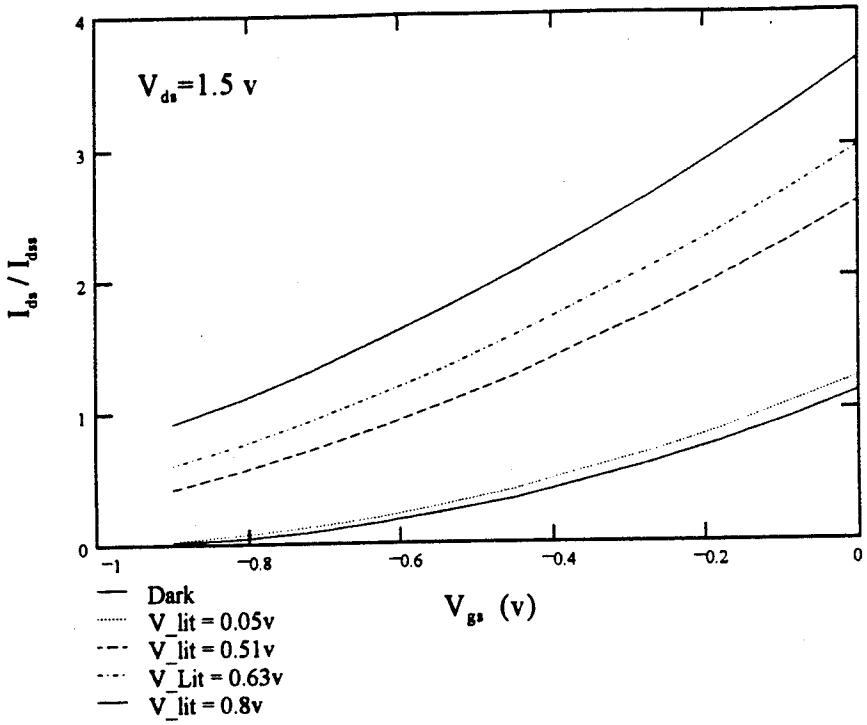

Figure 6 Photo-induced Changes in I_{ds} vs. V_{gs}

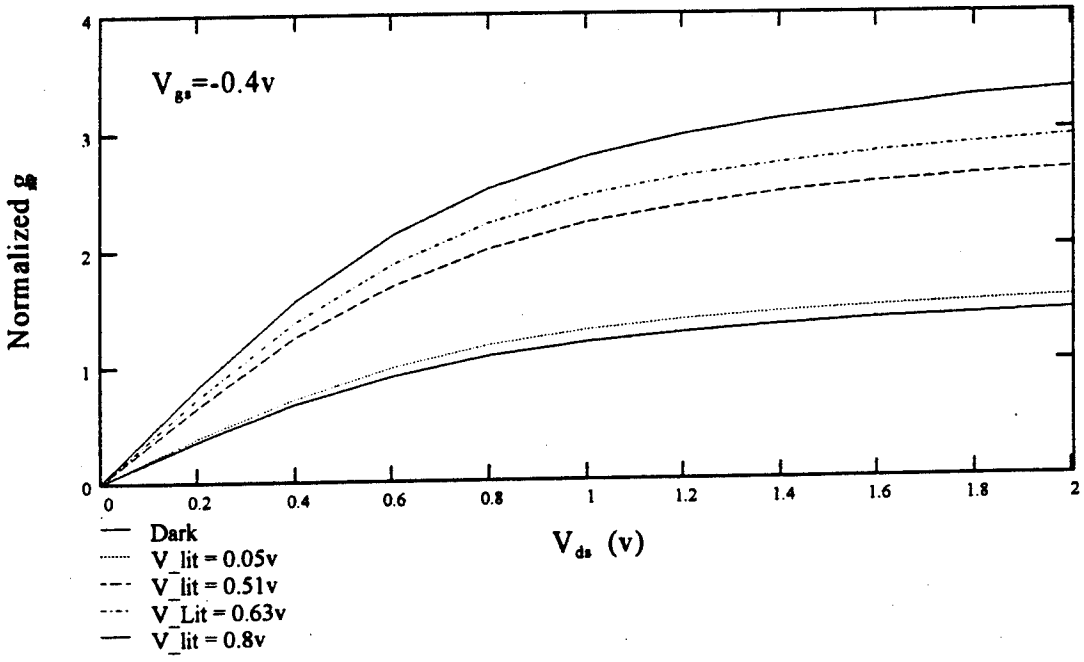

Figure 7 Transconductance Variations vs. V_{ds}

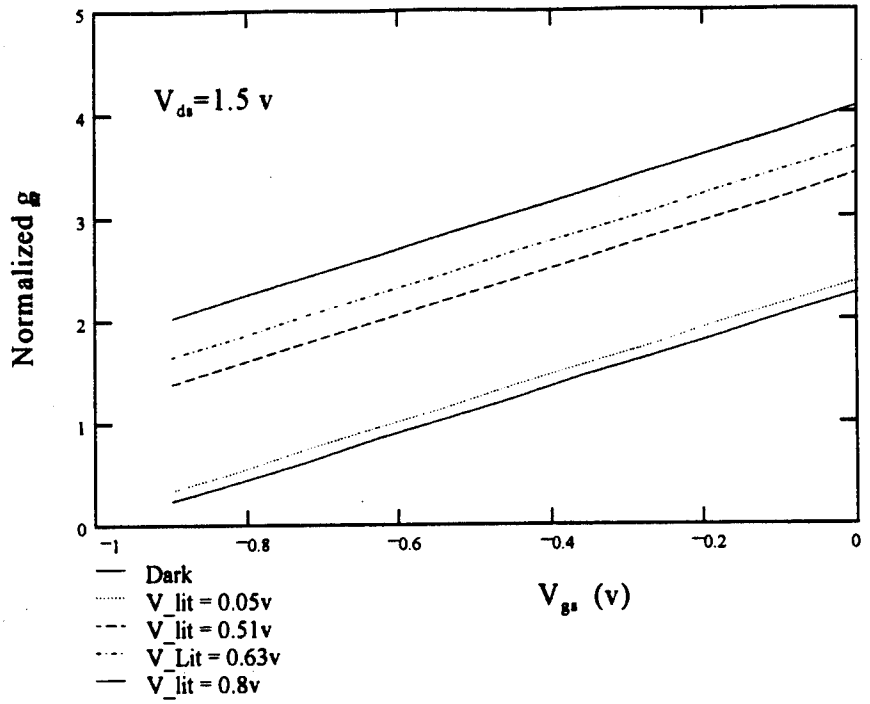

Figure 8 Transconductance Increases with Optical Power vs. V_{gs}

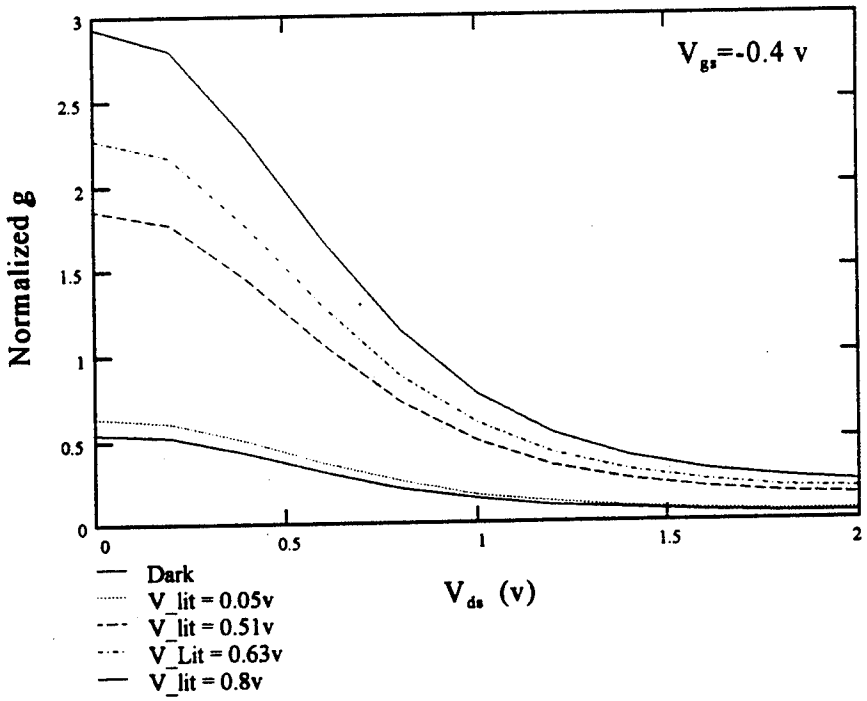

Figure 9 Optically Induced Changes in Drain Conductance vs. V_{ds}

6.3.2 S-Parameter Measurements - Circuit parameter Extraction

In this Section, a method for extracting circuit parameters from S-parameter measurements is presented. The S-parameter measurements were measured at one bias point and for a range of RF frequencies from 1.5 GHz to 2.9 GHz. Using an HP8702 network analyzer, the MESFET S-parameters have been measured with the source grounded and both the gate and drain looking into 50Ω loads.

The first step in converting from S parameters to circuit elements is to calculate the admittance matrix [Y] as follows:

$$[Z] = ([U]-[S])^{-1}([U]+[S]) \qquad (6\text{-}4)$$
$$[Y] = [Z]^{-1}$$

Therefore, [Y] is written in terms of the S parameters:

$$Y = \begin{bmatrix} \dfrac{(1-S_{11})(1+S_{22})-S_{12}S_{21}}{(1+S_{11})(1+S_{22})-S_{12}S_{21}} & \dfrac{-2S_{12}}{(1+S_{11})(1+S_{22})-S_{12}S_{21}} \\ \dfrac{-2S_{21}}{(1+S_{11})(1+S_{22})-S_{12}S_{21}} & \dfrac{(1+S_{11})(1-S_{22})-S_{12}S_{21}}{(1+S_{11})(1+S_{22})-S_{12}S_{21}} \end{bmatrix}$$

Sometimes the S12 value is very small and can be set to zero. This case is discussed in Chapter 8 because the unilateral assumption is valid for the amplifier circuit considered in that chapter. Also, de-embedding inductance values requires an iteration procedure which is not complicated. Any number of texts describe the de-embedding process[2].

From the MESFET circuit the Y elements of the matrix are found to be as follows:

$$[Y]=\begin{bmatrix} \dfrac{j\omega Cgs}{1+j\omega R_i Cgs}+j\omega Cgd & -j\omega Cgd \\ \dfrac{g_m e^{-j\omega\tau}}{1+j\omega R_i Cgs}-j\omega Cgd & \dfrac{1}{rds}+j\omega(Cds+Cgd) \end{bmatrix}$$

Next, the real and imaginary parts of [Y] are separated, and then the circuit elements can be extracted:

$$Re\{Y\}=\begin{bmatrix} \dfrac{R_i\omega^2 Cgs^2}{1+(\omega R_i Cgs)^2} & 0 \\ \dfrac{g_m\cos(\omega\tau)}{1+(\omega R_i Cgs)^2} & \dfrac{1}{rds} \end{bmatrix}$$

$$Im\{Y\}=\begin{bmatrix} \dfrac{\omega Cgs}{1+(\omega R_i Cgs)^2}+\omega Cgd & -\omega Cgd \\ \dfrac{g_m\sin(\omega\tau)-\omega R_i Cgs}{1+(\omega R_i Cgs)^2}-\omega Cgd & \omega(Cds+Cgd) \end{bmatrix}$$

The circuit elements are as follows:

$$Cgd=-\frac{Im\{Y12\}}{\omega}$$

$$Cds=\frac{Im\{Y22\}}{\omega}-Cgd$$

$$Cgs=\frac{Im\{Y11\}}{\omega}-Cgd$$

$$\frac{1}{rds}=Re\{Y22\}$$

$$R_i=\frac{1-\sqrt{1-\dfrac{4Re^2\{Y11\}}{(\omega Cgs)^2}}}{2Re\{Y11\}}\approx\frac{Re\{Y11\}}{(\omega Cgs)^2}$$

$$g_m e^{-j\omega\tau}=g_{mr}+j\,g_{mi}$$

$$g_{mr} = \mathrm{Re}\{Y21\} - \mathrm{Im}\{Y21\}R_i C_{gs}\omega - \omega^2 R_i C_{gs} C_{gd}$$

$$g_{mi} = \mathrm{Re}\{Y21\}R_i C_{gs}\omega + \mathrm{Im}\{Y21\} + \omega C_{gd}$$

The value of τ can be extracted for all frequencies with the following equation

$$\tau = \frac{-1}{\omega}\tan^{-1}\left(\frac{g_{mi}}{g_{mr}}\right)$$

At frequencies less than or equal to 10-12 GHz (approximately $(\omega C g R_i)^2 << 1$) τ, can be approximated as follows because the Re{Y21} is the only significant term[3]:

$$\tau \approx \left(\frac{-\mathrm{Im}\{Y21\}}{\omega} + g_m R_i C_{gs} + C_{gd}\right)\frac{1}{g_m}$$

It should be noted that τ is a term that becomes increasingly significant with higher frequencies.

The angle of the S-parameters does not change when light is injected (Figure 10). In Figure 11 the heterodyned locked laser beat at 2.0 GHz was injected into the MESFET active area. In Figure 12 and Figure 13 a single modulated laser is injected at frequency of 2.5 GHz and 2.0 GHz respectively. The only notable difference between the heterodyne beat injection (Figure 11) versus the single modulated laser injection (Figure 13) is that the optical effect is lower when the heterodyne signal is injected because the beat has less optical power. The effect of the optical power level is shown in Figure 14. Also, the photo-effect is a DC effect in the common source circuit because the external circuit cannot support oscillation. There is no change based on the frequency injected.

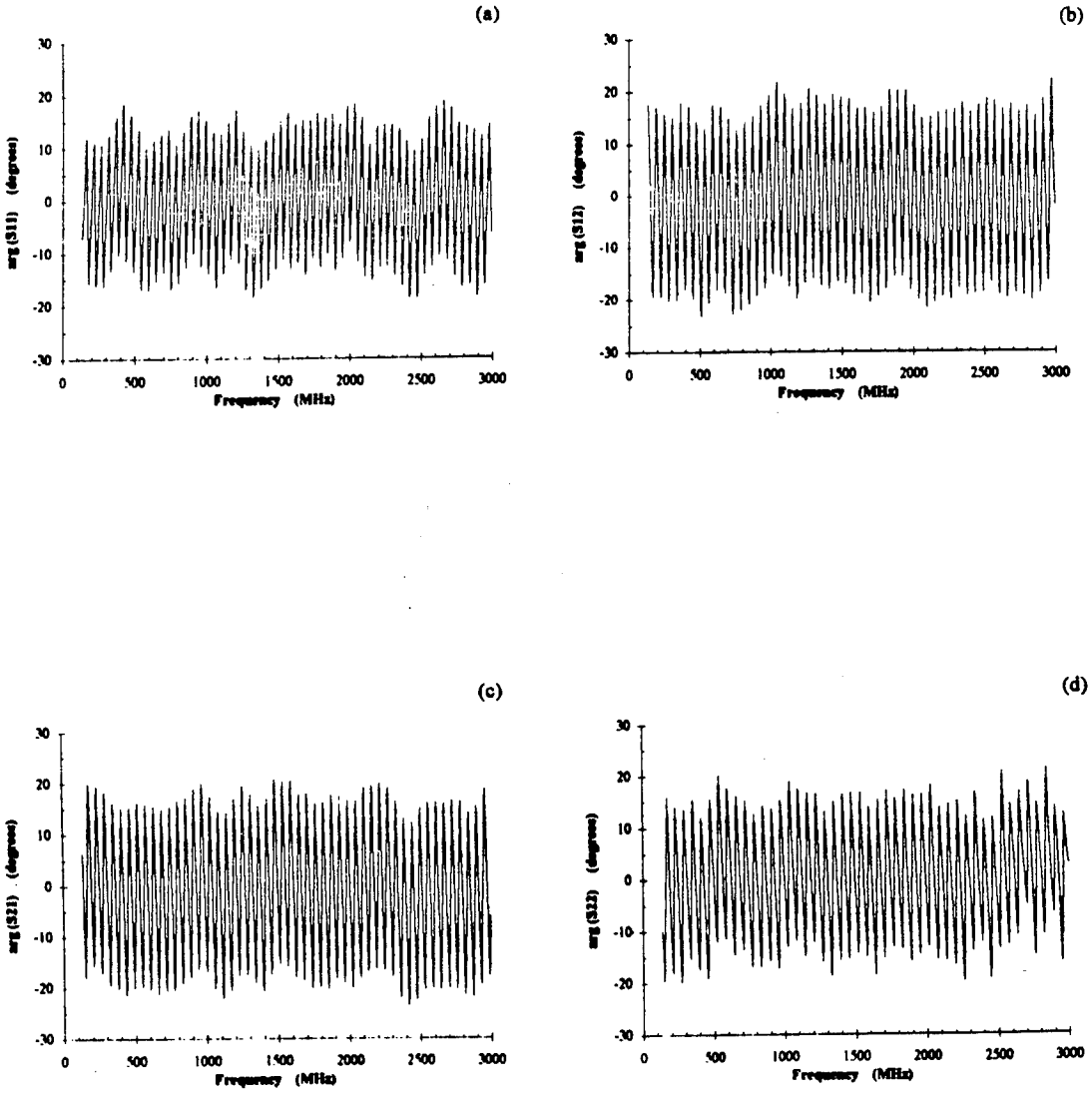

Figure 10 DC MESFET S-Parameter Angle

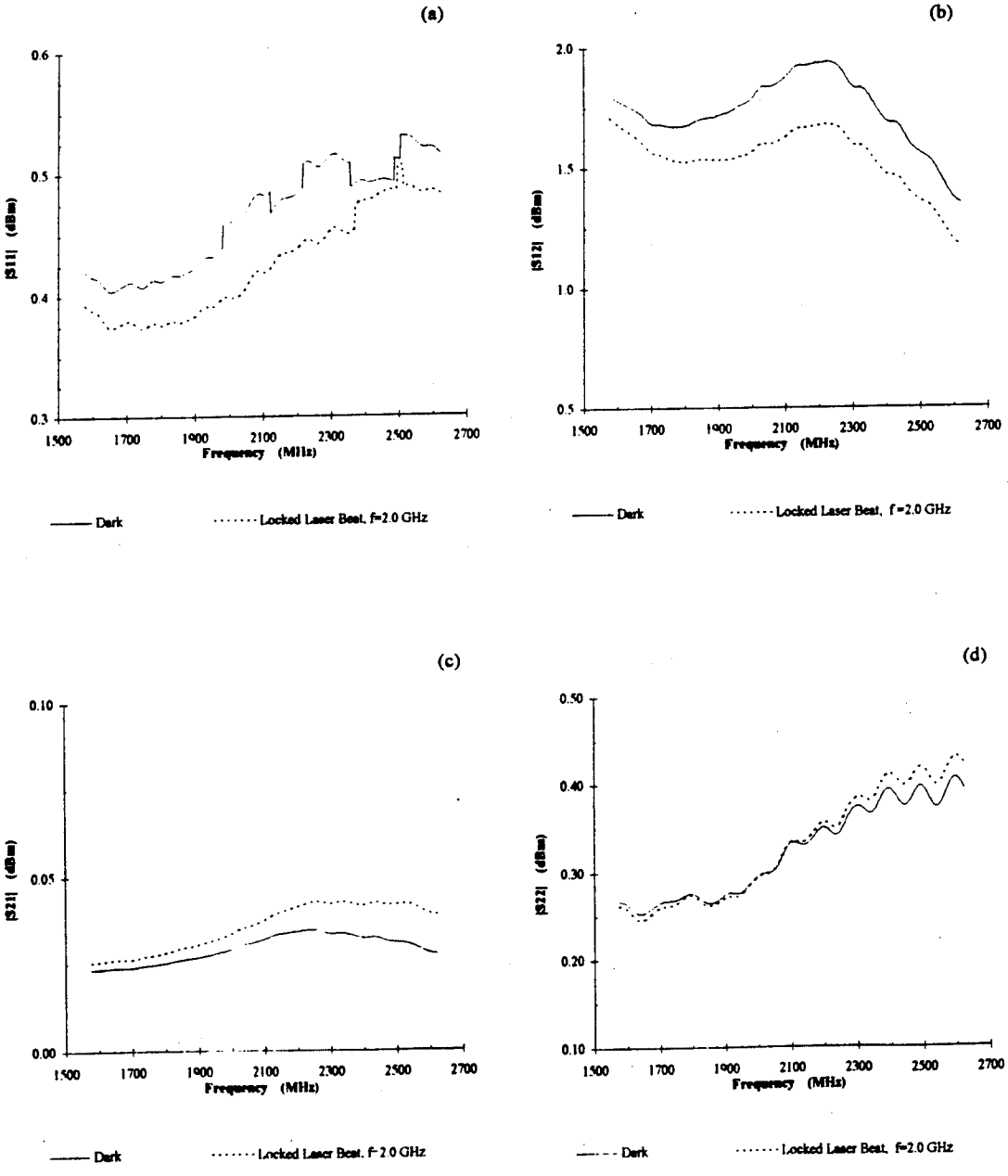

Figure 11 Common Source MESFET |S| with 2.0 GHz beat Injected

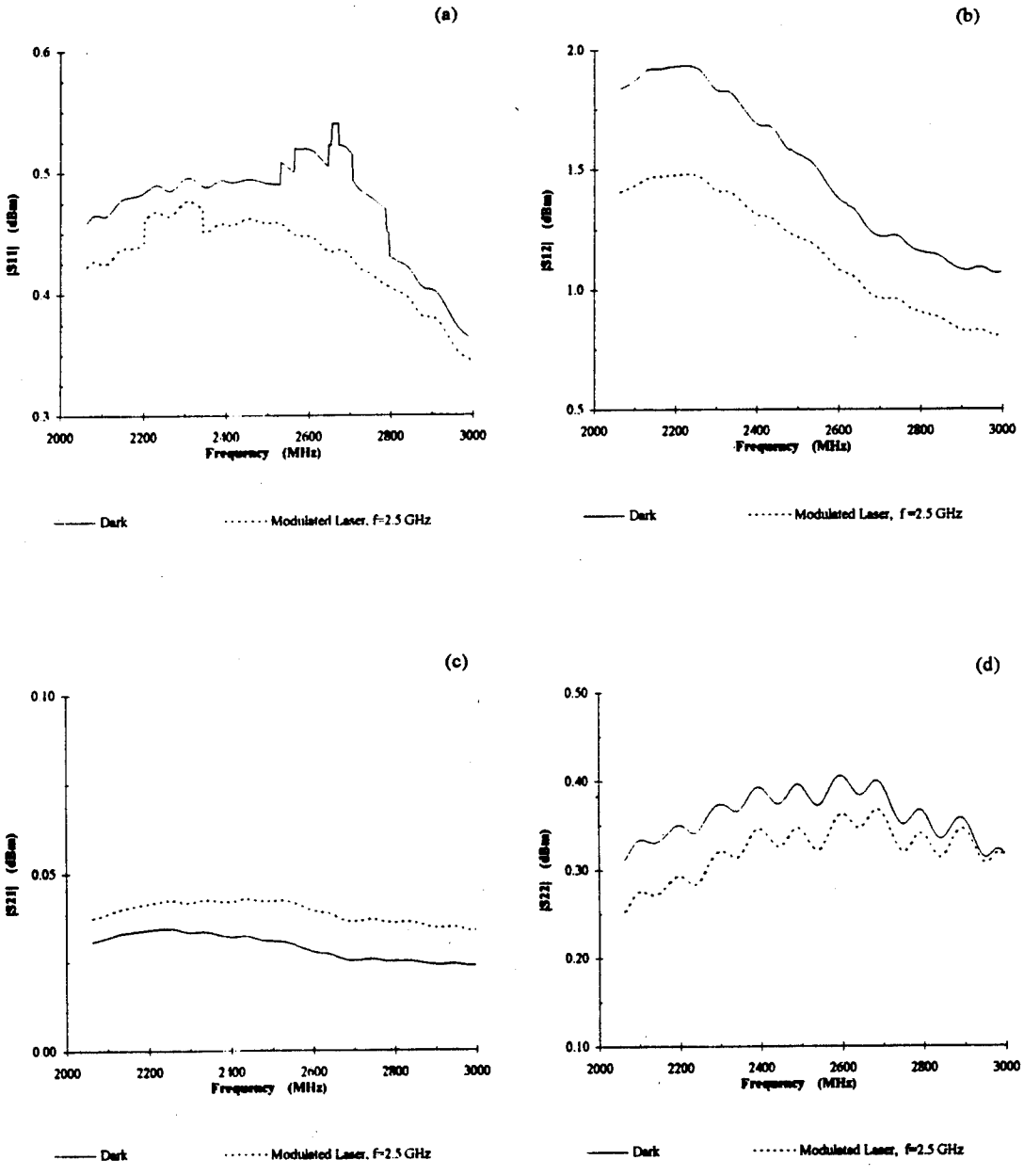

Figure 12 Common Source MESFET's |S| with Single Modulated Laser @ 2.5 GHz

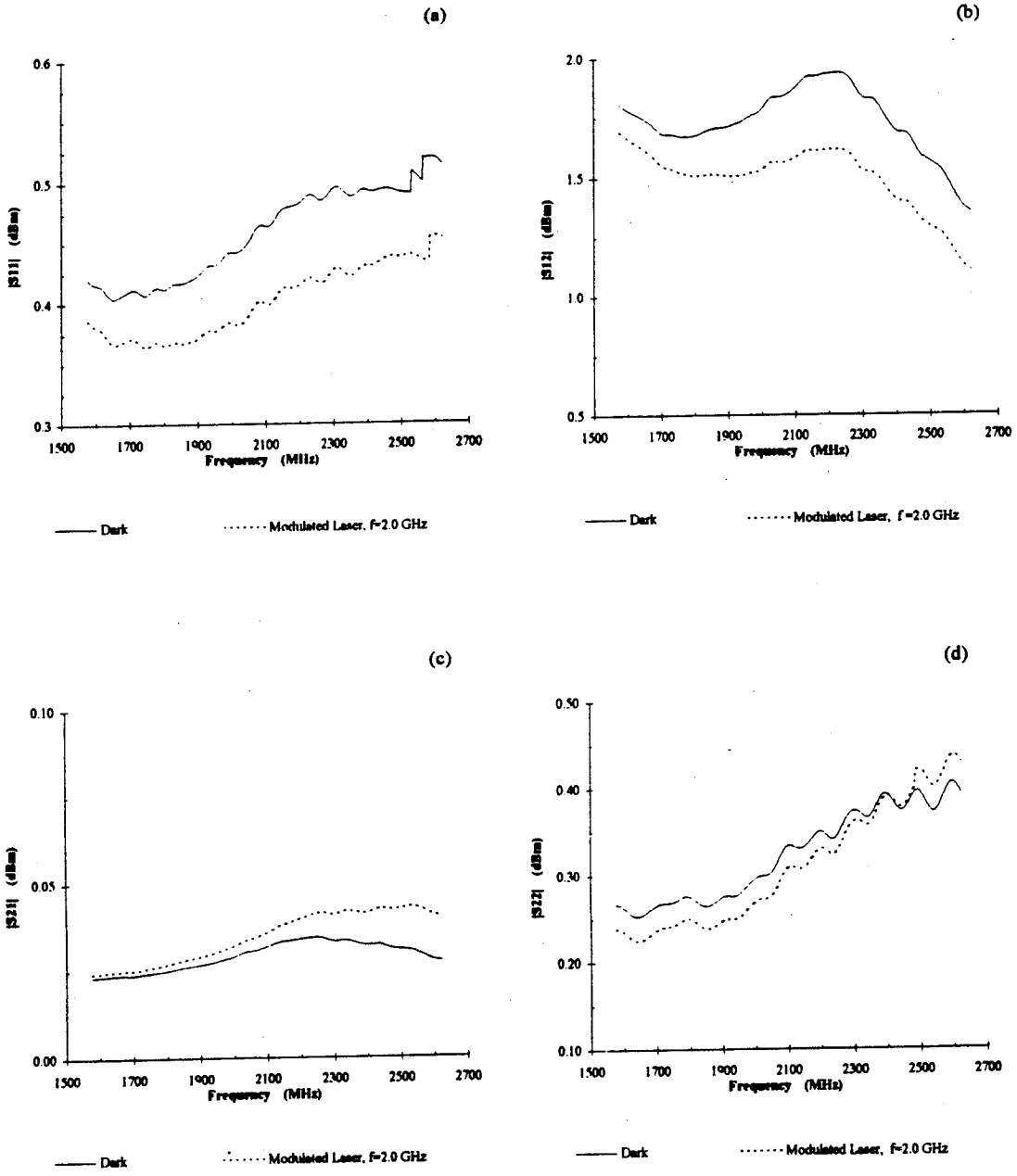

Figure 13 Common Source MESFET's |S| with Single Modulated Laser @ 2.0 GHz

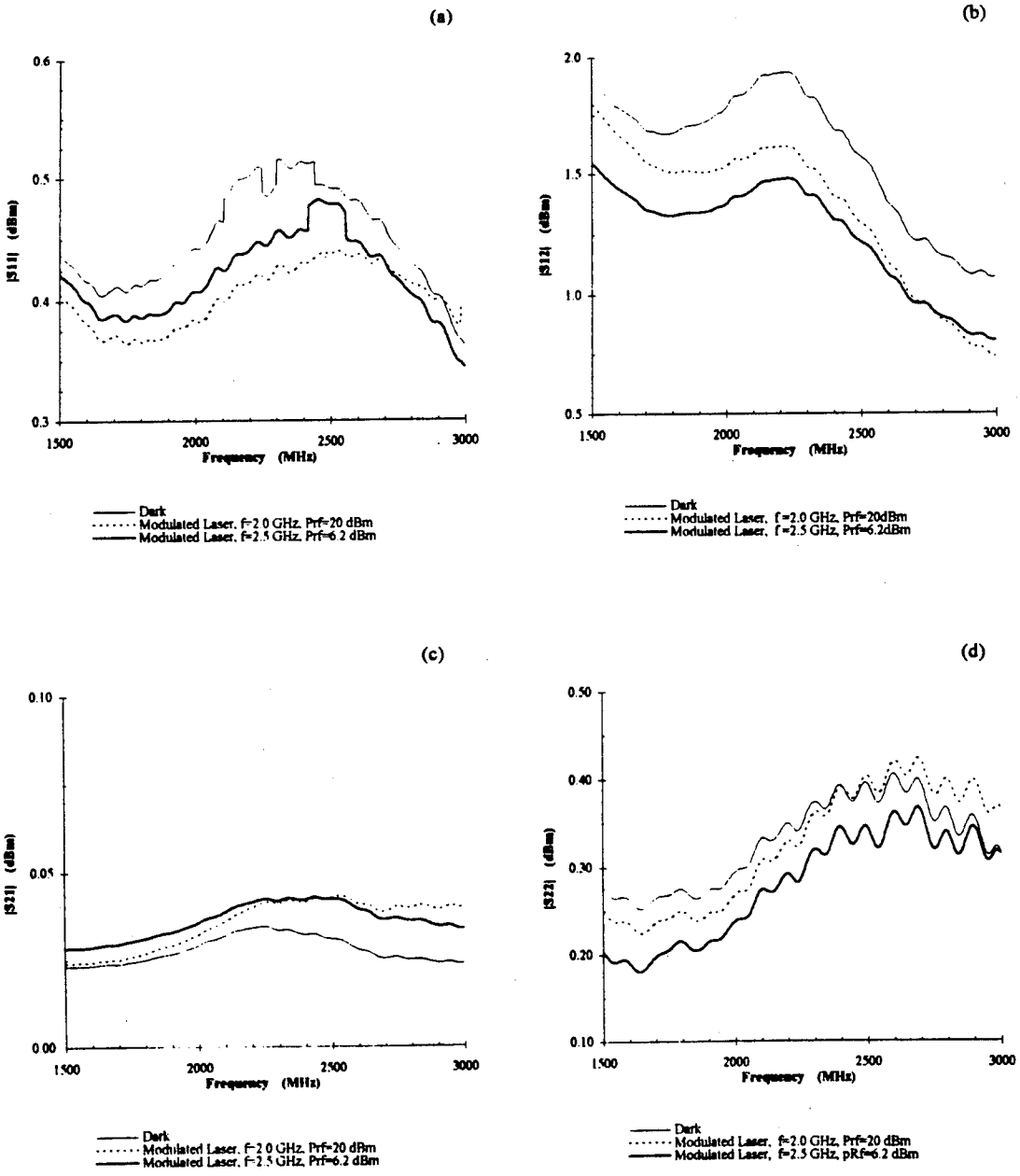

Figure 14 Effects of Laser Modulation Power on Common Source |S|

6.3.3 Parasitics

The drain and source ohmic contacts have a series parasitic resistance associated with the doping levels of the active channel region and a resistance associated with the ohmic doping level. Since the active region doping concentration changes with absorbed optical energy, the series contact resistance in the active region also changes. Using the Fukui method[4], the parasitic resistances are presented. Because the parasitics are dependent on the doping levels, the illuminated MESFET does undergo a change proportional to the change in photo-generated carrier density in the active channel.

$$R_p = \frac{1.1\,L}{z\,a\left(\frac{N_d + \Delta n}{10^{16}}\right)^{0.82}}$$

With $N_d = 10^{17}$ cm^{-3}, $\alpha=10^4$ cm^{-1}, a=0.15μm, z=0.3mm, lifetime of 10^{-6}s, L=2-3μm optical intensity of 30W/cm^2, the increase in carrier density Δn is about 10^{-16} cm^{-3} which is 10% of the doping concentration of the epitaxial layer (N_d). Therefore, a decrease in series contact resistance of 10% is the resultant change in parasitic under illumination. The units in the calculation are given with the values. Simons has calculated the parasitics with a similar but more rigorous method with the result of 10-15% change in the series contact parasitic resistances.

6.3.4 Effects from the Gate Bias Circuit

In this section the effect of the gate bias circuitry is discussed based on experimental data. Refer to Chapter 3.5.3 for more details regarding the effect the gate circuitry has on the illuminated operation of the MESFET. When a large resistance is placed on the gate (59.7KΩ) and the MESFET is illuminated, the gate is essentially open circuited and the voltage read is the photo-voltage V_{ph}. In Chapter 3.5.3, theoretical calculations and experimental data are given for V_{ph}.

In Figures 15-19, the y axis is the voltage across R_g. The V_{Rg} is the voltage across the gate to ground v_{gs} (measured) minus the power supply voltage V_{gs} (measured). This is shown in the following diagram.

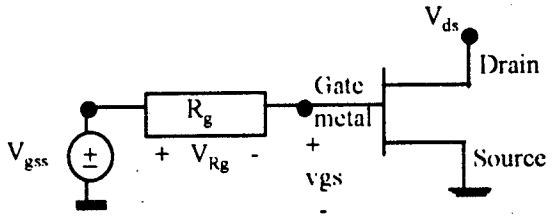

In Figure 15, with the same gate resistance (59.7KΩ) a drain voltage is applied which causes photoconductive changes in the active channel region and subsequently the current in the gate. Overall, KCL must be satisfied. Figure 16 measures the voltage drop as a function optical power. The legend represents the value of the gate bias (V_{gss}) set at the power supply. Figure 17 and Figure 18 show the photo-effect for dark and optical power of 0.34mW and 2.7mW.

In Figure 19, the gate resistance is now 596Ω which is several orders of magnitude lower than the previous data, and the voltage drop was measured. The

voltage drop is in the mV range and varies slightly as the optical power injected increases.

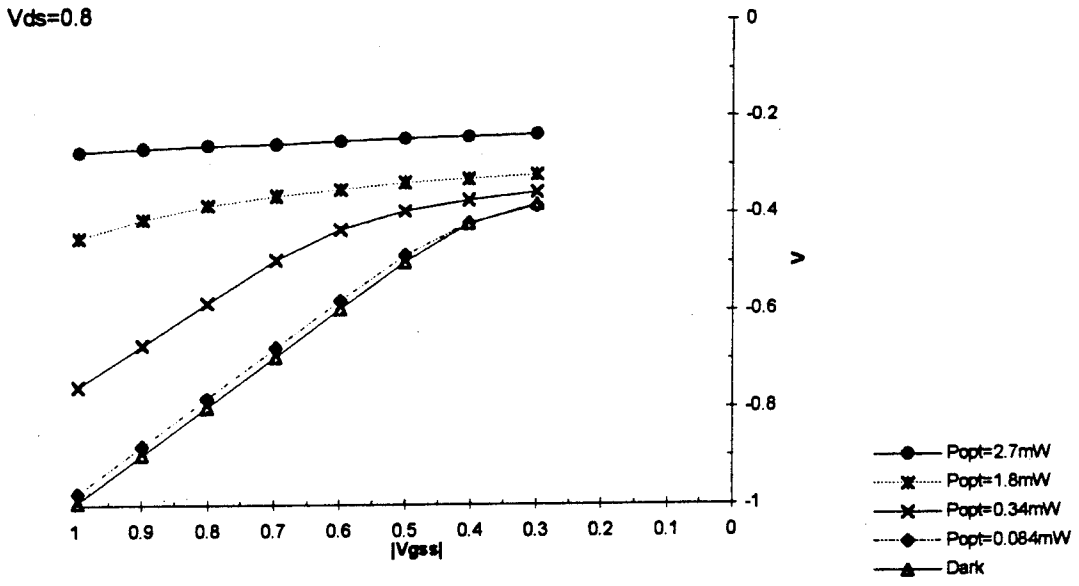

Figure 15 V with V_{ds} =0.8v, R_g =59.7KΩ

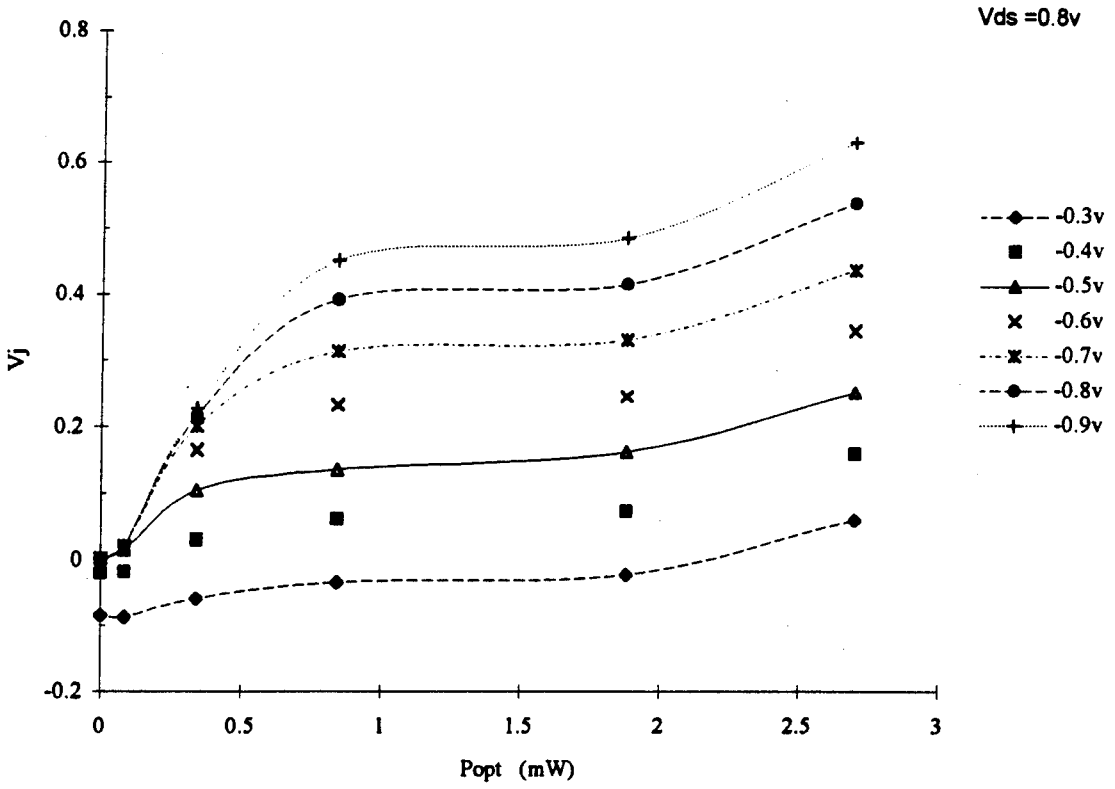

Figure 16 V versus optical Power with V_{ds}=0.8v, R_g=59.7KΩ

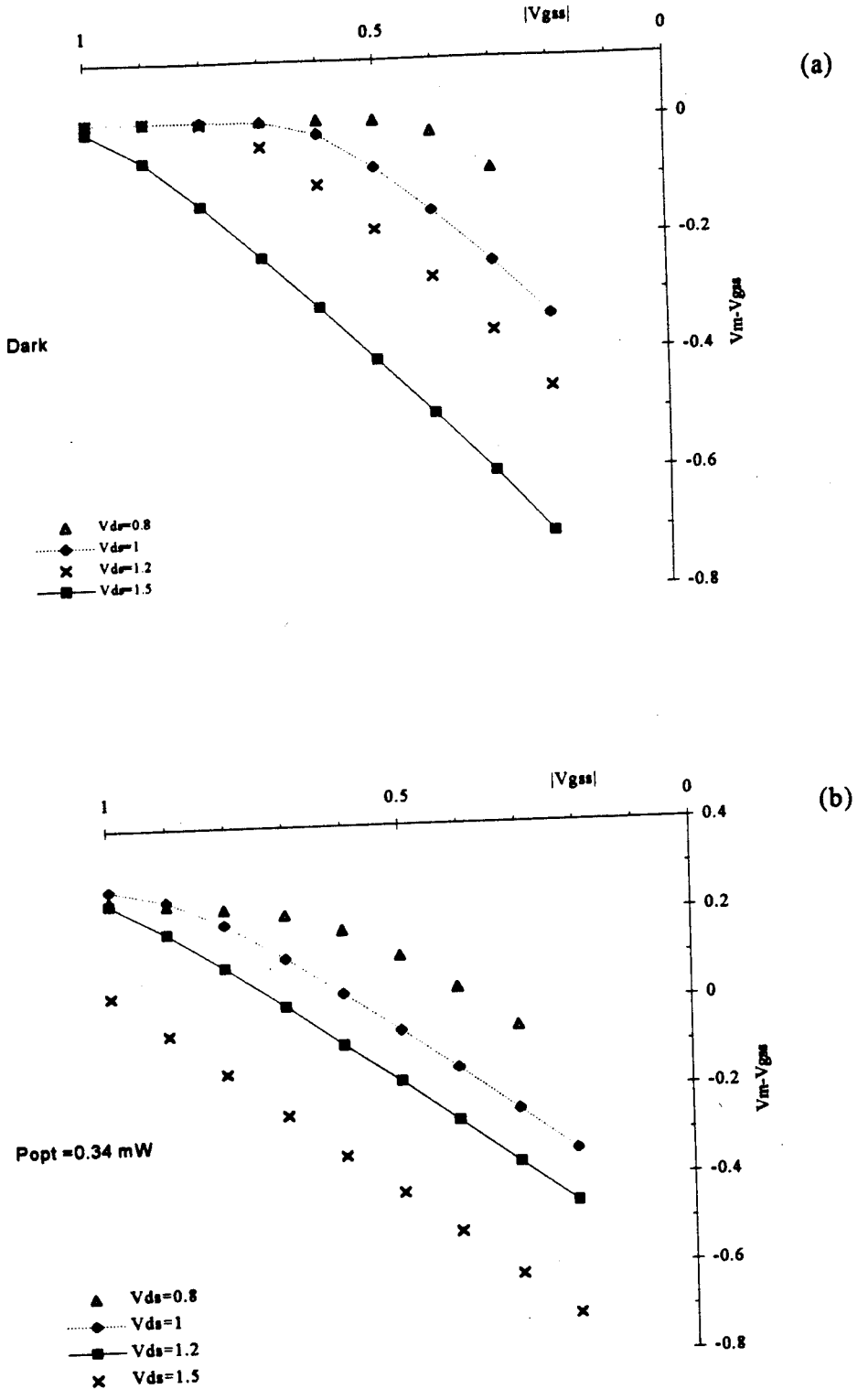

Figure 17 V versus applied gate bias as a function of V_{ds}; a)Dark, b)P_{opt}=0.34mW

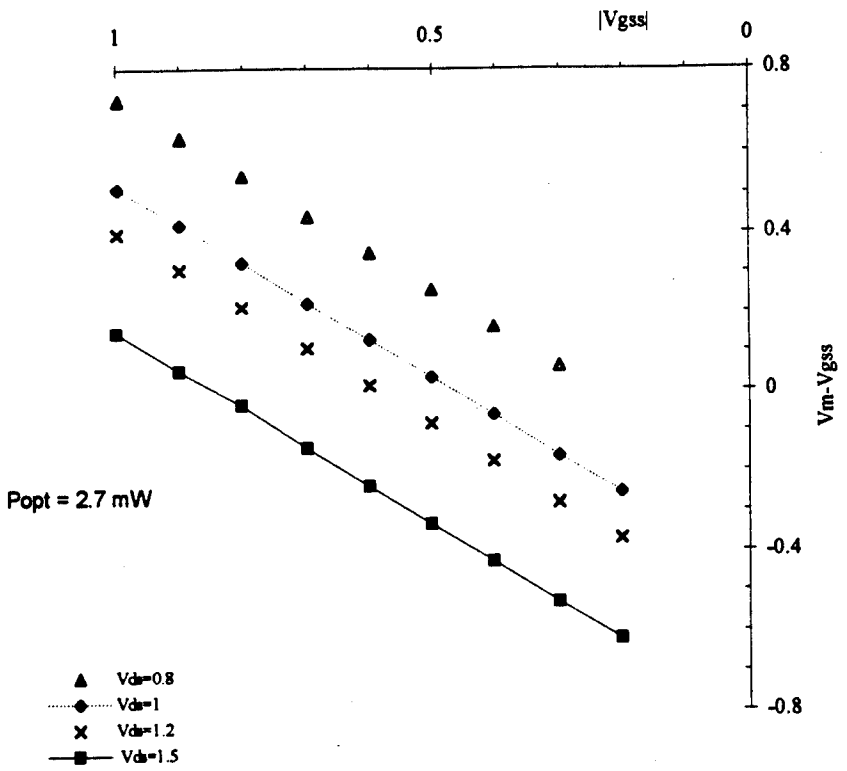

Figure 18 V versus applied gate bias as a function of V_{ds} for P_{opt}=2.7mW

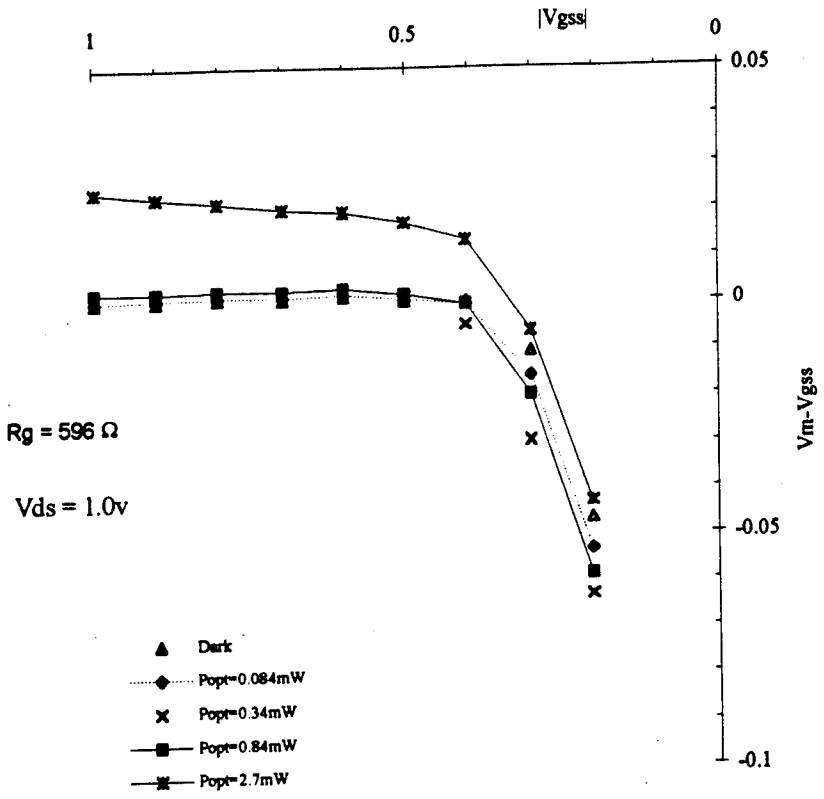

Figure 19 V as a function of optical power with Vds=1.0v, Rg=597Ω

6.4 Conclusion

The large signal model was derived and is used extensively in Chapter 8 to explain changes in the amplifier gain due to g_m and S21. S-parameter measurements were completed for one bias point. The photo-induced changes in the MESFET S-parameters were on average 12%. The photo-induced change in carrier concentration in the active region was shown to decrease the parasitic series contact resistance 10-15%. An external gate resistance was shown to effect the device response to an optically injected signal.

6.6 References - Chapter 6

[1] R.A. Pucel,, H.A. Haus, and H. Statz, "Signal and Noise Properties of GaAs Microwave Field-Effect Transistors", Advances in Electronic and Electron Physics, edited by L.Marton, Academic Press, vol.38, 1975, pp.195-265.

[2] Walter R. Curtice, "A MESFET Model for Use in the Design of GaAs Integrated Circuits", *IEEE Transactions on Microwave Theory and Techniques*, vol. MTT-28, no.5, May 1980, pp.448-456.

[3] J. Michael Golio, Microwave MESFETs & HEMTs, Artech House, Inc., 1991.

[4] H. Fukui, "Determination of the Basic Device Parameters of a GaAs MESFET", *Bell System Technical Journal*, vol.58, 1979, pp.771-797.

CHAPTER 7

MICROWAVE OSCILLATOR INJECTION

7.1 Introduction

This chapter describes optically induced phenomenon in microwave MESFET oscillator circuits. The main results are (1) the oscillator phase noise at 1 KHz from the carrier is the decreased by 45 dBc/Hz when locked to the modulated lasers in Section 7.5.1 Phase Noise Measurements, (2) incidental frequency noise is extinguished when locked to a modulated optical signal in Section 7.5.2 AM Noise Measurements, and (3) circuit model approach fails to predict asymmetric locking behavior which is the result of wavelength effects (7.4.3 Non-symmetric Locking Bandwidth).

The locked laser system provides optical mode phase stability and is limited only by the linewidth of the RF sweeper which is 10 KHz in these experiments. To corroborate the position that the locked laser system provides superior oscillator mode locking, an effort was made to isolate differences based on various types of injected signals. The oscillator circuit without injection is characterized. The five injected optical signals are unmodulated (or DC) laser light, modulated unlocked and locked single laser light, and the unlocked and locked modulated heterodyne beat

signal between the reference and the slave lasers. See Section 5.5 Experiments Conducted for more information on the experiments conducted. The oscillators discussed in this chapter have been designed to operate at nominal frequency of 5 GHz and 3 GHz. See Chapter 5.7 Microwave Circuit Fabrication for more details on the oscillator design specifications and motivation.

The first section presents the current-voltage (I-V) characteristics and DC impedance of the MESFET oscillator. The oscillator output spectrum , frequency tuning range and locking characteristics are studied and compared to electrical injection. Stochastic processes, such as white noise, produce frequency and amplitude modulation (FM, AM). In general, AM is invariably accompanied by phase noise and some amount of incidental frequency modulation (FM). The oscillator phase noise is determined and shown to decrease with increasing optical mode stability. In fact, the incidental FM is extinguished under the correct locking conditions. The model predictions and DC MESFET results of Chapter 6 are used to explain the experimental results. The final section will conclude.

7.2 History of Oscillator Injection

The nonlinear theory of electric oscillations were described by Van der Pol in the 1920's[1]. His paper provides rigorous details of the nonlinear oscillations and uses physical realities as approximations. The consideration of the physical realities of oscillations was a major step in analytically describing and solving the nonlinear

problem. A much referenced study in the area of locking phenomenon was produced in 1946 by Robert Adler[2]. Adler's equation gives the phase of the pulled oscillation as a function of time. It has been proven that the Adler Locking Equation can be derived from the Van der Pol Equation. Starting with Adler's equation, a Fourier series solution has been developed to express the spectrum of a pulled oscillator[3]. Over the next three decades, Van der Pol's theory was a basis for many other theories in oscillating phenomenon[4,5,6]. When IMPATT and Gunn diodes became available in the 1970's, the interest in injection locking became an important area of research because these devices provided a microwave negative resistance necessary for oscillation. Kurokawa recognized the practical limitations in Van der Pol's development when applied to microwave oscillators. The main limitations cited are the impossibility of expressing the current flow as an instantaneous function of applied voltage, and the complexity of describing the interaction of active devices in microwave networks via a second order differential equation. These networks contribute to the oscillation and are an important aspect of microwave oscillator design. The quasi-static and dynamic analyses of locking range and stability, and modulation noise were detailed by Kurokawa[7] and have become modern analysis tools for microwave oscillation studies.

Throughout the 1970's , work in the area of electrical injection locking of microwave devices continued. In a comprehensive study, Sato showed that electrical injection locking and a phased locked loop (PLL) can be used to stabilize oscillations and suppress noise respectively[8]. This is analogous to the study done in this Thesis where the injection method is optical and the PLL is effectively the

locked laser system. Noise suppression under optical injection is described in 7.5.1 Phase Noise Measurements. Electrical injection of a stable signal is accomplished by superimposing the RF signal onto the DC bias of the input port. Subharmoinc electrical injection locked oscillator experiments have also been studied[9,10] as well as phase locking of active device oscillators[11]. The problems with electrical injection are (1) the system is limited by the number of the stable sources, (2) the cost of providing multiple stable sources is prohibitive, and (3) electrical interference at microwave frequencies is serious problem.

Optically injected microwave oscillators are shown in this Thesis to provide solutions to the latter difficulties without adding extra components to the system. The goal is to lock the oscillator frequency without effecting the system cost, limiting the size, and without signal interference. Indirect optical injection locking is defined in the literature as detecting an optical signal by a high speed photodiode and then using the amplified electrical output to lock an oscillator. This is a misnomer because the signals are distributed via optical fiber, but the injection process is electrical. In the late 1970's at Hughes and early 1980's in a combined study between LORAL-ATL and Drexel University, indirect locking was studied. Yen and Barnoski at Hughes used a Silicon bipolar transistor oscillator with frequency ranging to 1.8 GHz and observed fundamental and subharmonic locking as well as transistor switching[12]. The switching is consequence of the inevitable DC contribution to the signal. Wahi, Herczfeld, et.al., evaluated indirect locking based on locking range and FM noise characteristics. Their results showed a decrease in the FM noise of the oscillator when injected with the electrical signal from the

photodiode[13]. A comparison of this work to noise measurements in this Thesis reveals that our locked laser system decreases the noise to its fundamental limits (See 7.5.1 Phase Noise Measurements). In 1992, Ma, Esman, et.al., updated experiments involving indirect optical injection and showed an 8 MHz locking bandwidth and discussed applications for fiber-optic communications , clock recovery and coherent demodulation schemes[14]. The applications of injection locking had previously centered on phased array radar.

Direct optical injection locking, which is the subject of this chapter, uses the photosensitive properties of semiconductor devices (e.g., GaAs MESFETs or IMPATTs) to receive the optical signal directly. During the last decade, work has been conducted on injecting MESFETs with light from LEDs and describing the effects in the device. Sun, Gutmann and Borrego, who have also established significant models of FET devices, specified the photo-effects in common-source and common-drain GaAs MESFET oscillators which revealed that the common source is five times as optically sensitive as the common drain[15,16]. This is attributed to changes in the effective space charge density in the gate depletion layer which effects the gate to source capacitance (C_{gs}) and therefore, the oscillation frequency. Although gate photo-voltage is developed on the order of 60% of the gate bias, this change does not affect the frequency as directly as C_{gs}. Goldberg, et.al., used laser sources and first proposed using modulation at relaxation frequencies of lasers to produce a comb of sidebands which are optically injection locked into FET oscillators[17]. This provides frequency stable signals which may be applied to phased array radar applications. Optical injection locking in MESFET

oscillators was demonstrated in 1982 by deSallees and Forrest[18] which complimented the fundamental study by Borrego, et.al. This study measured the FM noise of the injected oscillator. Locking of IMPATT oscillators was studied by Seeds, Forrest, et.al., in 1987[19] which presented analytical and modeling studies of optical tuning and locking and measured the tuning of W-Band IMPATT up to 9 MHz. In this Thesis an accurate and thorough characterization of optically induced MESFET behavior has been completed. The tuning range of 40 MHz is a key result (Figure 7 and Figure 8). In 7.3.3 Frequency Tuning under Illumination, the bias conditions are shown to influence the magnitude of the optical effects on the MESFET.

Controlling the frequency of a microwave oscillator circuit with RF direct modulated laser has been reported[20],[21],[22]. Esman, et al., have shown locking bandwidths up to 2.6 MHz, a phase tuning range up to 187^{O} and experimental agreement with small signal injection locking theory for silicon (Si) bipolar transistor. In this work, a laser transmits the carrier, subcarrier and data to a voltage controlled Si bipolar oscillator (VCO). The best results were seen when focused near the tank circuit and not the bipolar transistor[23] although the beam was at the edge of the gold bonding pad which is highly reflective. Because Si devices are based on bipolar carriers, the optical response of the Si bipolar device is mainly photoconductive (i.e., the separation and collection of generated electron-hole pairs along the channel). See Section 3.2 Classification of Optical Processes.

7.3 Optically Induced Effects on Circuit Parameters

The following section characterizes the changes to fundamental oscillator circuit parameters under illumination. The current-voltage (I-V) curves and DC impedance and frequency tuning as a function of bias voltage are presented for different classifications of optical signals: no optical injection, unmodualted (or DC) laser light, modulated unlocked and locked single laser light, and the unlocked and locked modulated heterodyne beat signal between the reference and the slave lasers. MESFET theory and modeling are treated in *Chapter 3*. The oscillators discussed in this Thesis have been designed to operate at nominal frequency of 5 GHz and 3 GHz.

The rationale for these measurements is to link the DC parameter measurements of Chapter 6.3 to the oscillator case and to link the photo-induced processes to the injected signal type. Because the MESFET device is embedded in a microwave network which is a more complicated system than described in Chapter 6, the association to the DC measurements is vital in order to distinguish the photo induced effects. Due to equipment unavailability at the frequency of interest, it was not possible to measure the scattering parameters (S-parameters) and therefore, the frequency dependent characteristics for the oscillator accurately. However, RMS measurements were completed that give insight into the oscillator operation under illumination.

The oscillator measurements were taken on the HP8562A with span of 10 MHz, reference level of 0 dBm, attenuation level of 10dBm, resolution and video

bandwidths of 100 KHz and 1 KHz respectively. These measurements were taken with a single unmodulated laser injected into the MESFET. The laser bias current was 91.8 mA, and the temperature was stabilized at 15.49°C. The resultant laser wavelength is 822.75 nanometers which was measured with HP70951A Optical Spectrum Analyzer in span of 10 nanometers. The optical power at the measurement plane was 1.9 mW which is calculated to be 41.8 μW as it reaches the MESFET GaAs. The total power absorbed in 0.5 μm depth of the GaAs is 24.7 μm. This amount of power was purposely selected to be large to guarantee the maximum optical effect.

7.3.1 Current-Voltage Characteristics

The current- voltage (I-V) characteristics of the designed oscillator circuits are presented in this section. The drain to source bias voltage (V_{ds}) was swept from 1.2 v to 3v in increments of 0.05v for each gate to source voltage (V_{gs}). The HP6624A DC Power Supply was used to provide bias on the oscillator which also provides a voltage reading. A HP3478A multimeter and Keithly 199 multimeter were used to measure the drain voltage and current respectively. In order to understand the MESFET operation at pinchoff, it was necessary to select a V_{gs} value that would be negative enough to maintain a reverse bias junction when the Schottky photo-voltage is developed. Four values of V_{gs} were used: -0.2, -0.5, -0.8, -1.0.

The drain current increases 3-5 mA when 24.7 mW of optical power is absorbed. These results are presented in Figure 1 Oscillator Drain Current vs. Vds under Illumination and Figure 2 Oscillator Drain Current vs. |Vgs| under Illumination. In the graphs, the illuminated cases are represented by dashed lines while the solid lines are the unilluminated data. Also, in Figure 2, the three values of V_{ds} are given for each V_{gs}: 1.2v, 1.5v, 3.0v. Modulated laser illumination increases the DC current by larger. amounts than the unmodulated light.

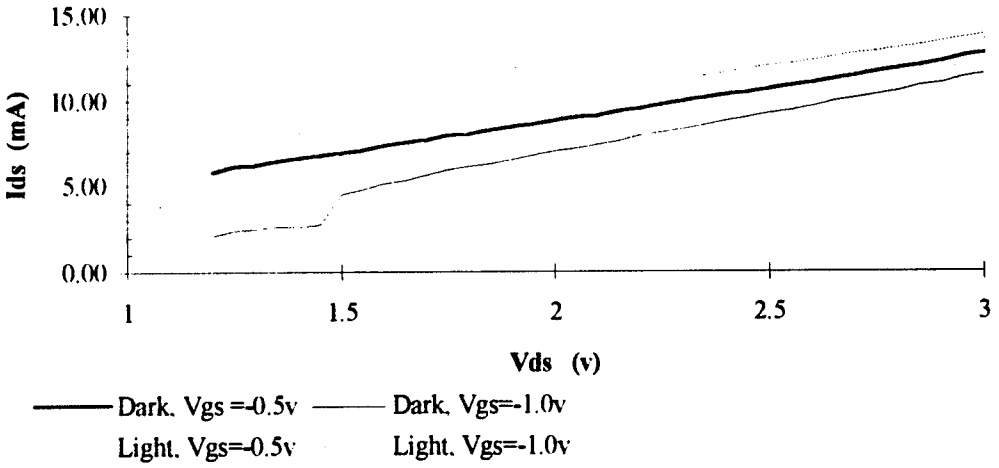

Figure 1 Oscillator Drain Current vs. V_{ds} under Illumination

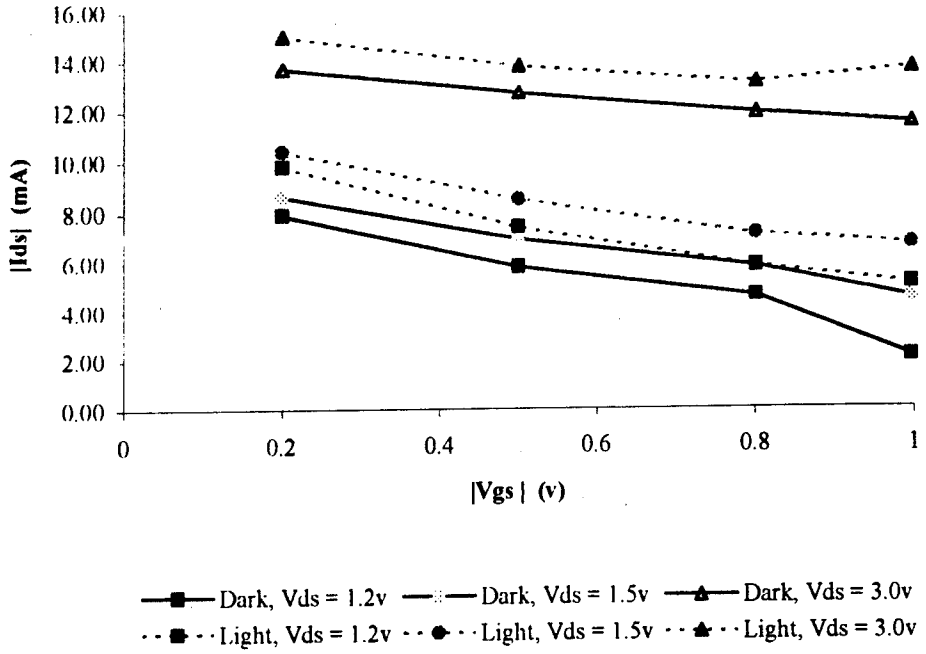

Figure 2 Oscillator Drain Current vs. $|V_{gs}|$ under Illumination

7.3.2 Characteristics of Oscillator Impedance and Output under Illumination

It is understood and described in many models that the MESFET impedance is related to the bias voltages[24]. When the MESFET in the oscillator is illuminated, the Schottky photo-voltage that develops adds to the existing gate to source bias voltage (V_{gs}). This immediately effects the circuit impedance (Figure 3 Drain to Source Impedance change) and subsequently, the oscillator's matching network circuit. The maximum change in impedance when illuminated was 20% lower than the dark case (190Ω to 150Ω). $|Z_{ds}|$ was measured under identical bias conditions (V_{gs}= -0.52v, V_{ds}=1.5v) with various levels of injected optical power. The oscillator impedance from the drain to source $|Z_{ds}|$ has the largest impact on the oscillator output power. The MESFET circuit model in Section 6.2 is a standard MESFET circuit from which the output at the drain is determined to be equal to (7-1).

$$\text{Gain} = g_m * r_{ds} \qquad (7\text{-}1)$$

Table 1 Impedance Characteristics under modulated illumination

Modulated Optical Power Measured (mW)	**Modulated Optical Power Injected @ ω_{inj}** (nW)	$\|Z_{ds}\|$ {Dark $\|Z_{ds}\|$ = 187Ω} (Ω)
1.64	409	152.51
1.7	395	152.84
1.81	371	149.75
2.1	321	150.05
2.2	306	150.05

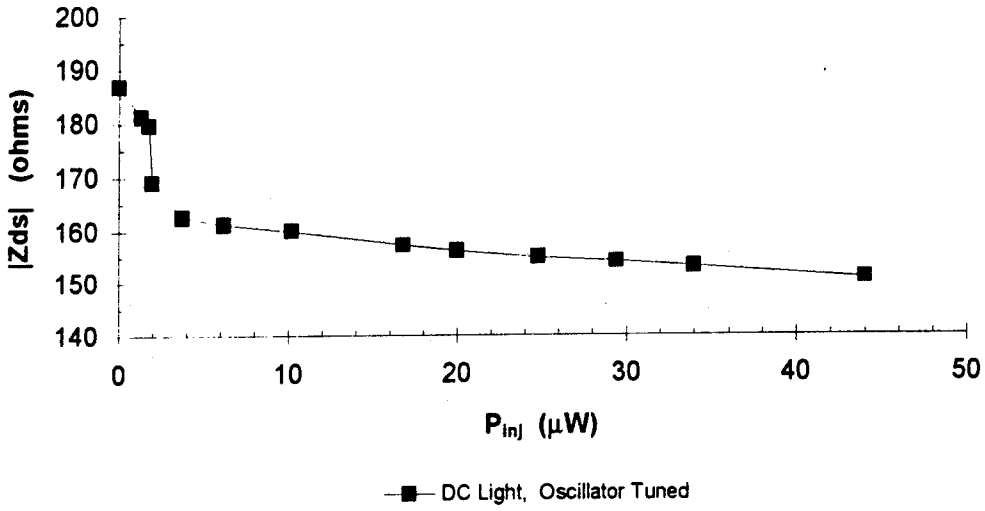

Figure 3 Drain to Source Impedance change as a function of injected optical power

While Figure 3 demonstrates the changes in $|Z_{ds}|$ under dc illumination, Table 1 gives the results under modulated illumination with the oscillator locked. Ideally, a network analyzer must be used to get a correct measurement of the frequency dependent circuit parameters. However, this diagnostic tool was not available in the frequency range of interest. These measurements are RMS values of the overall circuit impedance. The voltage from the drain to ground (source) and the current flowing from the drain to the bias supply were measured from which the impedance was calculated. The measurements were taken albeit crudely, but the results are informative. In *Chapter 5 and 6*, S-parameter measurements were taken with a low frequency network analyzer for the standalone MESFET and the amplifier which are converted to circuit characteristics.

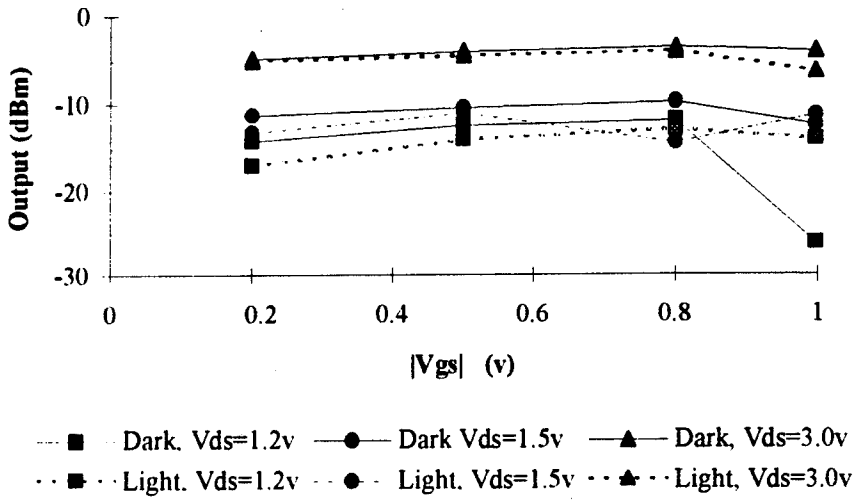

Figure 4 Oscillator Output vs. $|V_{gs}|$

Since the drain-source impedance is a primary factor in the output gain of the circuit, the output power is reduced if the matching network is not optimum because reflections occur. It was not possible to compensate experimentally for the mismatch because there were no external stub tuners available. Figure 4 Oscillator Output vs. |Vgs| and Figure 5 Oscillator Output vs. Vds show that the magnitude of the output change is on the order of 17% lower depending on the bias state with 41.8 mW of optical power injected.

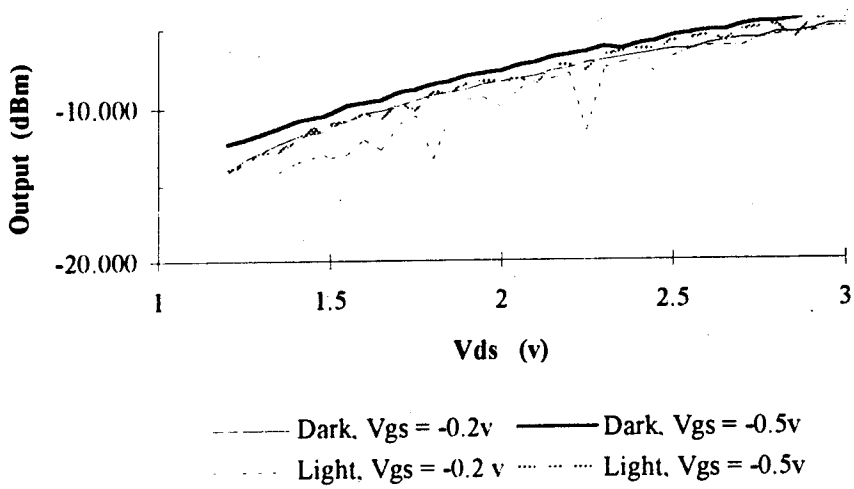

Figure 5 Oscillator Output vs. V_{ds}

7.3.3 Frequency Tuning under Illumination

With 41.8 mW of unmodulated optical power injected, the MESFET oscillators, designed in this experiment, are shown to frequency tune 10-20 MHz when biased well below threshold, but at more negative values of V_{gs}, 40 MHz tuning was realized (3 GHz oscillator). The bias conditions affect the magnitude of the optically induced changes in the frequency because the MESFET circuit parameters(C_{gs}, g_m), which influence the frequency, are functions of bias. These measurements were taken with a single unmodulated laser injected into the MESFET of the oscillator.

The maximum frequency f_u of oscillation depends on the cut-off frequency f_c of the current gain to the first order which is related to the transconductance g_m and the gate to source capacitance C_{gs}. In the following, R_o is the sum of the internal resistance from the gate to the source R_i (sometimes referred to as the gate charging resistor), the gate series resistance due to metallization R_g, and source contact resistance R_s. The feedback capacitance C_{gd} must be low, the output conductance must be high and the parasitics R_s, R_g, L_s must be low to maximize f_u.

$$f_u = \frac{f_c}{\sqrt{R_o g_d + 2\pi f_c R_g C_{gd}}}$$

$$f_c = \frac{g_m}{2\pi C_{gs}}$$

The Curtice large signal MESFET model[25] uses first order semiconductor junction theory applied to a two-terminal Schottky diode structure to derive the following capacitance expressions:

$$C_{gs} = \frac{C_{gs0}}{\sqrt{\{1 - \frac{V_{gs}}{V_{bi}}\}}}$$

where V_{bi} is the built in potential of the Schottky gate, and C_{gs0} is the zero bias gate-source capacitance. More rigorous MESFET theory and modeling results are given in *Chapter 3 and 5*. The transconductance is also related to the gate-source voltage:

$$g_m = I_{ds}\left[\frac{2}{V_{gs} - V_{t0}}\right]$$

where V_{t0} is the pinchoff potential. Additional discussion and details on MESFET optical effects modeling is in *Chapter 3 and 5*.

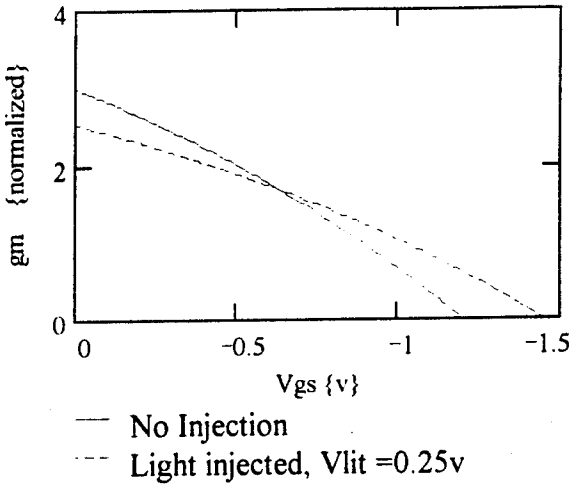

Figure 6 Transconductance vs. gate to source voltage

Figure 7 and Figure 8 show the changes in the oscillation frequency under the same level of dc light injection (41.8 mW) for various bias points. The largest magnitude increases of 40 MHz are observed when the circuit is biased above pinchoff (i.e., large negative values of V_{gs}). Since the transconductance g_m is directly related to V_{gs}, and the frequency is related to g_m, the characteristics of g_m near pinchoff are a source of the 40 MHz frequency tuning results. Under illumination, the transconductance is less than the dark case until pinchoff and then is greater at gate biases beyond pinchoff (Figure 6 Transconductance vs. gate to source voltage). This is attributed to the Schottky photovoltage V_{LIT} that develops which is superimposed on the bias voltage V_{gs}. The end result is a total gate to source potential that is more positive by the amount of V_{LIT}. The shifts in gm, as well as the other circuit parameters, are bias dependent.

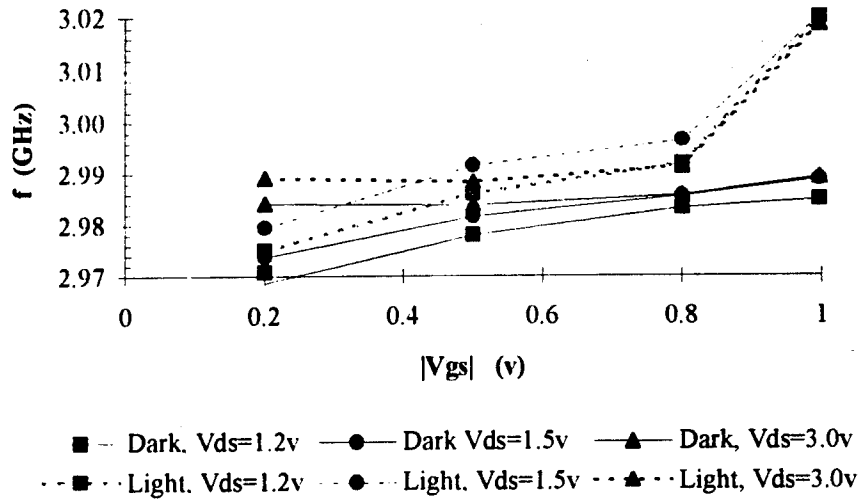

Figure 7 Effect of Light on the Oscillator Frequency vs. $|V_{gs}|$

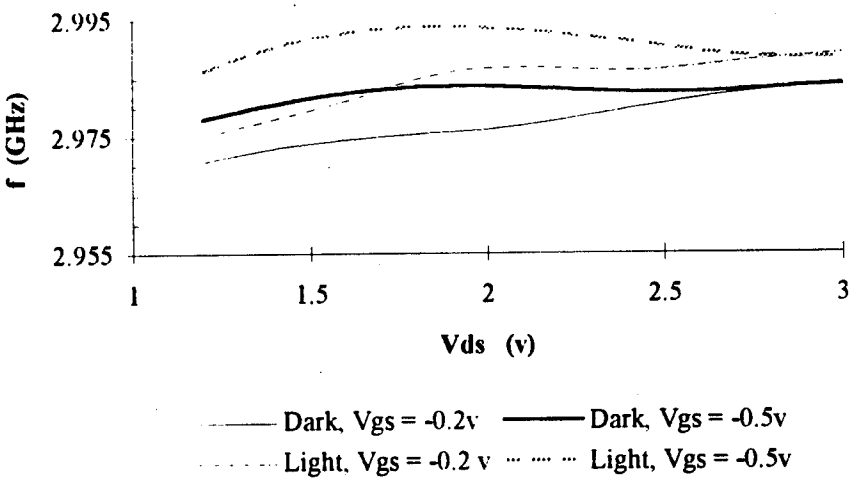

Figure 8 Effect of Light on the Oscillator Frequency vs. V_{ds}

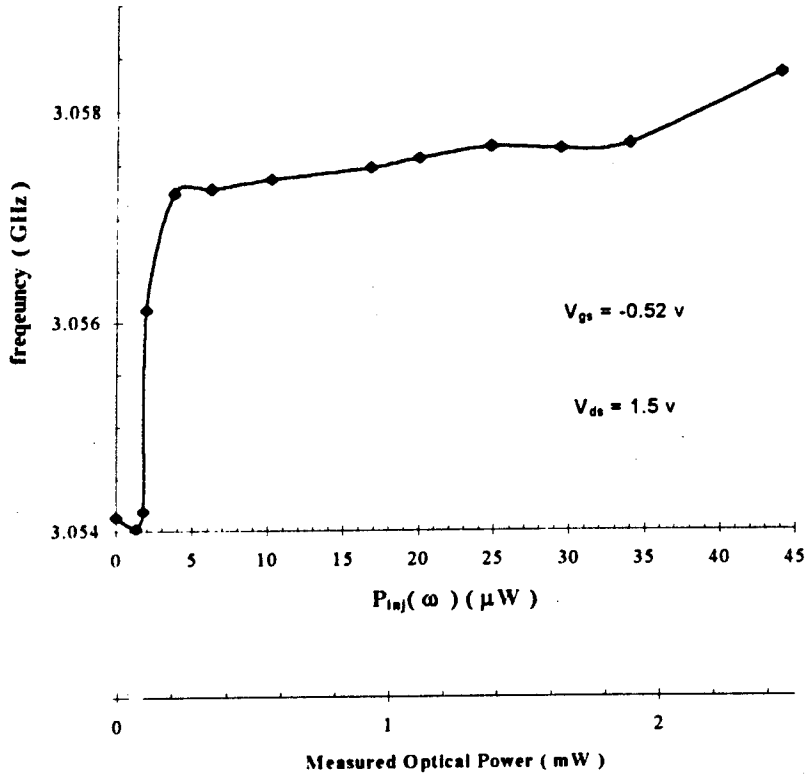

Figure 9 Frequency as a function of injected optical power

In Figure 9, the bias point was fixed (V_{gs} = -0.52 v, V_{ds} = 1.5 v) while the modulated injected light level was varied. The bias point was chosen to correspond with the bias levels used in the spectrum and locking experiments, but however, at this bias the tuning response is much less than the maximum shown under different bias conditions (Figure 7 and Figure 8).

7.4 Locking Characteristics

The locking characteristics of the oscillator are studied in detail in this section. First, the oscillator spectrum, locking bandwidth and locking gain are presented when different types of signals are injected including no injection, electrical injection, and various classes of optical signal injection. Locking range and locking gain results are discussed in the context of Kurokawa's development and Adler's equation. The region of validity of Adler's Locking Equation is also discussed. Theoretical discussion with experimental proof is given in Section 7.4.2 Locking Model to verify that no locking occurs (i.e., Adler's theory fails) when the injected frequency is less than the free running frequency of the oscillator. This locking model explains the injection phenomenon and the AM and FM noise origins which are presented in 7.5 Oscillator Noise Behavior. Also, in *Chapter 4*, the semi-classical laser rate equations are compared to microwave oscillator equations which lead to identical locking predictions.

7.4.1 Oscillator Spectrum

The motivation for this section is to understand the overall locking attributes of the oscillator circuit. The influence of a stable injected signal on the oscillator frequency is readily interpreted. These experiments are the basis for the phase noise calculations presented and discussed in Section 7.5.1 Phase Noise Measurements.

See Section 5.5 Experiments Conducted for more detailed description. Several types of experiments were conducted to determine differences in the oscillator spectrum under various injected signals. First are the optically injected cases which are followed by direct electrical signal injection on the oscillator gate port.

In Figure 10 Oscillator Spectrum the free running oscillator (A1 and A2) is compared to optically induced changes in the oscillator output. All experiments in Figure 10 were conducted with the oscillator output detected by the HP8562A Spectrum Analyzer. The span is 2 MHz, the resolution and video bandwidths are 30 KHz and 3 KHz respectively, the attenuation level is 20 dBm, and reference level equals 10dBm for all cases. Table 2 gives the bias conditions for the oscillator, the amount of injected optical power, the magnitude of the DC drain to source impedance ($|Z_{ds}|$) and the resultant free running frequency. The reason that two bias conditions were used in these experiments was to produce a frequency to which the Reference & Slave could be tuned. It is extremely difficult experimentally to tune all three lasers with current and temperature without experiencing optical mode hops. It was necessary to start with the free running oscillator frequency equal to 2.959 GHz (A2) to lock the oscillator to the locked laser cases E-I.

The first row of Figure 10 is the oscillator output when a single laser is injected with an optical power of 0.4 mW measured before the focusing optics which calculates to approximately 20 μW impinging onto the MESFET active region. There is no laser locking for these experiments (B-D). B demonstrates a 4.5 MHz positive frequency shift from the free running oscillator A1. When an unmodulated

(or DC) beam is injected, a frequency shift occurs which is the result of the Schottky photo-voltage developed across the depletion region of the MESFET. The photo-voltage adds to the gate to source voltage (V_{gs}). The consequence of the DC light induced frequency shift is important because this is the frequency that determines the locking range *not* the free running oscillator frequency. The frequency injected must be greater than the oscillator frequency (after the shift) for locking to occur. In Section 7.4.2 Locking , the bounds on the locking range are discussed further. B is also important because we can see that the DC optical signal appears to increase the oscillator noise. This is in fact the case. Because of increased quantum noise generated between the photon-electron interactions in the MESFET, the output spectrum of the oscillator deteriorates when the DC optical signal is injected. The skirt of the spectrum is increased by 10dBm in B which means that the overall noise floor of the oscillator is increased. The increase in the DC level of the oscillator simply a result of Equation (7-3)

$\mathcal{E}_1$ = Free Running Oscillator Field = $E_1 e^{j\omega_1 t}$

$\mathcal{E}_2$ = Unmodulated (DC) Injected Laser Field = E_2

$\mathcal{E} = \mathcal{E}_1 + \mathcal{E}_2$

$$I = \mathcal{E} * \mathcal{E}^* = E_1^2 + E_2^2 + 2E_1E_2\cos(\omega_1)t \qquad (7\text{-}2)$$

Case C depicts the spectrum when a single modulated laser at 3.0025 GHz is injected into the oscillator but does not lock the oscillator. By using micrometer positioning stages in the experiment, the laser beam is intentionally misfocused at the

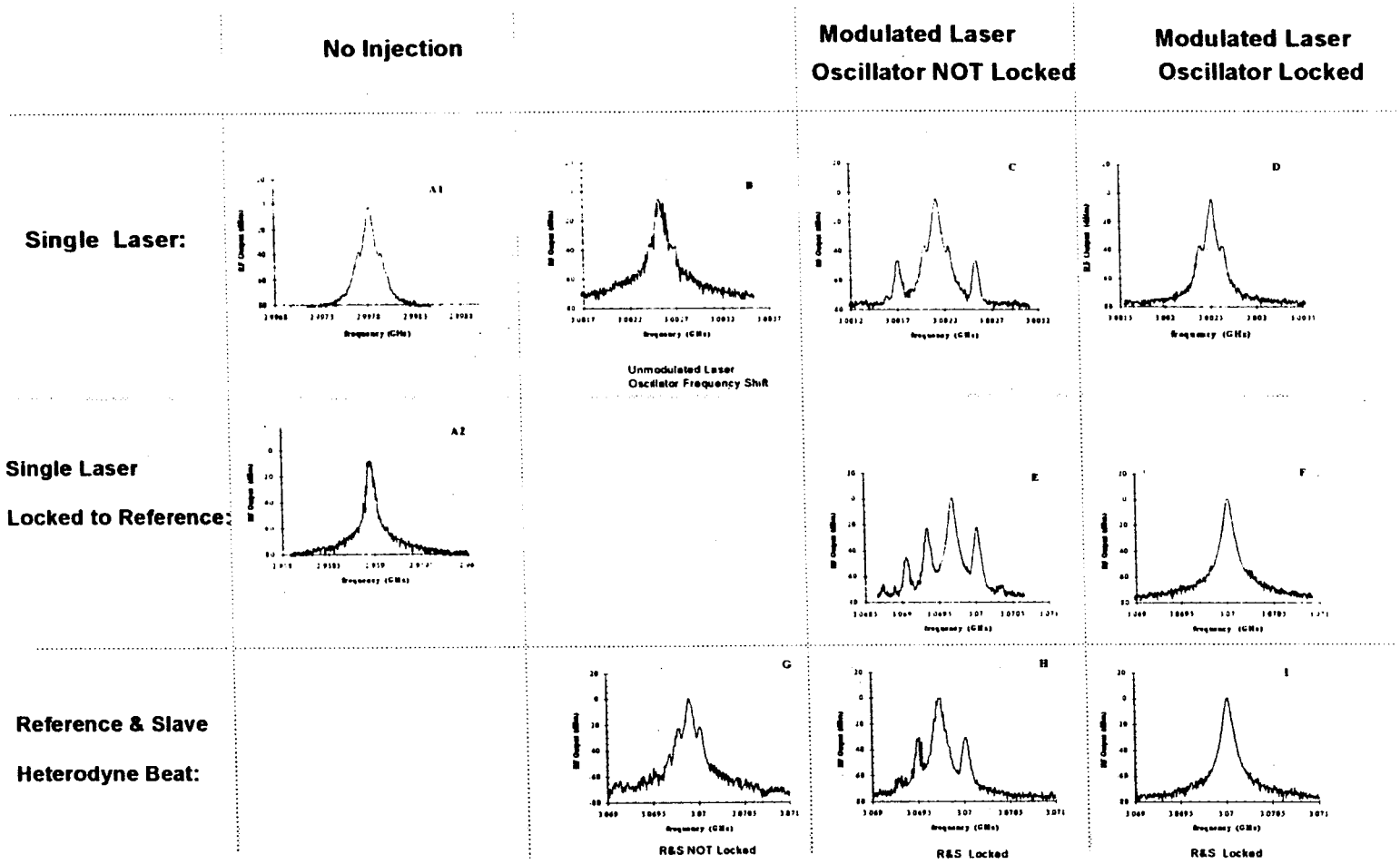

Figure 10 Oscillator Spectrum

Table 2 Oscillator Bias Conditions

Reference: Figure 10	V_{gs} v	V_{ds} v	$P_{optical\ Measured}$ mW	$P_{optical\ Calculated}$ µW	I_{ds} mA	$\|Z_{ds}\|$ Ω	f GHz
A1 - Free Running	-0.3	1.2			7.36	163	2.998
B-D - No Laser Locking			0.4	20	8.38	141	3.002115
A2 - Free Running	-0.55	1.5			7.32	194	2.959
E-I - Laser Locking			2.2	104.9	8.46	167	

MESFET plane. The focusing system was designed to bring the laser beam to its tightest gaussian spot at the system focal plane (i.e., the MESFET) and when it is misfocused, the amount of optical power actually reaching the GaAs active region decreases exponentially. The gaussian analysis and subsequent power calculations are dealt with completely in Section 5.3 Experimental Free Space Optical System for MESFET Injection. The intermodulation products between the DC shifted frequency (3.002115 GHz) and the modulated frequency of the laser (3.0025 GHz) are readily seen. The intermodulation frequency (IF) is 385 KHz which produce significant products at 3.0017 and 3.0025 GHz (Products = Sifted Frequency ±385 KHz). By bringing the beam back into focus at the MESFET, the single modulated laser locks the oscillator in Case D to the laser modulation frequency of 3.0025 GHz. The result of single laser modulation on the oscillator spectrum is given by equation (7-3).

$\mathcal{E}_1$ = Free Running Oscillator Field = $E_1 e^{j\omega_1 t}$

$\mathcal{E}_2$ = Modulated Injected Laser Field = $E_2 e^{j\omega_2 t}$

$$\mathcal{E} = \mathcal{E}_1 + \mathcal{E}_2$$

$$I = \mathcal{E} * \mathcal{E}^* = E_1^2 + E_2^2 + 2E_1E_2\cos(\omega_1 - \omega_2)t \qquad (7\text{-}3)$$

The second row in Figure 10 is the injection case for a single modulated laser at 3.07 GHz which is locked to a reference laser. This stabilizes the modulated laser mode relative to the reference laser. Only the modulated laser is injected into the oscillator. Case E shows the unlocked oscillator with IF equal to ±300 KHz. Case

F shows the oscillator locked. The frequency difference between A2 and F is 111 MHz. Although 10% of this can be attributed to DC component of the light shifting the free running oscillator frequency, this shows a superior locking characteristic which is attributed to the careful design of the focusing system.

The third row in Figure 10 represents the heterodyne beat at 3.07 GHz of the reference and slave lasers injected into the oscillator. If the reference and slave lasers are not locked, their beat signal is broad (See Section 2.4 Characteristics of the Modulated Laser Spectrum) and this is directly superimposed onto the oscillator spectrum, G. In H, the heterodyne laser beat is locked and injected into the oscillator. The oscillator experiences severe mode competition when it is unlocked (H). Finally, in Case I, the oscillator is locked to the reference and slave beat note at 3.07 GHz.

A consequence of the injection phenomenon is a broader frequency span at the noise floor due to the additional DC component added to the oscillator mode. Table 3 compares the spans. The largest normalized spans are the unlocked oscillator cases (B and G). In particular, the unmodulated light injection B increases the DC level the greatest amount because there is no frequency component in the injected light (7-2). This is due to the amplitude noise (7.5.2 AM Noise Measurements) that is added to the oscillator. In G, the reference and slave are not locked and their heterodyned beat increases the amount of noise about the oscillation frequency. This laser beat is shown in Figure 2.4b Laser Linewidth. The main result here is that the locking provides frequency stability (i.e., reduced phase noise) at the expense of a slightly increased span at the noise floor. The single laser case D

increased the span 1.2 times the free running oscillator, and the heterodyned laser locked case I resulted in a modest 1.08 increase which is well within the range of experimental error. Case I is 10% better than case D. Locking a single modulated laser to a reference laser, F, will lock the oscillator frequency but increases the span to 1.54.

When comparing F to D or to I, several observations about the lock quality can be made:

1. Injecting a single locked laser F into an oscillator deteriorates the spectrum by 40% over the single laser, D, or heterodyne, I, cases. This is because the locking of a single laser adds to the noise floor. in the heterodyne case the differences subtract from each other and none.

Table 3 Frequency Span during Lock

Injection Case (Refer: Figure 10)	Frequency Span @ -70 dBm floor	Normalized Span = $\frac{\text{Light}}{\text{Dark}}$	
A1	500 KHz		
B	1.7 MHz	B÷A1	3.4
D	600 KHz	D÷A1	1.2
A2	650 KHz		
F	1.0 MHz	F÷A2	1.54
G	1.8 MHz	G÷A2	2.77
I	700 KHz	I÷A2	1.08

2. Heterodyne improves somewhat on the single laser case. Because the heterodyne eliminates the dc. The difference between D and I is not significant which is mainly attributed to the experimental conditions. The heterodyne beat had 10-20% less power at the injected frequency than the single modulated laser. This can be seen by measuring the response of the oscillator (P_{osc}) and the frequency from the oscillation (Δf) for several laser modulation powers (P_{rf}). The normalized oscillator output is plotted for different levels of laser modulation power and shown in Figure 11. The locking model (7.4.2 Locking Model) further explains the influence of modulation power required to produce on a strong stable lock.

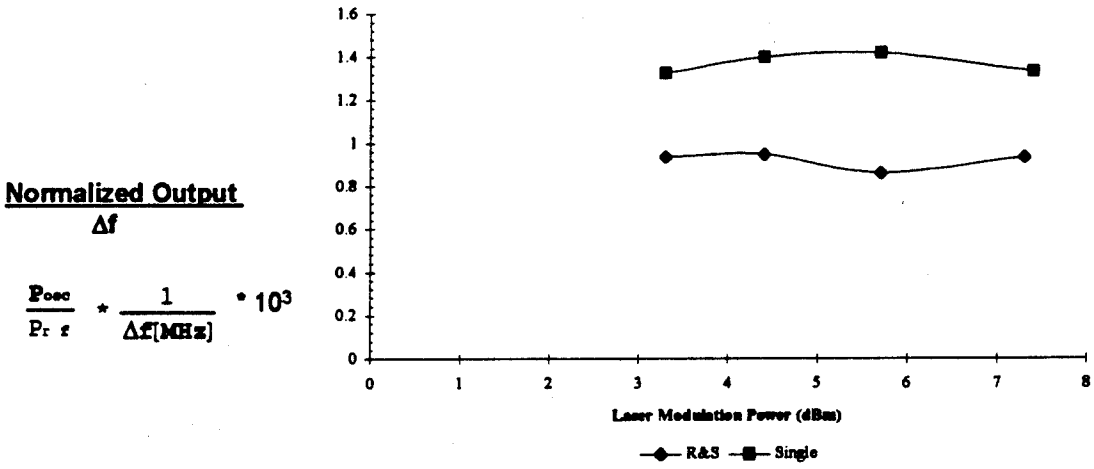

Figure 11 Single & Heterodyne Oscillator Power per frequency

7.4.2 Locking Model

In this section, the influence of modulation power and frequency on locking characteristics is presented. Adler's equation deals with the locking bandwidth of pulled oscillations. It is experimentally shown that the theory fails if the injected frequency is less than the free running oscillator frequency. Both electrical and optical injection experiments show that locking occurs only if the injected frequency is greater than the free running oscillator frequency.

The frequency range or bandwidth over which locking occurs is related to the amount of power injected into the device and the quality factor Q_{ext} of the total oscillator circuit. Kurokawa used quasi-static and dynamic analyses to explain the most important phenomenon of microwave oscillators, AM and FM noise and locking in terms of linear networks[26]. The design of oscillators starts with the concept of negative resistance which can be described as a source of electrical energy. Negative resistance implies an active device but the reverse is not necessarily true. IMPATT diodes are two terminal devices which are inherently negative resistance devices, but however, the MESFET may require an external network to create the negative resistance. In the oscillators designed for this Thesis, the microstrip and the MESFET together create this phenomenon. In general, a negative resistance is a nonlinear function of the RF current flowing through it. In the design of microwave oscillators, S-parameters analysis is the common means of design. However, to gain insight into the processes, Kurokawa's model is used to quantitatively discuss the properties of injection locked oscillators in a convenient

and straightforward manner. Any oscillator can be modeled as nonlinear impedance dependent on the current passing through it $\bar{Z}(A)$ shown in Figure 12 Nonlinear microwave oscillator model. The reference plane is located at the device terminals. This model is then redrawn in terms of the circuit impedance seen from the device $Z(\omega)$ and the device impedance $\bar{Z}(A)$ in Figure 13a.

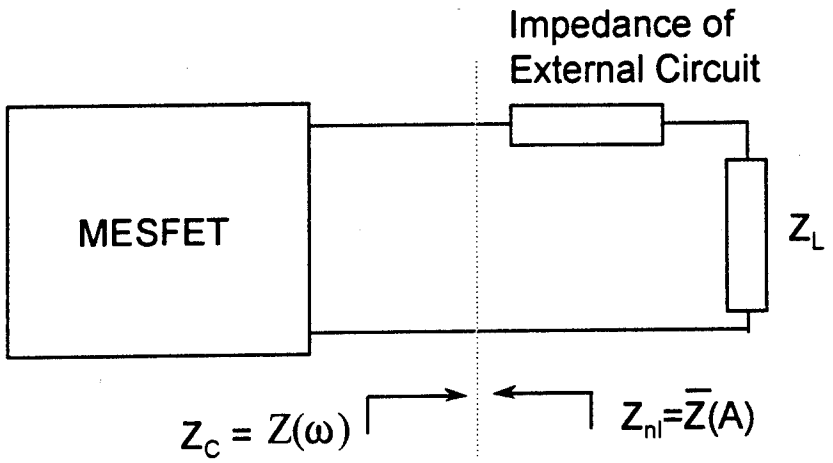

Figure 12 Nonlinear microwave oscillator model

The reference plane is at the MESFET contacts because the external circuit and load impedances which are combined to represent the total impedance looking into the cavity from the output port of the MESFET. This total impedance is a strong function of ω and RF current amplitude. The second reason is that there is a separation between passive and active elements, and therefore, once the device current is obtained, the oscillator output can be calculated using a passive linear transfer function approach. The equation of the free running oscillation is the following:

$$[Z_{nl}(I,\omega) + Z_c(\omega)]I = 0 = [Z(\omega) - \overline{Z}(A)]I$$
$$Z_t = R_t + jX_t \equiv Z_{nl}(I,\omega) + Z_c(\omega)$$

The current is not equal to zero but finite. Therefore, Z_t must be equal to zero which means the nonlinear negative reactance and the passive reactance sum to zero.

$$Z(\omega) - \overline{Z}(A) = 0$$
$$Z(\omega) = \overline{Z}(A)$$

The locus of the circuit impedance and the negative of the device impedance are drawn on the complex plane in Figure 13b. The arrow points to increasing ω in the $Z(\omega)$ line and increasing RF current amplitude A in the device line Z(A). The onset and stability of the oscillation can be studied with impedance diagrams. However, the immediate concern is the quasi-static analysis of injection locking.

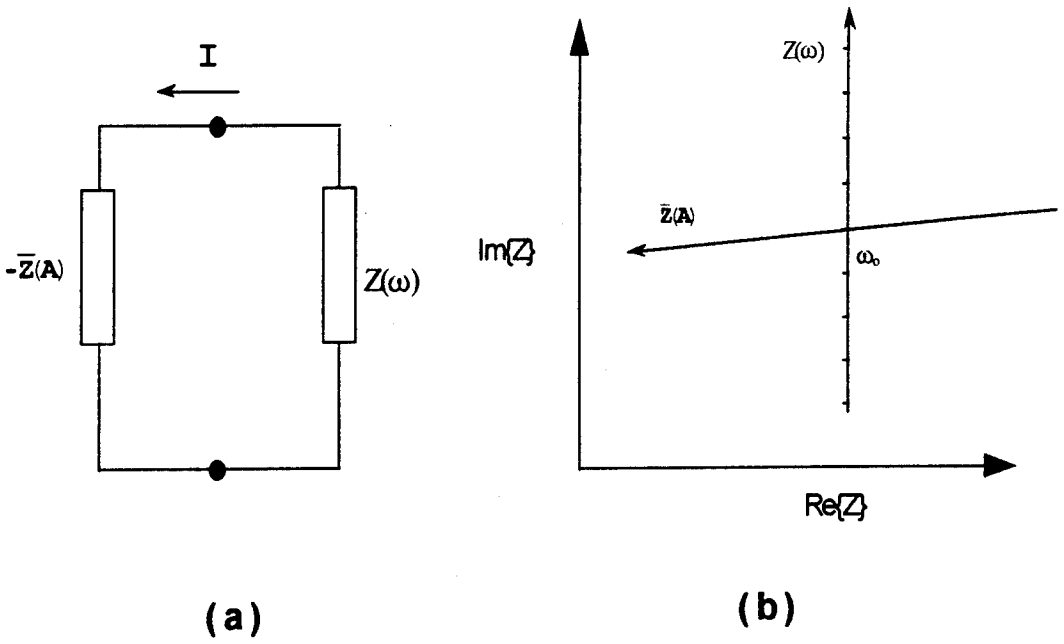

Figure 13 a) Microwave oscillator equivalent circuit, b) Impedance locus and device line

The case of oscillator injection can be represented by an additional voltage source E in series with the passive impedance (Figure 14a). For small signal assumptions, the magnitude of the injected signal is small compared to the free running oscillation, and the RF current is approximated by Ao. Because these are valid assumptions for the injection levels, the injection vector length is not varied as the operating point moves. For now, it is not necessary to distinguish between optical or electrical signal injection which will be discussed later. In the following equations, the injected signal frequency is ω_{inj}, and the phase difference between the current and the injected voltage is ϕ:

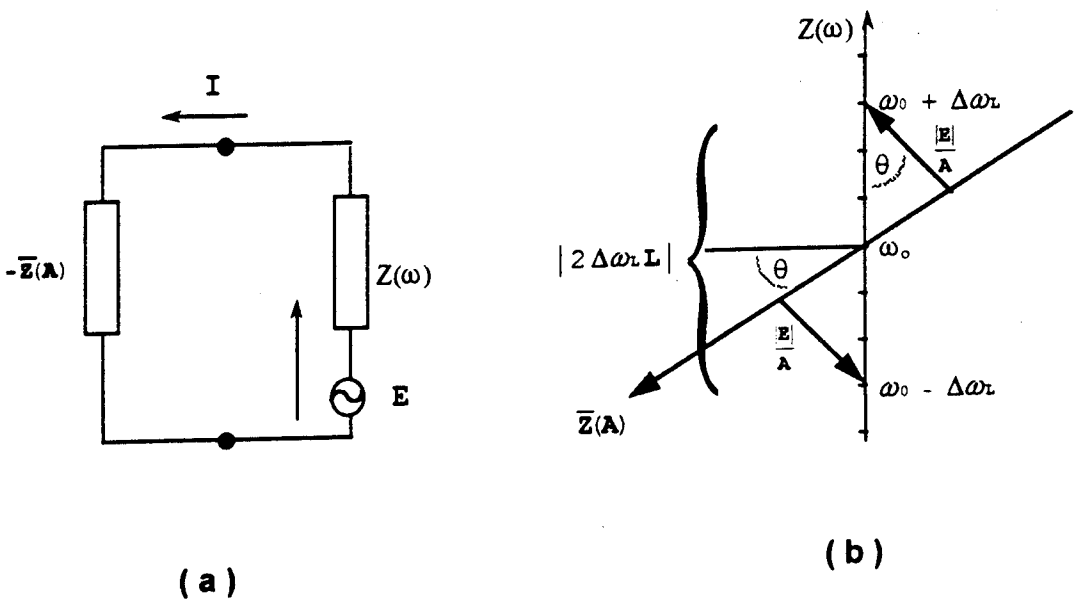

Figure 14 a) Injected oscillator equivalent circuit, b) Relation between the injection vector, impedance locus, device line and locking range

$$\left[Z(\omega_{inj}) - \overline{Z}(A)\right]I = E$$

$$Z(\omega_{inj}) = \overline{Z}(A) + \frac{|E|}{A_o} e^{-j\phi}$$

Using the latter equation, the construction of the impedance locus diagram under locking conditions can be completed (Figure 14b). If the magnitude of the injected voltage is constant but the injected frequency is varied, the injection vector $\frac{|E|}{A}$ will be anchored at the corresponding current value on the $\overline{Z}(A)$ line and point to different frequencies on the $Z(\omega)$ line. If the injected amplitude is changed with a

constant frequency, the injection vector tail will move along the device line $\overline{Z}(A)$ and the head remains fixed at $Z(\omega_{inj})$.

When the distance from $Z(\omega)$ to the device line $\overline{Z}(A)$ becomes longer than $\frac{|E|}{A}$, the injected frequency is outside of the locking range $2\,\Delta\omega_L$ {i.e., $(\omega_o - \Delta\omega_L) < \omega_{inj} < (\omega_o + \Delta\omega_L)$ }. The locking range must satisfy the following:

$$|\,2\,\Delta\omega_L L\cos\theta\,| = \frac{|E|}{A_o}$$

where θ represents the inclination of the device line from the direction perpendicular to the impedance locus. When the device line and impedance locus are perpendicular, $\cos\theta=1$ and the equation reduces to the well known form of Adler's equation. Adler's equation neglects the variation of the reactance with the RF current A flowing through it (i.e., $\mathrm{Im}\{Z(A)\} = X(A)$). In Adler's derivation, $\cos\theta$ is absent or equal to 1; this means the device line and the impedance locus are perpendicular. This is fine for systems where devices respond instantaneously to external forces. This is interpreted as X(A) is at most a constant absorbed by the impedance $Z(\omega)$. For microwave oscillators, the nonlinear device reactance is indeed important because it provides the a link to saturation factors present in the device.

The locking equation can be written in terms of the free running oscillator power P_{osc}, the injection power P_{inj}, and the external quality factor Q_{ext} of the resonant circuit (not the loaded Q) with the following substitutions:

$$P_{osc} = \frac{1}{2} R_L A_o^2$$

$$P_{inj} = \frac{1}{2} \frac{|E|^2}{4R_L}$$

$$Qext = \omega_o \frac{L}{R_L} \approx \frac{1}{\sqrt{LC}} \frac{L}{R_L}$$

The total locking range is given by $2\Delta\omega_L$:

$$\Delta\omega_L = \frac{\omega_o}{Q_{ext} \quad \cos\theta} \sqrt{\frac{P_{inj}}{P_{osc}}}$$

$$Q_{ext} = \frac{\omega_o L}{R_L}$$

The development for microwave oscillators is analogous to the theory for laser oscillation in *Chapter 2.6*. *Chapter 4* gives a comparison between microwave and optical oscillation terminology.

To study the oscillator locking properties, the oscillator was locked to a single modulated laser under various levels of injection $P_{inj}(\omega_{inj})$ at various injected frequencies ω_{inj}. The level of laser modulation (β) is an important parameter in the locking process. The voltage level at the first modulation sideband(ω_{inj}) is approximately a first order Bessel function J1(β) for direct frequency modulation of semiconductor lasers[27].

$$E = J_o(\beta) E_o \sin(\omega_o t) + \sum_n J_n(\beta) E_o \sin\{\omega_o + n\omega_m\} + \sum_n (-1)^n J_n(\beta) E_o \sin\{\omega_o - n\omega_m\}$$

The optical wave is given by $E_o\exp\{j\{\omega_o t) + \beta\sin(\omega_m t)\}$. β is the modulation index. The observed optical intensity at a given sideband is the square of the corresponding coefficient. The level of injection $P_{inj}(\omega_{inj})$ was calculated by computing the square of $J1(\beta)$ which is multiplied by the measured optical intensity times the percentage of power absorbed by the device ($\approx$2%).

In Figure 15, the minimum $P_{inj}(\omega_{inj})$ to lock the oscillator is plotted versus the frequency bandwidth ($\Delta\omega = \omega_{inj} - \omega_{osc}$). The data was observed by fixing ω_{inj} and then varying the laser modulation power until lock was achieved. The minimum laser modulation power is shown on the far right scale while the left scale shows the actual injected power at ω_{inj}. The locking gain is the ratio of the power of the free running oscillator to the power injected (Figure 16 Locking Gain vs. Injected Optical Power) and is used in the literature to measure the lock quality[28]. The locking range or bandwidth Δf is the frequency range over which the oscillator remains locked to the injected signal. The normalized frequency range $\Delta f/f_{inj}$ is plotted versus injected power and versus gain. The characteristic 20 dB/decade slope of the locking bandwidth curve versus gain is shown in Figure 18.

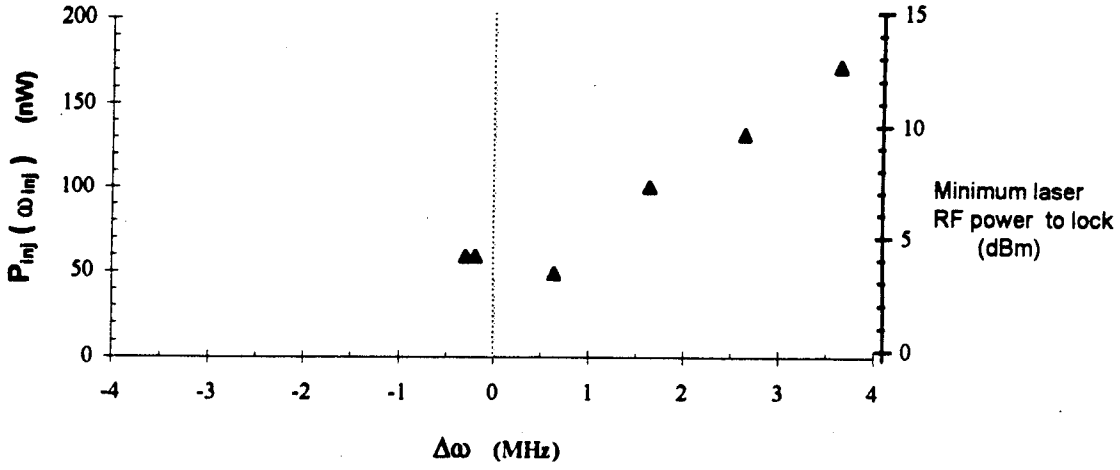

Figure 15 Minimum Laser Modulation Power vs. Oscillator Locking Range

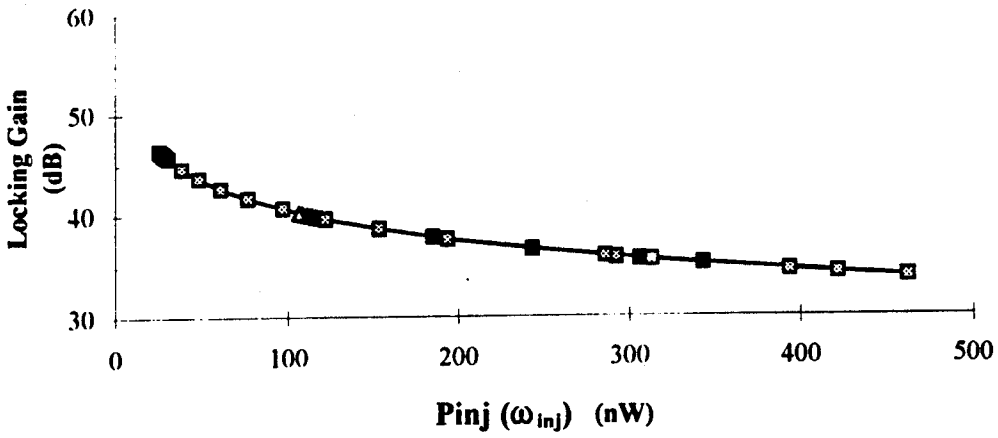

Figure 16 Locking Gain vs. Injected Optical Power

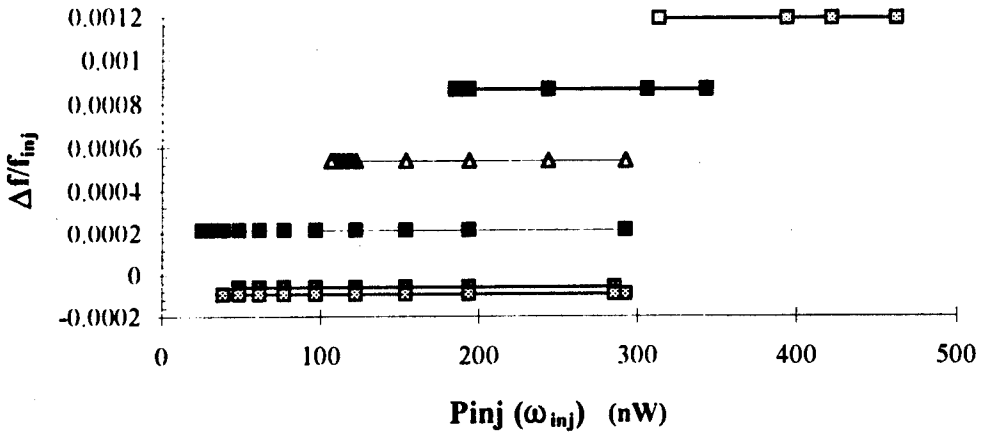

Figure 17 Locking range versus injected optical power

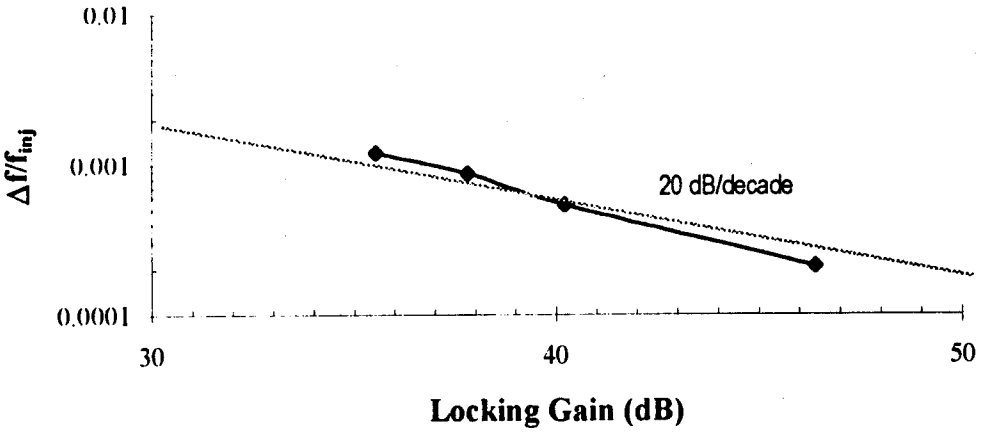

Figure 18 Locking bandwidth versus locking gain

When the injected signal is out of locking range but within the gain bandwidth of the circuit, the oscillator acts as an amplifier of the injected signal. After eliminating RF radiation in the lab room, the unlocked peak of the injected signal was clearly visible (Figure 19 Out of Locking Range - Oscillator amplifies injected signal). Under these conditions, the circuit can be considered a type of negative resistance amplifier for which the device line and impedance locus have no intersection (Figure 20 Relationship between Z(w) and Z(A) for a negative resistance amplifier).

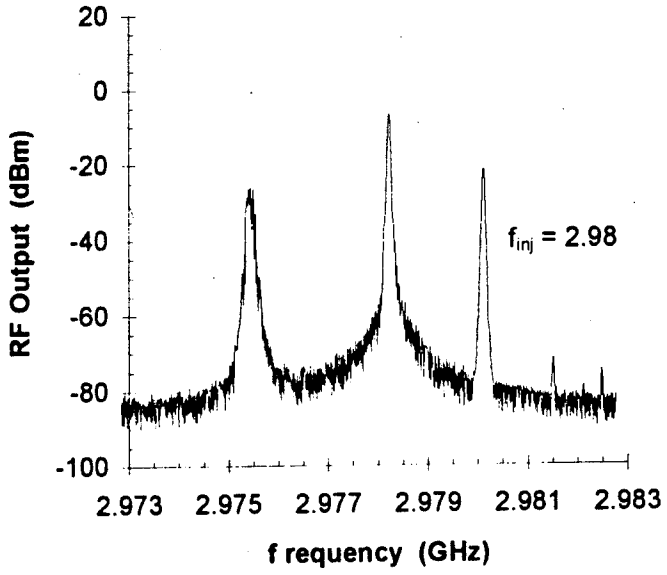

Figure 19 Out of Locking Range - Oscillator amplifies injected signal

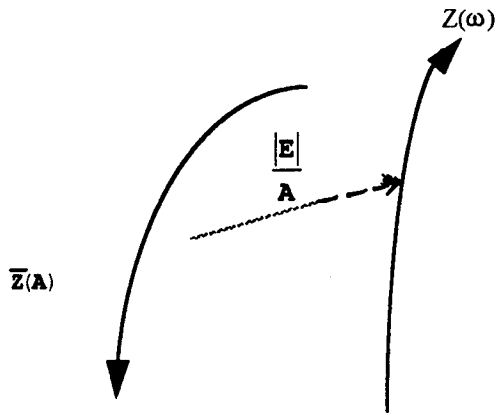

Figure 20 Relationship between Z(ω) and Z(A) for a negative resistance amplifier

7.4.3 Non-symmetric Locking Bandwidth

The locking model describes a symmetric locking bandwidth $2\Delta\omega_L$ { $(\omega_o - \omega_{inj}) < \Delta\omega_L < (\omega_o + \omega_{inj})$ }around the free running oscillator frequency. However, for the experiments conducted for this Thesis, the locking bandwidth was decidedly one sided. The oscillator locked only when the injected frequency was greater than the free running oscillator frequency $\omega_{inj} > \omega_o$ except within small negative bandwidth well within the frequency noise range of the oscillator.

Figure 21 Locking bandwidth versus injected optical power shows the experimental data. The injected power was fixed and the injected frequency was incremented away from the free running oscillator frequency until the oscillator would not lock. The unlocked points are joined by a curve to delineate the unlocked from the locked regions. For Δf greater than zero, the locking bandwidth reached

approximately 4 MHz. However, for Δf less than zero, there was no locking for all frequency and power combinations with the exception points shown around Δf equal to -200 KHz. The instantaneous oscillator frequency could be anywhere within the noise band due to frequency fluctuations. To assure that the data was taken outside of the frequency noise range, data was taken for frequency magnitudes greater than 1 MHz. At 1 MHz and greater, the noise drops off significantly. There was no locking at -1 MHz as indicated in Figure 21).

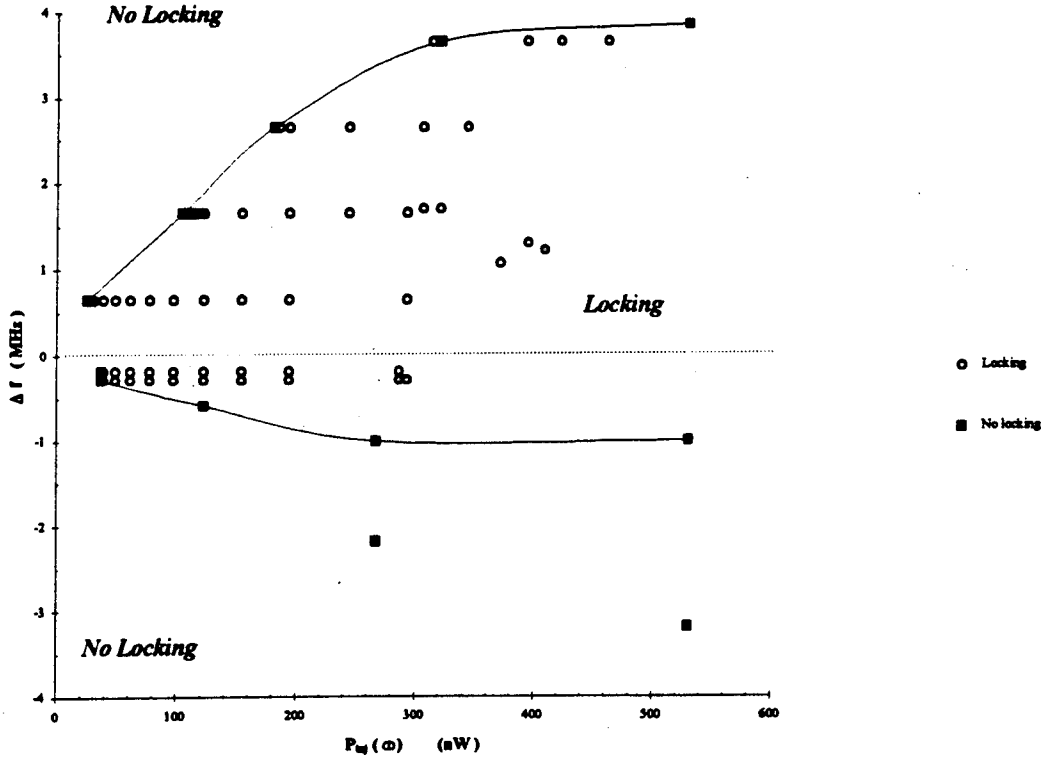

Figure 21 Locking bandwidth versus injected optical power

Since the frequency tunes with injected optical power, there was the possibility that the shift was forcing the frequency out of the locking range before the oscillator could lock to the injected frequency. An effort was made to inject the oscillator with unmodulated optical power and to note the shifted frequency. Without changing the power level, the laser was modulated at a frequency within the bandwidth of the shifted frequency of the oscillator. Locking observations were then completed with the same nonsymmetric bandwidth results: The oscillator locked only when the injected frequency was greater than the shifted oscillator frequency $\omega_{inj} > \omega_{shifted}$.

Since electrical injection of oscillators was well established, the locking bandwidth was measured with an electrical RF signal superimposed on the oscillator gate. The results were the same. The spectrum of the oscillator is shown in Figure 22 Locking Characteristics: (A) free running oscillator, (B) the locked electrically injected output $f_{inj} > f_{osc}$, (C) the unlocked electrically injected output $f_{inj} < f_{osc}$, (D) the locked optically injected output $f_{inj} > f_{shifted}$, (E) the unlocked optically injected output $f_{inj} < f_{shifted}$.

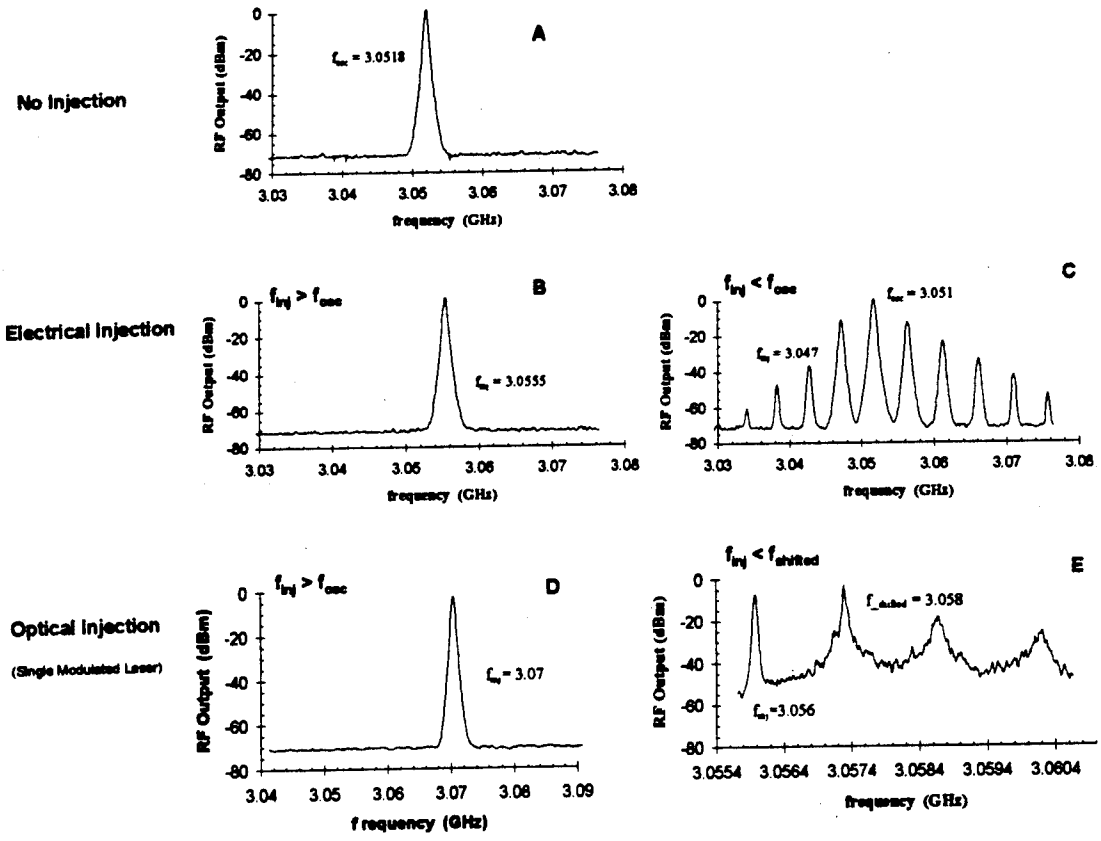

Figure 22 Locking Characteristics

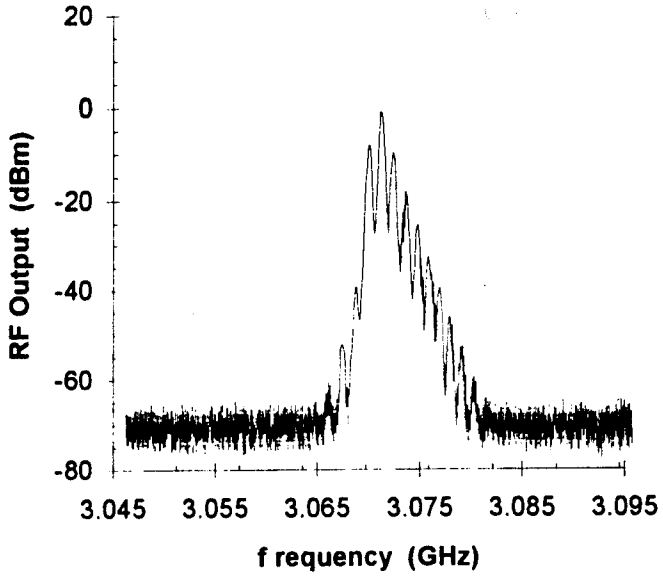

Figure 23 Unlocked spectrum

Circuit analysis techniques and Adler's equation do not provide for the effect of transmission lines which is the reason for the asymmetric locking bandwidth. In the design of the transmission lines in the microstrip circuit (See *Chapter 5*), the gate stub, which provides the resonance through feedback, is not symmetric about the gate feed line. Given the microstrip dielectric and physical dimensions and the design frequency (3 GHz in this case), the gate stub had to be placed at the end of the matching line. Therefore, only wavelengths smaller than the design frequency can be physically supported by the stub. Since the frequency is inversely proportional to the wavelength, locking occurs if the injected wavelength is smaller than the free running oscillator wavelength:

$$\omega_{inj} > \omega_o \quad \text{or equivalently} \quad \lambda_{inj} < \lambda_o$$

7.5 Oscillator Noise Behavior

The free running oscillator is subject to stochastic noise processes which mix with the free running oscillator and produces modulation of the carrier. This noise modulates

the free running oscillator frequency both in amplitude and in angle. Oscillator noise can be explained starting with the static model used in the previous section and expanding it with a dynamic analysis. This section will give the basis for both amplitude and frequency noise in oscillators and the rationale for oscillator noise reduction when it is injected. Experimental measurements of the phase noise and the amplitude noise are given in 7.5.1 Phase Noise Measurements and 7.5.2 AM Noise Measurements respectively.

The device line and impedance locus diagrams of 7.4.2 Locking Model are the starting point for quantitative understanding of the oscillator noise origins. Noise is represented by a voltage source on the device line $e_n(t)$ as shown in Figure 24a. The device line is "modulated" by the noise which causes the line to vibrate both longitudinally and transversely as shown in Figure 24b. The longitudinal vibration gives rise to amplitude noise about the free running oscillator frequency ω_o. The transverse changes in the device line represent changes in the frequency noise. Under the assumption of small signals, the device line vibrations due to amplitude noise are small. However, noticeable amplitude modulation noise occurs because of the transverse vibration of the line when the locking frequency is not in the center of the locking bandwidth..

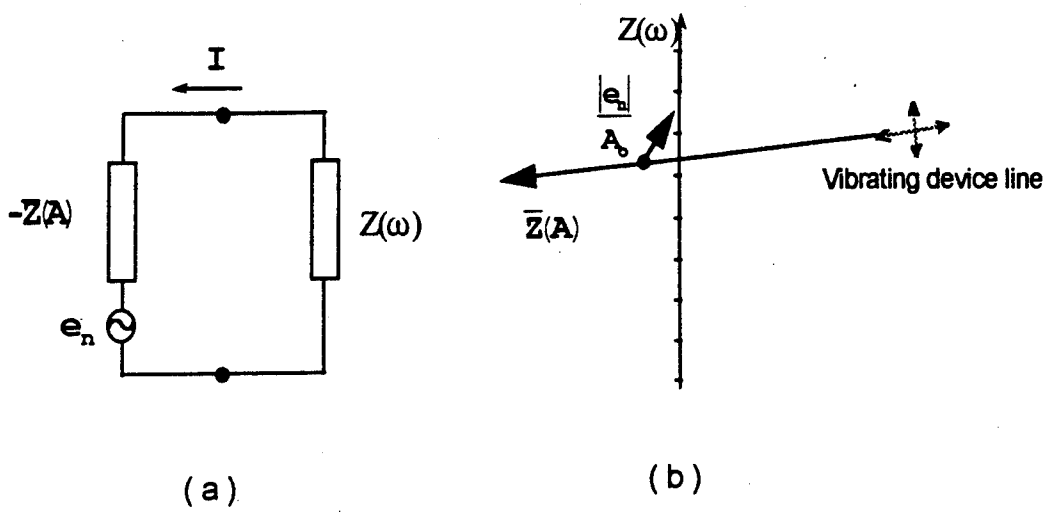

Figure 24 a) Model of Oscillator Noise, b) Vector relationships

In the case of the injection locked oscillator (Figure 25) the head of the injection vector ($|E|/A$) is locked to ω_{inj}. Since the injection frequency point is fixed, the amount of frequency noise is virtually eliminated. As a result of the transverse movement of the device line, the injection vector direction and the current phase changes. Therefore, the locked oscillator still will exhibit some small amount of FM noise which is attributed to the latter considerations. Also, note that the phase changes at a rate that is inversely related to the magnitude of the vector. Therefore, increases in injection level decrease the frequency noise as is supported by experimental data in the next sections. Note that the phase is the rate of change of the frequency. Since the injection vector length is constant and its head is fixed, the transverse vibration adds more amplitude noise to that caused by the longitudinal movement.

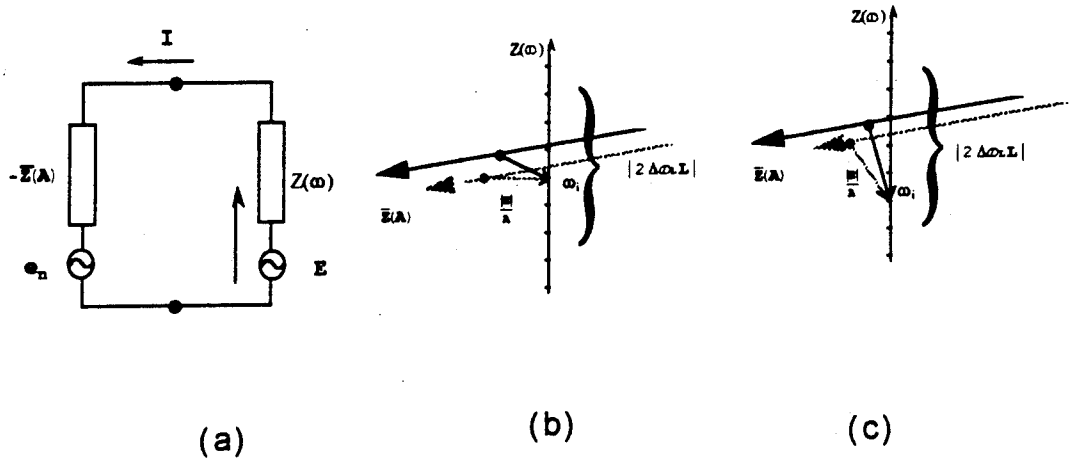

(a) (b) (c)

Figure 25 a) Noise and injection model, b)ω_i middle of locking bandwidth, c) ω_i near end of the locking bandwidth

Since both the RF current amplitude A and phase ϕ are slowly varying functions of time, the time derivatives are replaced in the frequency domain by the following.

$$\frac{d^n}{dt^n}\mathrm{Re}\left\{Ae^{j(\omega t+\phi)}\right\} \rightarrow \mathrm{Re}\left\{\left[j\left(\omega+\frac{d\phi}{dt}\right)+\frac{1}{A}\frac{dA}{dt}\right]^n Ae^{j(\omega t+\phi)}\right\}$$

From the static analysis in 7.4.2 Locking Model, the frequency variables ω are then replaced with the following:

$$\omega \rightarrow \left[j\left(\omega+\frac{d\phi}{dt}\right)+\frac{1}{A}\frac{dA}{dt}\right]$$

The static equation of the oscillator becomes

$$\mathrm{Re}\left\{\left[j\left(\omega+\frac{d\phi}{dt}\right)+\frac{1}{A}\frac{dA}{dt}\right]-\overline{Z}(A)\right\}Ae^{j(\omega t+\phi)} = |E|\cos(\omega_{inj}t+\psi)+e_n(t)$$

where ψ is the phase of the locking signal which is a slowly varying function of time. The result is integrated over the period of one RF cycle, splitting the results into real and imaginary components and ignoring higher order derivatives of dϕ/dt and dA/dt,

$$\mathrm{Re}\left\{Z\left(\omega_{inj}+\frac{d\phi}{dt}-j\frac{1}{A}\frac{dA}{dt}\right)-\bar{Z}(A)\right\}A =$$

$$|E|\cos(\phi+\psi)+\frac{2}{\tau}\int_{t-\tau}^{t} e_n(t)\cos(\omega_{inj}t+\phi)dt$$

$$-\mathrm{Im}\left\{Z\left(\omega_{inj}+\frac{d\phi}{dt}-j\frac{1}{A}\frac{dA}{dt}\right)-\bar{Z}(A)\right\}A =$$

$$|E|\sin(\phi+\psi)+\frac{2}{\tau}\int_{t-\tau}^{t} e_n(t)\sin(\omega_{inj}t+\phi)dt$$

From the dynamic equations, the high frequency noise components and the oscillator's response to modulated injected signals can be studied.

7.5.1 Phase Noise Measurements

The frequency modulation (FM) noise is discussed in this section. Section 7.5.2 AM Noise Measurements discusses the amplitude noise induced. The short term stability of the device is a characteristic of the FM or phase noise. The noise is considered in terms of modulating the existing frequencies of the oscillator. In the following discussion, the term carrier means the frequency of the oscillator, and modulation frequency refers to the noise frequency mixing with the free running frequency. The effective modulation spectrum contains many frequency components. All of the energy surrounding the carrier can be interpreted in terms of frequency modulation by a random signal of limited spectrum (i.e., noise).

First, the origins of frequency noise are classified in Table 4 Noise Relationship to Frequency. The experimental results show the greatest noise reduction in the realm of white FM noise and flicker phase modulation. Noise in the area of f^4 would require more sophisticated apparatus than designed for these experiments.

Table 4 Noise Relationship to Frequency

Noise	Relationship to frequency
Random Walk FM	f^{-4}
Flicker FM	f^{-3}
White FM	f^{-2}
Flicker Phase Modulation	f^{-1}
White Noise of Phase	-

As described in 7.5 Oscillator Noise Behavior, the phase may simply be described as the rate of change of the frequency. Prior to more rigorous phase noise measurements and calculations, three measurements were taken to show the change of frequency over a time (Figure 26 Frequency Stability over time). In this experiment, the oscillator output spectrum was observed oh HP8562A Spectrum Analyzer while summing the maximum signal for a period of ten seconds. For no optical injection (Figure 26 a), the oscillator output spread 100 KHz while in the cases of the locked oscillator, the spreading was on the order of 10 KHz for both a single modulated laser (Figure 26 b) and for the reference and slave heterodyned beat (Figure 26 c). The measurements were taken with Vgs equal to -0.55v, Vds is 1.5v, Ids with no injection was 7.51mA, and Ids with optical injection is equal to 8.23mA. The free running oscillator frequency was nominally 3.065 GHz. In both (b) and (c), the injected signal was at 3.070 GHz which is exactly the frequency of the signal's peak. The resolution and video bandwidths were 3 KHz, the reference level was 10 dB, and the attenuation was 20 dB, and the span was 500 KHz.

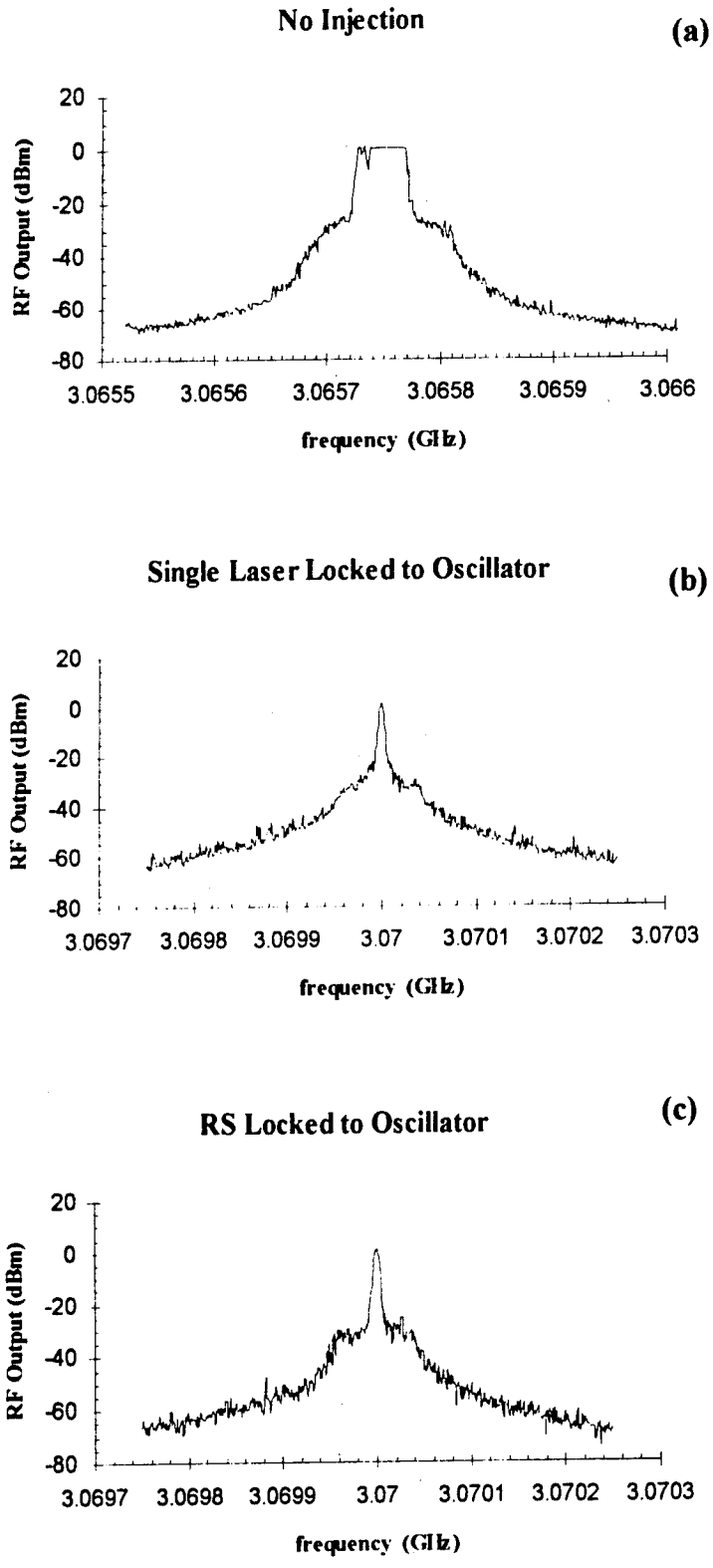

Figure 26 Frequency Stability over time

Two types of noise were measured: the frequency deviation $\Delta\nu$ and the single sideband phase noise $\mathcal{L}(f_m)$. The power spectral density (PSD) of the frequency deviation is denoted by $S_{\Delta\nu}(f_m)$. The oscillator field can be described as a sinusoid with a phase noise term added to include the randomly fluctuating phase $\phi(t)$:

$$E(t) = E_o \sin(2\pi\nu_o t + \phi(t)) = E_o \sin(\Phi(t))$$

The nominal frequency ν_o is equal to $\omega_o/2\pi$. The fraction frequency fluctuations or deviation is the $\Delta\nu.(t)/\nu_o$.

$$\nu(t) = \frac{1}{2\pi}\frac{d\Phi(t)}{dt}$$
$$= \frac{1}{2\pi}\left(\omega o + \frac{d\phi(t)}{dt}\right)$$

Solving for the frequency deviation:

$$\frac{d\phi}{dt} = \nu(t) - \nu_o$$

$$\frac{\partial\nu}{\nu_o} = \frac{\nu(t) - \nu_o}{\nu_o} = \frac{1}{\nu_o}\frac{d\phi(t)}{dt}$$

The single sideband phase noise $\mathcal{L}(f_m)$ is defined as the power ration of the noise level to the carrier. In this context, the random phase noise modulates the free running oscillator frequency which is termed the carrier.

$$\mathcal{L}(fm) = \frac{P_{noise}}{P_{carrier}} = 10\log\frac{P_{noise}}{P_{carrier}} \qquad \left[\frac{dBc}{Hz}\right]$$

The frequency terms are related through the definition of the modulation index m.

$$m = \frac{\Delta f}{f_m} = \Delta\phi$$

The peak frequency deviation is related to the peak phase deviation by f_m (ν_o). Additional information on the modulation index is developed in 7.5.2 AM Noise Measurements.

$$20\log\frac{m}{2} = 20\log\frac{\Delta\nu_o}{f_m} = 20\log\frac{\Delta\nu_{rms}}{\sqrt{2}f_m} = 10\log(\frac{P_{noise}}{P_{carrier}}) + 3dB$$

The power spectral densities (PSD) of the deviations can now be defined. The bandwidth used to measure the signal is denoted by BW. The PSD of the phase deviation is $S_\phi(f_m)$:

$$S\phi(f_m) = \frac{\Delta\phi^2_{rms}}{BW} = \frac{1}{f_m{}^2} \quad S_{\Delta\nu}(f_m) \qquad \left[\frac{rad^2}{Hz}\right]$$

Converting to decibels and relating to the single sideband noise and the PSD of the frequency deviation:

$$S_\phi(f_m) = 20\log\frac{\Delta\phi}{BW} \qquad \left[\frac{dB\ rad}{Hz}\right]$$

$$= \mathcal{L}(f_m) \quad [\frac{dBc}{Hz}] \quad + 3\ dB$$

$$= S_{\Delta\nu}(f_m)\ [\frac{dBHz}{Hz}] \quad - \quad 20\log(\frac{f_m}{1\ Hz})$$

The frequency deviation PSD is $S_{\Delta\nu}(f_m)$:

$$S_{\Delta\nu}(f_m) = \frac{\Delta\nu^2_{rms}(f_m)}{BW} \qquad \left[\frac{Hz^2}{Hz}\right]$$

$$= 20\log\frac{\Delta\nu}{1\ Hz} = 20\log\frac{f_m}{1\ Hz} + \mathcal{L}(f_m)\ [\frac{dBc}{Hz}] + 3\ [dB] \qquad \left[\frac{dB\ Hz}{Hz}\right]$$

To accurately compare the measured noise characteristics, it is necessary to normalize the measurements. The standard method is using an equivalent per Hertz representation of the power level. From the theory of stochastic processes, power can be converted to power level that would be measured in any other bandwidth centered about the same frequency f_m. If W1 is the energy per unit of time of the output spectrum and BW1 is the bandwidth of the measurement, then the power is W1*BW1. This is shown in Figure 27 Bandwidth normalization. The signal used in this figure is an actual trace of the oscillator output with out light injection. In 7.8 Supplement, this unlocked signal with exact axis and the oscillator output locked to a modulated laser at a frequency of 5.012 GHz is presented for reference. Note the decrease in frequency deviation for the light injected case.

Next, the energy in a second bandwidth BW2 can be calculated:

$$\frac{W1}{W2} = \frac{BW2}{BW1}$$

Noting that the square of the RMS voltage is power, the latter equation becomes:

$$\frac{E1}{E2} = \sqrt{\frac{BW2}{BW1}}$$

Finally the equivalent per Hertz representation of the measured signal is as follows:

$$E_{1\,Hz} = \sqrt{\frac{1}{BW1}}$$

In this manner, the bandwidth of the measurement BW1 can be converted to an equivalent per Hertz bandwidth BW2.

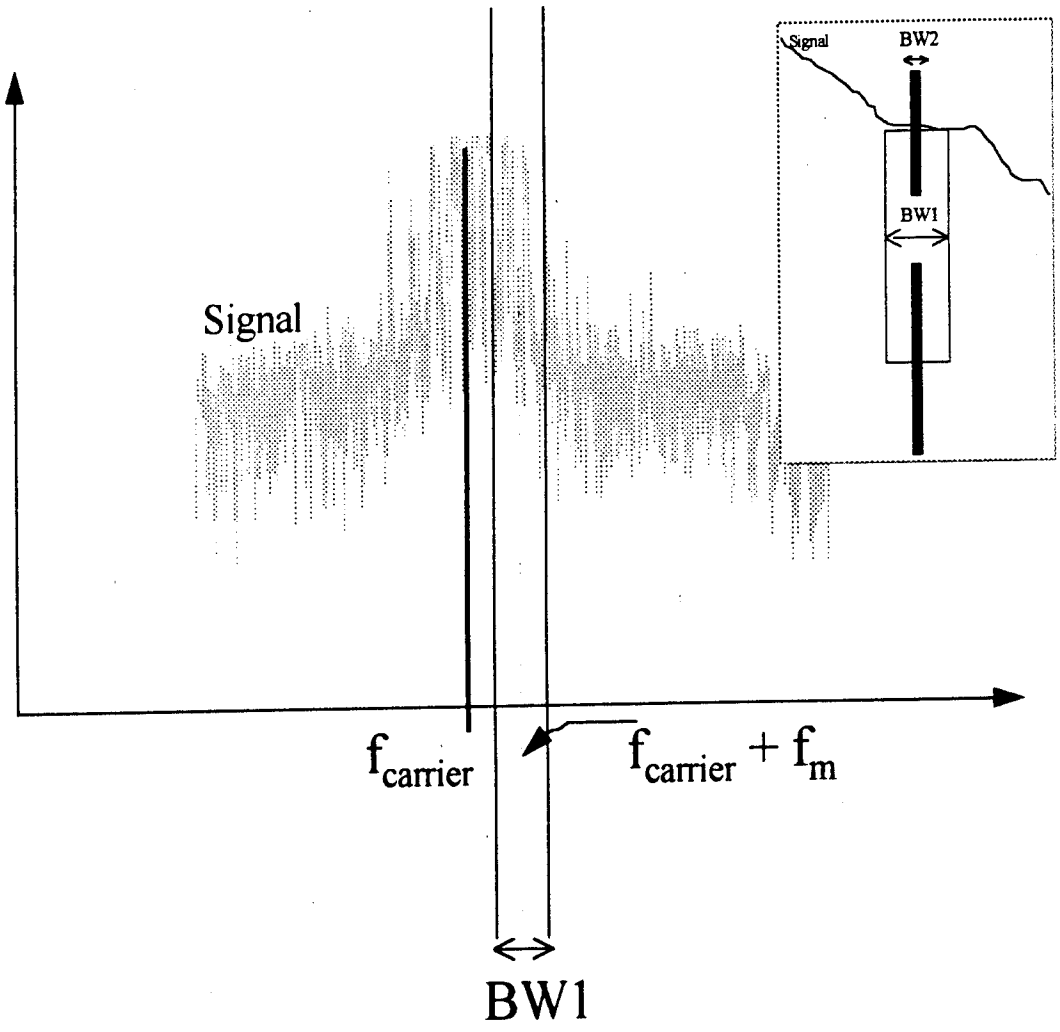

Figure 27 Bandwidth normalization

In Figure 28, the PSD of the frequency deviations $S_{\Delta v}(f_m)$ and in Figure 29 the single sideband phase noise $\mathcal{L}(f_m)$ are plotted for three cases: no injection (dark), modulated master injected and locked to the microwave oscillator, and the heterodyned beat (reference and the slave) produced from the locked lasers. For each case, five measurements were at spans of 10, 50 and 100 KHz, 1 and 100 MHz in order to obtain fine enough resolution to plot the noise near the carrier (i.e., within 100 KHz). In all cases, the oscillator bias was set at Vgs=-0.55v and

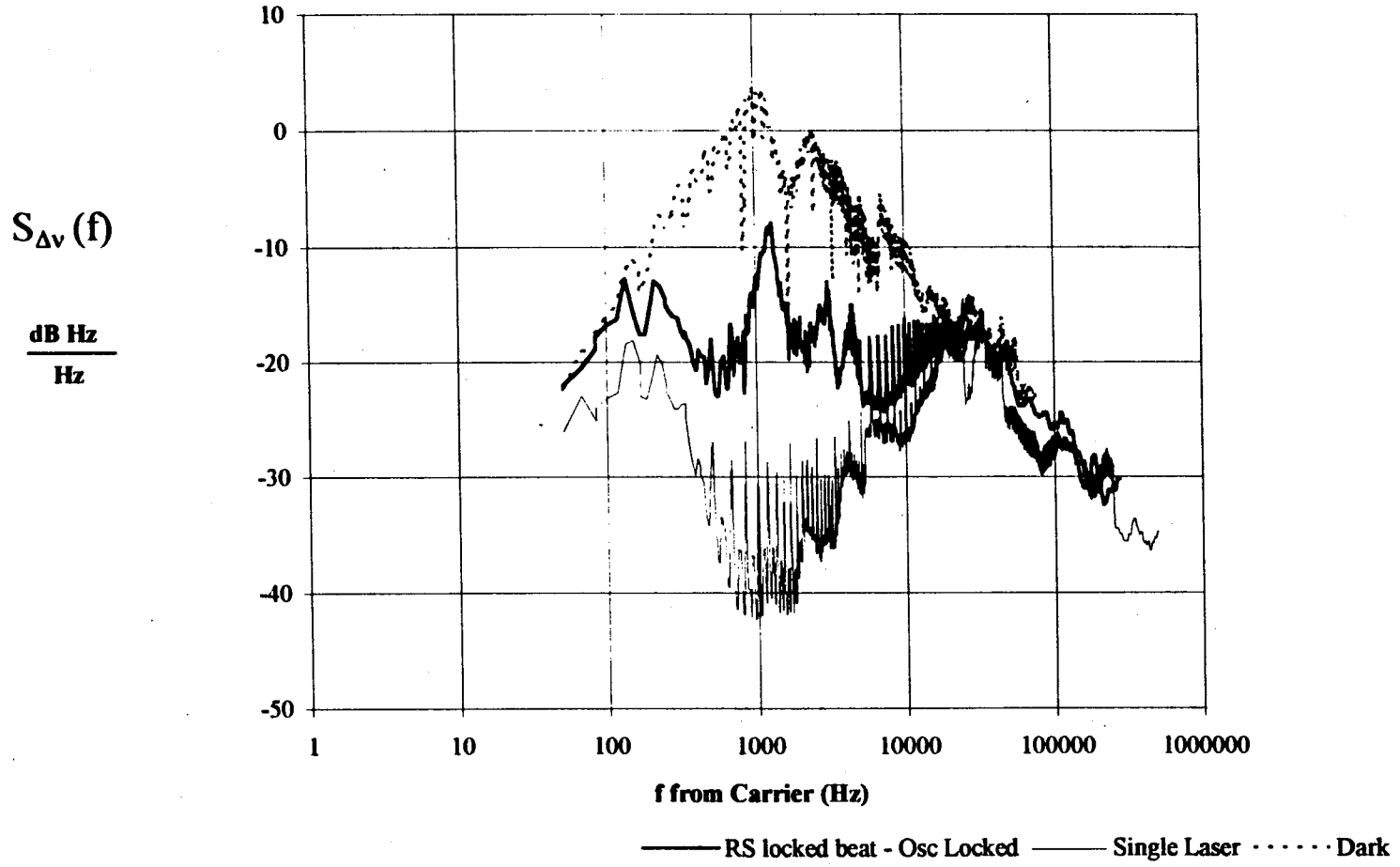

Figure 28 Power Spectral Density of Frequency Fluctuations

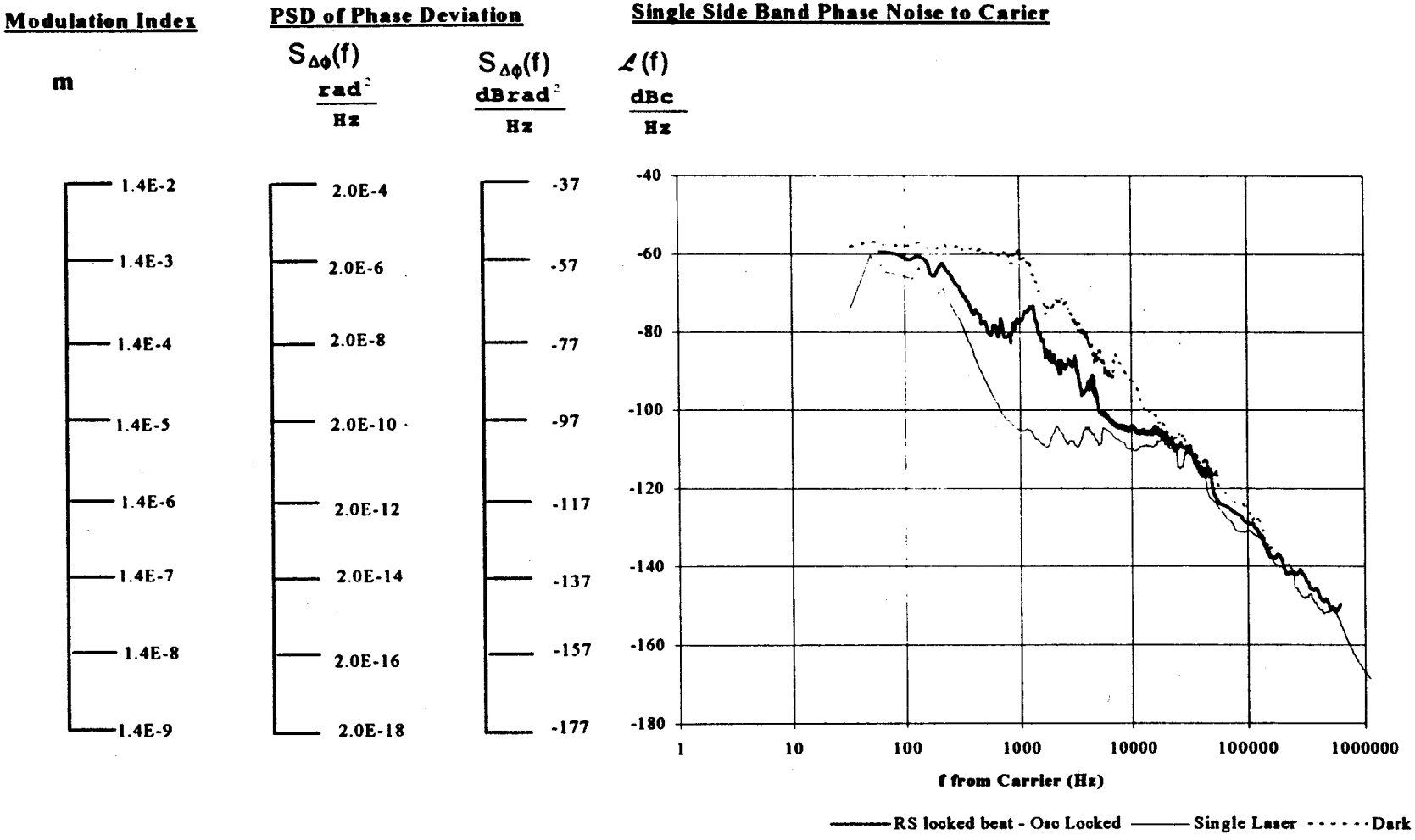

Figure 29 Phase Noise

Vds=1.348v. The laser modulation frequency was 2.9805 GHz. The detected spectra were used to compute $\mathcal{L}(f_m)$ and $S_{\nu\nu}(f_m)$ on an equivalent per Hertz basis via the previous set of equations. Corrections for the analyzer's log amplifier (1.45 dB) and the IF the detector (1.05 dB) were added to the calculations. Also, the bandwidth shape factor was used to adjust for the finite extent of the gaussian shaped resolution bandwidth filter of the analyzer (1.2*Resolution Bandwidth of the measurement). In both $S_{\nu\nu}(f_m)$ and $\mathcal{L}(f_m)$, the most striking decrease in noise occurs for the single modulated laser injection rather than for the heterodyned beat injection. This is directly attributed to the magnitude of power injected. For the single modulated laser, the amount of optical power is measured was 2.2mW while for the heterodyned beat case it is 0.4mW. As described in *Chapter 5*, the amount of power absorbed in the GaAs is 2% of the measured power. Therefore, the single laser power is 44μW and the beat power is 8μW. In Figure 25 and the surrounding discussion of Section 7.5, the magnitude of the injection vector plays a significant role in stopping the frequency movement about the injected frequency. The difference in phase noise magnitude between the single laser and heterodyned beat at 1000Hz from the carrier is 20%. Also, the ratio of the two injected power levels is 20%.

Furthermore, the phase noise of the optically injected oscillator reported here are better than those previously reported. At 1KHz from the carrier, $\mathcal{L}(f_m)$ is -105 dBc/Hz for the single laser, and -80 dBc/Hz for the heterodyned beat. In a comparison of injection methods, Daryoush detected an optically modulated signal

with a photodiode and injected an oscillator with the photodiode's output. At 1 KHz from the carrier, -57 dBc/Hz was achieved[29]. At 10 KHz from the carrier, $\mathcal{L}(f_m)$ is -110 dBc/Hz for the single laser, and for the heterodyned beat -105 dBc/Hz compared to -70 to-80 dBc/Hz at 10 KHz reported by DeSalles[30].

7.5.2 AM Noise Measurements

The free running oscillator is subject to stochastic noise processes which mix with the free running oscillator and produces modulation of the carrier. This noise modulates the free running oscillator frequency both in amplitude and in angle. This section discusses the amplitude modulation of the oscillator which will be termed AM Noise. Section 7.5.1 Phase Noise Measurements discusses the noise induced FM.

Pure AM or FM signals always have equal sidebands, but when the two are present simultaneously, the modulation vectors usually add in one sideband and subtract in the other. The phase relations between the carrier and sidebands are different for AM and for FM. The components of both types vectorially add which may result in lower sidebands. Asymmetrical sidebands, therefore, indicate both AM and FM. The vector relationships for AM are

$$E(t) = A(1 + m\cos\omega_m t)\cdot\cos\omega_c t$$

$$= A\cos\omega_c t + \frac{m+A}{2}\cos(\omega_c + \omega_m)t + \frac{m-A}{2}\cos(\omega_c - \omega_m)t \qquad (7\text{-}4)$$

The first term is the carrier component, the second is the upper sideband, and the last term is the lower sideband. Phase and frequency modulation are both special cases of angular modulation. The vector relationships for FM are

$$E(t) = A\cos(\omega_c t + m\sin(\omega_m t) + \phi(t) \qquad (7\text{-}5)$$

The representation of the AM phasors, rotating at different angular velocities, are diagrammed in Figure 30a . The carrier, ω_c, is assumed to be stationary, and the sideband vectors are drawn relative to the carrier in Figure 30b . A narrowband (i.e., $m<<\pi/2$) FM vector diagram is given in Figure 30c.

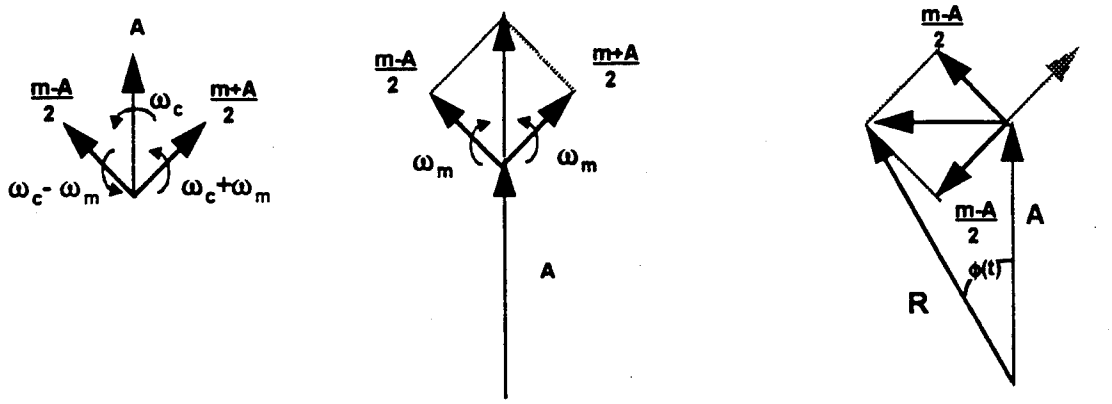

a) Phasors rotating at different angular velocities

b) AM - Sideband phasors relative to the carrier

c) Narrowband FM

Figure 30 Modulation Vector Diagram

The phasor composition of the envelope of an AM signal is show in Figure 31. The quadrature components always cancel which is represented vectorially as the sideband phasors remaining collinear with the carrier components.

When the peak deviation of the incidental FM is small relative to the spectrum analyzer bandwidth, the Fast Fourier Transform (FFT) can be used to isolate the amount of AM from the FM. The degree of AM (i.e., modulation index m) can be calculated by measuring the average amplitude of the carrier and first sideband.

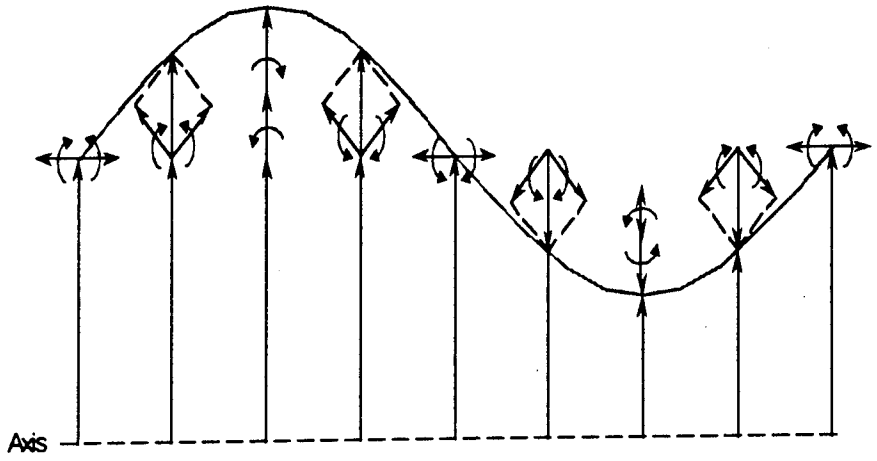

Figure 31 Phasor Composition of AM Signal Envelope

$$E_{sidbeand} - E_c = 20\log(\frac{m}{2}) \qquad [dB] \qquad (7\text{-}6)$$

The HP8562A FFT function was used to measure the AM of the oscillator. The oscillator output is the input signal to the spectrum analyzer. The peak of the oscillator was centered in a 500 KHz span before demodulation. Next, AM contribution is demodulated by selecting zero span and a resolution bandwidth of 3 KHz which is narrow enough to resolve the spectral components and large enough to negate the effect of the incidental FM and pass the AM unattenuated.. The analyzer sets itself in sample-detection mode and takes a single sweep. From this sample, a DFT on the array is performed with a Hanning window and the log magnitude is stored. The frequency starts at zero and ends at the maximum frequency which is determined by the sweep time.

$$T = \text{sampling period} = \frac{\text{Sweep Time}}{\#\text{trace elements}}$$
$$f_{max} = \frac{1}{2*T} \qquad (7\text{-}7)$$

For the oscillator, any AM and FM exist because of noise modulating (ω_m) the free running oscillator frequency (ω_c). When the oscillator is locked to the stable modulated optical signal, there is a significant reduction (≈20 dBm) in the amount of AM. The AM noise was measured for five cases: (1) Free running laser with no injection (dark), (2) Single modulated laser not locked to the oscillator, (3) Single modulated laser locked to the oscillator, (4) Heterodyned beat not locked to the oscillator, (5) Heterodyned beat not locked to the oscillator.

The AM noise is extinguished when the oscillator is locked to either the single laser or the heterodyne beat optical signal. However, the aggregate noise level increases when the optical signal is injected but not locked to the oscillator. This is consistent with the increased span observations of Table 3 Frequency Span during Lock in Section 7.4.1 Oscillator Spectrum.

The noise differences between the single laser and heterodyne beat are not significant because the noise is extinguished to the noise floor of the analyzer. When these cases were plotted, there was a random ± 5 dBm difference between these experiments.

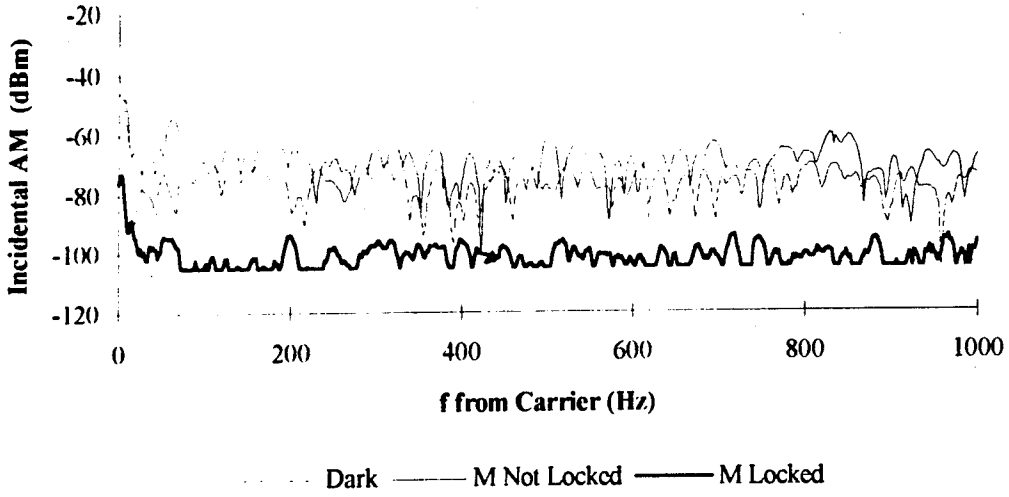

Figure 32 Reduction of AM Noise when Locked to Single Modulated Laser

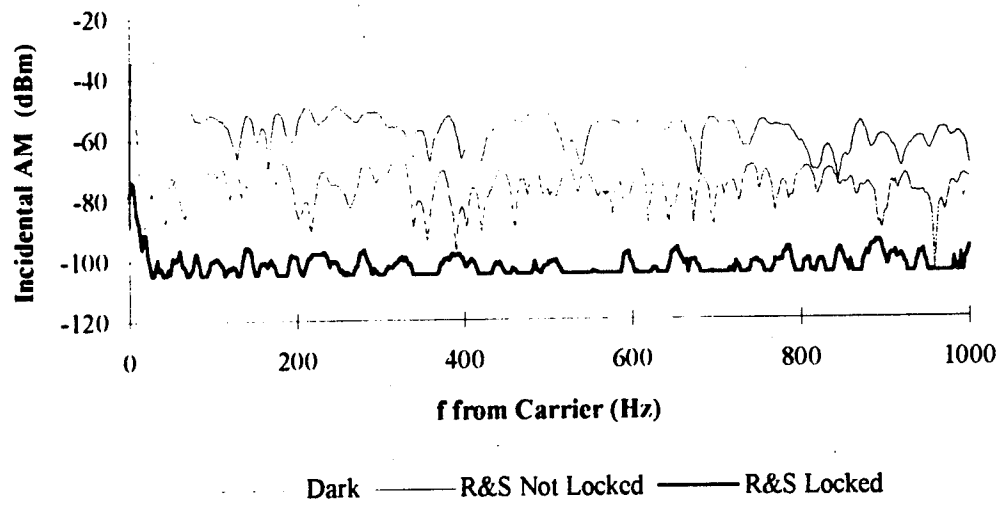

Figure 33 Reduction of AM Noise when Locked to Heterodyne Laser Beat

7.6 SPICE Model

The oscillator has been modeled via SPICE simulation. This is a qualitative simulation because the active element in the model is a JFET not a MESFET. However, care was taken to change the model capacitances to more closely approximate a MESFET. Also, the SPICE model is similar for both types of devices. Therefore, proof of principle is achieved.

In Figure 34,the optical signal is modeled a current source from the drain to the source[31]. The current source represents the minority carriers that are generated when optical energy is absorbed (See Chapter 3).

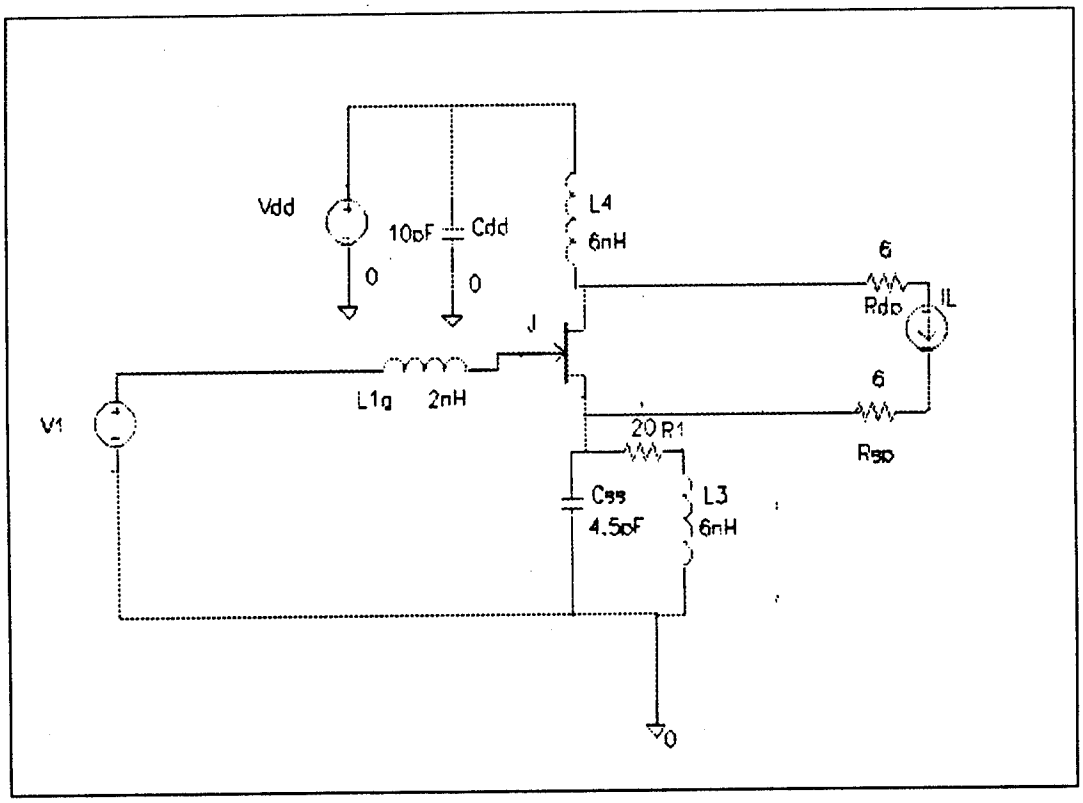

Figure 34 SPICE Oscillator Model

Figure 35 a is the free running oscillator output from the SPICE simulation. The current source I_{I_L} was set to DC value which caused the frequncy to shift (Figure 35 b). This was also shown in the lab results of Figure 10. In Figure 36, the injected light is modulated and locked to the oscillator. There is an increase in the harmonic content when the model is locked. Notice the third harmonic in Figure 36 which does not exist in the unlocked case of Figure 35. Next, the light was modulated near the second harmonic of our model oscillator. The oscillator injection locked at its second harmonic (Figure 37 b). The oscillator output when DC light is injected shifts the frequency; this is shown for emphasis in Figure 37 a. The phenomenon of locking a microwave oscillator to an optical signal has been modeled qualitatively with this SPICE approach.

The current source that represents the optically injected signal is given by:

$$I_{I_L} = I_{ampl}[1 + m\ \sin(\omega_{inj}t)]$$

where ω_{inj} is the injected frequency, I_{ampl} is the dc amplitude current level produced by optical signal injection ,and m is the modulation index. The shift in the oscillator current when illuminated was measured and fedback to the SPICE model via I_{ampl}. . However, the method detailed in Chapters 3 and 6 could have been used to predict the change in oscillator current I_{ampl} given the injected optical power level. In all SPICE results, the bias voltages, frequency and Iampl values are specified on the Figures.

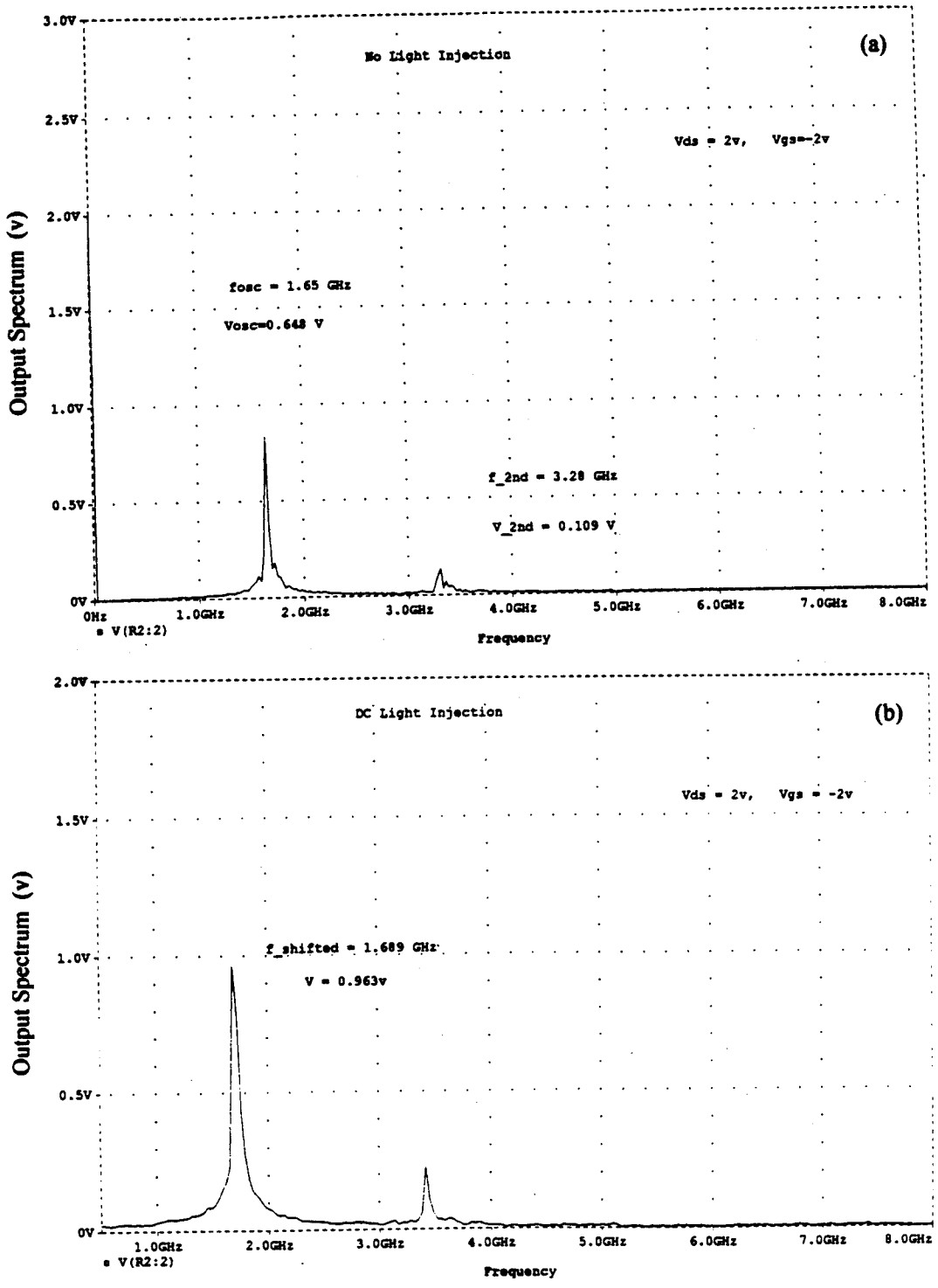

Figure 35 SPICE Output; a) Dark, b) DC Light injection

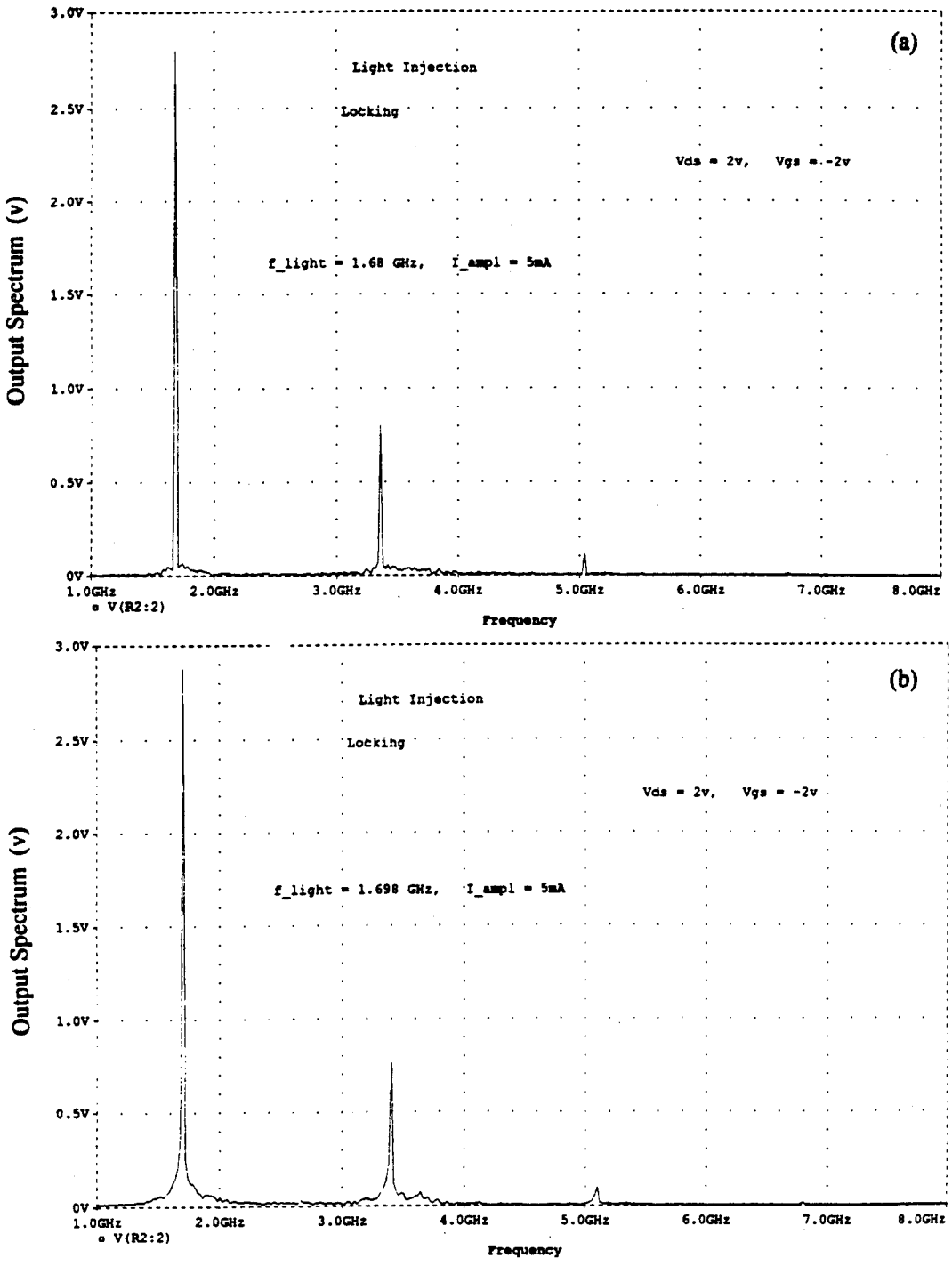

Figure 36 Modulated Laser Injection - Spice Model Results

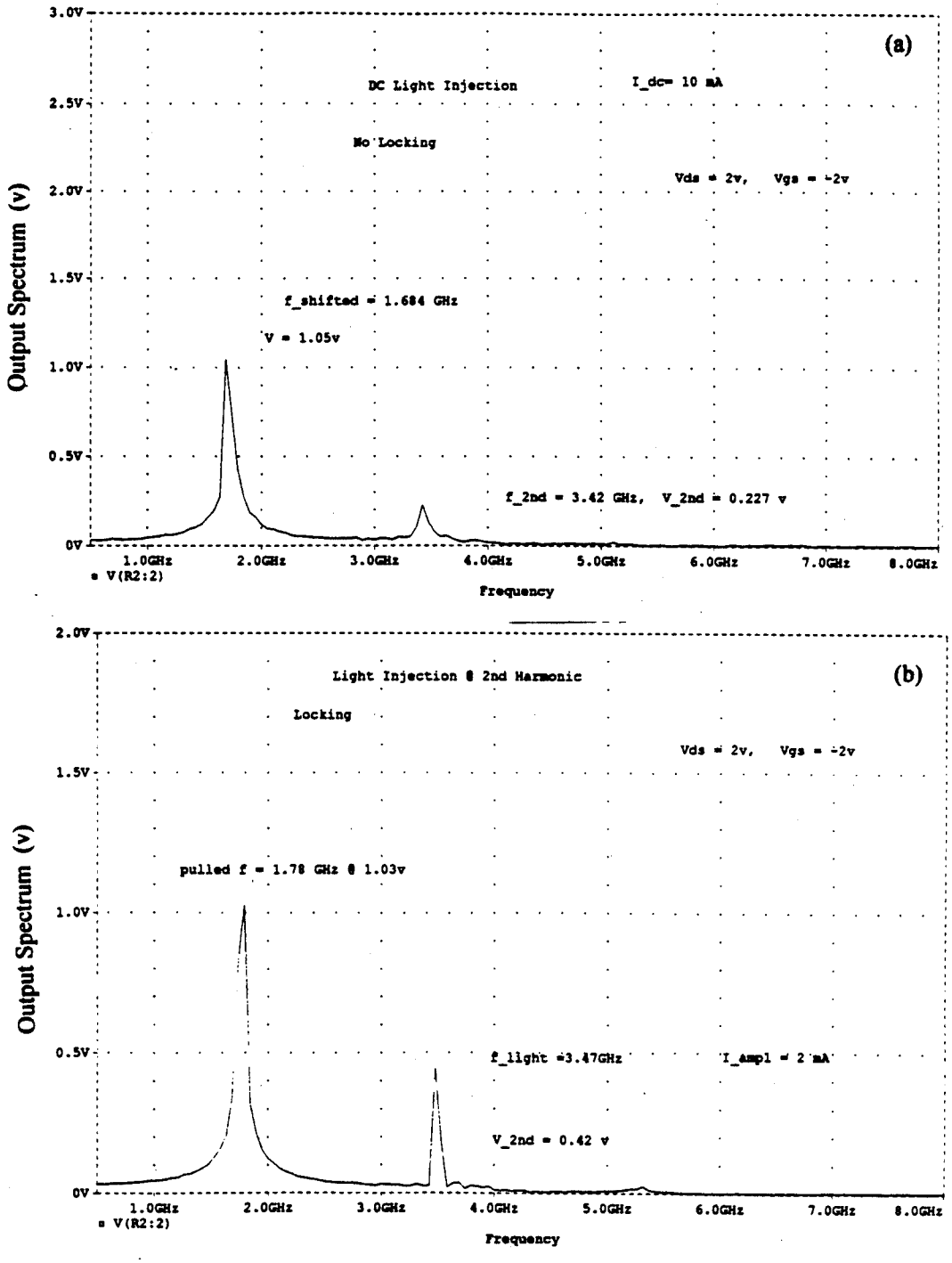

Figure 37 Second Harmonic Locking; a) DC frequency Shift, b) Locked at 3.47GHz

7.7 Conclusion

The oscillator spectrum has been studied under optical injection. The MESFET's current, impedance, and ultimately, frequency are influenced by an optical signal. The output spectrum characteristics of the oscillator were experimentally shown to improve when locked to a modulated laser. The model was used to describe locking and phase noise produced by random frequency fluctuations. The best reduction of phase noise reported to date was realized. The main results are (1) the oscillator phase noise at 1 KHz from the carrier is the decreased by 45 dBc/Hz when locked to the modulated lasers, and (2) incidental frequency noise is extinguished when locked to a modulated optical signal. The heterodyned beat note was anticipated to reduce the oscillator phase noise beyond the single modulated laser injection case because of the 10 times narrower optical linewidth (refer to *Chapter 2.4.2* for optical linewidth results). This was not the case in the experiment because the optical power level of the beat note. The oscillator was modeled with a SPICE circuit simulation and shown to exhibit the same locking characteristics as the experimental device.

7.8 Supplement

The following results are the 5GHz oscillator output spectrum for the case of no injection and with modulated laser light injected at 5.012 GHz. Not only is the locking to the laser frequency observed (Figure 39 and Figure 41), but the reduction in phase noise is easily seen by comparing the free running oscillator (Figure 38 and Figure 40) to the locked oscillator spectrum at the spans and resolution listed on the figures.

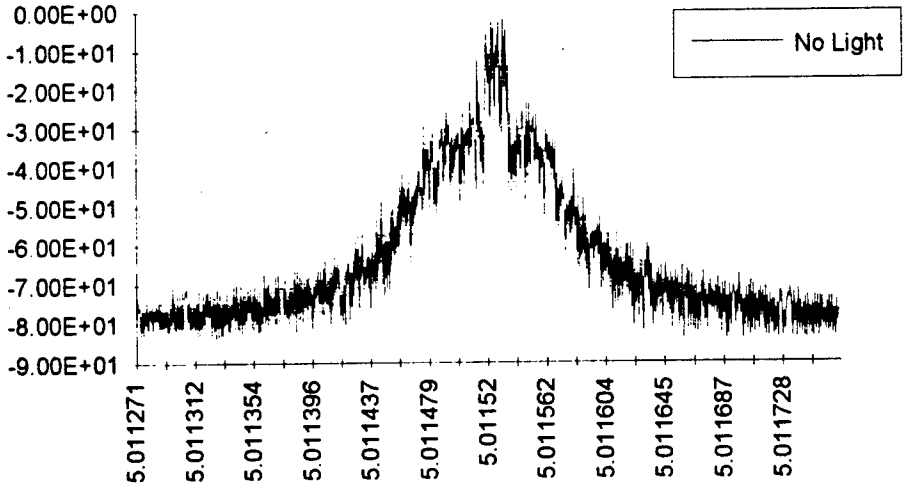

Figure 38 Free running Oscillator (resolution bandwidth =3KHz, span=500KHz)

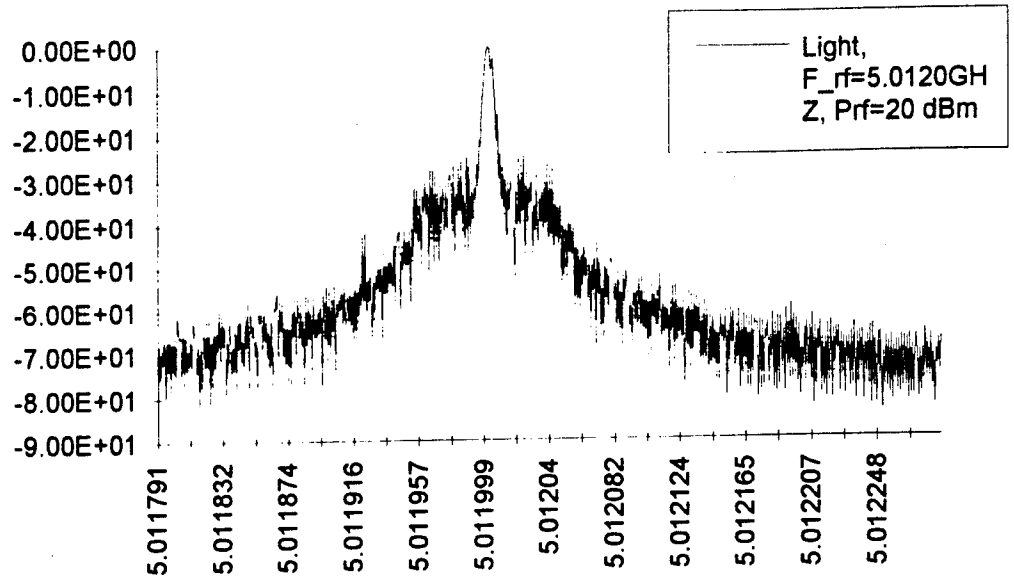

Figure 39Oscillator locking at 5.012GHz (resolution bandwidth =3KHz, span=500KHz)

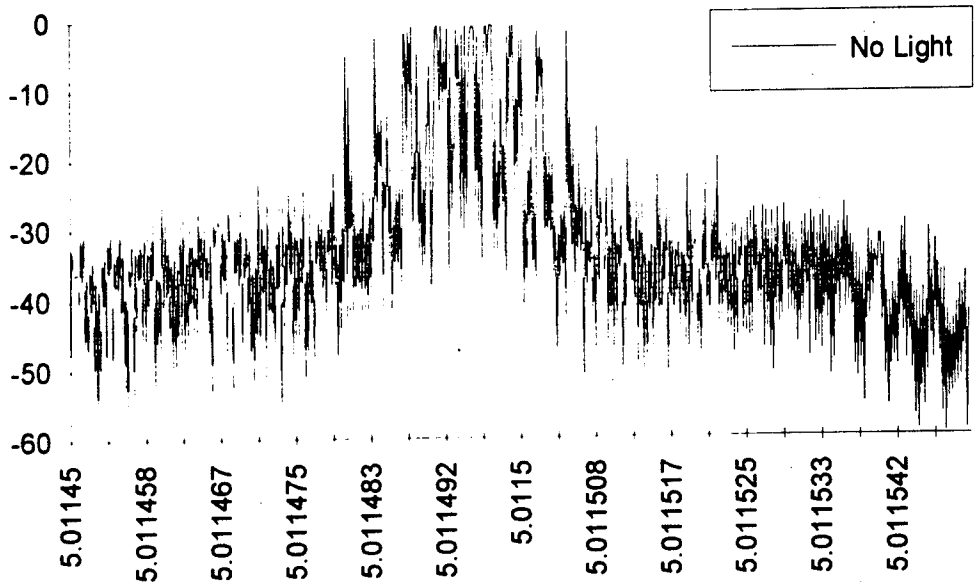

Figure 40Free running Oscillator (resolution bandwidth =3KHz, span=100KHz)

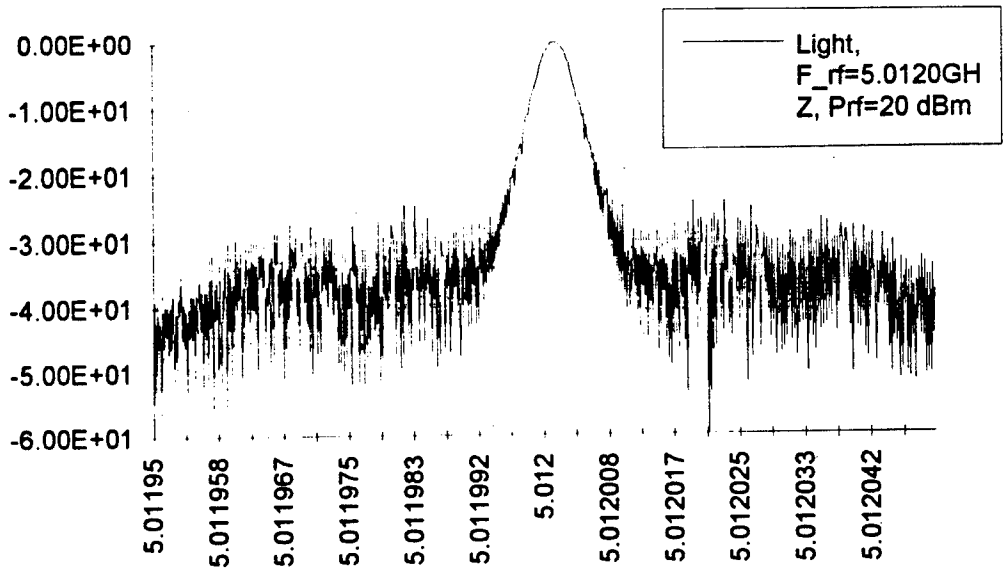

Figure 41Oscillator locking at 5.012GHz (resolution bandwidth =3KHz, span=100KHz)

7.9 References - Chapter 7

[1] B. Van Der Pol, "The Nonlinear Theory of Electric Oscillations", *Proceedings of the IRE*, vol. 22, no.9, September 1934, pp.1051-1086.

[2] Robert Adler, "A study of Locking Phenomena in Oscillators", *Proceedings of IRE and Waves and Electrons*, vol. 34, 1946, pp.351-357.

[3] T.J. Buchanan, "The Frequency Spectrum of a Pulled Oscillator", *Proceedings of the IRE*, August 1952, pp.958-961.

[4] N.Krylov, and N.Bogoliubov, Introduction to Nonlinear Mechanics, Prinseton, N.J., Princeton University Press, 1943.

[5] R.D.Huntoon and A.Weiss, "Synchronzaiton of oscillators," *Proc. IRE*, Vol. 35, pp.1415-1423, Dec.1947.

[6] J.C. Slater, Microwave Electronics, NY., Van Nostrand, 1950, pp.205-210.

[7] K. Kurokawa, "Injection locking of microwave solid state oscillators, " *Proc. IEEE*, vol.61, pp.1386-1410, 1973.

[8] G. Sato, "stabilized oscillators by using injection locking and phase-locked loop, " *Electron. Commun. Japan*, vol. 54-B, pp.59-65, 1971.

[9] H.G. Oltman, and C.H. Nonnemaker, "Subharmonically Injection Phase-Locked Gunn Oscillator Experiments", *IEEE Transactions on Microwave Theory and Techniques*, vol. MTT-17, September 1969, pp.728-729.

[10] C.H. Chien, and G.C. Dalman, "Subharmonically Injected Phase-locked IMPATT-Oscillator Experiments", *Electronics Letters*, vol.6, no.8, April 1970, pp.240-241.

[11] R.C. Shaw, and H.L. Stover, ""Phase-Locked Avalanche Diode Oscillators", *Proceedings of the IEEE*, vol. 54, April 1970, pp.710-711.

[12] H. W. Yen, M. K. Barnoski, "Optical injection locking of FET oscillators using fiber optics", *Appl.Phys. Lett.*, vol. 32, pp.182-184, 1978.

[13] A.S. Daryoush, P. Wahi, P.R. Herczfeld, and Z. Turski, "Comparison of Indirect Optcial Injection Locking Techniques of Multiple X-Band Oscillators", *IEEE MTT-S Digest*, June 1986, pp.615-618.

[14] Z Ma., M.H. White, R.D. Esman, et.al. "A High-Performance Optically Injected Synchronous Oscillator", *IEEE Photonics Technology Letters*, vol.4, no.4, April 1992, pp.405-408.

[15] H. J. Sun, R. J. Gutmann and J. M. Borrego, "Photoeffects in common-source and common-drain microwave GaAs MESFET oscillators", *Solid State Electronics*, vol. 24, pp.935-940, 1981.

[16] H. J. Sun, R. J. Gutmann and J. M. Borrego, "Optical Tunin in GaAs MESFET Oscillators", *1981 IEEE MTT-S International Microwave Symposium Digest*, pp.40-42.

[17] L. Goldberg, C. Rauscher, J.F. Weller, and H.F. Taylor, "Optical Injection Locking of X-Band FET Oscillator using Coherent Mixing of FaAlAs Lasers", *Electronics Letters*,vol. 19, no. 20, September 29, 1983, pp. 848-850.

[18] A. A. DeSalles, "Optical control of GaAs MESFETs", *IEEE Trans. Microwave Theory and Tech.*,vol. MTT-31,pp.812-820, 1983.

[19] A.J. Seeds, J.F. Singleton, S.P. Brunt, and J.R. Forrest, "The Optical Control of IMPATT Oscillators", *IEEE Journal of Lightwave Technology*, vol. LT-5, no. 3, March 1987, pp. 403-411.

[20] D. C. Buck, M. A. Cross, "Optical injection Locking of FET Oscillators using fiber optics", *IEEE MTT-S Digest*, pp.612-614, 1986.

[21] R. D. Esman, L. Goldberg, and J. F. Weller, "Optical phase control of an optically injection-locked FET microwave oscillator", *IEEE Trans. Microwave Theory and Tech.*, vol. 37, pp. 1512-1518, October 1989.

[22] S. E. Lipsky and A. S. Daryoush, "Fiber-optic Methos for injection-locked oscillators", *Microwave Journal*, pp.80-88, January 1992.

[23] R. D. Esman, K. J. Williams, M. H. White, and V. Uzunoglu, "Microave subcarrier and clock recovyer by an optically injected CPSO", *IEEE Photonics Tech. Lett.*, vol. 3, pp.179-181, February 1991.

[24] R.A. Pucel, H.A.Haus, and H.Statz, "Signal and Noise Proberties of GaAs Microwave Field-Effect Transistors", Advances in Electronic and Electron Physics, editted by L.Marton, Academic Press, vol.38, 1975, pp.195-265.

[25] W.R. Curtice, "A MESFET Model for Use in the Design of GaAs Integrated Circuits," *IEEE Transactions on Microwave Theory Tech.*, Vol. MTT-28, 1980, pp.448-456.

[26] K. Kurokawa, "Injection locking of microwave solid state oscillators, " *Proc. IEEE*, vol.61, pp.1386-1410, 1973.

[27] S., Kobayashi, Y. Yamamoto, M. Ito, and T. Kimura, "Direct Frequency Modulation in AlGaAs Semiconductor Lasers", *IEEE Journal Of Quantum Electronics*, vol.18. vol.4. April 1982, pp.582-595.

[28] R. N. Simons, "Microwave Performance of an Optically Controlled AlGaAs/GaAs High Electron Mobility Transistor and GaAs MESFET", *IEEE Transactions on Microwave Theory and Techniques*, vol. MTT-35, no.12, December 1987, pp. 1444-1455.

[29] P.R. Herczfeld, A.S. Daryoush, A. Rosen, A.K. Sharma, and V.M. Contarino, "Indirect Subharmonic Optical Injection Locking of a Millimeter-Wave IMPATT Oscillator", *IEEE Transactions on Microwave Theory and Techniques*, vol. MTT-34, no. 12, December 1986, pp.1371-1375.

[30] A. A. DeSalles, "Optical control of GaAs MESFETs", *IEEE Trans. Microwave Theory and Tech.*,vol. MTT-31,pp.812-820, 1983.

[31] D.Warren, J.Michael Golio, and E. Johnson, "Simulation of Optically Injection-Locked Microwave Oscillators Using a Novel SPICE Model", *IEEE Transactions on Microwave Theory and Techniques*, vol. 36, no.11, November 1988, pp.1535-1539.

CHAPTER 8

MICROWAVE AMPLIFIER INJECTION

8.1 Introduction

Presented in this chapter are the photo-induced characteristics of a microwave MESFET amplifier circuit. The rationale for this study is to provide a high speed electro-optically integrated mechanism for receiving optical signals. Integration is possible because of the small size of MESFET devices and GaAs compatibility with other optical components. The experiments in this chapter demonstrate that the MESFET amplifier can recover information from an RF modulated laser and optical FM and AM signals. These results show that high speed square wave modulated optical signals (i.e., digital information) may also be detected in this manner. Digital data systems can be interconnected via optical interconnects such as holographic matrices or optical polymer backplanes with MESFET amplifiers as the receivers.

The characteristics of the MESFET amplifier under illumination are presented. The theory of Chapter 3 is used to predict changes in the amplifier circuit current and conductance to within 3.25-5.3% of the measured values. The fluctuation of the large signal current is calculated and represents a conductance of

the overall circuit. Because the device parameters are measured for the entire amplifier circuit, the conductance is slightly different than the large signal intrinsic MESFET transconductance g_m. Changes in the amplifier output power, the current, the impedance are also measured.

The MESFET amplifier optically induced effects on the S parameters are measured for the dark(no injection) case and several types of optical injection to isolate potential differences based on various types of injected signals. There were only small differences measured between the locked and unlocked laser cases; differences which can be directly attributed to the power level of the optical signal.

The amplifier was injected with optical RF, FM and AM signals. RF spectrum was measured for two types of optical signals: modulated locked single laser light, and locked modulated heterodyne beat signal between the reference and the slave lasers. The quality of the recovered signal is also discussed. The measured phase noise of the received signals is verified.

8.2 Illuminated Amplifier Characteristics

In general, small signal and medium power microwave amplifier applications are well suited for GaAs MESFETs. Optical absorption into the active region alters the transconductance which subsequently changes the gain of the amplifier circuit. The gain of an amplifier is the transconductance in parallel with resistance to the first order. Since the optically injected signal is isolated from the circuit electrically, this additional MESFET input (the light) provides a coupling mechanism free from the constraints of electronics.

The theory of amplifier design with Y or S-parameters is well established[1,2,3], and therefore, is not detailed in this Thesis. The amplifier circuit, designed and used in these experiments, is described in Chapter 5. The amplifier designed for these experiments is a common-source type configuration which usually is the most stable since there is less feedback (i.e., C_{dg} is small).

With a large resistance (59.7 KΩ) connected to the gate, the voltage across the terminals is close to the open circuit voltage of the junction. When light is injected, the edge of the depletion region is pinned to almost the open circuit value. The photovoltage is developed when carriers are excited out of the depletion region. This reduces the width of the Schottky barrier region which causes the channel to open wider. Therefore, the transconductance is also effected by illumination. When the device is near pinchoff and light is injected, the largest changes in the channel and the gain will exist. Although the changes in gain magnitude are largest with the gate effectively open circuited, the resistance imposes a limitation on the rate at which the

gain can be varied. If C_{gs} is near 1pF and the gate resistance is 59.7 KΩ, then the RC time constant is approximately 60ns. In applications where the gain is adjusted optically, the time constant is not an issue. In direct detection of modulated optical signals, the dc light component charges the capacitor and time constant does not effect the ability to receive a signal. Therefore, there is a consideration of the maximum gain changes versus the speed at which the changes may take place.

Without light injection, the gain variation is substantial (>12dB) as a function of V_{gs}. When illuminated, the gain variation is small (≤ 3dB) as V_{gs} is changed and approaches pinchoff. This is due to the pinning effect when illuminated.

In Figure 1, the amplifier output versus V_{gs} is shown for several values of V_{ds} and for both dark and light cases. The experiments were conducted in 0.1v increments of V_{ds} from 0.8v to 1.5v and in 0.2 increments of V_{gs} from -0.2v to -0.8v. In the dark cases, the drastic drop off near pinchoff is nearly 12 dB down. However, in the light cases, the drop off is less than 3 dB.

When V_{gs} is close to pinchoff, as much as 15-20 dB increase in amplifier output is realized. In Figure 2, the gate bias was set to -0.8v with a RF signal of -10dBm (a) and -30dBm (b) at the amplifier input. Although the gate bias was a few tenths away from pinchoff, the photo-induced increase in the amplifier is greater than 12 dB.

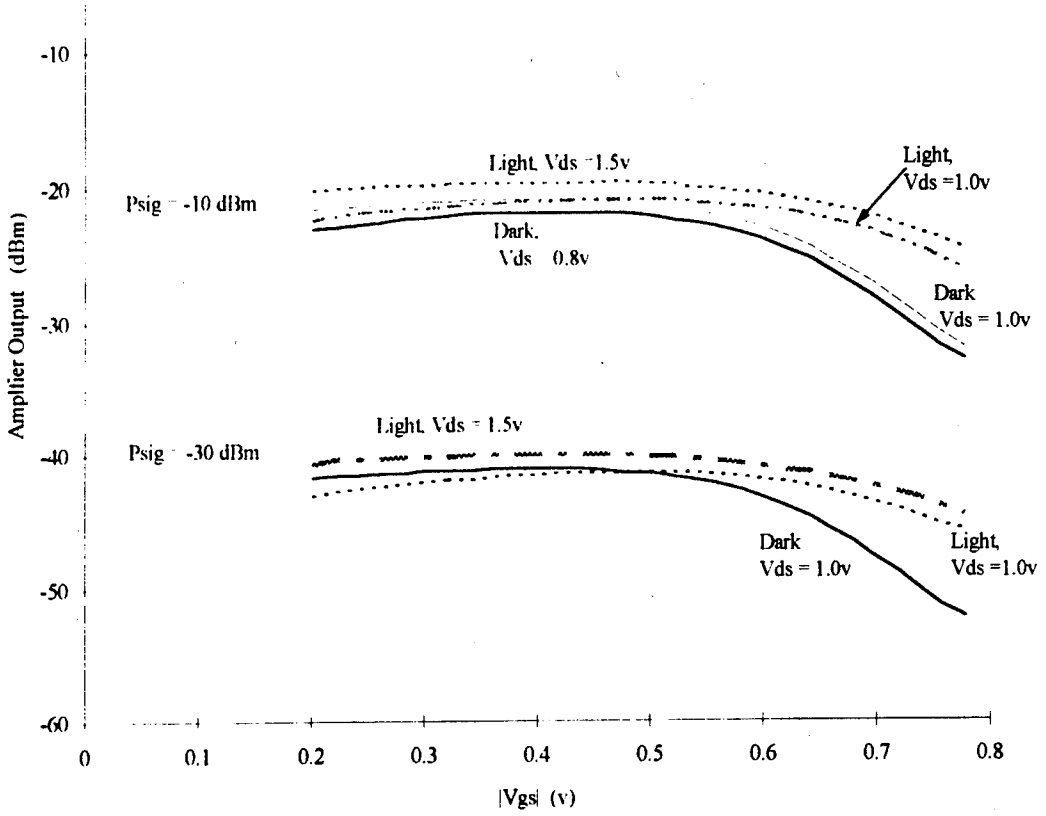

Figure 1 Amplifier output

With small resistance on the gate (<1KΩ), the gate junction is nearly shorted. and the photocurrent generated is nearly the short circuit current I_{SC} of the diode equation. In this case the increase in the channel conductivity alter the transconductance by 5-10%. In the barrier region between the active channel and the substrate there is a secondary photovoltaic effect which is believed to be small and contribute nothing to the changes in g_m. In Chapter 3, the diode model (used in solar cell analyses) of the gate junction was described. The resistance on the gate

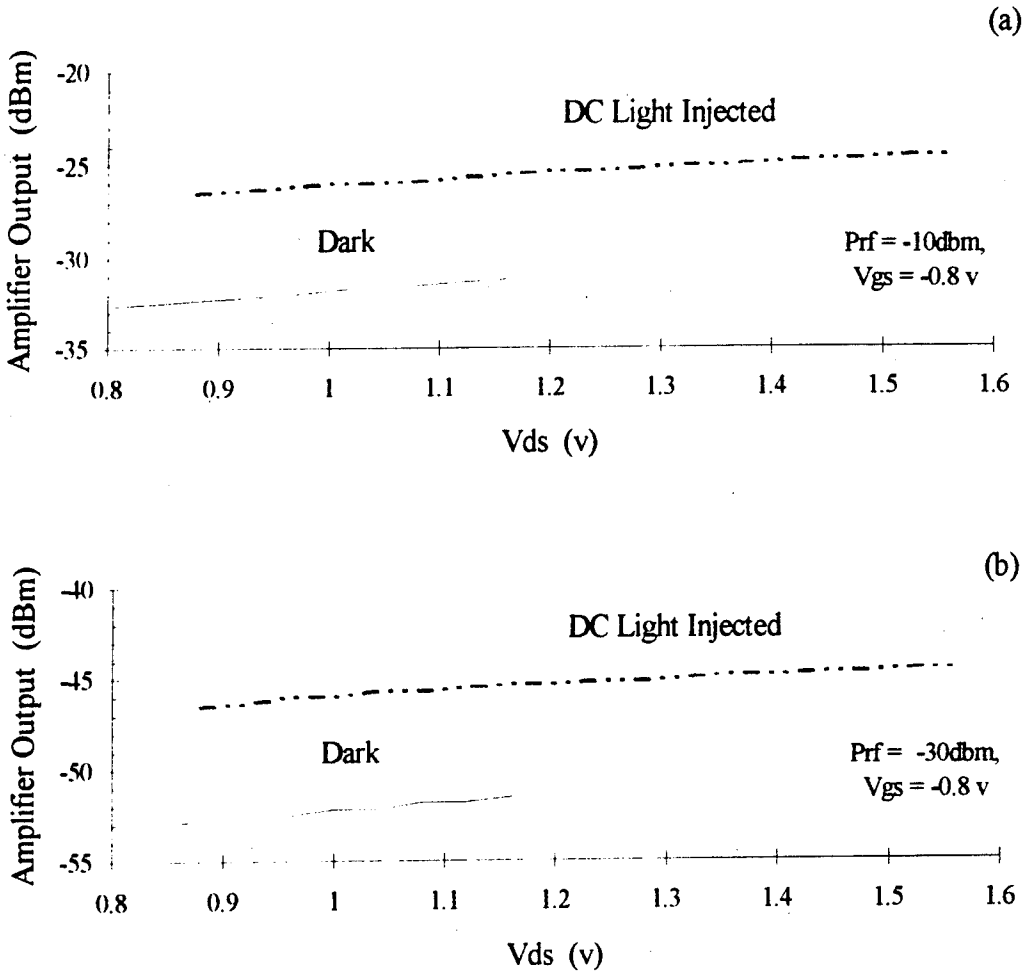

Figure 2 Photo-induced Increase in Amplifier Output

bias circuitry is indeed high (10-20 KΩ), and therefore, the pinning effect is anticipated. Furthermore, because the diode equation is a logarithmic function, the amplifier output is approximately a logarithmic function of the incident optical power. Therefore, the MESFET can be used as compressive photodetector.

8.3 Optically Induced Effects on Circuit Parameters

The Statz-Raytheon large signal MESFET circuit model is used in series expansion form to model the effects of illumination on the circuit parameters. The I_{ds} expansion used in the following discussion was computed for a fixed value of V_{ds}. The approximate Statz model was completely detailed in *Chapter 3 and 6* as a function of V_{ds} and V_{gs}. The reasons for the fixed V_{ds} approach to the expansion are (1) the greatest increase in gain occurs when V_{gs} is near pinchoff, (2) the measured amplifier current is relatively flat when V_{ds} is varied (Figure 3), and (3) the transconductance from the gate to the source is primary contributor to the amplifier output. The gate source transconductance is computed with V_{ds} fixed.

In Figure 4, the current for fixed V_{ds} of 1.0v is graphed for both the dark and illuminated cases. The photo-induced current increase is due to both the excited minority carriers and a small photovoltaic effect.

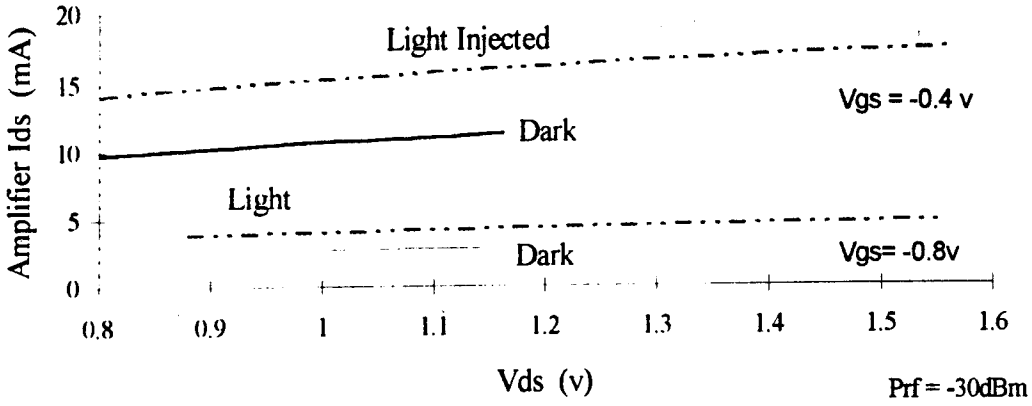

Figure 3 Amplifier current vs. Vds

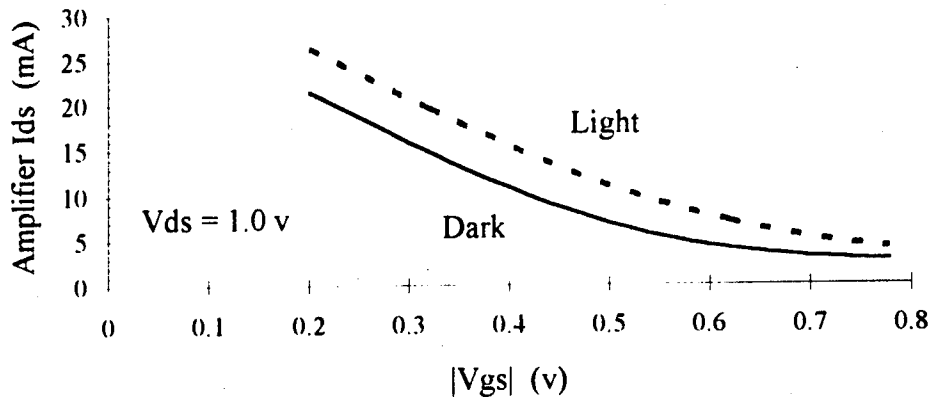

Figure 4 Amplifier current vs. Vgs

The drain to source current I_{ds_m} is represented by a third order equation in Vgs as follows:

$$I_{ds\_m}(V_{gs}) = I_{dss}\left(s_0 + s_1 V_{gs} + s_2 V_{gs}^{\ 2} + s_3 V_{gs}^{\ 3}\right) \qquad (8\text{-}1)$$

The coefficients of the polynomial are function of V_{ds} and the pinchoff potential V_{to}. Our expansion is completely developed in *Chapter 3*. The approximate Statz model of (8-1) is plotted against the experimental data in Figure 5 with the error bars shown to emphasize the excellent fit ($< 8\ \%\Delta$). Also, in Figure 6, the exact and approximate Statz equations are graphed along with the experimental I_{ds} data. In the same Figure, the experimental data was fitted to a third order polynomial. This was done to identify the coefficients and any changes when light is injected and to compare the model to the actual data on the basis of our expansion.

The measurements made are for the entire amplifier circuit: MESFET plus parasitics and matching impedances. Therefore, additional voltage drops must be considered when modeling these incremental fluctuations. Furthermore, in the light injection cases, the current contains an additional voltage superimposed on the gate bias that is directly related to the number of holes generated due to the energy of the photons. Therefore, these two cases cause the voltage presented to the intrinsic MESFET to be slightly different than that which was set on the bias power supply. To take into account these two cases, the $I_{ds\ m}$ equation may be written as follows:

$$I_{ds\ m}\left(v_{gs} + V\right) = \begin{bmatrix} s_0 + s_1 V + s_2 V^2 + s_3 V^3 \\ s_1 + 2 s_2 V + 3 s_3 V^2 \\ s_2 + 3 s_3 V \\ s^3 \end{bmatrix} \begin{bmatrix} 1 \\ v_{gs} \\ v_{gs}^2 \\ v_{gs}^3 \end{bmatrix} I_{dss}$$

where v_{gs} is the gate bias voltage and the superimposed voltage is V.

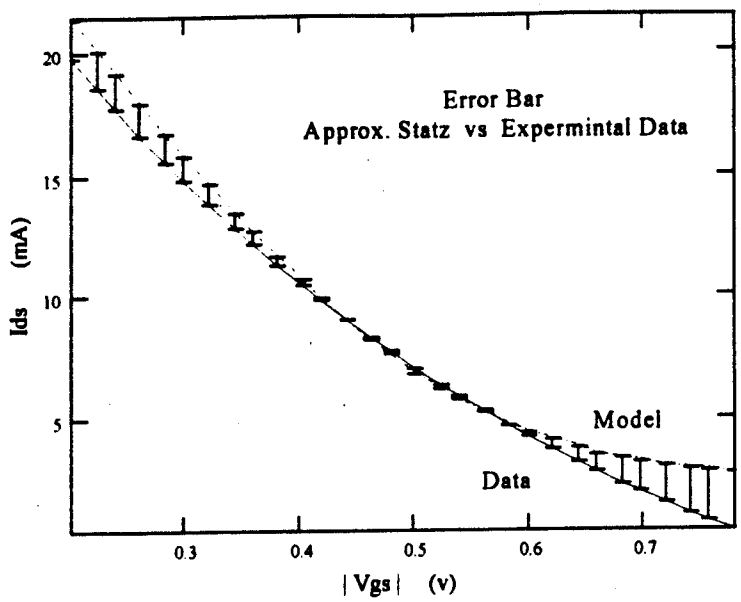

Figure 5 Approximate Statz Model vs. Experimental Data with no light injection - Amplifier I_{ds} vs. $|V_{gs}|$

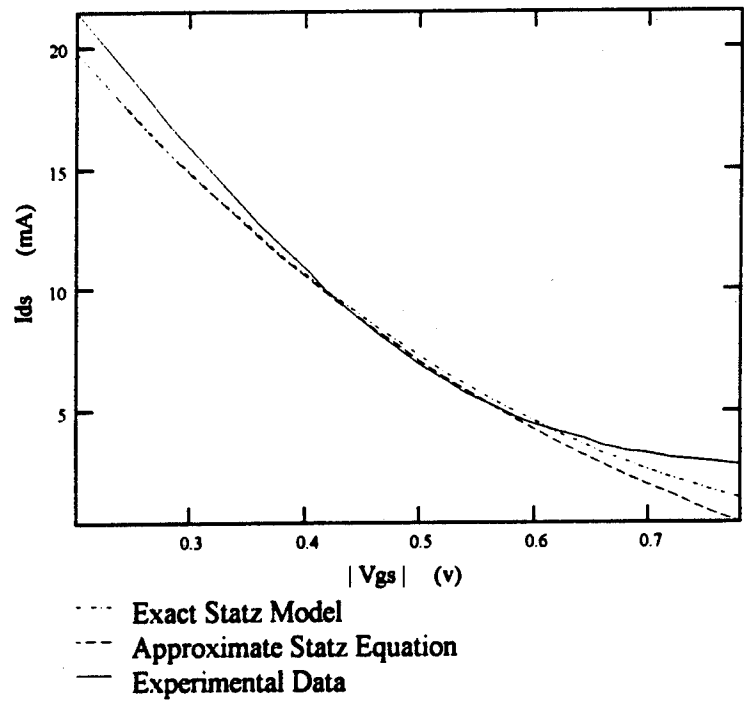

Figure 6 Exact Statz, Approximate Statz, and Experimental Data with no Light injection - Amplifier I_{ds} vs. $|V_{gs}|$

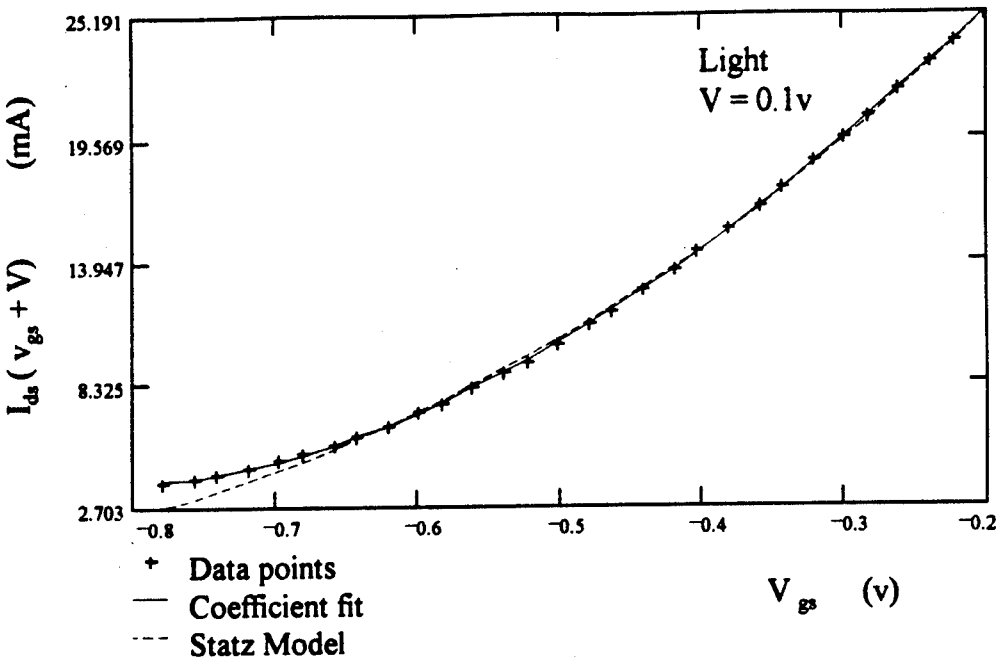

Figure 7 Light injected Amplifier Ids model compared with experimental data

For the illuminated MESFET, the current is calculated for V (experimentally derived) of 0.09v and plotted against the measured data in Figure 7. The experimental data was fitted to a polynomial to compare coefficients with the approximated Statz model.

The coefficients of the models are given in Table 1. In this Table, the coefficients in the approximate Statz model are denoted by **s**. These coefficients are multiplied by the drain saturation current which has been experimentally derived. In the dark case, $I_{dss\text{-}D}$ is 16.83 mA (column **b**), and for the injected light case, $I_{dss\text{-}L}$ is 17.94 mA (column **d**). Columns **a** and **c** are the coefficients for the third order polynomial fit to the experimental data for the dark and light injection cases respectively.

Table 2 Coefficients for g_{m_m}

I_{ds} Coefficients						
		Dark			Light Injection	
	Approximate Statz Model	Experimental Data Fit	Approximate Statz Model (I_{dss-D} = 16.83)	Experimental Data Fit	Approximate Statz Model (I_{dss-L} = 17.94)	
	s	a	b = s * I_{dss-D}	c	d = s* I_{dss-L}	e = Ids(v_{gs}-0.09)
0	1.927	36.377	32.433	38.005	34.57423	28.02
1	4.336	82.532	72.979	66.864	77.79651	67.74
2	3.011	41.658	50.678	10.101	54.02336	57.67
3	-0.753	-11.724	-12.674	-25.043	-13.5103	-13.51

Table 1 Coefficients for Amplifier I_{ds}

g_m Coefficients										
	Dark					Light Injection				
	Experimental Data Fit	Approximate Statz Model		$g_m(v_{gs})$= Derivative using I_{ds} coeff (Table 1- column a)		Experimental Data Fit	Approximate Statz Model		$g_m(v_{gs})$= Derivative using I_{ds} coeff (Table 1- column c)	
	f	g	$g_m(v_{gs}+.15)$ h	i	$g_m(v_{gs}+.15)$ j	k	l	$g_m(v_{gs}+.655)$ m	n	$g_m(v_{gs}+.15)$ p
1	69.243	72.98	56.92	82.532	69.243	21.399	77.80	-10.36	66.86	21.399
2	93.868	101.36	112.76	83.316	93.868	118.62	108.47	161.14	20.2	118.62
3	-35.172	-38.02	-38.02	-35.172	-35.172	-75.13	-40.53	-40.53	-75.12	-75.13

In column **e**, the model includes a superimposed voltage of 0.09v on the existing bias V_{gs} for the light injection case. This superimposed voltage was measured (Chapter 3). Without the superimposed voltage (column **d**), the model has a tremendous error of as much as 50%, but with the 0.09 volts superimposed (column **e**), the difference is less than 4 %.

When the model fit is compared to the overall polynomial, the error is less than 8% in the dark (column **b**) and less than 4% in the light (column **e**) case. This is shown in Figure 8. The error is a function of the polynomial variable V_{gs}. In the dark case, there is a substantial difference in the second order coefficient (modeled vs experimental fit). This directly influences the highest error of 8% which occurs lower magnitudes of V_{gs} when the coefficient term is most influential. For the illuminated case, the error is relatively flat and less than 4%.

As discussed in *Chapter 3*, the sources of error in between the model and the actual data are due primarily to uncertainty of device parameters. However, the difference of 4-8% is sufficient to prove the theory. Given more time, the experimental setup and the model could both be improved to reduce the difference even further.

Chronologically, the amplifier gain measurements were completed first (Figure 14). In executing these experiments, it was discovered that there exists a gate bias at which the dark amplifier output is greater than the optically injected amplifier output (Figure 14 Gain crossover). Since the tranconductance is directly proportional to the amplifier output, it should and does exhibit the same crossover phenomenon as the output. The transconductance crossover is shown in Figure 9.

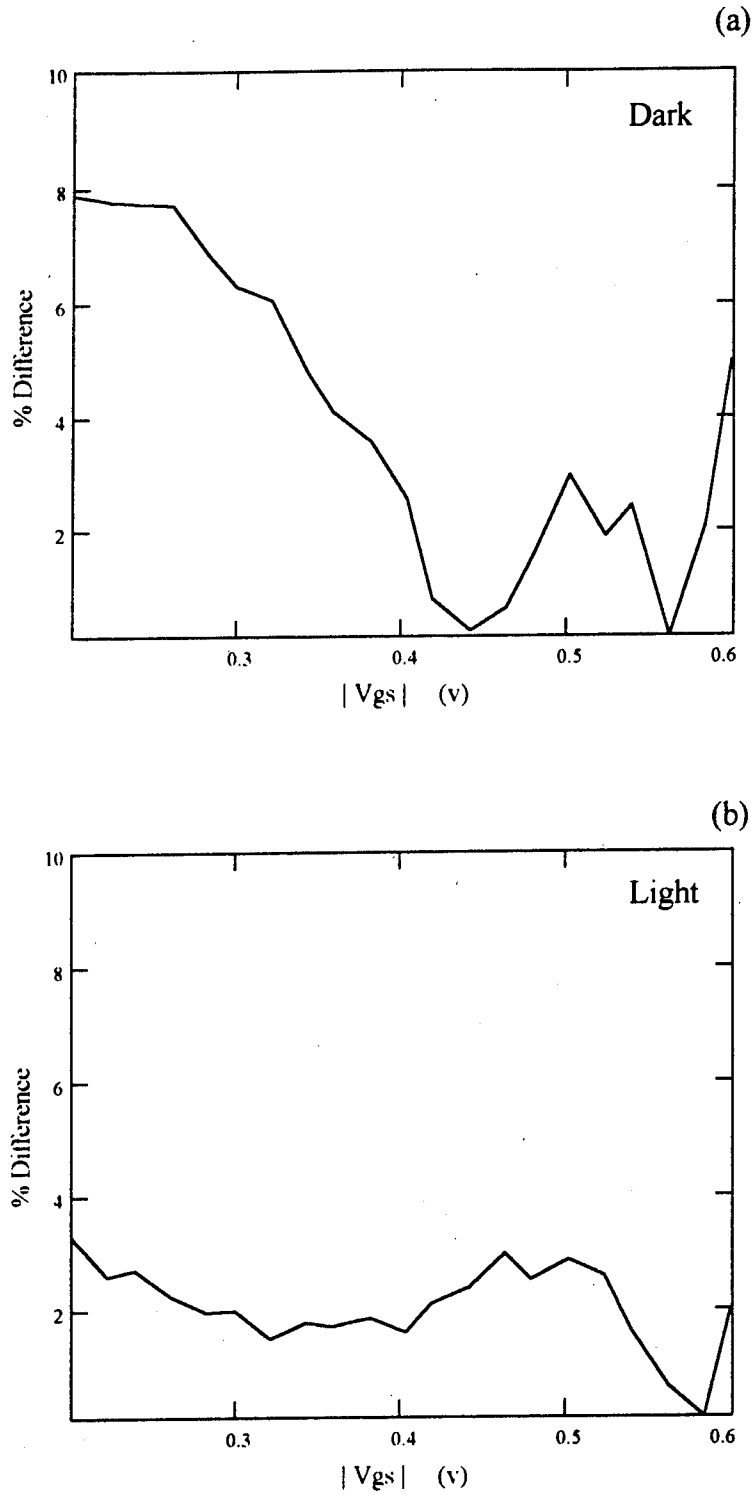

Figure 8 %Error in Ids between the approximate Statz Model and the experimental data; a) Dark, b) Light

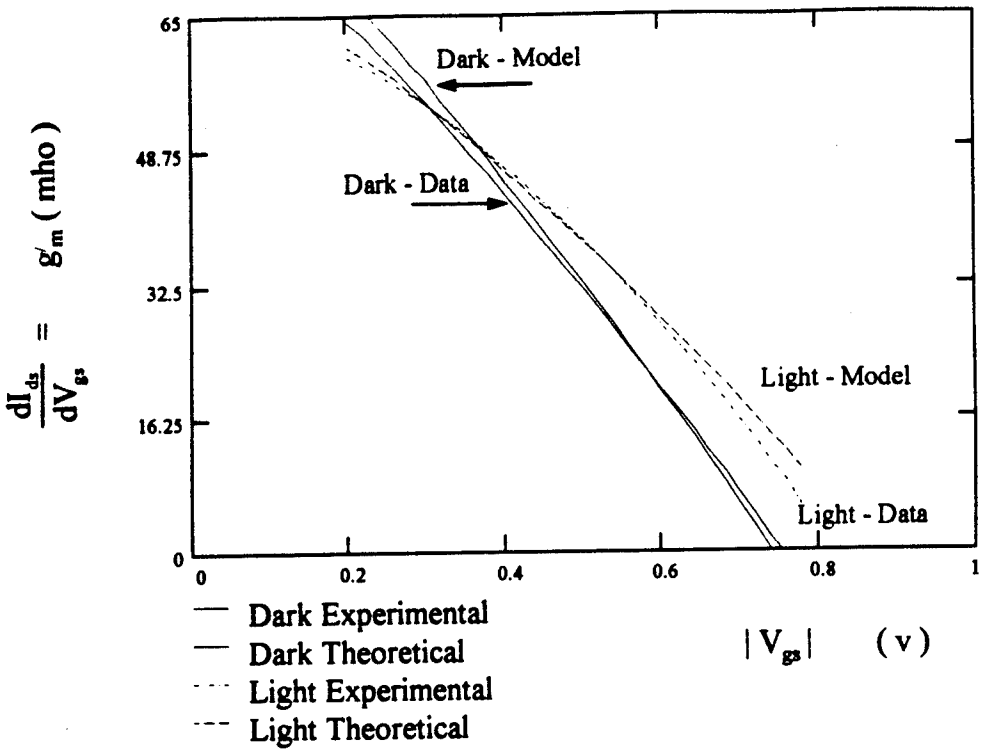

Figure 9 Conductance deviation vs. |Vgs|

The rate of change of the current as a function of gate bias is the transconductance g_{m_m}. It is a function of V_{gs} at a fixed value of V_{ds} and can be computed from the derivative of our approximate Statz I_{ds_m} equation.

$$g_{m\_m} = I_{dss}\left(s_1 + 2\,s_2 V_{gs} + 3\,s_3 V_{gs}^{\,2}\right) \tag{8-2}$$

The numerical derivative has been computed from the experimental I_{ds} data. Again, the purpose of these computations was to verify the gain crossover. Additional voltage drops must be considered when modeling these fluctuations, and in the light injection case, the current contains an additional voltage superimposed on the gate bias. Therefore, the transconductance can be re-written:

$$g_{m\_m}(v_{gs}+V)=\begin{bmatrix} s_1+2s_2V+3s_3V^2 \\ 2\,(s_2+3s_3V) \\ 3\,s^3 \end{bmatrix}\begin{bmatrix} 1 \\ v_{gs} \\ v_{gs}^2 \end{bmatrix} I_{dss} \qquad (8\text{-}3)$$

where v_{gs} is the gate bias voltage and the superimposed voltage is V.

In Figure 9, the transconductance is given for the dark and light injected experimental and theoretical cases. There are several points to note: (1) the experimental-to-model fit is good for the dark case 5% (Figure 10 b) and for the light injection case 3% (Figure 11 b), (2) the crossover voltage is not the same for the actual data and the model (Figure 9), and (3) the fit is dependent on the polynomial variable V_{gs}.

Figure 10 (a) and Figure 11 (a) are the dark and light transconductance respectively. The numerical derivative of the measured current was fitted to a second order polynomial. These coefficients are compared against the approximate Statz model coefficients in Table 2.

First, the experimental I_{ds} data was fitted to a polynomial (8-1) with coefficients in Table 1 - columns **a** and **c**. The numerical derivative was taken on the data and fitted to another polynomial (8-4) with coefficients in Table 2- columns **f** for the dark and **k** for the illuminated case.

$$g_{m2}(V_{gs}) = f_1 + f_2 V_{gs} + f_3 V_{gs}^{\ 2} \qquad (8\text{-}4)$$

The derivative of (8-1) is expressed in (8-2). The coefficients should be equal to the coefficients in (8-4); the coefficients of **f** and **i** for the dark and of **k** and **n** for the light should be equal. They are not. The additional voltage drop of 0.15v added in **j** and **p** reconciles the experimental data to the fitted.

Therefore, the same additional voltage drop is added to the Statz coefficients (column **h** and **m**). (8-3) was used to include additional voltage drop of 0.15v (columns **h**, **j** and **p**). Although the model for the dark case produced excellent results directly (Figure 10), an iterative process to converge on a fit for the illuminated Statz model of the transconductance was necessary. The results of the model iteration are plotted in Figure 11. The light effects were not an overall DC additive or a change in the $I_{dss\text{-}1}$ value. They were highly dependent on the voltage expressed in the g_m equations. In the final analysis, the model required an additional 0.505v drop (0.15v+0.505v=0.655v); however this forced too much of a DC term in row one of the coefficients matrix in (8-3). The resultant equation is as follows:

$$g_{m\ m}\left(v_{gs}+V\right)=\left\{\begin{bmatrix} s_1+2s_2V+3s_3V^2 \\ 2\left(s_2+3s_3V\right) \\ 3\,s^3 \end{bmatrix}\begin{bmatrix} 1 \\ v_{gs} \\ v_{gs}^2 \end{bmatrix}-\begin{bmatrix} +2s_2V+3s_3V \\ 0 \\ 0 \end{bmatrix}\right\} I_{dss}$$

The match is excellent (< 3% out to v_{gs} = -0.6v) for the approximate Statz illuminated model (column **m**).

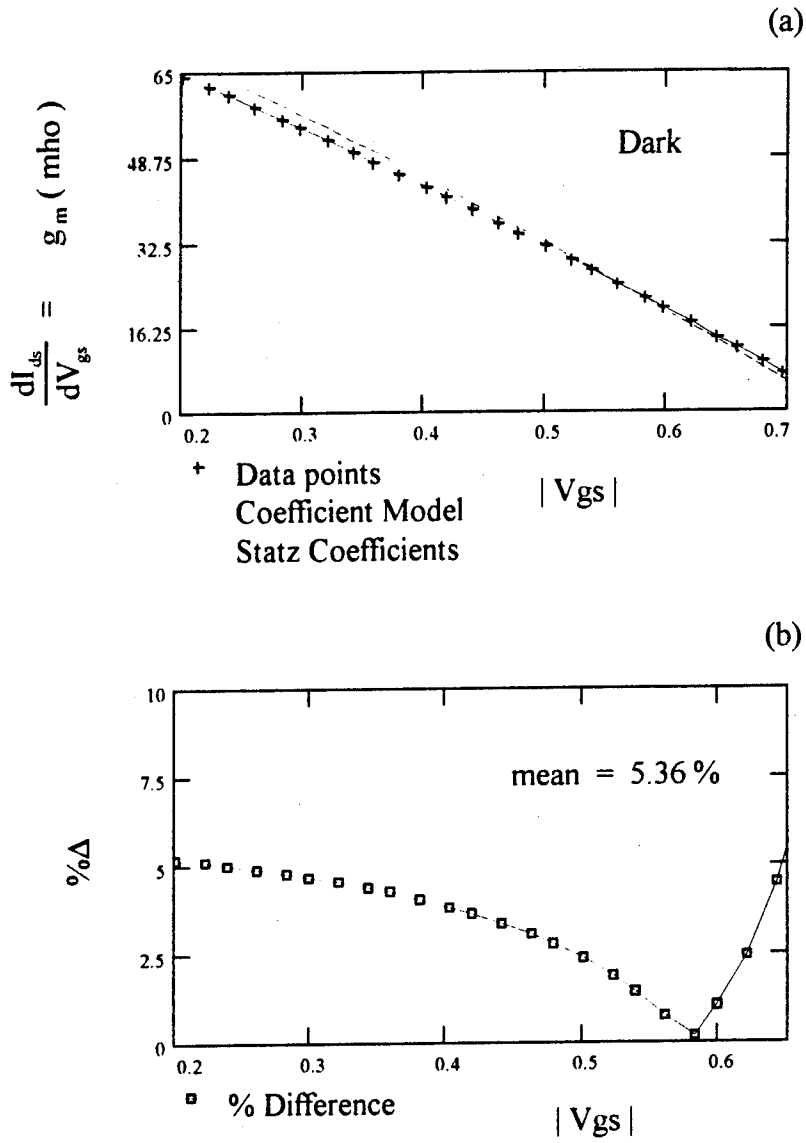

Figure 10 Dark Conductance Model vs. Experimental ; a) g_m, b) % Error

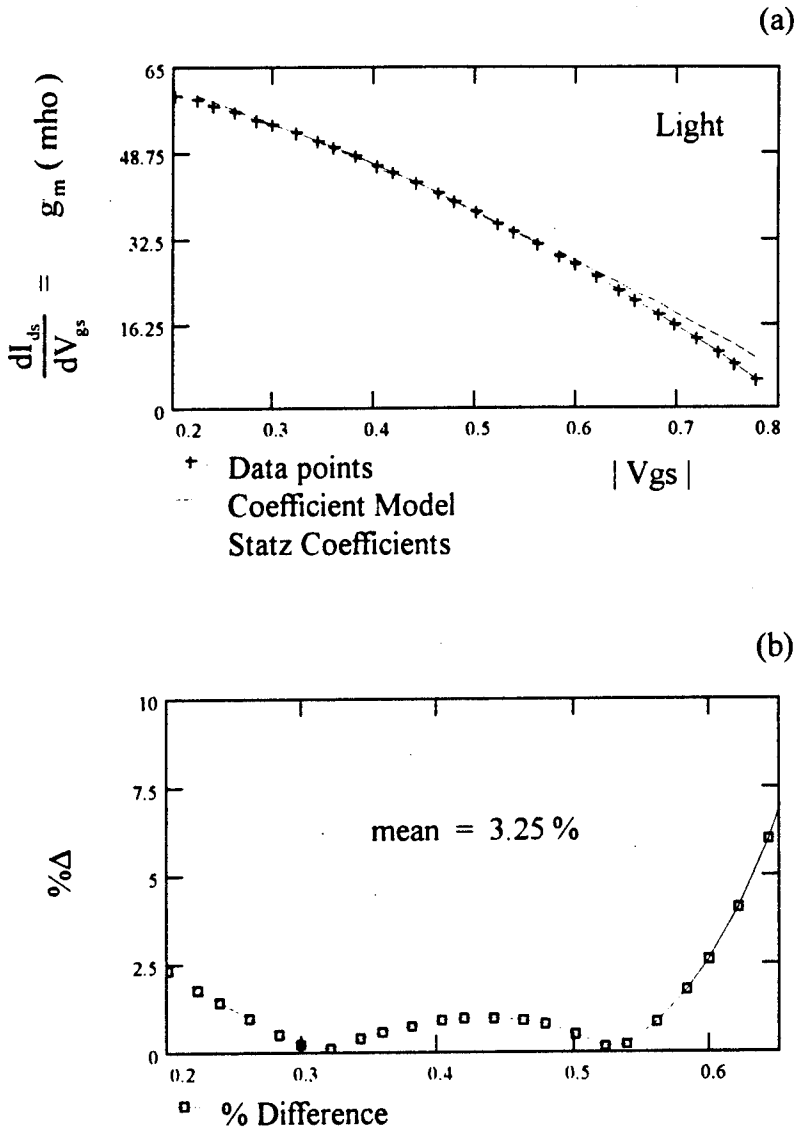

Figure 11 Light Injected Conductance Model vs. Experimental ; a) g_m, b) % Error

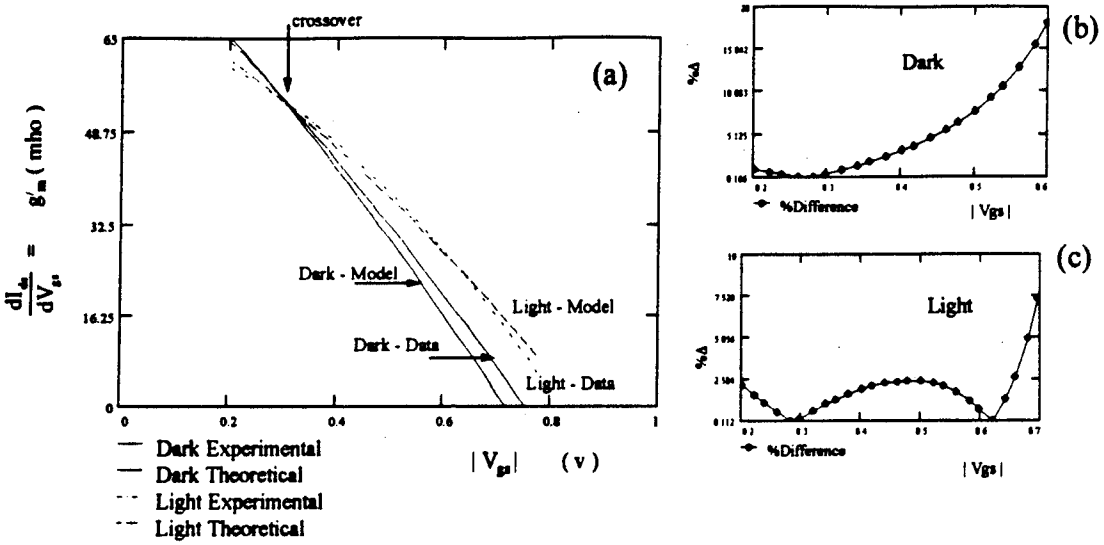

Figure 12 Conductance with variation in model parameters; a)g_m, b) %Error - Dark, c) %Error - Light

In Figure 12, a slightly different superimposed voltage and subsequently different coefficients were used. In (a) the gain crossover bias is exactly the same for the model and the experiment. The percent difference between the model and the data is good for certain range of bias voltage: less than 5% up to 0.5v for the dark (b) and less than 2.6% up to 0.65v for the light (c). The light case shows roughly the same shape and magnitudes as in Figure 11 b. However, the dark case exhibits a huge exponential departure at higher bias points (e.g., 20% at 0.6v).

The model has shown that the MESFET must be sufficiently reverse biased (V_{gs} near pinchoff) so that the transconductance and subsequently the amplifier gain will be larger when illuminated than under dark conditions. Also, it is necessary to be near pinchoff to obtain the maximum possible gain increase.

In Figure 13, the amplifier output is plotted for three values of gate bias as the drain to source bias is varied. There is an RF signal on the amplifier input is set at -10dBm power level on the RF sweeper. In (a), V_{gs} is near forward bias condition and the light case is lower output power than the dark. In (b), the outputs under illumination and dark are almost the same. In (c), as V_{gs} draws near to pinchoff and is sufficiently reverse biased, the light injection causes increase in the amplifier output level.

Figure 14 illustrates the output crossover as V_{gs} is varied to near pinchoff. The largest differences in the gain are at pinchoff. In this Figure, the gate signal power level is indicated, and Vds is 1.0v for each set of data. The output follows the transconductance exactly.

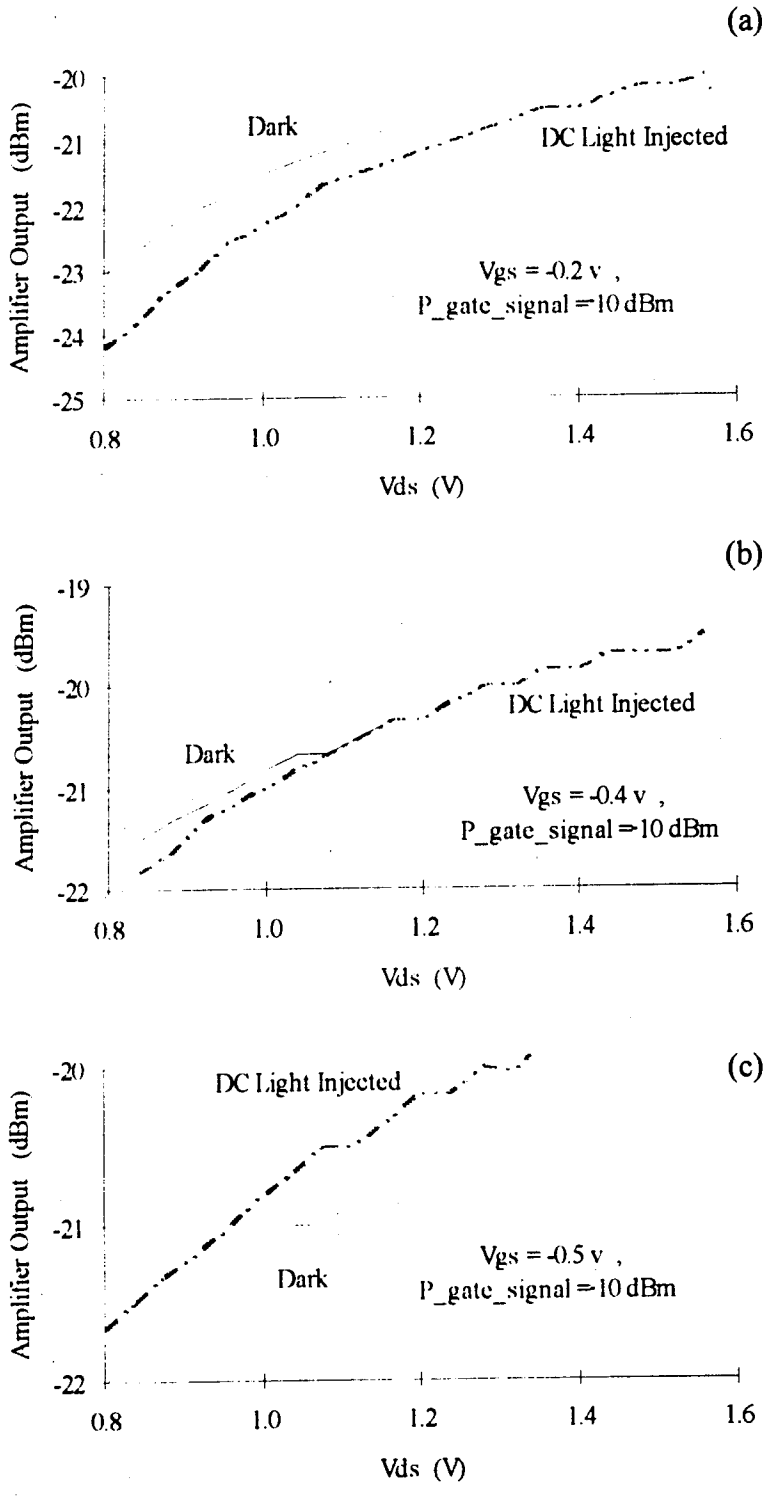

Figure 13 MESFET crossover: a) Gain lower, b) Gain approximately equal, c) Gain higher

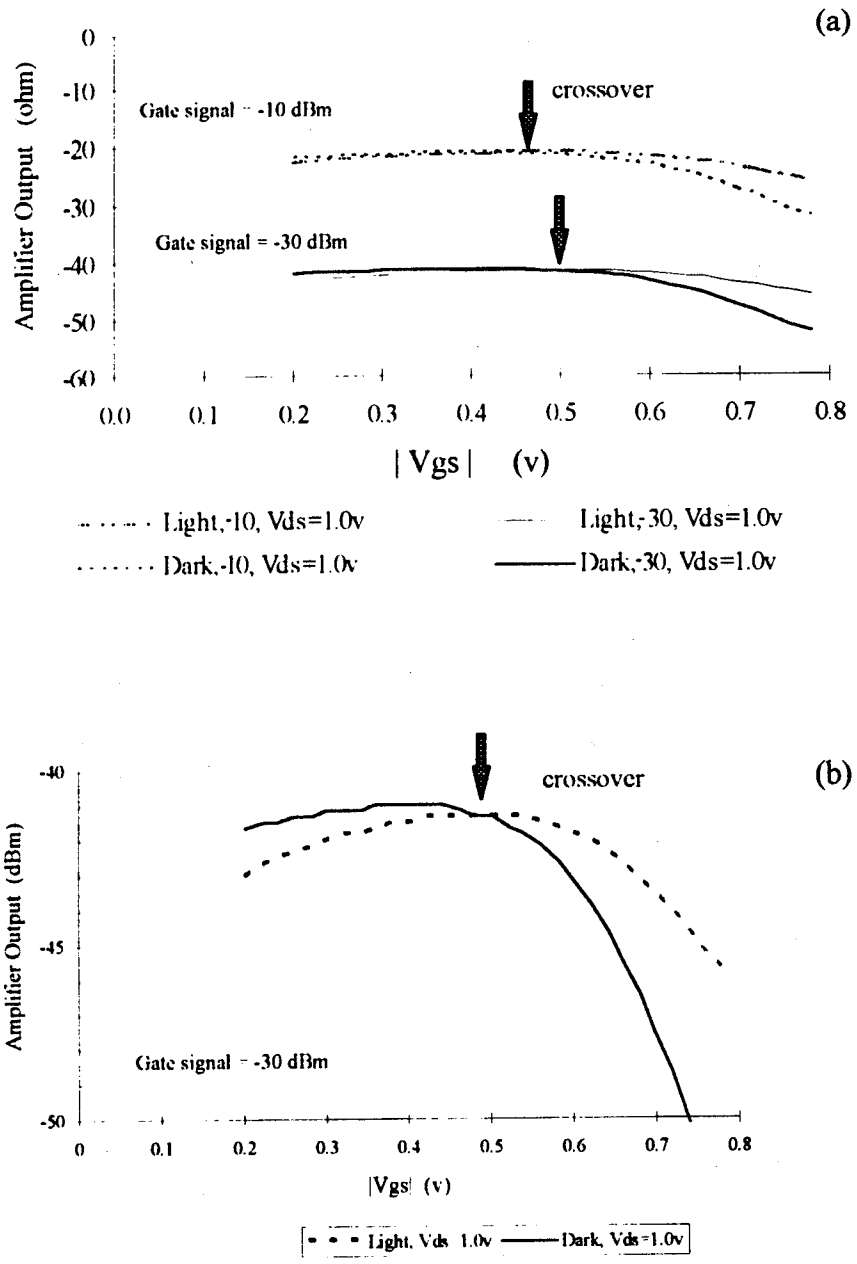

Figure 14 Gain crossover

The amplifier output impedance $|Z_{ds}|$ is defined as follows.

$$|Z_{ds}|=|Z_{out}|=\frac{V_{out}}{I_{out}}=\frac{V_{out}}{I_{ds\_m}}$$

The measured values of the output voltage V_{out} from the amplifier output to ground is Vds minus the external drop. The current is calculated from the approximate Statz model for the theoretical graphs and is measured for the experimental plots. Figure 15 is the result of the modeled values and the experimental values for V_{ds} equal to 1.0v. The measurements were taken with an electrical signal on the amplifier input (P_{sig}) of -10dBm and -30dBm as set on the RF source. The gate bias was swept in 0.1v increments from -0.2v to -0.8v. The drain bias was measured in steps of 0.1v from 0.8v to 1.2 v (dark) and 1.6v (light).

The experimental data is given in Figure 16 (a) versus $|V_{gs}|$ for V_{ds} equal to 1.0v and in Figure 16 (b) versus V_{ds} for V_{gs} equal to -0.2v. For the dark case, the |Z| does not vary as a function of the input signal level (-10 or -30 dBm). However, there is a noticeable change in |Z| when illuminated as a function of the input signal level. The effect of the light depends on the signal level at the amplifier input. Furthermore, |Z| is greater in the dark cases than in the illuminated because the additional voltage drop (discussed in the next paragraph) is not present in the dark.

Figure 17 is |Z| for several values of V_{ds}. In this Figure, the dark (V_{ds}=0.8v) and light (V_{ds}=1.5v) cases practically overlap beyond a gate bias of 0.55v. This is the same gate bias crossover ($\approx$ 0.55v) as shown in g_m (Figure 14). At this point the gate pinning effect begins to effect the circuit. When illuminated, as minority carriers are generated, there is a multiplicative effect. The drain to source voltage

has a voltage drop across the intrinsic and extrinsic elements proportional to the photo-induced current. In Figure 17 , V_{ds} equal to 0.8v dark is approximately equal to V_{ds} of 1.5v light after $|V_{gs}|$ of greater than or equal to 0.55v (g_m crossover bias). The difference between the dark and light voltages is nearly equal to 0.655v (1.5-0.8=0.7v $\approx$ 0.655v). The drop is the same amount the gate suffered in the modeling of g_m toward the forward bias side. On the drain side, it is toward the negative side. To preserve Kirchoff's voltage law, the drop around the loop is conserved:

$$V_{out} = V_{ds} = V_{ds\_set} - 0.655$$
$$V_{gs} = V_{gs\_set} + 0.655$$

Therefore, the additional voltage drop in the model is confirmed from a secondary approach.

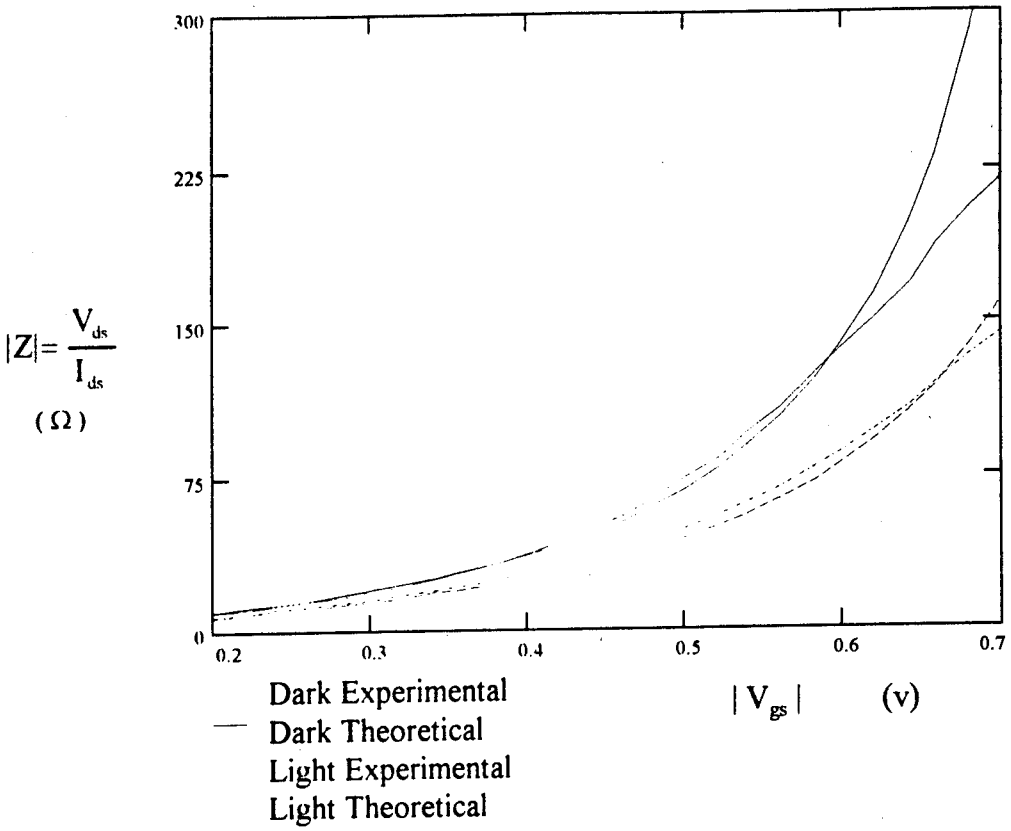

Figure 15 Experimental and simulated impedance

(a)

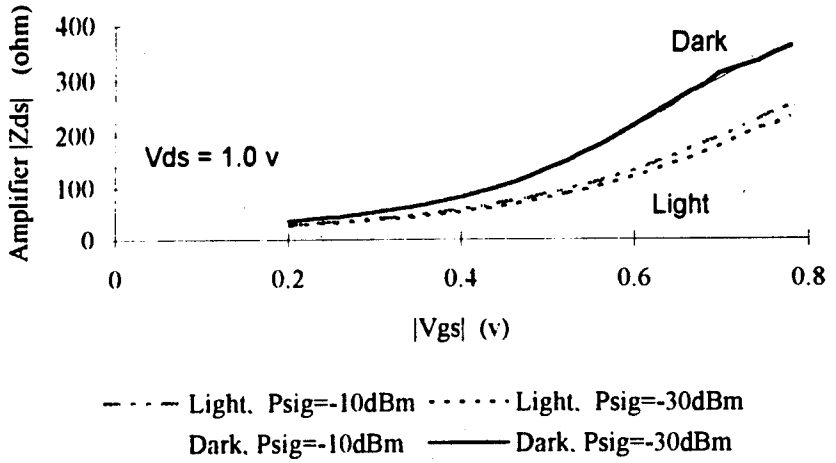

(b)

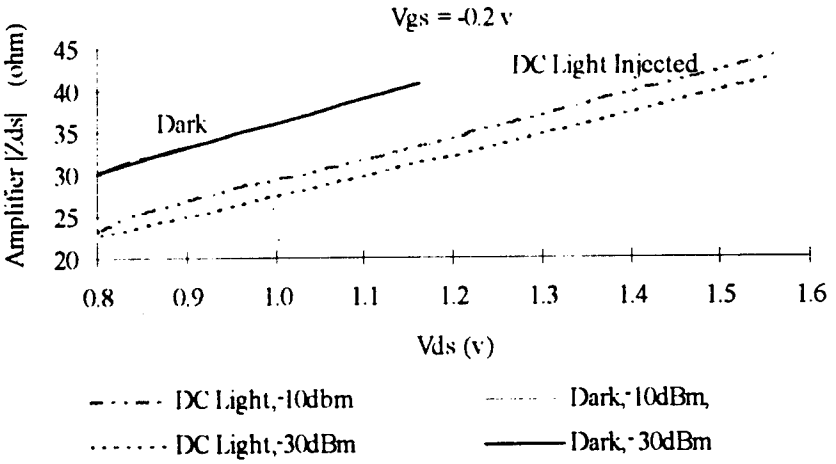

Figure 16 Amplifier output impedance variation with Light; a) vs. $|V_{gs}|$, b) vs. V_{ds}

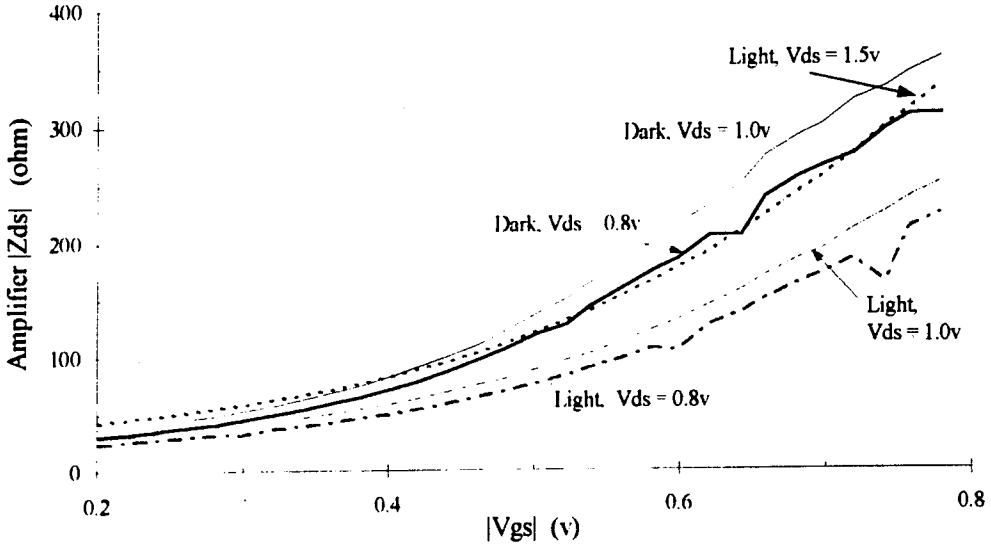

Figure 17 Amplifier impedance changes with light injection

8.3.1 S-parameter Measurements

Using an HP8702 network analyzer, the amplifier S-parameters have been measured. Using the extraction methods described in *Chapter 6*, the photoeffects are identified with circuit parameters. First, S parameter measurements are completed with no light injection, DC light injection, for modulated single laser injected and with the locked heterodyned beat injected. Next, the admittance [Y] matrix is used to extract information regarding circuit parameters effected by the light injection. The argument of the S and Y parameters were unchanged when light was injected. Figure 19 shows the argument of the S parameter measurements.

The amplifier gain is centered around the 1 GHz frequency value. Since there was extreme experimental difficulty to lock lasers at 1 GHz due to the mode profiles of the laser and because the amplifier center band was at 1 GHz, the purpose of the experiments in this section are twofold; (1) to investigate the effects of DC light, (2) to determine if the modulated light at frequencies away from 1 GHz has any effect. The experiment was set up to determine if the frequency component of the injected light would be detectable in the S-parameters and if the light would change the impedance of the MESFET enough to shift the amplifier band and to see if there was significant changes in the 2-port matrix at the injected frequency.

DC light was injected into the MESFET (Figure 20). The single laser was modulated at 2.0 and 2.5 GHz and injected into the amplifier (Figure 21). Also, the locked and unlocked beat note at 2.0 and 2.5 GHz was injected (Figure 22).

To limit the variables in the experiments of this Thesis, the same MESFET was used in all experiments. Because the characteristics of the Fujitsu MESFET exhibited stability difficulties at frequencies higher than 1.8 GHz, it was virtually impossible to get stable amplification at higher frequencies. Therefore, the oscillators were easy to design at 3 and 5 GHz, but an amplifier was not realizable at 3-5 GHz. Because the feedback of the MESFET was too strong, the amplifier stability criteria dictated operation at 1 GHz even with external elements. Therefore, the goals were set as described in the previous paragraph. Also, in 8.4-Amplifier Spectrum, 1GHz AM and FM optical signals are detected perfectly from the amplifier to prove the frequency detection capabilities of the optically injected MESFET amplifier circuit.

First, the definition of the amplifier gain is developed. The unilateral assumption will be described and shown to be valid about the center frequency (1 GHz) of the amplifier. An expression for the change in gain from dark to illuminated will be developed based on S parameters. The admittance matrix [Y] is written in terms of both S-parameters and circuit elements for specific case of the unilateral assumption. In Chapter 6, the conversion between Y and S parameters is given for general case. Finally, from the Y matrix the amplifier gain is shown to be directly proportional to the transconductance g_m as was described in the previous section from a circuit theory viewpoint.

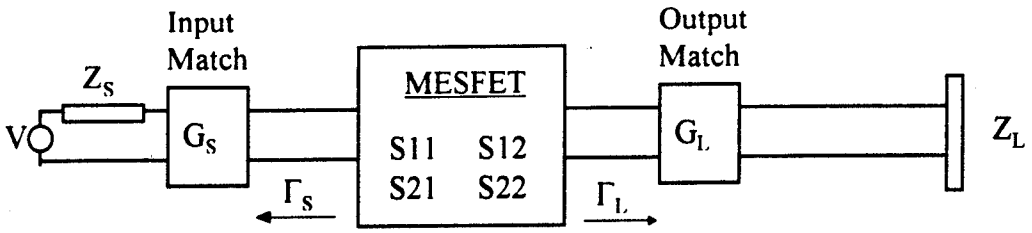

Figure 18 Amplifier circuit matching elements

The transducer gain G_T is defined as the ratio of power delivered to the load P_L over the power available from the source P_{avs}. Although other definitions of gain exist, G_T is most commonly used as an amplifier figure of merit. The gain depends on the input and output matching elements. The transducer power gain of the amplifier is written

$$G_T = \frac{|S21|^2 \left(1-|\Gamma_S|^2\right)\left(1-|\Gamma_L|^2\right)}{|1-\Gamma_{in}\cdot\Gamma_S|^2\,|1-\Gamma_{out}\cdot\Gamma_S|^2}$$

where the input reflection coefficient Γ_{in} is given by

$$\Gamma_{in} = S11 + \frac{S21\cdot S12\cdot\Gamma_L}{1-S22\cdot\Gamma_L}$$

where the output reflection coefficient Γ_{out} is given by

$$\Gamma_{out} = S22 + \frac{S21\cdot S12\cdot\Gamma_S}{1-S11\cdot\Gamma_S}$$

A special case of the transducer gain is defined as the unilateral gain. The unilateral assumption effectively says that changes in the input and output matching conditions can be neglected. Therefore, the input and output reflection coefficients are approximately S11 and S22 respectively.

$$\Gamma_{in} \approx S11$$
$$\Gamma_{out} \approx S22$$

The unilateral assumption is valid when the figure of merit U is less than a few tenths of dB[4].

$$U = \frac{|S12|\,|S21|\,|S11|\,|S22|}{(1-|S11|^2)(1-|S22|^2)}$$

In the vicinity of amplifier design frequency of 1 GHz, |S12| is 0.027 dB which is small enough to justify the unilateral assumption at 1 GHz. Therefore, the unilateral transducer gain ($G_{TU}=G_oG_SG_L$) can be written as follows:

$$G_{TU} = \frac{|S21|^2\left(1-|\Gamma_S|^2\right)\left(1-|\Gamma_L|^2\right)}{|1-S11\cdot\Gamma_S|^2\,|1-S22\cdot\Gamma_S|^2} = G_oG_SG_L$$

where the intermediate gains (G_o, G_S, G_L) are defined as follows:

$$G_o = |S21|^2$$

$$G_S = \frac{\left(1-|\Gamma_S|^2\right)}{|1-S11\cdot\Gamma_S|^2}$$

$$G_L = \frac{\left(1-|\Gamma_L|^2\right)}{|1-S22\cdot\Gamma_S|^2}$$

In the design of the amplifier, the gain is maximized when the source and load matching elements equal the complex conjugates of S11 and S22.

$$\Gamma_S \approx S11^*$$
$$\Gamma_L \approx S22^*$$

The latter equations can also be used in G_{TU} if the conjugate matching condition is present. Note from Figure 20, Figure 21, Figure 22 that S11 and S22 vary only slightly when illuminated. Therefore, change in amplifier gain from the dark to the illuminated state can be written in terms of the change in G_o.

$$\Delta G \approx \zeta(G_{o\_Light} - G_{o\_Dark}) \approx \zeta(|S21|^2_{Light} - |S21|^2_{Dark})$$

where ζ is a constant that represents the small changes in G_S and G_L. Therefore, the change in |S21| represents the change in gain at 1 GHz.

The next issue is to determine the circuit parameter that corresponds to |S21|. In the previous section 8.3, we determined the output of the amplifier is proportional to g_m which we will prove now from a two port equivalent viewpoint.

First, the conversion from S matrix to Y matrix is completed as follows:

$$[Z] = ([U] - [S])^{-1}([U] + [S])$$
$$[Y] = [Z]^{-1}$$

where [U] is the identity matrix. The unilateral assumption at 1 GHz is valid. Therefore, with S12 set to zero, the admittance matrix [Y] is rewritten in terms of the S parameters as follows:

$$[Y] = \begin{bmatrix} \frac{(1 - S11)}{(S11 + 1)} & 0 \\ \frac{-2 \cdot S21}{(S11 + 1) \cdot (S22 + 1)} & \frac{(1 - S22)}{(S22 + 1)} \end{bmatrix} \qquad (8\text{-}6)$$

In Chapter 6, the [S] to [Y] conversion process is detailed without the simplifying unilateral assumption, and the Y parameter circuit solution is also given. Here, the Y matrix is developed under unilateral assumption which yields Y21 equal to zero per (8-6).

$$[Y]=\begin{bmatrix} \dfrac{j\omega Cgs}{1+j\omega R_i Cgs} & 0 \\ \dfrac{g_m e^{-j\omega\tau}}{1+j\omega R_i Cgs} & \dfrac{1}{rds}+j\omega Cds \end{bmatrix}$$

The DC value of the real part of Y21 yields the transconductance g_m:

$$\lim_{\omega \to 0}\left(\mathrm{Re}\{Y21\} \right) = \lim_{\omega \to 0}\left(\frac{g_m \cos(\omega\tau)}{\sqrt{1+(\omega R_i Cgs)^2}} \right) = g_m$$

Figure 20, Figure 21, Figure 22 are the S parameter measurements for the amplifier with DC light, a single modulated laser and the locked heterodyne beat respectively. Each graph has the dark measurements for reference. In all three Figures, the gain |S21| is in (c). The magnitude of the increase is approximately 1.02 v. The measurements were taken with V_{gs} at -0.5v, V_{ds} equal to 1.50v. In the dark case, the I_{ds} equals 15.1 mA and when injected with 60μW of optical power the current 19.7-21.23 mA. The RF power modulating the laser was set at 6.2 dB and at a frequency of 2.5 GHz. The RF frequency had little effect on the amplifier S parameter; however, the amplifier recovered the RF optical signal on the output when viewed on a spectrum analyzer. In the stable amplification frequency range around 1 GHz, the three optical signals all had the same effect; to increase the gain as shown in the Figures 20, 21, 22 (c). Very little change in the S11 and S22 magnitudes has been detected near 1 GHz. In the vicinity of 2 GHz, there is a significant change in S12 for all cases. However, the unilateral assumption is not valid, and therefore, Y12 is not zero. Y12 in is given by the following:

$$Y_{12} = \frac{-2\,S_{12}}{(1+S_{11})(1+S_{22}) - S_{12}\,S_{21}} = -j\,\omega\,C_{gd}$$

At the higher frequency, the gate to drain capacitance C_{gd} becomes important. This strong feedback at higher frequencies is exactly the reason that made this particular Fujitsu MESFET an excellent oscillator and made it virtually impossible it to amplify at 2 GHz in a stable manner. This was discussed at the beginning of this section on page-336.

The change in C_{gd} is related to the change in gate voltage due to carrier generation in the depletion region (C=dQ/dV or C=I/ωV).

The external amplifier circuit impedances have not been explicitly discussed. The extraction procedure set forth in Chapter 6 discusses de-embedding of parasitics and external inductances for a two port MESFET; source grounded, gate and drain looking into 50Ω loads. The S parameters presented in Figures 19, 20, 21 have a slightly higher overall magnitude than if the external impedances were de-embedded. The measured S parameters are given by

$$S\_measured = \begin{bmatrix} S11 & S12 \\ S21 & S22 \end{bmatrix} = S_{output}\,S_{mesfet}\,S_{input}$$

which yields the Y parameters (without the unilateral assumption) as follows:

$$[Y_{total}] = \begin{bmatrix} \dfrac{(1-S_{11})(1+S_{22}) - S_{12}\,S_{21}}{\Delta} & \dfrac{-2\,S_{12}}{\Delta} \\ \dfrac{-2\,S_{21}}{\Delta} & \dfrac{(1+S_{11})(1-S_{22}) - S_{12}\,S_{21}}{\Delta} \end{bmatrix}$$

$$= Y_{output}\,Y_{mesfet}\,Y_{input}$$

where Δ is given by $\Delta = (1+S_{11})(1+S_{22}) - S_{12}\,S_{21}$

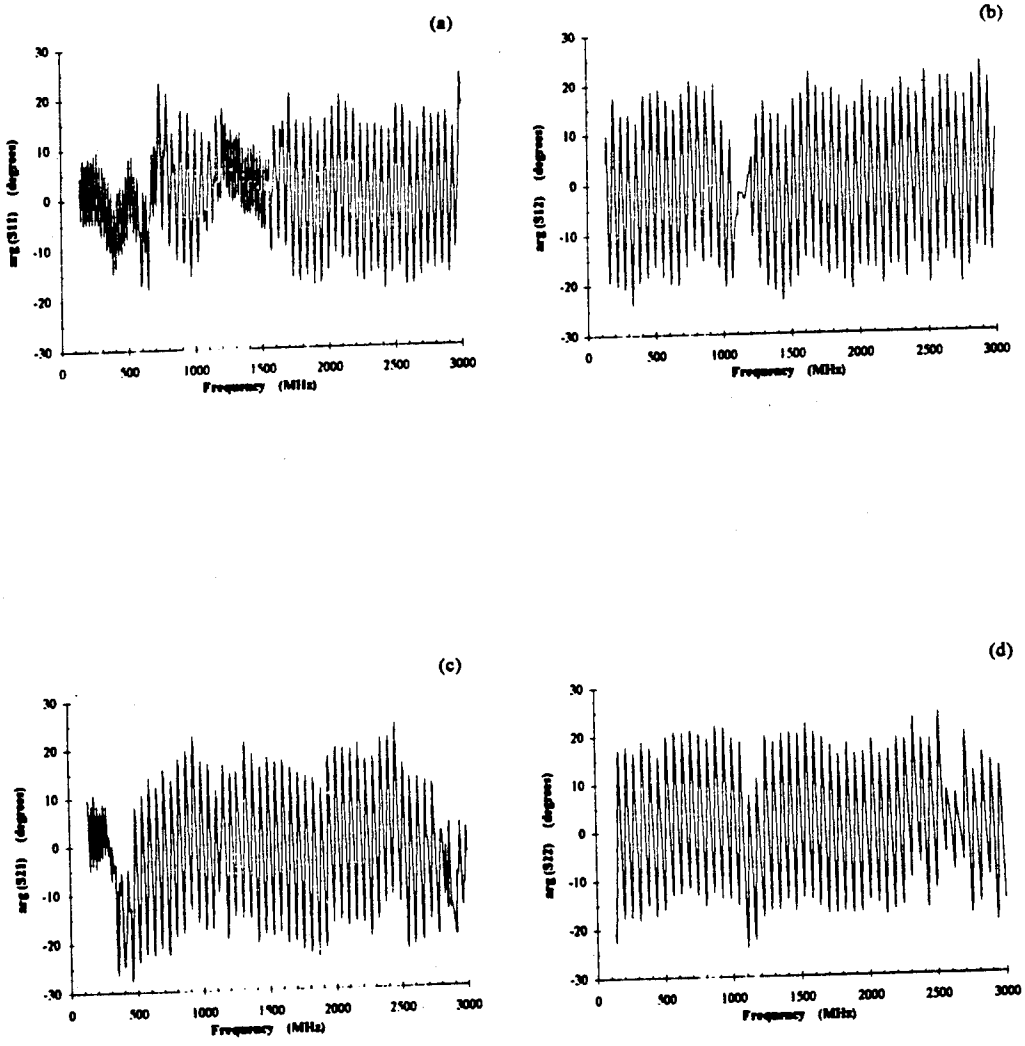

Figure 19 Amplifier S Parameter Angle

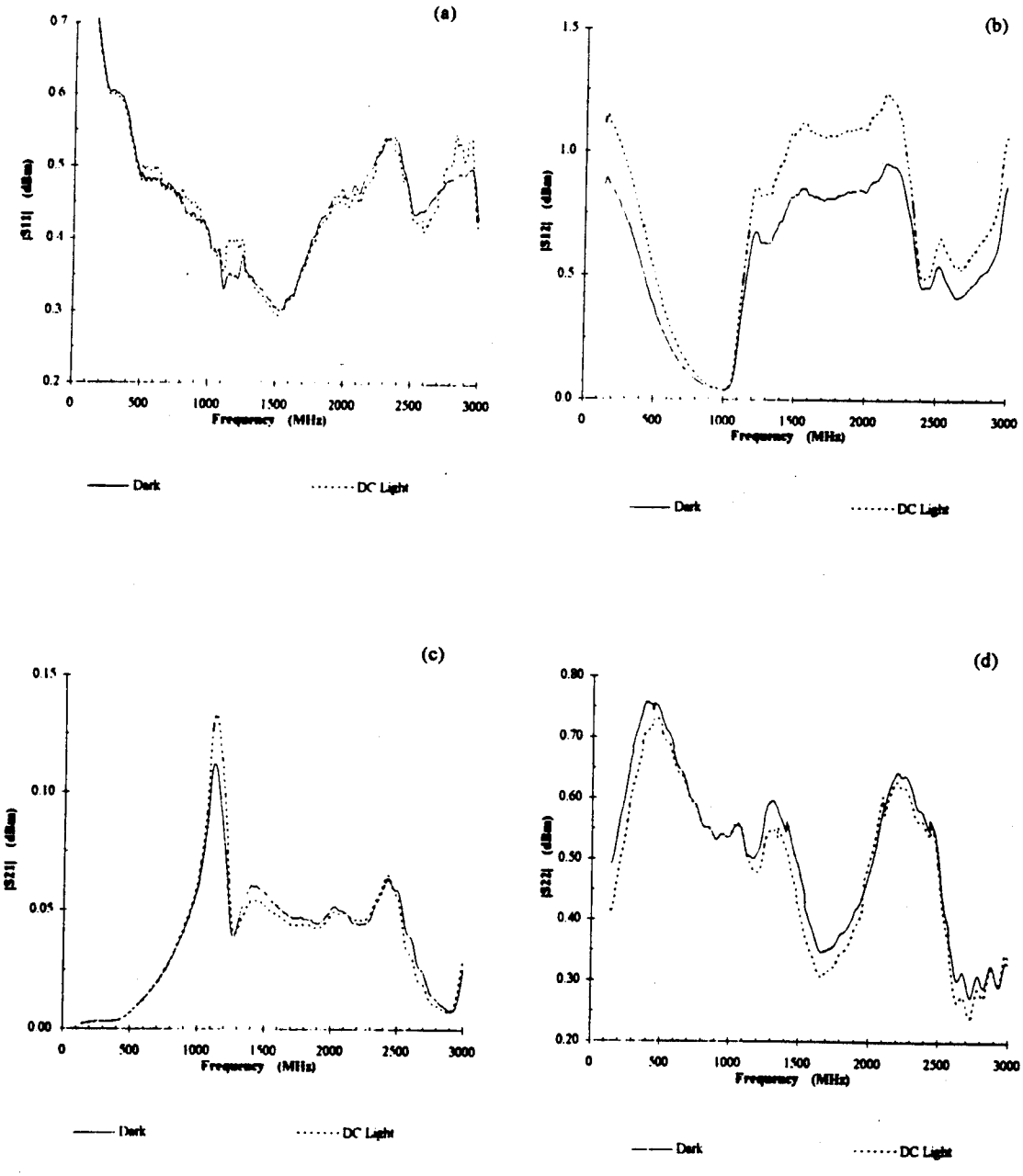

Figure 20 DC Light Effects on Amplifier |S|

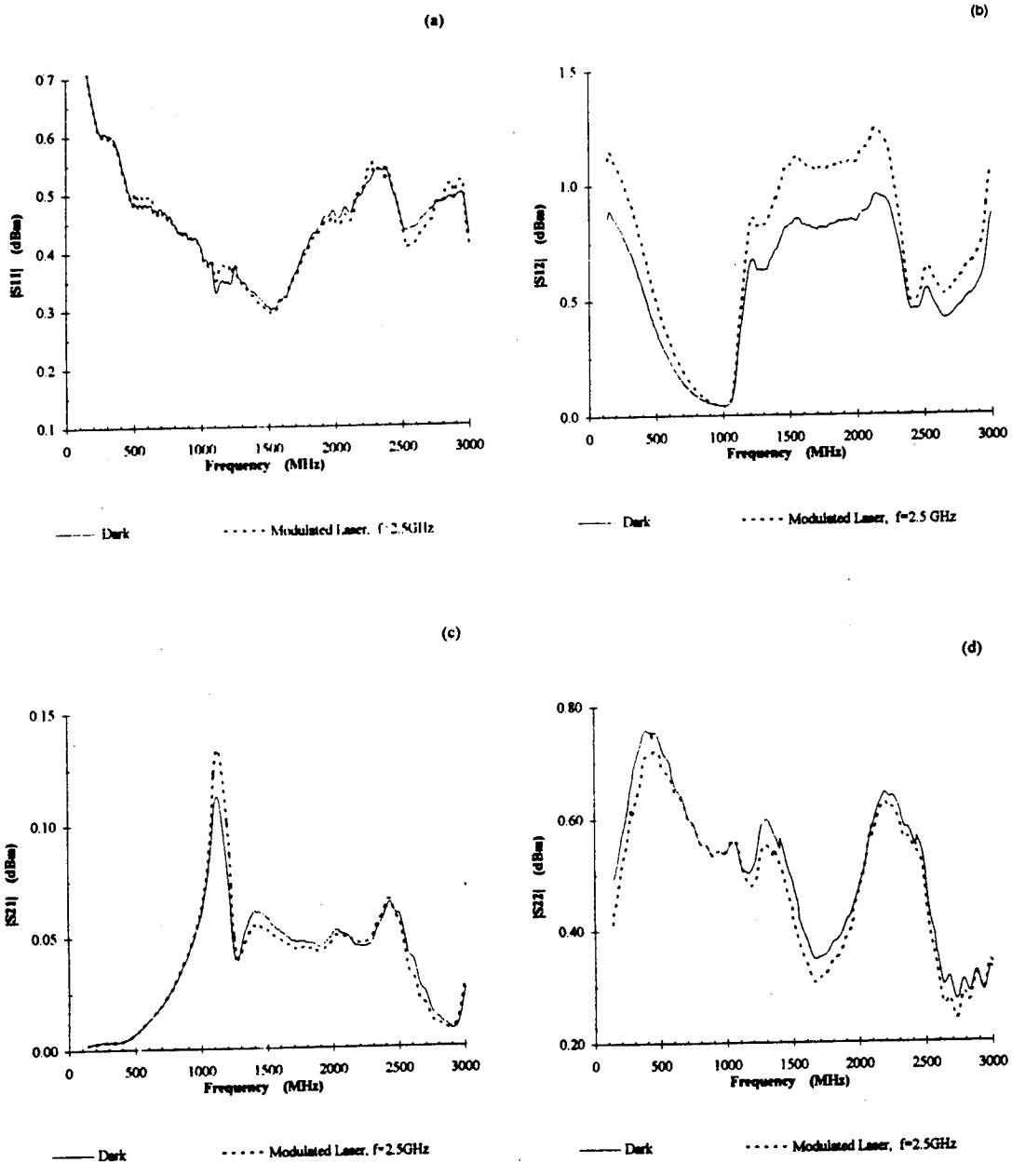

Figure 21 Optical Effects on |S| When Single Modulated Laser Is Received by Amplifier

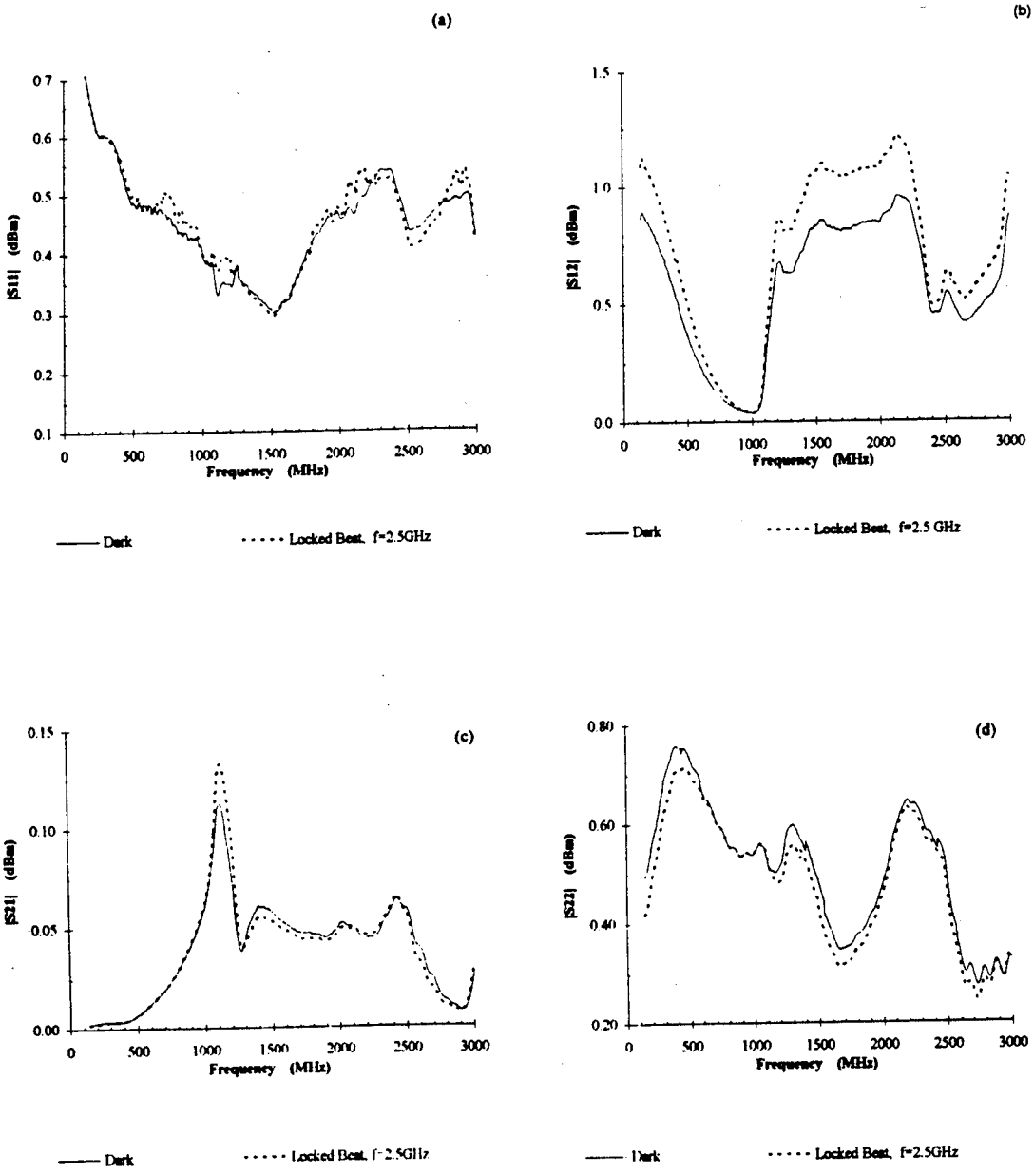

Figure 22 Heterodyne Beat is Received by Amplifier Changes in |S|

8.4 Amplifier Spectrum

The purpose for this Section is to demonstrate that the amplifier accurately detects modulated optical signals and to present a simple circuit simulation technique to represent the injection.

First, a single laser was modulated at RF frequency of 2.5 GHz. The optically modulated signal was injected into the active MESFET area of the amplifier circuit. There were no electrical signals on the input to the amplifier with the exception of DC bias supplies. The output of the amplifier was fed into HP8562A Spectrum Analyzer and is presented in Figure 23. V_{gs} was equal to -0.55, and V_{ds} was equal to 1.50v. The optical power injected is 60 μW. In the dark, I_{ds} was equal to 6.4mA, and the voltage drop across the drain bias to ground (V_{ds_read}) is 1.431v. Illuminated, I_{ds} was equal to 11.10 mA and V_{ds_read} was 1.381v. The output impedance at the drain was 224Ω in the dark and 124Ω with light injected. Although there is some impedance mismatch at 2.5 GHz, the amplifier output is still large enough to detect the optical signal easily as shown in Figure 23. As detailed in 8.2 Illuminated Amplifier Characteristics, the largest increase in gain from dark to light is obtained for V_{gs} as close to pinchoff as possible. A better impedance match at 2.5GHz and a gate bias close to pinchoff proves to be the best combination to maximize the circuit gain. An interesting outcome of these experiments is that the DC optical power will shift the operating point of the MESFET circuit due to increases in carriers and subsequent photo-voltages, and therefore, the optical signal can turn the amplifier output on and off.

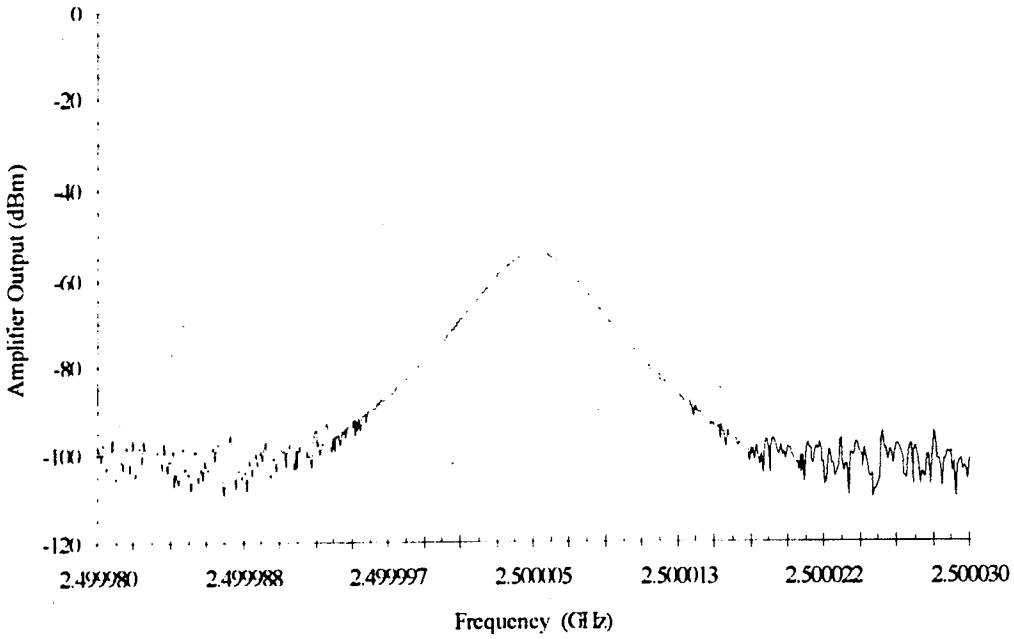

Figure 23 Amplifier received optical RF signal at 2.5 GHz

In Figure 24, the single sideband phase noise of the amplifier output has been measured. The signal is extremely stable in frequency and amplitude. In Chapter 6, the responsivity of the MESFET is approximately 30 A/W (V_{ds} = 1.5v , V_{gs} = -0.5v).

Under the same circuit bias conditions, the amplifier was injected with an optical signals with RF amplitude modulation and frequency modulation. The amplifier output for the AM and FM injected signals is in Figure 25 (a) and (b) respectively. The laser AM was set to 50% and the FM was 1 KHz deviation. Both of these signals were generated at 1 GHz. The 50% AM swing is easily detected. Also, the characteristic flat spectrum at the FM carrier is easily detected.

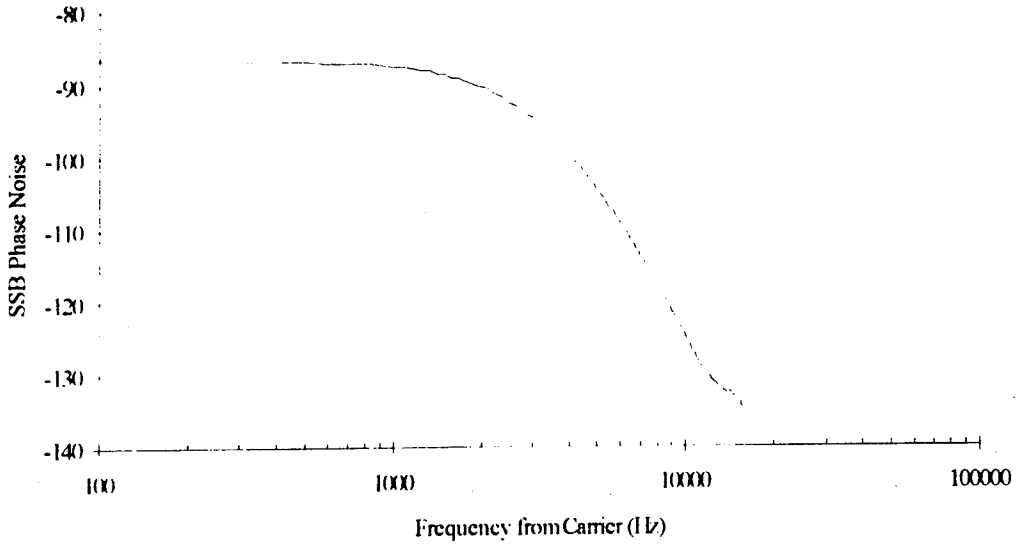

Figure 24 Single Sideband Phase Noise of Amplifier received optical signal

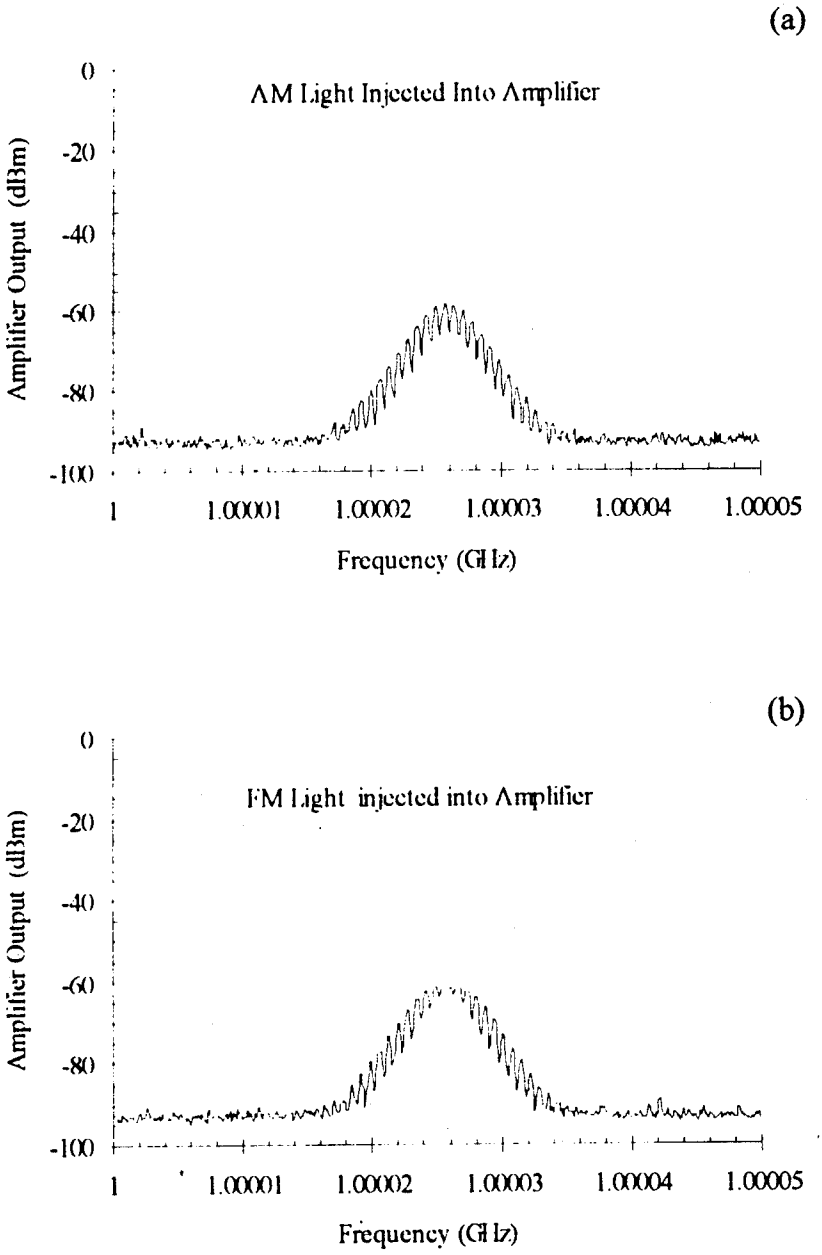

Figure 25 Received Optical Signal Modulation: a) AM , b) FM

In Figure 26, a simple common source amplifier circuit is shown with V_{dd} to represent the drain to source bias, V_1 is the gate to source bias, I_L is the current source that represents the light injection, and J is the active device. SPICE uses a modified Curtice Model to simulate JFETs which is the same model used to describe MESFETs with different constants. Since the physics of the two devices are similar and because they can both be fabricated from optically active GaAs, the simulation presented here is reasonable. In designing microwave circuits, the transmission line and electrical frequency effects are of utmost concern. Although microwave libraries exist for SPICE, they were not available at the time of the simulation and not available on the computer platforms being used. Therefore, due to library availability, the model is a proof of principle and not an exact simulation of the amplifier that was constructed for the laboratory experiments. The value of IL is determined from the equations in Chapters 3 and 6 and from experiment. The modeling of optical carrier generation is fully covered in these Chapters. The purpose here is to show the results of the amplifier circuit simulation.

The simulations were performed in two ways: (1) superimposing an electrical RF input onto the gate of the active device without the light source included to simulate electrical operation of the amplifier, and (2) without the electrical RF input and with the light (current) source to simulate optical RF signal injection. The electrical RF signals were important to assure circuit operation at GHz frequencies. The JFET model parameters were changed to compensate for the slightly different capacitance and resistance values in a typical MESFET.

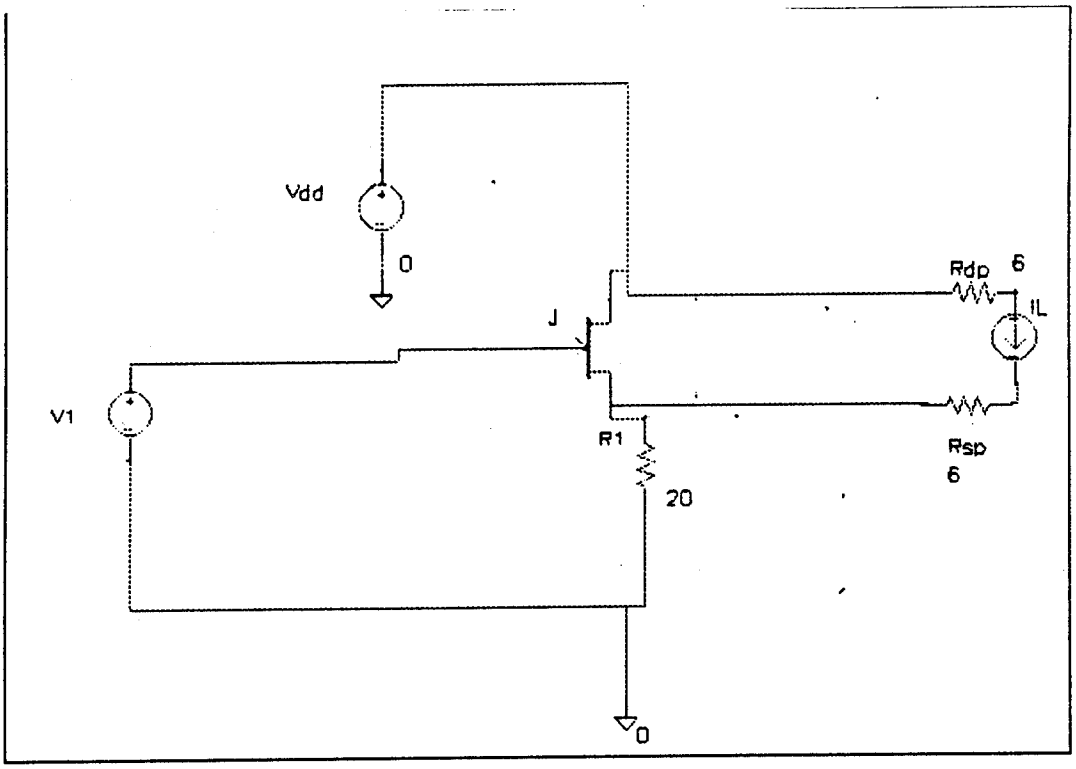

Figure 26 Optically Injected Amplifier Circuit

In Figure 27the circuit response to an RF signal at 1.2 GHz is determined and in Figure 28, the response to an FM signal with carrier at 1.2 GHz: (a) the electrical RF input, (b) corresponding output to the electrical RF, (c) optically injected signal represented by the current source I_L, and (d) corresponding output to the optical RF signal. The RF and FM signals were recovered at the output for the optical injection cases as expected. In the previous chapters, the rationale for the model has been defended.

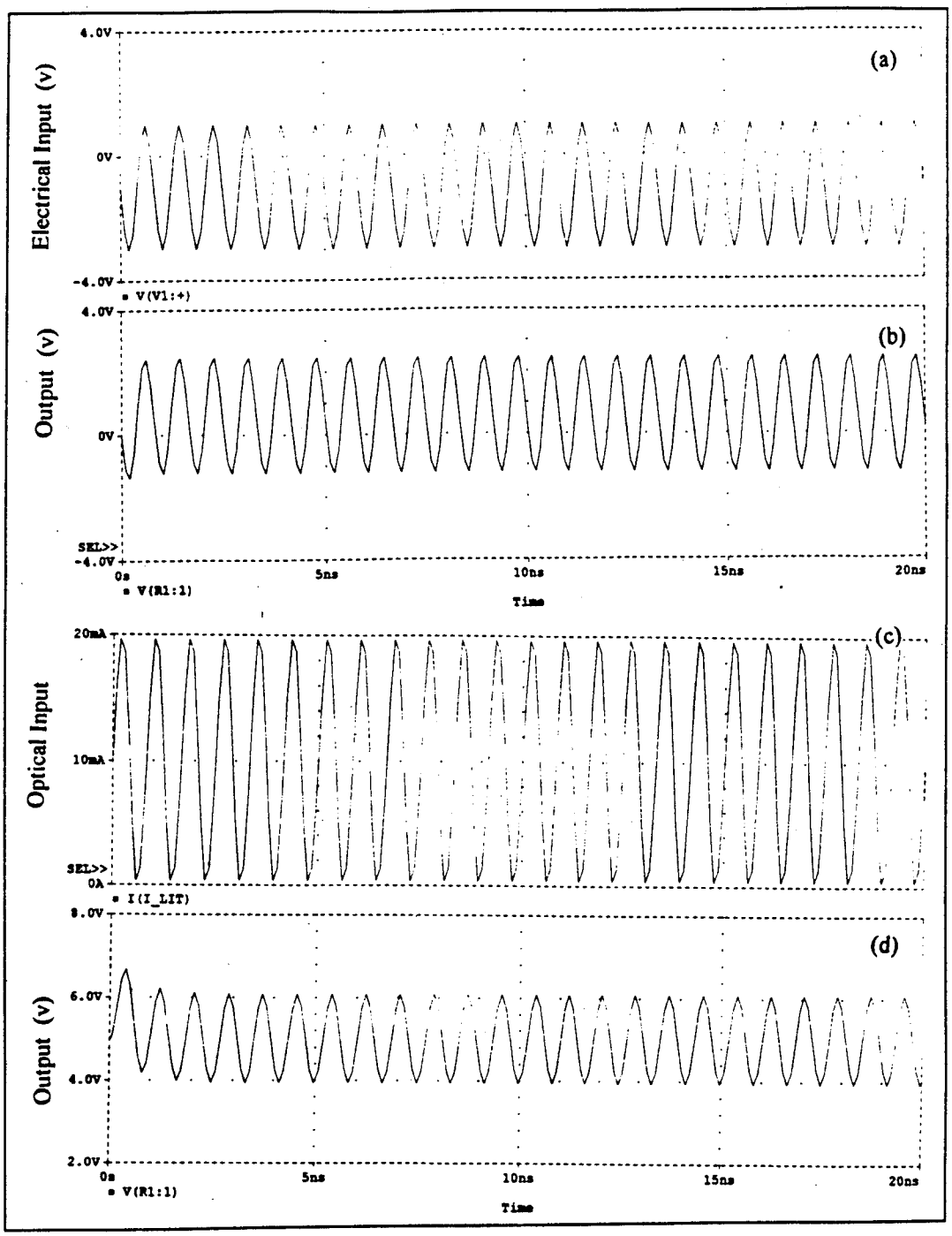

Figure 27 Circuit Simulation of amplifier detecting an RF optical signal

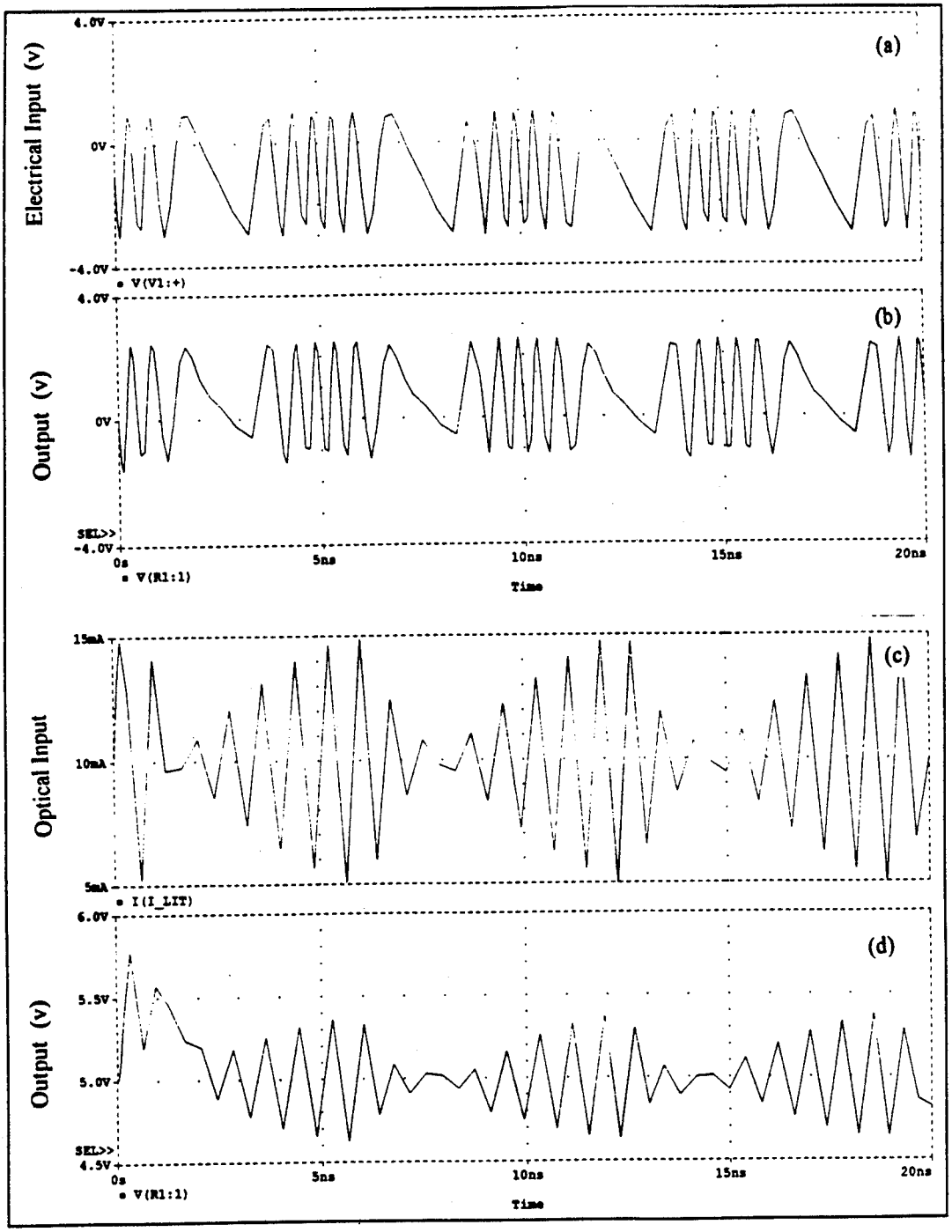

Figure 28 Circuit Simulation of amplifier receiving FM optical signal

In Figure 27, the voltage source was peak to peak 3v with a -2v offset at 1.2 GHz (a), and the current source was peak to peak 20mA at 1.2GHz (c). In Figure 28, the voltage source was peak to peak 3v with a -2v offset at a carrier frequency of 1.2 GHz and modulation frequency of 200MHz (a), and the current source had an offset of 5mA with peak to peak value of 10mA with 1.2GHz carrier frequency and 200MHz modulation frequency (c).

8.5 Conclusion

In this Chapter, experimental and theoretical evidence has proven that the microwave amplifier is a unique method for detecting optical signals. The gain increases when illuminated were found to be most profound when the amplifier is biased near to pinchoff. The gain was shown to be directly related to S21 which under the unilateral assumption at DC is the transconductance g_m. A modified Statz model was developed to model the MESFET effects within 3-5% error. The model fits works best for the illuminated cases because of the pinning effect which means less voltage variation. A SPICE model was developed and shown to produce a qualitative simulation of the amplifier when optically injected.

8.6 References - Chapter 8

[1] W.R. Curtice, and M. Ettenberg, "A Nonlinear GaAs FET Model for use in the Design of Output Circuits for Power Amplifiers", *IEEE Transactions on Microwave Theory and Techniques*, vol. MTT-33, no. 12, December 1985,

[2] K.L. Kotzebue, "Microwave Transistor Power Amplifier Design by Large Signal Y Parameters", *Electronics Letters*, vol.11, no.11, May 29, 1975, pp.240-241.

[3] W.H. Leighton, R.J. Chaffin, and J.G. Webb, "RF Amplifier Design with Large-Signal S-Parameters", *IEEE Transactions on Microwave Theory and Techniques*, vol. MTT-21, no.12, December 1973, pp.809-814.

[4] David M. Pozar, Microwave Engineering, Addison-Wesley Publishing Company,1990, pp. 240-244, 611-626.

CHAPTER 9

APPLICATIONS

9.1 Introduction

In this Chapter applications of the locked laser system and the optically injected microwave MESFET devices are discussed.

Optical injection of microwave active devices is analogous to adding an extra terminal to a device through which the optical signal can control the output of the MESFET. The MESFET, used as an optically sensitive microwave element, is an effective way to exploit the benefits of low loss, high bandwidth, electromagnetically immune single mode fiber in microwave applications. Optical injection of microwave MESFET devices can be used for phase locking, frequency tuning, and increasing the gain of amplifiers.

The locked laser system is a method for implementing a viable frequency or wavelength division multiplexing (WDM) scheme. The optical effects of MESFET devices open the door for realizable integrated microwave optics devices. The locked microwave oscillator can be used in a number of applications including phased array radar and high speed clock control and distribution. High speed optical

signals may be detected directly into a MESFET amplifier circuit and thereby, eliminate the need for photodiodes followed by post amplification.

A brief introduction in the first section is followed by a discussion of integrated microwave optics devices in Section 9.2. Applications to phased array radar (9.3), microwave communications (9.4), particularly channel multiplexing and coherent detection, and digital clock distribution (9.5) are presented. In Section 9.6, the applications section is summarized.

Theoretical and experimental work has been conducted to analyze an optically injected MESFET subsystem integrated in a MIMIC environment[1,2,3,4]. Optically injected MESFETs can replace the detector and preamplifier stages and also, reduce the overall system signal-to-noise ratio because the signal will be internally amplified via the GaAs MESFET transconductance.

Optically injected MESFET circuits can be used in a number of ways. When an optical signal is injected into the active regions of amplifier circuits, information such as AM or FM signals are detected (Figure 1). A reduction in phase noise of over 40 dB is possible when the microwave oscillator is locked to an optical carrier (Figure 2). Furthermore, a MESFET, which is biased just below threshold, can be switched ON when an optical beam is incident and switched OFF when the signal is off (Figure 3). A gated circuit of this type is very useful as the first element in a digital optical receiver subassembly.

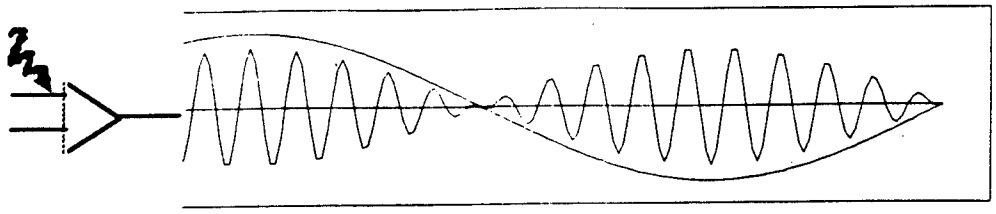

Figure 1 Amplifier circuit receives information optically

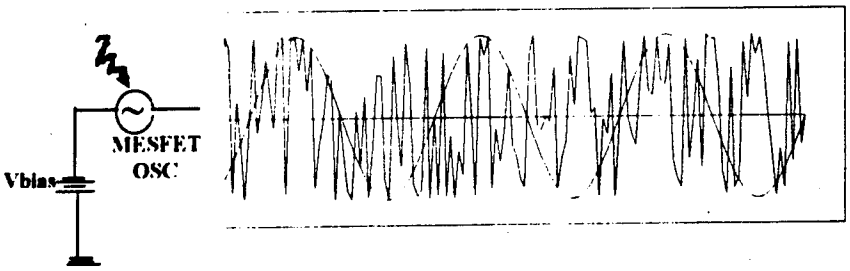

Figure 2 Oscillator circuit locks to optical signal providing reduced phase noise

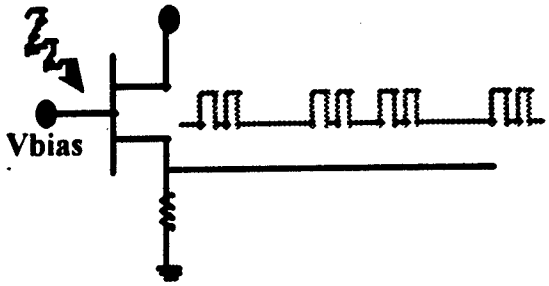

Figure 3 Gated MESFET provides a method to optically switch the device

9.2 Integrated Microwave Optics.

The MESFET uses the same material and fabrication technology as optoelectronic devices such as light emitting diodes (LEDs) and lasers. This makes the field of integrated microwave and optical systems on a single wafer possible. The new generation of monolithic photonic-microwave devices could serve as optical control of switches, attenuators, phase shifters, and mixers. Photodiodes cannot be easily fabricated onto a microwave monolithic integrated circuits (MIMIC) because of additional processing steps and hence, additional cost and complexity. The MESFET, HEMT or HBT, which could be readily fabricated on the same wafer as a MIMIC, represent an alternative to the photodiode or other traditional optical detector. Furthermore, optical materials and polymers could be used to manufacture back planes for signal distribution. Therefore, integration of the optical receiver and microwave circuit is achieved which enables system miniaturization, reduced system noise, and immunity from electromagnetic interference.

9.3 Phased Array Radar

Phased array antenna systems require oscillator frequency stability and frequency tuning to synchronize and to steer the radar direction. The antenna system must have the individual MIMIC transmit-receive modules synchronized to a

master oscillator to coherently combine the fields in space which will ultimately form a single beam[5]. A GaAs MESFET oscillator circuit, illuminated with a microwave modulated optical signal, will lock completely to the stable optical frequency. The oscillators can be built inexpensively yet provide the necessary synchronization to a stable master oscillator. Locking bandwidth of 5 MHz and frequency tuning of 40 MHz were reported in this thesis. If the oscillator design were optimized so that the gate stub was centered about the matching line, then twice the tuning and bandwidth would be possible. Esman, Goldberg and Weller have demonstrated locking bandwidths of 2.6 MHz. Locking ranges as high as 4 MHz have been reported with a common drain FET[6].

Future generations of phased array radar systems as well as satellite-borne communication systems need several thousand active radiating elements to form a pencil beam for tracking and communication. GaAs MIMICs will be distributed and arranged in antenna architectures for advanced phased array radar used by tactical aircraft. These arrays use the rapidly varying phases of the radiating elements to control the beam. Currently, beam steering is performed electronically but could be executed all optically. The oscillator's frequency could be tuned by optical injection instead of through control circuits electrically. Figure 4 shows the modulated locked laser system feeding a fiber trunk. The fiber is subsequently distributed to the active antenna elements to produce the radar's phase taper. The active elements are MESFET oscillators which are injected and locked to the optical signal.

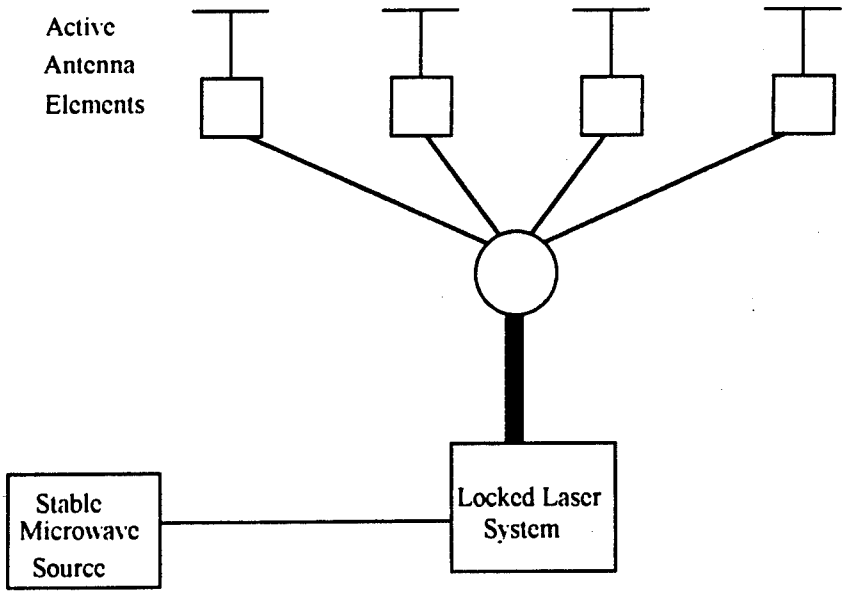

Figure 4 Optical control of a phased array radar system

9.4 Microwave Communications

Optical communications has come of age and matured in commercial applications. Serial transfer protocols have been designed to exploit fiber transmission as well as to minimize the number of installed fiber channels required in a system application. In this section, the method to optically generate microwave frequencies is presented. This method is then used in a wavelength division multiplexed (WDM) optical fiber transmission system to transmit and receive microwave channels. The microwave subcarrier is generated via optical injection locking[7]. Next, coherent detection of information is implemented optically using a MESFET amplifier as the detector and an optically gated ON-OFF MESFET to sample and hold the signal information.

9.4.1 Microwave signal generation

The locked laser system, described in *Chapter 2*, produces a stable optical beat note at the modulation frequency of the Master laser. The Master laser is modulated by a local oscillator which generates sidebands locked to the Reference laser. Each of the sidebands are separated by the Master's modulation frequency. Next, Slave lasers are modulated with lower frequency information and are referred to as channels. The Slaves are locked to individual sidebands of the Master. The heterodyned optical signal between each of a locked Slave and the Reference produces a beat note at that microwave modulation frequency.

In Figure 5, each of the lines represent the frequency spectrum of the laser. The spacing of the Master laser output is at the local oscillator frequency which is shown here as 5 GHz. The reference and the slave(s) frequency difference generate a heterodyned beat note at multiples of the Master's modulation frequency (5, 10,...GHz). This is an optical subcarrier system. Each of the slave lasers has been modulated at lower frequency for example 1 GHz.

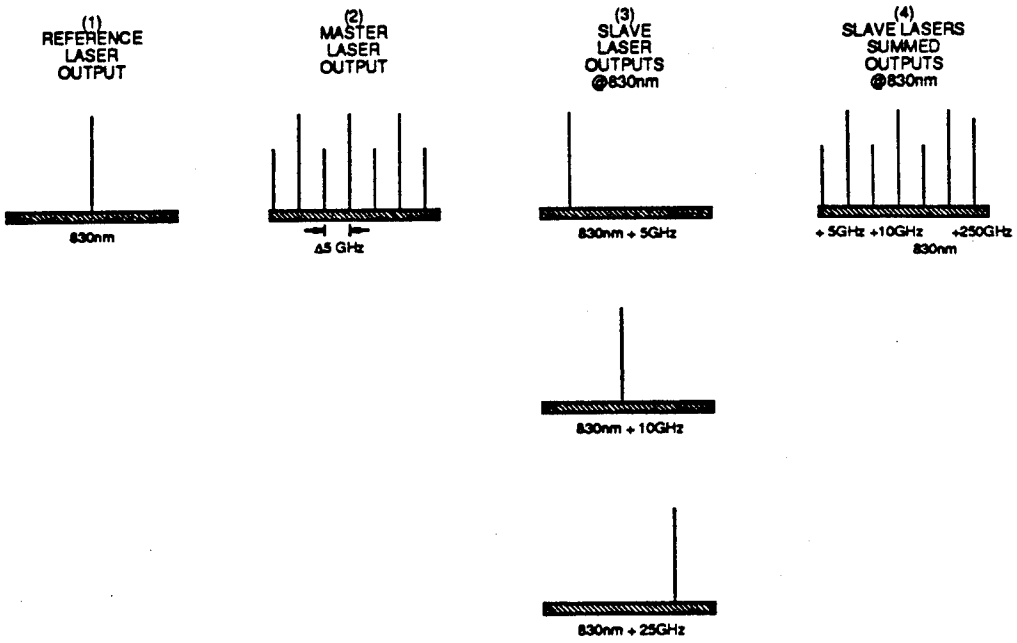

Figure 5 Microwave frequency generation at the transmitter

9.4.2 Channel Multiplexing

Strategies for enabling single channel data rates to be extended have been the subject many articles in the last decade. Increases in the capacity of a channel can be achieved by raising the data rate and by using the channel's bandwidth as efficiently as possible. To more efficiently use the bandwidth of a single mode fiber, wavelength division multiplexing (WDM) techniques have been studied. In Section 9.4.3, coherent detection is discussed.

The full bandwidth of an optical fiber channel can be separated into sub-channels via multiplexing in wavelength or frequency. Frequency or wavelength

division multiplexing (WDM) is one tactic that can be used to increase the information capacity of a fiber. The magnitude of the optical bandwidth of a multiplexed system is on the order of 200 THz (λ =1.55 μm, f=194 THz, $\Delta\lambda$=0.06nm, Δf = 9 GHz) as shown in Figure 6. Nonlinearites (eg., Raman Scattering and four wave mixing) exist which degrade this bandwidth, and it is still possible to maintain a tremendous capability.

A significant obstacle with WDM implementations is frequency stability. Due to spontaneous events, semiconductor laser diodes exhibit frequency drifts which cause the multiplexed channel locations to change. It is impossible to know a priori the magnitude of the random shifts. Therefore, it is impossible to recover the multiplexed information. WDM could be used if the optical source is stable enough to allow demultiplexing at the receiver. Injection locked laser sources are one method to eliminate the randomization of frequency and therefore, to increase the amount of information carried on a single mode fiber.

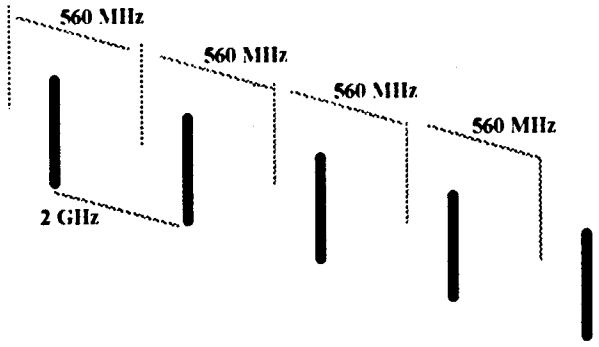

Figure 6 WDM Channel Spacing: subchannels modulated at 560Mbit/s, channels separated by 2 GHz

The locked laser subsystem is the highest capacity of conventional WDM methods. Common WDM methods use separate lasers for each channel[8], design diffraction gratings to produce the wavelength separation, or use subcarrier frequencies to carry each channel[9],[10].

WDM schemes, which use separate tunable lasers that are offset in frequency, are somewhat limited[11]. The tunability of the laser cavity around its natural frequency is only a few nanometers, and the frequency drift rate is slightly different for each laser diode. Increasing the channel spacing, which decreases the capacity, is required to protect against frequency drifts in this common WDM method.

Subcarrier systems are similar to the locked laser system used in this thesis[12],[13],[14],[15]. The modulated microwave carrier is modulated with sub-frequencies which then modulates a laser. The modulation frequency response of a laser and the intermodulation beat interference are the main problems with such subcarrier schemes[16]. Diffraction grating techniques present many technical difficulties: grating size is difficult to produce, free space alignment requires stringent mechanical control. Based on the mechanical restrictions, the channel spacing for a diffraction grating is limited to a few nanometers.

Additionally, chromatic dispersion, polarization mode dispersion and nonlinear effects (e.g., Raman scatter, four wave mixing) interact and reduce the feasible bandwidth of single and multi-channel coherent systems[17]. To achieve multigiagbit transmission, it is necessary to compensate for these anomalies.

Reducing wavelength chirp eliminate dispersion problems. Modifications of the dispersion characteristics of the transmission medium are conceivable. Implementation of heterodyne detection, which uses electrical group delay equalizer in the IF to counter dispersion, is also possible.[18]

A locked laser subsystem could be a key element in a viable WDM system. As shown in *Chapter 2*, the locked laser system reduces wavelength chirp and harmonic spreading which is necessary in order to realize a WDM system.

A microwave modulated laser (Master), which produces sidebands at evenly spaced frequencies decaying in magnitude, is injection locked to a reference laser. When the modulation frequency is the relaxation frequency of the Master laser, then a stable comb of frequencies will be generated. The Master is injected into a series of modulated lasers each of which constitute the channels of the WDM scheme. The channel lasers (Slaves) can be easily modulated at 1GHz (or 1 gigabit per second) (See Figure 5 Microwave frequency generation at the transmitter). The frequencies of the locked lasers are initially tuned to within the locking bandwidth via Peltier electronic cooling device. Once the tuning is complete, each of the channels is then determined. WDM channels can be extracted using RF down converters and standard microwave techniques. The information modulated on the Slave is represented in Figure 7 as Channels. The slaves are then coupled together and transmitted to the receiver. The reference is sent on its own fiber to the receiver. At the receiver in Figure 8 WDM Receiver, the Reference is used to down convert the Slave Channels. Optical heterodyne receivers can be used to convert the WDM

channels into a series of RF channels. Finally, using microwave techniques, the Channels are mixed with local oscillators, detected and filtered.

Multiple channel systems have interference produced from the coherent detection process. Direct detection terms at baseband, adjacent channel cross products and image band signals are produced within the coherent receiver[19]. If restrictions on the channel spacing are implemented, the effects of the intermodulation products can be eliminated. Channel spacing for Heterodyne receiver is 2-5 times the total channel bandwidth with a double balanced receiver system at the low end. Image band interference can be eliminated with a homodyne system.

The type of modulation and detection classify coherent detection methods. Intensity modulation (IM) with direct detection is easy to implement and most straightforward. This is not without its price, however. This scheme suffers from the lowest signal to noise ration (SNR) of the most common coherent methods. 5-20 dB improvement in the SNR beyond that of IM with direct detection can be realized by the use of an amplitude shift key (ASK, or AM) with heterodyne detection. If frequency shift keying (FSK, or FM) with a heterodyne detection is used, or if AM with homodyne detection is used, the SNR is improved by a minimum of 3 dB from the ASK-heterodyne detection system[20]. FSK has the problem of requiring twice the bandwidth of PSK which is not a problem when the available bandwidth of the locked laser subsystem is considered. Furthermore, phase shift keying (PSK or PM) with heterodyne detection[21 22] yields an additional 3 dB

improvement. and with homodyne detection yields 6 dB improvement from the FM systems[23]

Advantages of heterodyne detection are improved receiver sensitivity, good frequency selectivity and direct light amplification is possible because the noise frequencies outside the signal bandwidth are easily rejected. Frequency selectivity is important because the IF of the amplifier is sharper than the optical filter and FDM will yield extremely fine carrier separation. There are some technical problems which include frequency stability of semiconductor laser diodes, spectral purity, polarization control, availability of laser amplifiers. Frequency stability constraint is severe. With an IF of 0.2 to 2.0 GHz, and signal frequency of approximately 200 THz, the stability of the laser must be 10^{-5} to 10^{-6}. The spectral purity must be improved because any phase fluctuation deteriorates the bit error rate (BER). Injection locked lasers provide a stable frequency and spectral purity, and the ability to direct modulate the laser by superimposing the RF onto the drive current. Automatic frequency control (AFC) systems have been studied to stabilize the laser frequency[24] but are not as robust as a locked laser system. Active polarization correction at the input of the receiver, polarization diversity receivers and single-polarization-single-mode fibers are methods of polarization control. Spectral width requirements for optical sources based on the modulation format are given in Table 1.

Table 1 Linewidth requirements for given BER

Modulation	Sensitivity = average # photons/bit for 10^-9 BER[25]	Linewidth / Bit Rate
ASK Homodyne	18	
ASK Heterodyne	36-40	<20%[26], 10-50%[27]
FSK heterodyne	36-40	<20%
DPSK	14	0.3 - 0.5% [28]
PSK Homodyne	9	0.05-0.01%[29]
PSK Heterodyne	18-20	0.1-0.5%[30]

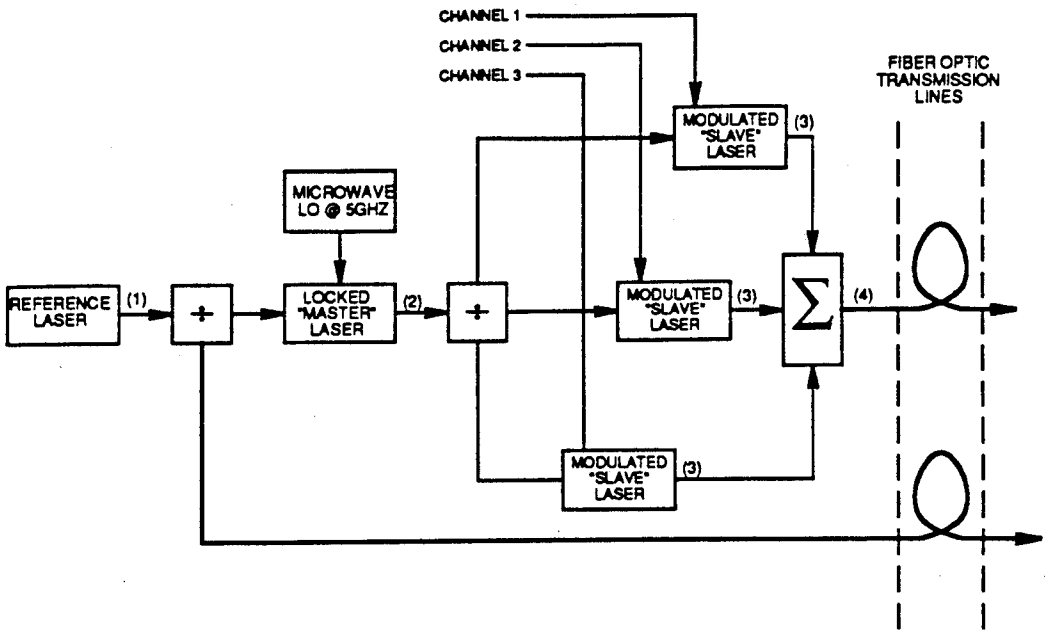

Figure 7 WDM Transmitter

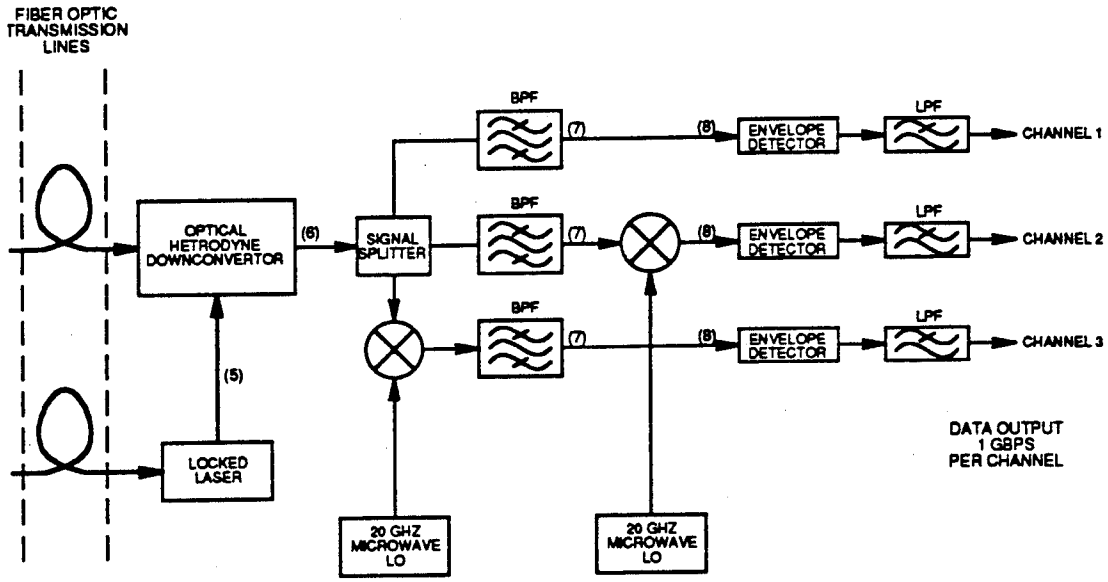

Figure 8 WDM Receiver

9.4.3 Optical Signal Detection and Amplification

Integration of the optical receiver section with functional electronics is a method of receiving signals without adding overhead to the system. With coherent detection methods, it is possible to reduce total system noise if the optical receiver is a microwave circuit. Light injection into the active region of a microwave amplifier is shown to be a viable method. Using the MESFET as an optical receiver replaces the standard receiver subassembly (e.g., photodetector plus pre-amplifier) in a system and, additionally, is a part of the operating circuit. The benefits of the MESFET as an optically sensitive element are well suited as a low-noise novel receiver in coherent detection schemes.

Direct electrical connections are the conventional methods to control a microwave MESFET. Many electrical connections cause interference and noise problems as well as the difficulty of physically providing the electrical connection. To overcome the problem of EMI, optics can be used to transmit a modulated signal via fiber and to detect it with a high speed PIN photodiode. The photodiode output is amplified and electrically injected into a microwave synchronous oscillator via the MESFET gate[31,32,33]. The photodiode and amplifier add noise to the overall system. The idea is to detect an RF modulated optical signal without adding extra elements. This can be accomplished by using the light sensitive properties GaAs MESFET. Direct optical control of MESFETs can result in gain control of amplifier circuits, lower overall signal to noise characteristics, immunity from electromagnetic interference and electrical isolation. Figure 9 is a schematic of a standard optical

(a)

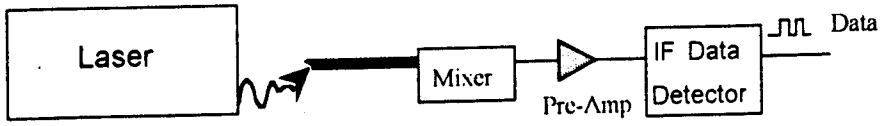

(b)

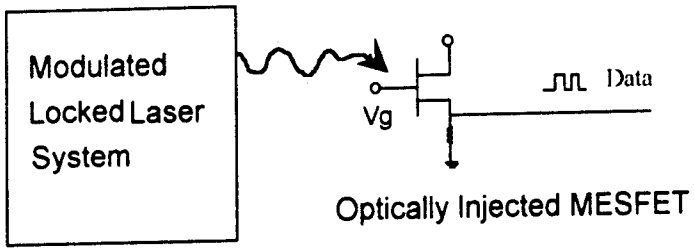

Figure 9 Optically injected MESFET amplifier replaces conventional detection technology

receiver subassembly (a) versus the injected MESFET amplifier receiving and amplifying the optical signal directly without mixers, post amplification or IF detectors.

To fully integrate the high speed analog detection, the optical signal injects a MESFET that is surrounded by a latch circuit. This sample and hold circuit is shown in Figure 10 where Vin represents the photovoltage (i.e., the injecting optical signal onto the MESFET active region). The sample and hold circuit can be simply thought of as a switch and a capacitor. When the switch is closed, the voltage across the capacitor tracks the input. When the switch is opened the capacitor holds the instantaneous value of the voltage. The switch can be a bipolar transistor, a FET

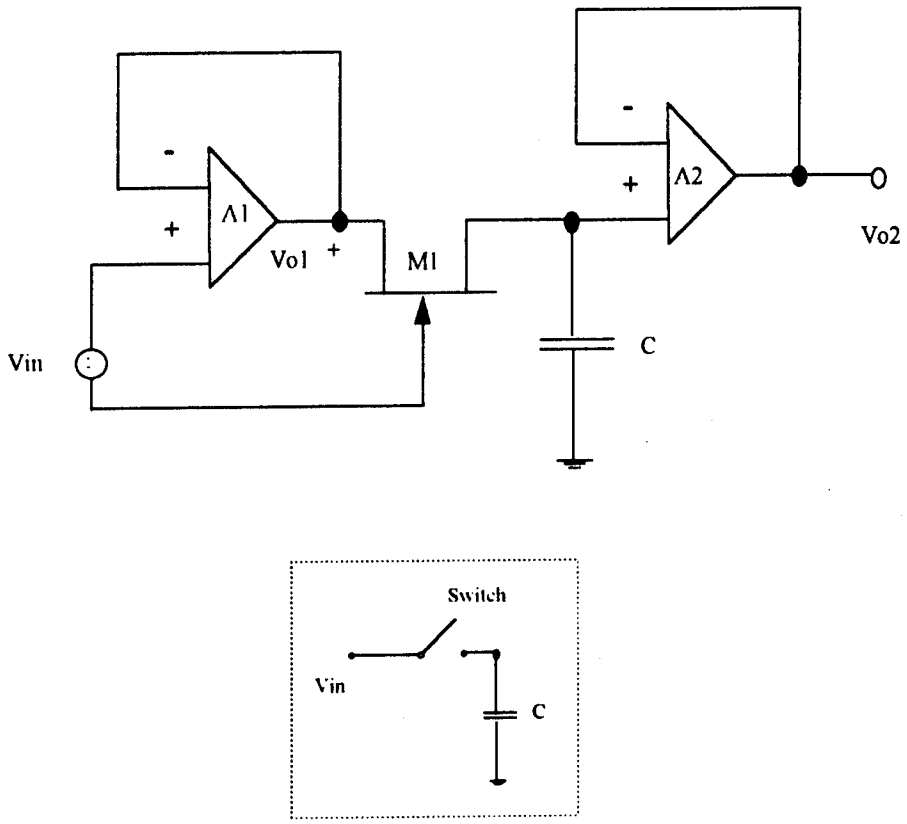

Figure 10 Sample and hold circuit

controlled by a gating signal, such as an injected optical signal, or CMOS transmission type gate. As discussed in the introduction of this Chapter, an optically gated MESFET can be switched 100% ON when injected and OFF. The capacitor should be implemented with a dielectric that retains the voltage impressed upon it (polymers are excellent). Some dielectrics are sensitive to a polarization which causes the stored voltage to decay or exhibit dielectric absorption which causes

capacitor to have memory of a previous charge, and therefore, these dielectrics would not be useful in this application.

A simple practical sample and hold circuit is shown in Figure 10. If the input signal V_{in} is zero, then both V_{o1} and V_{o2} are zero. If the input is on, then the instantaneous voltage across the capacitor follows V_{in} with a time constant τ. If the output resistance of the input operational amplifier (A1) is R_{o1} and the MESFET M1 has an output resistance r_{DS}, then the time constant τ is equal to $(R_{o1} + r_{DS})C$. Now, if V_{in} is shut off, then the capacitor is isolated from any load through A2, and therefore, holds the voltage from the charge cycle. The acquisition time is the time the capacitor needs to change from one level to a new input level after the switch is closed and is related to the maximum current that A1 can deliver since $dV_{cap}/dt = I/C$. Circuit methods can be used to bolster the current to the capacitor; thereby, reducing the acquisition time.

It is conceivable that the circuit can be implemented using optical polymers and MESFET devices. Also, the output of the latch may feed directly into a waveguide switching element that addresses some other device. This is a truly integrated microwave-optic device.

9.5 Digital Clock Control and Distribution

Another application of optically injected oscillators is clock distribution and synchronization. A synchronous computer architecture is based on clock networks that do not exhibit significant clock skew. Computer speeds are increasing. Computer boards are becoming more and more dense. The quantity of boards, which comprise a system, is also increasing. These factors restrict the ability to distribute clocks in the hundreds of MHz without clock synchronization problems. Although non-synchronous architectures exist, they are more complicated to implement and slower than their synchronous counterparts. It is possible to optically distribute a modulated clock signal which is injected into a MESFET oscillator as shown in Figure 11.

The MESFET oscillator is locked to the heterodyned locked optical signal. The oscillator is a direct interface to the optical signal. Because the optical signal is locked and the optical power required to lock to the oscillator is small, it is possible to distribute and lock to many oscillator circuits. Each oscillator frequency will be totally locked to the optical signal and, therefore, exactly identical. This system provides identically frequency locked signals which make it perfect for clock distribution applications.

Each board can have one or more MESFET oscillators depending on the board density and required clock network. Each MESFET oscillator will be optically injection locked to the modulated signal and therefore, achieve clock

synchronization. It is our proposal to apply optically injection locked oscillators to clock distribution networks in computer applications.

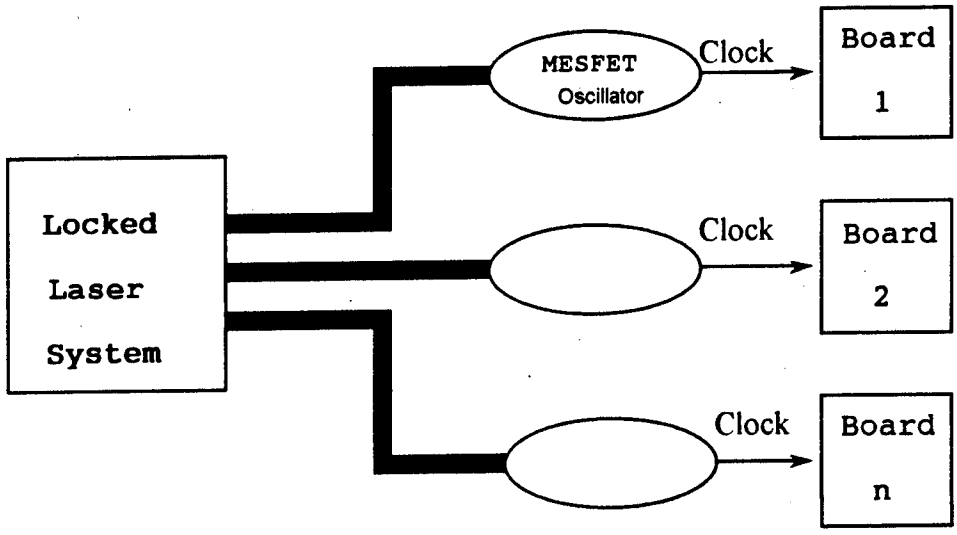

Figure 11 Computer Clock distribution and control

9.6 Conclusion

The locked laser system was applied to a WDM microwave communications link. The locked lasers provide narrower linewidths, reduced frequency chirp and reduced harmonic spreading which are all necessary attributes of a WDM system. Also, the optically injected MESFET circuits were applied to a phased array radar system, to coherent detection and amplification of high speed communications data, to an optically gated sample and hold circuit and to computer clock distribution and control. In all cases, the stabilized frequency and the ability to control a microwave circuit optically are enhancements to existing applications. In this thesis, experimental and theoretical data have been presented that can advance these applications.

9.7 References - Chapter 9

[1] R. Glatz, A.S. Daryoush, and P.R. Herczfeld, "Theoretical and Experimental Analysis of Optically Tuned Patch Antenna", *AP-S International Symposium Digest: Antennas and Propagation*, IEEE, New York, 1987.

[2] A.S. Daryoush, "Optical Synchronization of Millimeter-Wave Oscillators for Distributed Architectures", *IEEE Transactions on Microwave Theory and Techniques*, vol.38, no.5, May 1990, pp.467-475.

[3] Z Ma., M.H. White, R.D. Esman, et.al. "A High-Performance Optically Injected Synchronous Oscillator", *IEEE Photonics Technology Letters*, vol.4, no.4, April 1992, pp.405-408.

[4] A.S. Daryoush, P. Hercfeld, et.al., "Optical Beam Control of mm-Wave Phased Array Antennas for Communications", *Microwave Journal*, March 1987, pp.97-104.

[5] A.S. Daryoush, "Optical Synchronization of Millimeter-Wave Oscillators for Distributed Architectures", *IEEE Transactions on Microwave Theory and Techniques*, vol.38, no.5, May 1990, pp.467-475.

[6] D.C. Buck, and M.A. Cross, "Optical Injection Locking of FET OScillators using Fiber Optics", *IEEE-MTT-S Digest*, 1986, pp.611-614.

[7] R.D. Esman, K.J. Williams, and V. Uzunoglu, "Microwave Subcarrier and Clock Recovery by an Optically Injected CPSO", *IEEE Photonics Technology Letters*, vol.3, no.2, February 1991, pp.179-181.

[8] R. Kersten, and M. Rocks, "Wavelegth Division Multiplexing in Optical Communication Systems", *IEEE Journal of Optical Communications*, vol.4, no.2, 1982, pp.93-100.

[9] R. Olshansky, V.A. Lanzisera, and P.M. Hill, "Subcarrier Multiplexed Lightwave Systems for Broad-Band Distribution", *IEEE Journal of Lightwave Technology*, vol.7,no.9, September 1989, pp.1329-1341.

[10] T.E. Darcie, et.al., "Wide-Band Lightwave Distribution System Using Subcarrier Multiplexing",*IEEE Journal of Lightwave Technology*, vol.7,no6, June 1989, pp.997-1004.

[11] Peter J. Heim, and Phillip C. McClay, "Frequency Division Multiplexed Microwave and Baseband Digital Optcial Fiber Link for Phased Array Antennas", *IEEE Transactions on Microwave Theory and Techniques*, vol.38, no.5, May 1990, pp. 494-500.

[12] S.C. Liew, and K. Cheung, "A Broad-Band Optical Network Based on Hierarchical Multiplexing of Wavelengths and RF Subcarriers", *IEEE Journal of Lightwave Technology*, vol.7, no.11, November 1989, pp.1825-1838.

[13] R. Olshansky, V.A. Lanzisera, and P.M. Hill, "Subcarrier Multiplexed Lightwave Systems for Broad-Band Distribution", *IEEE Journal of Lightwave Technology*, vol.7,no.9, September 1989, pp.1329-1341.

[14] Robert Olshansky, Vincent Lanzisera, and Paul Hill, "Design and Performance of Wideband Subcarrrier Multiplexed Lightwave Systems", *14th European Conference on Optical Communication* (ECOC 88) (Conf.Publ.No.292) 1988, p.14306, vol.1.

[15] T.E. Darcie, et.al., "Wide-Band Lightwave Distribution System Using Subcarrier Multiplexing",*IEEE Journal of Lightwave Technology*, vol.7,no6, June 1989, pp.997-1004.

[16] S. Betti and A. Fioretti, "Numerical Analysis of Intermodulation Interferce in an Optical Coherent Multichannel System", *IEEE Journal of Lightwave Technology*, vol.LT-5, no.4., April 1987,pp.587-590.

[17] David W. Smith, "Techniques for Multigigabit Coherent Optcial Transmission", *Journal of Lightwave Technology*, vol. 5, no.10, October 1987, pp.1466-1478.

[18] David W. Smith, "Techniques for Multigigabit Coherent Optcial Transmission", *Journal of Lightwave Technology*, vol. 5, no.10, October 1987, pp.1466-1478.

[19], David W. Smith, "Techniques for Multigigabit Coherent Optcial Transmission", *Journal of Lightwave Technology*, vol. 5, no.10, October 1987, pp.1466-1478., p.1469

[20] J.Garrett and G. Jacobson, "The effect of laser linewidth on coherent optical receivers," *Jourant of Lightwave Technology*, vol. LT-5, no.4, pp.551-563, April 1987.

[21] L.G. Kasovsky, "Performance analysis and laser linewidth requirements for optical PSK heterodyne communications systems, " *Journal of Lightwave Technology*, vol.LT4, pp.415-524, 1986.

[22] G. Nicolson, "Probability of error for optical heterodyne DPSK system with quantum noise, " *Electronics Letters*, vol. 20, pp. 1005-1007, 1984.

[23] J.G. Hodgkinson, "Receiver analysis for synchronous optical fiber transmission systems, " *Journal of Lightwave Technology*, vol.LT-5, no.4, pp.573-586, April 1987.

[24] T. Okoshi, and K. Kikuchi, "Hetrodyne-Type Optical Fiber Communications", *Journal of Optical Communications*, vol.2, no.3, 1981, pp.82-88.

[25] Richard A. Linke, and Alan H. Gnauck, "High-Capacity Coherent Lightwave Systems", *Journal of Lightwave Technology*, vol.6, no.11, November 1988, pp.1750-1769.

[26] I.W. Stanley, G.R. Hill, and D.W. Smith, "The Application of Coherent Optical Techniques to Wide-Band Networks",*IEEE Journal of Lightwave Technology*, vol.LT-5, no.4, April 1987, pp.439-450.

[27] J.Garrett and G. Jacobson, "The effect of laser linewidth on coherent optical receivers," *Jouranl of Lightwave Technology*, vol. LT-5, no.4, pp.551-563, April 1987.

[28] G. Nicolson, "Probability of error for optical heterodyne DPSK system with quantum noise, " *Electronics Letters*, vol. 20, pp. 1005-1007, 1984.

[29] J.G. Hodgkinson, "Receiver analysis for synchronous optical fiber transmission systems, " *Journal of Lightwave Technology*, vol.LT-5, no.4, pp.573-586, April 1987

[30] L.G. Kasovsky, "Performance analysis and laser linewidth requirements for optical PSK heterodyne communications systems, " *Journal of Lightwave Technology*, vol.LT4, pp.415-524, 1986.

[31] Z. Ma, M. H. White, K. J. Williams, R. D. Esman, and V. Uzunoglu, "A high performance optically injected synchronous oscillator", *IEEE Photonics Technology Letters*, vol.4, pp.405-408, April 1992.

[32] A. Daryoush, "Optical Synchronization of Millimeter-wave oscillators for distributed architectures", *IEEE Trans. Microwave Theory and Tech.*, vol. 38, pp.467-476, May 1990.

[33] P.Wahi, et.al, "Comparison of indirect optical injection locking techniautes of multiple X-band oscillators", *IEEE MTTT-S Digest*, pp. 615-618, 1986.

CHAPTER 10

THESIS CONCLUSIONS

This Thesis studied the modulation properties of an injection locked laser system. When injection locked, reduced noise and increased harmonic content occur which were shown experimentally and theoretically in Chapter 2. Also, the transfer function was developed for the modulated locked laser system. In Chapter 3, the photo-effects in a MESFET device were the result of increases in minority carrier concentration. The optical gain was found to be more than 100. Although hole currents are generated, their addition to existing currents is a small effect. The most significant effect is the effective voltage developed in the space charge region created by the concentration of minority carriers. This voltage is transverse to the channel and was modeled with the Schottky barrier diode equations. Experimental measurements of the photo-voltage match reasonably well with the Schottky model. In Chapter 6, a large signal model has been adapted to include the optical effect by superimposing the photo-voltage onto the existing gate bias.

In Chapter 4, the theory of oscillation and injection phenomenon was studied. The laser and microwave oscillator were shown to follow the same model. This work allows both the laser and oscillator to be modeled with the same theory by a substitution of the constants. Chapter 5 detailed the experimental phase of this research. Engineering problems were documented so that any future work will be

able to learn from this research. Also, enhancements to the system, such as pig-tail MESFET with an optical fiber, and growing a micro-lens on the fiber endface, were given in Chapter 5.

The microwave oscillator was characterized under various locking conditions in Chapter 7. The reduction of phase noise due to direct optical injection locking of a microwave oscillator was reported. Details of the optical spectrum under locking conditions were shown experimentally. Frequency shifts of 40 MHz were found when biased near pinchoff. Also, the circuit elements were measured with and without light injection. The oscillator was simulated via SPICE with good qualitative results. The simulation showed locking and increased harmonic content when locked.

The microwave amplifier was injected with various modulation formats in Chapter 8 as a method for detecting optical signals directly into an active device. The large signal model, that was developed in Chapter 6, showed excellent results. An error 3-5% was calculated between the theoretical and measured circuit parameters. The amplifier gain was shown to result from g_m or S21 both analytically and experimentally. Also, the amplifier was simulated via SPICE with good qualitative results.

In Chapter 9, applications of the optically injected microwave oscillator and amplifier were discussed. WDM, integrated microwave-optics, phased array radar and computer clock control are some of the areas that could benefit from transmitting signals via optical fiber and utilize the low phase noise and increased harmonic content of an injection locked oscillator.

BIBLIOGRAPHY

Robert Adler, "A study of Locking Phenomena in Oscillators", *Proceedings of IRE and Waves and Electrons*, vol. 34, 1946, pp. 351-357.

G.P. Agrawal , "Power Spectrum of Directly Modulated Single Mode Semiconductor Lasers", *IEEE Journal of Quantum Electronics*, vol.QE-21, pp. 680-698, 1985.

G.P. Agrawal , and Shen, T.M. , "Pulse-Shape Effects on Frequency Chirping in Single-Frequency Semiconductor Lasers Under Current Modulation", *Journal of Lightwave Technology*, vol.-LT-4, no.5, May 1986, pp. 497-503.

G.P. Agrawal , Intensity Dependence of the Linewidth Enhancement Factior and Its Implications for Semiconductor Lasers, *IEEE Photonics Technology Letters*, vol.1, no.8, August 1989, pp. 212-214.

G.P. Agrawal , N.K. Dutta, and N.A. Olsson, "Reduced Chirping in Coupled-cavity-semiconductor Lasers", *Journal of Applied Physics*, vol.45, no.2, July 15, 1984, pp. 119-121.

G.P. Agrawal , R. Roy, "Effect of Injection-Current Fluctuations on the Spectral Linewidth of Semiconductor Lasers", *Physical Review*, vol.37, no.7, April 1, 1988, pp. 2495-2501.

W. Baechtold , "Noise Behavior of Schottky Barrier Gate Field-Effect Transistors at Microwave Frequencies", *IEEE Transactions on Electron Devices*, vol.ED-18, No.2, February 1971, pp. 97-104.

S. Betti and A. Fioretti, "Numerical Analysis of Intermodulation Interferce in an Optical Coherent Multichannel System", *IEEE Journal of Lightwave Technology*, vol.LT-5, no.4., April 1987,pp. 587-590.

Kjell Blotekjaer , "Transport Equations for Electrons in Two-Valley Semiconductors", *IEEE Transactions on Electron Devices*, vol. ed-17, no. 1, January 1970, pp. 38-47.

Max Born and Emil Wolf, Principles of Optics, Pergamon Press, 1989.

R.H. Bube , Photoconductivity of Solids, John Wiley & Sons, Inc., 1960.

R.H. Bube , Photoelectronic properties of semiconductors, Cambridge University Press, 1992.

T.J Buchanan , "The Frequency Spectrum of a Pulled Oscillator", *Proceedings of the IRE*, August 1952, pp. 958-961.

D.C. Buck , and M.A. Cross, "Optical Injection Locking of FET Oscillators using Fiber Optics", *IEEE-MTT-S Digest*, 1986, pp. 611-614.

C. Chang , and D.S. Day, "Analytic Theory for Current-Voltage Characteristics and Field Distribution of GaAs MESFET's", *IEEE Transactions on Electron Devices*, vol. 36, no.2, Februrary 1989, pp. 269-280.

C.H. Chien , and G.C. Dalman, "Subharmonically Injected Phase-locked IMPATT-Oscillator Experiments", *Electronics Letters*, vol.6, no.8, April 1970, pp. 240-241.

C.R. Crowell and S.M.Sze, "Current Transport in Metal-Semiconductor Barriers," *Solid State Electron.*, vol.26, pp. 705-709, Nov./Dec. 1966.

W.R. Curtice , and M. Ettenberg, "A Nonlinear GaAs FET Model for use in the Design of Output Circuits for Power Amplifiers", *IEEE Transactions on Microwave Theory and Techniques*, vol. MTT-33, no. 12, December 1985.

Walter R. Curtice , "A MESFET Model for Use in the Design of GaAs Integrated Circuits", *IEEE Transactions on Microwave Theory and Techniques*, vol. MTT-28, no.5, May 1980, pp. 448-456.

T.E. Darcie , et.al., "Wide-Band Lightwave Distribution System Using Subcarrier Multiplexing",*IEEE Journal of Lightwave Technology*, vol.7,no6, June 1989, pp. 997-1004.

R.B. Darling , "Analysis of Microwave Characteristics of Photoconductive IC Structures", *IEEE Journal of Lightwave Technology*, vol. LT-5, no. 3, March 1987, pp. 325-339.

R.B. Darling , "Optical Gain and Large-Signal Characteristics of Illuminated GaAs MESFET's", *IEEE Journal of Quantum Electronics*, vol. QE-23, no.7, July 1987, pp. 1160-1171.

R.B. Darling , "Transit-Time Photoconductivity in High-Field FET Channels", *IEEE Transactions on Electron Devices*, vol. ed-34, no.2, Fegruary 1987, pp. 433-443.

A.S. Daryoush , P. Wahi, P.R. Herczfeld, and Z. Turski, "Comparison of Indirect Optcial Injection Locking Techniques of Multiple X-Band Oscillators", *IEEE MTT-S Digest*, June 1986, pp. 615-618.

A. Daryoush, "Optical Synchronization of Millimeter-wave oscillators for distributed architectures", IEEE Trans. Microwave Theory and Tech., vol. 38, pp. 467-476, May 1990.

A.S. Daryoush, "Optical Synchronization of Millimeter-Wave Oscillators for Distributed Architectures", *IEEE Transactions on Microwave Theory and Techniques*, vol.38, no.5, May 1990, pp. 467-475.

A.S. Daryoush, P. Hercfeld, et.al., "Optical Beam Control of mm-Wave Phased Array Antennas for Communications", *Microwave Journal*, March 1987, pp. 97-104.

A.A. DeSalles, "Optical Control of GaAs MESFETs", *IEEE Transactions on Microwave Theory and Techniques*, vol.mtt-31, no.10, October 1983, pp. 812-820.

A.A. DeSalles, "Optical Effects in HEMTs", *Microwave and Optical Technology Letters*, vol.3, no.10, October 1990, pp. 350-354.

A.A. DeSalles, and M.A. Romero, "AlGaAs/GaAs HEMT's Under Optical Illumination", *IEEE Transactions on Microwave Theory and Techniques*, vol. 39, no.12, December 1991, pp. 2010-2017.

R. D. Esman , K. J. Williams, M. H. White, and V. Uzunoglu, "Microwave subcarrier and clock recovery by an optically injected CPSO", *IEEE Photonics Tech. Lett.*, vol. 3, pp. 179-181, February 1991.

R. D. Esman , L. Goldberg, and J. F. Weller, "Optical phase control of an optically injection-locked FET microwave oscillator", *IEEE Trans. Microwave Theory and Tech.*, vol. 37, pp. 1512-1518, October 1989.

R.D. Esman , K.J. Williams, and V. Uzunoglu, "Microwave Subcarrier and Clock Recovery by an Optically Injected CPSO", *IEEE Photonics Technology Letters*, vol.3, no.2, February 1991, pp. 179-181.

H.J. Fukui , "Determination of the Basic Device Parameters of a GaAs MESFET", *Bell System Technical Journal*, vol.58, no.3, March 1979, pp. 771-797.

H. Fukui , "Optimal Noise Figure of Microwave GaAs MESFET's",*IEEE Transactions on Electron Devices*, vol.ED-26, no.7, July 1979, pp. 1032-1037.

J.C. Gammel and J.M. Ballantyne, "Integrated photoconductive detector and waveguide structure", *Applied Physics Letters*, vol36, no.2, Janurary 15, 1980, pp. 149-151.

J.C. Gammel and J.M. Ballantyne, "The OPFET: A new high-speed optical detector, " *Proc. IEDM*, pp. 120-123, 1978.

J.C. Gammel, and J.M. Ballantyne,"The OPFET: A New High Speed Optical Detector", *Proc. IEDM*, 1978, pp. 120-123."

J. Garrett and G. Jacobson, "The effect of laser linewidth on coherent optical receivers," *IEEE Journal of Lightwave Technology*, vol. LT-5, no.4, pp. 551-563, April 1987.

Bernard G. Glance , "An optical Heterdoyne Mixer Providing Image-Frequency Rejection", *IEEE Journal of Lightwave Technology*, vol.LT-4, no.11, November 1986, pp. 1722-1725.

R. Glatz, A.S. Daryoush, and P.R. Herczfeld, "Theoretical and Experimental Analysis of Optically Tuned Patch Antenna", AP-S International Symposium Digest: Antennas and Propagation, IEEE, New York, 1987.

L. Goldberg, C. Rauscher, J.F. Weller, and H.F. Taylor, "Optical Injection Locking of X-Band FET Oscillator using Coherent Mixing of FaAlAs Lasers", *Electronics Letters*,vol. 19, no. 20, September 29, 1983, pp. 848-850.

J. Michael Golio, Microwave MESFETs & HEMTs, Artech House, Inc., 1991.

J. Graffeuil, P. Rossel, and H. Martinot, "Light-induced effects in GaAs FETs," *Electron Lett.*, vol. 15, pp. 439-441, 1979.

A.B. Grebene, and S.K. Ghandhi, "General Theory for Pinched Operation of the Junction-Gate FET", *Solid State Electronics*, Pergamon Press 1969, vol.12, pp. 573-589.

R.N. Hall, "Electron-hole Recombination in Ge", *Phys Rev.*, vol.87, 1953, p.387.

Peter J. Heim , and Phillip C. McClay, "Frequency Division Multiplexed Microwave and Baseband Digital Optcial Fiber Link for Phased Array Antennas", *IEEE Transactions on Microwave Theory and Techniques*, vol.38, no.5, May 1990, pp. 494-500.

Charles H. Henry "Theory of Linewidth of Semiconductor Lasers", *IEEE Journal of Quantum Electronics*, vol. QE-18, no.2, February 1982, pp. 259-264.

Charles H. Henry, "Theory of the Phase Noise and Power Spectrum of a Single Mode Injection Laser", *IEEE Journal of Quantum Electronics*, vol. QE-19, no.9, September 1983, pp. 1391-1397.

P.R. Herczfeld, A.S. Daryoush, A., Rosen, A.K Sharma, and V.M. Contarino, "Indirect Subharmonic Optical Injection Locking of a Millimeter-Wave IMPATT Oscillator", *IEEE Transactions on Microwave Theory and Techniques*, vol. MTT-34, no. 12, December 1986, pp. 1371-1375.

J.G. Hodgkinson, "Receiver analysis for synchronous optical fiber transmission systems, " *IEEE Journal of Lightwave Technology*, vol.LT-5, no.4, pp. 573-586, April 1987.

H.J. Hovel, "Solar Cells", Semiconductor and Semimetals, Academinc Press, 1975.

R.D. Huntoon and A.Weiss, "Synchronzaiton of oscillators," *Proc. IRE,* Vol. 35, pp. 1415-1423, Dec.1947.

K. Iswashita , and K. Nakagawa, "Suppression of mode partition noise by laser diode light injection, " *IEEE Journal of Quantum Electronics*, vol. QE-18, pp. 1669-1674, 1982.

L.G. Kasovsky , "Performance analysis and laser linewidth requirements for optical PSK heterodyne communications systems, " *IEEE Journal of Lightwave Technology*, vol.LT4, pp. 415-524, 1986.

R. Kersten , and M. Rocks, "Wavelegth Division Multiplexing in Optical Communication Systems", *IEEE Journal of Optical Communications*, vol.4, no.2, 1982, pp. 93-100.

H.C. Ki , S.H. Son, K. Park, andK.D. Kwack, "A Three-Section Model for computing I-V Characteristics fo GaAs MESFET's", *IEEE Transactions on Electron Devices*, vol. ed-34 no.9, September 1987, pp. 1929-1933.

K. Kikuchi , T. Okoshi, M. Nagamatsu, andN. Henmi, "Degradation of bit-error rate in coherent optical communications due to spectral spread of the transmitter and the lockal oscillator, " *IEEE Journal of Lightwave Technology*, vol. LT-2, pp. 1024-1033, 1984.

Francois M. Klassen , "On the Influence of Hot Carrier Effects on the Thermal HNoise of Field-Effect Transistors", *IEEE Transactions on Electron Devices*, vol.ED-17, no.10, October 1970, pp. 858-862.

S. Kobayashi , and T. Kimura, "Injection Locking Characteristics of an AlGaAs Semiconductor Laser", *IEEE Journal of Quantum Electronics*, vol.QE-16, no.9, September 1980, pp. 915-917.

S. Kobayashi , and T. Kimura, "Automatic Frequency Control in a Semiconductor Laser and an Optical Amplifier", *Journal of Lightwave Technology*, vol.LT-1, no.2, June 1983, pp. 394-402.

S. Kobayashi , and T. Kimura, "Optical Phase Modulation in an Injection Locked AlGaAs Semiconductor Laser", *IEEE Journal of Quantum Electronics*, vol.QE-18, no.10, October 1982, pp. 1662-1669.

S. Kobayashi, and T. Kimura, "Injection Locking in AlGaAs Semiconductor Laser", *IEEE Journal of Quantum Electronics*, vol.QE-17, no.5, May 1981, pp. 681-689.

S. Kobayashi, Y. Yamamoto, M. Ito, and T. Kimura, "Direct Frequency Modulation in AlGaAs Semiconductor Lasers", *IEEE Journal Of Quantum Electronics*, vol.18. vol.4. April 1982, pp. 582-595.

K.L. Kotzebue , "Microwave Transistor Power Amplifier Design by Large Signal Y Parameters", *Electronics Letters*, vol11, no.11, May 29, 1975, pp. 240-241.

N. Krylov, and N.Bogoliubov, Introduction to Nonlinear Mechanics, Princeton, N.J., Princeton University Press, 1943.

K. Kurokawa, "Injection Locking of Microwave Solid-State Oscillators", *Proceedings of the IEEE*, vol. 61, no. 10, October 1973, pp. 1386-1410.

Roy Lang , "Injection Locking Properties of a Semiconductor Laser", IEEE Journal of Quantum Electronics, vol. QE-18, no. 6, June 19882, pp. 976-983.

Roy Lang , and K. Kobayashi,"Suppression of the Relaxation Oscillation in the Modulated Output of Semiconductor Lasers", *IEEE Journal of Quantum Electronics*, vol.12, no. 3, March 19??, pp. 194-199.

M. Lax , "Classical noise in self sustained oscillators,", *Physics Review*, vol.160, pp. 290-307, 1967.

Kung S. Lee and Frank S. Barnes, "Microlenses on the end of single-mode optical fibers for laser applications", *Applied Optics*, vol.24, no. 19, pp. 3134-3139, October 1, 1985.

K. Lehovec , and R Zuleeg, "Voltage-Current Characteristics of GaAs J-FETs in the Hot Electron Range", *Solid State Electronics*, Pergamon PRess 1970, vol13, pp. 1415-1426.

W.H. Leighton , R.J. Chaffin, and J.G. Webb, "RF Amplifier Design with Large-Signal S-Parameters", *IEEE Transactions on Microwave Theory and Techniques*, vol.mtt-21, no.12, December 1973, pp. 809-814.

O. Lidoyne , Philippe B. Gallion, and D. Erasme, "Modulation Properties of an Injection-Locked Semiconductor Laser", *IEEE Journal of Quantum Electronics*, vol.27, no. 3, March 1991, pp. 344-351.

S.C. Liew , and K. Cheung, "A Broad-Band Optical Network Based on Hierarchical Multiplexing of Wavelengths and RF Subcarriers", *IEEE Journal of Lightwave Technology*, vol.7, no.11, November 1989, pp. 1825-1838.

Richard A. Linke , and Alan H Gnauck, "High-Capacity Coherent Lightwave Systems", *Journal of Lightwave Technology*, vol.6, no.11, November 1988, pp. 1750-1769.

S. E. Lipsky and A. S. Daryoush, "Fiber-optic Methos for injection-locked oscillators", *Microwave Journal*, pp. 80-88, January 1992.

Z. Ma, M. H. White, K. J. Williams, R. D. Esman, and V. Uzunoglu, "A high performance optically injected synchronous oscillator", *IEEE Photonics Technology Letters*, vol.4, pp. 405-408, April 1992.

A. Madjar, A.Paolella, P.Herczfeld, "Modeling the Optical Switching of MESFET's Considering the External and Internal Photovoltaic Effects", *IEEE Transactions on Microwave Theory and Techniques*, vol.42, no.1, January 1994, pp. 62-67.

A. Madjar, P. R. Herczfeld, and A. Paolella, "Analytical model for optically generated currents in GaAs MESFETs", *IEEE Trans. Microwave Theory and Tech.*, vol.40, pp. 1681-1691, 1992.

Alan Mickelson, Physical Optics,. 1992.

H. Mizuno , "Microwave characteristics of an optically controlled GaAs MESFET", *IEEE Trans. MTT*, vol.MTT-31, no.7, July 1983, pp. 596-599.

G. Nicolson , "Probability of error for optical heterodyne DPSK system with quantum noise, " *Electronics Letters*, vol. 20, pp. 1005-1007, 1984.

G. Nicolson "Probability of error for optical heterodyne DPSK system with quantum noise, " *Electronics Letters*, vol. 20, pp. 1005-1007, 1984.

O. Nilsson , Y. Yamamoto, and S. Machida, "Internal and External Field Fluctuations of a Laser Oscillator: Part II- Electrical Circuit Theory", *IEEE Journal of Quantum Electronics*, vol. QE-22, no.10, October 1986, pp. 2043-2051.

J.P. Noad , E.H. Hara, R.H. Hum, and R.I. Macdonald, "FET Photodectors: A Combined Studing Using Optical and Electron-Beam Stimulation", *IEEE Transactions on Electron Devices*, vol. ed-29, no.11, November 1982, pp. 1792-1797.

T. Okoshi , and K. Kikuchi, "Heterodyne-Type Optical Fiber Communications", *Journal of Optical Communications*, vol.2, no.3, 1981, pp. 82-88.

Robert Olshansk y, Vincent Lanzisera, and Paul, Hill, "Wideband Modulation of Semiconductor Lasers for Microwave-Multiplexed Lightwave Systems", *11th IEE International Semiconductor Laser Conference*, August 29-Sept 1, 1988, pp. 52-53.

R. Olshansky , and D. Fye, "Reduction of Dynamic Linewidth in Single-Frequency Semiconductor Lasers", *Electronics Letters*, vol.20, no., 22, October 25, 1984, pp. 928-929

R. Olshansky , V.A., Lanzisera, and P.M. Hill, "Subcarrier Multiplexed Lightwave Systems for Broad-Band Distribution", *IEEE Journal of Lightwave Technology*, vol.7,no.9, September 1989, pp. 1329-1341.

Robert Olshansky , Vincen Lanzisera, t, and Pau Hill,l, "Design and Performance of Wideband Subcarrrier Multiplexed Lightwave Systems", *14th European Conference on Optical Communication* (ECOC 88) (Conf.Publ.No.292) 1988, p.14306, vol.1.

H.G. Oltman, and C.H. Nonnemaker, "Subharmonically Injection Phase-Locked Gunn Oscillator Experiments", *IEEE Transactions on Microwave Theory and Techniques*, vol. MTT-17, September 1969, pp. 728-729.

Jacques I. Pankove , Optical Processes in Semiconductors, Dover Pulbications, Inc., New York, pp. 170-174, 202, 302-336.

Isabelle Petitbon, Philippe Gallion, Guy, Debarge, and Claude Chabran, "Locking Bandwidth and Relaxation Oscillations of Injection-Locked Semiconductor Laser", *IEEE Journal of Quantum Electronics*, vol. 24, no. 2, February 1988, pp. 148-154.

David M. Pozar , Microwave Engineering, Addison-Wesley Publishing Company,1990, pp. 240-244, 611-626.

R.A. Pucel , H.A. Haus, andH. Statz, "Signal and Noise Properties of GaAs Microwave Field-Effect Transistors", Advances in Electronic and Electron Physics, edited by L.Marton, Academic Press, vol.38, 1975, pp. 195-265.

A. Rose, "Performance of Photoconductors", *Proceedings of the IRE*, December 1955, pp. 1850-1869.

J.G. Ruch , "Electron Dynamics in Short Channel Field-Effect Transistors", *IEEE Transactions on Electron Devices*, vol. ed-19, May 1972, pp. 652-654.

P. Russer , and G. Arnold, "Direct Modulation of Semiconductor Injection Lasers", *IEEE Transactions on Microwave Theory and Techniques*, vol.30, no.11, November 1982, pp. 1809-1821.

G. Sato , "Stabilized oscillators by using injection locking and phase-locked loop, " *Electron. Commun. Japan*, vol. 54-B, pp. 59-65, 1971.

A. Schweighart, H.P. Vyas, J.M. Borrego, "Avalance diode structurse suitable for microwave-optical interactions", *Solid-State Electronics*, vol.21, no.9, September 1978, pp. 1119-1121.

A.J. Seeds, J.F. Singleton, S.P. Brunt, and J.R Forrest, "The Optical Control of IMPATT Oscillators", *IEEE Journal of Lightwave Technology*, vol. LT-5, no. 3, March 1987, pp. 403-411.

Anthony E. Seigman, Lasers, University Science Books, California, 1986, pp. 954-972.

R.C. Shaw , and H.L. Stover, ""Phase-Locked Avalanche Diode Oscillators", *Proceedings of the IEEE*, vol. 54, April 1970, pp. 710-711.

W. Shockley , and W.T.Read, "Statisitics of Reocombination of Holes and electrons", *Phys Rev*, vol87, 1952, p.832

W. Shockley , Electrons and Holies in Semiconductiors, Van Norstrand, Princetion, NJ, 1950.

W. Shockley , *Proc. IRE*, vol.40, pp. 1365-1376, 1952.

R.N. Simons and K. B. Bhasin, "Analysis of optically controlled microwave/millimeter wave device structures", *IEEE MTT-S Digest*, pp. 551-554, 1986.

R.N. Simons , and K.B. Bhasin, "Analysis of Optically Controlled Microwave-Millimeter-Wave Device Structures", *IEEE Transactions on Microwave Theory and Techniques*, vol. MTT-34, no.12, December 1986, pp. 1349-1355.

R.N. Simons, "Microwave Performance of an Optically Controlled AlGaAs/GaAs High Electron Mobility Transistor and GaAs MESFET", *IEEE Transactions on Microwave Theory and Techniques*, vol. MTT-35, no.12, December 1987, pp. 1444-1455.

J.C. Slater, Microwave Electronics, NY., Van Nostrand, 1950.

David W. Smith , "Techniques for Multigigabit Coherent Optcial Transmission", *Journal of Lightwave Technology*, vol. 5, no.10, October 1987, pp. 1466-1478., p.1469

W. Smith , Nature, vol.7, p.303, 1837.

I.W. Stanley, G.R. Hill, and D.W. Smith, "The Application of Coherent Optical Techniques to Wide-Band Networks",*IEEE Journal of Lightwave Technology*, vol.LT-5, no.4, April 1987, pp. 439-450.

H. Statz , H.A. Haus, and R.A. Pucel, "Noise Characteristics of Gallium Arsenide Field-Effect Transistors", *IEEE Transactions on Electron Devices*, vol.ED-21, No.9, September 1974, pp. 549-562.

D.T. Stevenson , and R.J. Keyes, "Measurement of Carrier Lifetime in Ge and Si", *J.Applied Phys*, vol26, 1955, p.190.

H.L. Stover, and R. Steir, "Locking of Laser oscillators by light injection," *Applied Physics Letters*, vol.8, pp. 91-93, February 6, 1966.

A.S. Sudbo, "The Frequency Chirp of Current Modulated Semiconductor Diode Lasers",*IEEE Journal of Quantum Electronics*, vol.QE-22, no.7, July 1986, pp. 1006-1008.

A.S. Sudbo, and L. Hafskjaer, "Modeling of the Frequency Modulation Response of Semiconductor Diode Lasers", *IEEE Journal of Quantum Electectronics*, vol.24,no.4, April 1988, pp. 625-634.

H.J. Sun , R. J. Gutmann and J. M. Borrego, "Optical Tuning in GaAs MESFET Oscillators", *1981 IEEE MTT-S International Microwave Symposium Digest*, pp. 40-42.

H. Sun , R. J. Gutmann and J. M. Borrego, "Photoeffects in common-source and common-drain microwave GaAs MESFET oscillators", *Solid State Electronics*, vol. 24, pp. 935-940, 1981.

Marc Surette , "Noise Properties of Injection Locked Semiconductor Lasers: Application to Optically Driven Phased Array Antennas", Ph.D. Thesis, University of Colorado, 1991.

S.M. Sze , Physics of Semicondcutor Devices, John Wiley& Sons, New York, first edition 1969.

S.M. Sze , Physics of Semiconductor Devices, John Wiley & Sons, NY, 1981.

R.S. Tucker , "Microwave Circuit Models of Semiconductor Lasers", *IEEE Transactions on Micro* Pope, *wave Theory and Techniques*, vol.MTT-31, no.3, March 1983, pp. 289-294.

B. Van der Pol, "The Nonlinear Theory of Electric Oscillations", *Proceedings of the IRE*, vol. 22, no.9, September 1934, pp. 1051-1086.

A. Van der Ziel, "Gate Noise in Field Effect Transistors at Moderately High Frequencies", *Proc. of IEEE*, 1963, pp. 461-467.

A. Van der Ziel, "Small-signal, High-frequency Theory of Field-Effect Transistors", *IEEE Transactions of Electron Devices*, vol. 11, 1964, pp. 128-135.

A. Vyas, H.P. Borrego, J.M. Gutmann,"the effect of hole versus electron photocurrent on microwave-optical interactions in IMPATT Oscillators", *IEEE Transactions on Electron Devices*, vol. ed-26, no. 3, March 1979, pp. 232-234.

P. Wahi , et.al, "Comparison of indirect optical injection locking techniautes of multiple X-band oscillators", *IEEE MTT-S Digest*, pp. 615-618, 1986.

D. Warren , J.Michael Golio, and E. Johnson, "Simulation of Optically Injection-Locked Microwave Oscillators Using a Novel SPICE Model", *IEEE Transactions on Microwave Theory and Techniques*, vol. 36, no.11, November 1988, pp. 1535-1539.

D. Welford , "A rate equation analysis for the frequency chirp modulated pwoer ratio of semiconductor diode laser," *IEEE Journal of Quantum Electronics*, vol. QE-21, pp. 1749-1751, 1985.

Y. Yamamoto, and I. Nobuyuki, "Internal and External Field Fluctuations of a Laser Oscillator: Part I- Quantum Mechanical Langevin Treatment", *IEEE Journal of Quantum Electronics*, vol. QE-22, no.10, October 1986, pp. 2032-2042.

H.W. Yen , M. K. Barnoski, "Optical injection locking of FET oscillators using fiber optics", *Appl.Phys. Lett.*, vol. 32, pp. 182-184, 1978.